Study of the Z Boson Production at the ATLAS Experiment with First Data

Dissertation an der Fakultät für Physik
der
Ludwig-Maximilians-Universität München

vorgelegt von
Matthias Schott
geboren in Nürnberg

München, Juni 2007

1. Gutachterin: Prof. Dr. Dorothee Schaile
2. Gutachter: Prof. Dr. Wolfgang Dünnweber

Datum der mündlichen Prüfung: 31.Juli.2007

Zusammenfassung

Am europäischen Forschungszentrum CERN werden zurzeit die letzten Installationsarbeiten am ATLAS Detektor beendet, um ab dem Jahr 2008 Proton-Proton Kollisionen bei einer Schwerpunktsenergie von 14 TeV präzise zu vermessen.

Eine detaillierte Messung des totalen Wirkungsquerschnitts und des transversalen Impulsspektrums der Z-Boson Produktion am LHC ist aus vielerlei Gründen wichtig. Zum einen liefert die Messung einen weiteren Test des Standardmodells, zum anderen ist die Analyse sensibel auf neue exotische physikalische Prozesse. Die Eigenschaften der Z-Boson Resonanz und deren Zerfall in zwei Myonen ist mit sehr hoher Präzision sowohl theoretisch vorhergesagt als auch bei den LEP Experimenten untersucht. Daher ist dieser Zerfall auch ein wichtiger Referenzprozess für die Kalibration und die Alignierung des ATLAS Detektors. Als ein letzter Grund ist zu nennen, dass die Produktion von Z-Bosonen am LHC einen großen Untergrund für andere Physikanalysen darstellt und folglich gut verstanden sein muss.

In dieser Arbeit wird eine Strategie aufgezeigt und diskutiert, wie der Wirkungsquerschnitt σ für den Prozess $pp \to \gamma^*/Z \to \mu^+\mu^-$ während der ersten Datennahme am ATLAS Experiment bestimmt werden kann. Als Ergebnis dieser Studie wird eine Genauigkeit von

$$\frac{\Delta\sigma}{\sigma} \approx 0.006(\text{stat}) \pm 0.008(\text{sys}) \, ^{+0.016}_{-0.008}(\text{pdf})$$

bei einer integrierten Luminosität von $50\,pb^{-1}$ unter der Annahme eines voll funktionsfähigen Detektors und unter Vernachlässigung der Unsicherheiten der Luminositätsmessung erwartet. Eine wichtige Zielsetzung bei der Entwicklung der Messstrategie war die Minimierung von Abhängigkeiten von Monte Carlo Simulationen. Folglich wurden mehrere Methoden zur Bestimmung des Detektorverhaltens aus Daten detailliert untersucht.

In einem zweiten Schritt wird ein Ansatz zur Messung des differentiellen Wirkungsquerschnitts $\frac{d\sigma}{dp_T^Z}$ des Transversalimpuls des Z-Bosons vorgestellt und diskutiert, der ebenfalls für die erste Datennahme entwickelt wurde. Im Gegensatz zur Messung des totalen Wirkungsquerschnitts wird bei dieser Messung eine dominierende statistische Unsicherheit erwartet. Es wird gezeigt, dass die erwartete Genauigkeit der Transversalimpulsmessung von Myonen die erstmalige Beobachtung von interessanten Effekten der Parton Dichte Funktionen schon mit ersten Daten ermöglicht.

Abstract

The ATLAS detector, currently in its final installation phase at CERN, is designed to provide precise measurements of 14 TeV proton-proton collisions at the Large Hadron Collider.

The measurements of the cross section and transverse momentum spectrum of the Z boson production at LHC provides first tests of the standard model in a new energy domain and may reveal exotic physics processes. Moreover, the properties of the Z boson resonance and its decay into two muons are known to very high precision from LEP experiments and hence can be used as a physics process for calibration and alignment. The Z boson production is also a common background process for many other physics analyses and must therefore be well understood.

This thesis describes a measurement strategy of the cross section σ for the process $pp \rightarrow \gamma/Z \rightarrow \mu^+\mu^-$ at the ATLAS experiment during its startup phase. As a result of this study a precision of

$$\frac{\Delta\sigma}{\sigma} \approx 0.006(\text{stat}) \pm 0.008(\text{sys}) \, ^{+0.016}_{-0.008}(\text{pdf})$$

is expected for an integrated luminosity of $50\,pb^{-1}$, assuming a fully operational ATLAS detector, not including uncertainties in the luminosity measurements. A major goal of the approach presented was to minimize the dependence on Monte Carlo simulations. Hence, several methods for the determination of the detector response based on data have been studied.

In addition, a strategy for the differential cross section measurement $\frac{d\sigma}{dp_T^Z}$ of the transverse momentum of the Z boson has been developed. In contrast to a measurement of the total cross section, it is expected that the statistical uncertainty dominates for the given integrated luminosity of $50\,pb^{-1}$. The predicted high p_T resolution of the ATLAS Inner Detector and the Muon Spectrometer allow for the first observation of interesting parton distribution effects, i.e. the so-called x-broadening, even with the limited statistics expected during the first data taking period.

Contents

I Overview **1**

1 Introduction **3**

2 Theory of Z Boson Production at LHC in a Nutshell **5**

2.1 The Standard Model of Particle Physics 5

2.2 Theory of Proton-Proton Collisions 10

2.3 Monte Carlo Generators 12

2.4 The Production of Z Bosons at the LHC 13

3 The Large Hadron Collider **15**

4 The ATLAS Experiment **17**

4.1 The ATLAS Detector 18

4.1.1 Magnet System 19

4.1.2 Inner Detector 20

4.1.3 Calorimetric System 22

4.1.4 Muon Spectrometer 25

4.2 Trigger System and Data Acquisition 29

4.3 Physics Program 31

4.3.1 The Higgs Boson 31

4.3.2 Supersymmetry 32

4.3.3 Beyond the Standard Model 32

4.3.4 Precision Measurements 33

4.4 ATLAS Computing 34

4.4.1 The ATLAS Software Framework 34

4.4.2 Grid Computing 36

II Muon Spectrometer Performance **39**

5 Expected Performance of an Ideal Muon Spectrometer Setup **41**

5.1 Definitions . . . 42

5.2 Results . . . 43

6 Validation of the MDT Chamber Simulation with Cosmic Rays **47**

7 Impacts of Random Misalignment on the Muon Spectrometer Performance **51**

III Production of the Z boson at LHC **57**

8 Cross-Section $\sigma(pp \to Z/\gamma^* \to \mu^+\mu^-)$ Measurement **59**

8.1 Event Selection . . . 60

8.1.1 Relevant Background Samples . . . 60

8.1.2 Cut Based Selection . . . 61

8.2 Background Estimation . . . 72

8.2.1 $Z \to \tau\tau$-background Estimation . . . 72

8.2.2 $t\bar{t}$-background Estimation . . . 72

8.2.3 QCD-background Estimation . . . 72

8.2.4 $W \to \mu\nu$-background Estimation . . . 75

8.2.5 Cosmic Muons . . . 76

8.3 In-situ Determination of Detector Efficiencies . . . 77

8.3.1 Tag and Probe Method . . . 77

8.3.2 Selection of Candidate Tracks . . . 78

8.3.3 Determination of the Muon Spectrometer Reconstruction Efficiency . . . 80

8.3.4 Determination of Inner Tracker Reconstruction Efficiencies . . . 84

8.3.5 Trigger Efficiencies . . . 85

8.3.6 Muon Isolation Efficiency . . . 88

8.4 Determination of the Muon p_T-Resolution . . . 91

8.5 Further Studies of Systematic Uncertainties . . . 96

8.5.1 Impact Parameter . . . 96

8.5.2 Impacts of Misalignment . . . 97

8.5.3 PDF Contributions . . . 97

8.6 Expected Precision of the $\sigma(pp \to Z/\gamma^* \to \mu^+\mu^-)$ Measurement . . . 98

8.6.1 Uncertainty of ε_{All} . . . 98

8.6.2 Further Uncertainties . . . 102

8.6.3 Overall Uncertainty . . . 102

9 Measurement of the p_T Spectra of the Z Boson **103**
9.1 Measurement of p_T^Z-Spectra . . . 103
9.1.1 Correction of Efficiency and Systematic Uncertainties . . . 105
9.1.2 Performance of the *Bin-by-Bin* Correction . . . 110
9.1.3 Expected Precision . . . 112
9.2 Observation of the x-Broadening Effect . . . 114
9.2.1 Theoretical Description of x-Broadening . . . 114
9.2.2 Proposed Method . . . 115
9.2.3 Observation Significance . . . 116

10 Conclusion and Outlook **119**

A Muon Software Validation **121**
A.1 Detection of Geometry Clashes . . . 121
A.2 The MuonValidation Package . . . 123
A.2.1 Simulation and Digitization Validation Results . . . 125
A.2.2 Validation of Muon Reconstruction . . . 127

B Resolution Determination with Cosmic Muons **129**
B.1 Sagitta study for the Cosmic Ray Measurement Facility . . . 129
B.1.1 Definitions and Algorithms . . . 129
B.1.2 Geant4 Simulation of the Cosmic Ray Measurement Facility . . . 131
B.1.3 Theoretical Expected Resolutions . . . 131
B.1.4 Results and Comparison between Real and Simulated Data . . . 133
B.1.5 Alignment . . . 137
B.2 H8 Testbeam and Further ATLAS Studies . . . 139
B.2.1 Setup of the Simulation . . . 139
B.2.2 Alignment at the ATLAS Muon Spectrometer . . . 140
B.2.3 Effects of Wire-Displacement . . . 140
B.2.4 Effects of the Single Tube Resolution . . . 141
B.3 Summary . . . 142

C Misalignment Impacts on the Muon Spectrometer **143**
C.1 Random Misalignment . . . 143
C.1.1 Implementation . . . 143
C.1.2 Shifts in Special Directions . . . 147
C.2 Egg-shape Layout Validation . . . 148
C.3 Alignment with the Process $Z \rightarrow \mu\mu$ . . . 151

D Details to the Total Cross-Section Measurement **155**

D.1 Alternative Method for Efficiency Determination 155

D.2 ATHENA Algorithm for the In-Situ Determination of Efficiencies 156

D.3 Further Determination Methods of p_T-Resolution 157

E Differential Cross-Section Measurement Details **161**

E.1 Improvement of the Muon p_T-Resolution for $Z \to \mu\mu$ Events 161

E.1.1 Z Boson Mass Constraint and Kinematic Fit 161

E.1.2 Improved Kinematic Fit 166

Bibliography **169**

Acknowledgments **175**

Curriculum Vitae **177**

Part I

Overview

"Falls Gott die Welt geschaffen hat, war seine Hauptsorge sicher nicht, sie so zu machen, dass wir sie verstehen können."

Albert Einstein[1]

Chapter 1

Introduction

About 20km west of Geneva city center and 100 meters underground, the largest experiment in human history is currently being setup. Two decades of planning, developing and building will come to an end in 2008, when the experiment comes finally into operation. Roughly 10,000 physicists from more than thirty nations all over the world have been working jointly to achieve this project, unified by the wish to understand the universe we live in. The core of the project is the Large Hadron Collider (LHC) and its four independent particle detectors ATLAS, CMS, ALICE and LHCb.

The ATLAS detector at the Large Hadron Collider will probe the modern theory of particle physics, commonly known as the standard model of particle physics, at energies which have never been reached under laboratory conditions before. Despite the great success of the standard model, it is not believed to be the final answer. Many open questions remain, e.g. the verification of mass generation by spontaneous symmetry breaking or the origin of the so-called dark matter, which is believed to contribute more than 80% to the overall matter content of the universe.

Before answering these questions at the ATLAS experiment, it is important to measure well known physics processes in order to understand the detector. One very interesting standard model process is the production of the Z boson, which has several important aspects. The measurement of its total cross section, i.e. the probability of its production, is per se an important test of the standard model predictions. Moreover, the decay of the Z boson into two leptons is an important background process for various other physics studies. Leptons, originating from Z bosons with large transverse momenta, may fake the signature of predicted new particles, which decay into high energetic leptons. Thus, not only the total cross section but also the differential cross section of Z boson production versus its transverse momentum must be understood in detail. As already mentioned, an important aspect of the Z boson and its decay into leptons is its well understood theoretical and experimental description. The

[1] 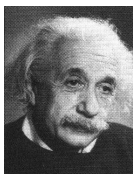

Albert Einstein was born on 14th of March 1879 in Ulm, Germany, and grew up in Munich. In the year 1905, Einstein published three pioneering theoretical works on the Brownian motion of molecules, on the photoelectric effect and the special theory of relativity. In 1915 Einstein formulated the general theory of relativity, which can be considered as one of the greatest achievements in theoretical physics for centuries, since there was no imminent experimental need for a new explanation of gravity.

expected high rate of producing Z bosons at LHC therefore offers the possibility to use this channel as a calibration benchmark for the whole ATLAS detector.

This thesis focuses on the decay of the Z boson into two muons, since this provides a relative clean signature which can be clearly discriminated from other processes.

The outline of this thesis is as follows. In chapter 2 a brief overview of the actual theoretical understanding of elementary particles and their interactions is given. This is followed by a short introduction to the Large Hardon Collider and the ATLAS experiment in chapter 3 and 4.

A crucial aspect of the cross-section measurement of the Z boson is the identification and the precise measurement of the high energetic muons and hence, special attendance was given to the Muon Spectrometer of the ATLAS detector. In chapter 5 a thorough discussion of its expected performance is given, based on detailed computer simulations. Several crucial aspects of this simulation can be validated with cosmic muons. This was done at the cosmic ray measurement facility in Garching, Germany, and the results are presented in chapter 6.

It is expected that the alignment of the Muon Spectrometer, i.e. knowing the exact positions of the various detector elements, is one of the most important aspects to ensure its design performance in the beginning of the experiment. The impact of possible misalignments on the performance was studied in detail and are briefly discussed in chapter 7.

Having validated and understood crucial aspects of the Muon Spectrometer and its simulation, the physics analysis of this thesis can be discussed. In chapter 8 the expected precision of the total cross-section measurement of $pp \rightarrow Z/\gamma^* \rightarrow \mu^+\mu^-$ with first data is presented. First data are defined within this thesis as the first recorded data with an collision energy of $14\,TeV$, corresponding to an integrated luminosity of $50\,pb^{-1}$. This chapter includes also a detailed discussion of methods for the determination of the performance of the Muon Spectrometer with recorded data.

Chapter 9 is dedicated to the study of the expected precision of differential cross-section measurements of $pp \rightarrow Z/\gamma^* \rightarrow \mu^+\mu^-$ versus the transversal momentum of the Z boson, again with first data. In particular the low transverse momentum regime of the Z boson was examined since this is sensitive to theoretical predictions of some models of the proton structure. The thesis closes with a conclusion and a brief outlook in chapter 10.

Various parts of this thesis have been presented at conferences and published in various journals [1–3] or as ATLAS notes[1] [4–8].

[1] ATLAS notes are internal documents of the ATLAS collaboration. Some of them are refereed by an internal committee [4, 5] and accessible for the public [6, 7].

"It is impossible to explain honestly the beauty of the laws of nature in a way that people can feel, without them having some deep understanding of mathematics. I am sorry, but this seems to be the case."

Richard P. Feynman[1]

Chapter 2

Theory of Z Boson Production at LHC in a Nutshell

2.1 The Standard Model of Particle Physics

The standard model of particle physics describes matter and their interactions in terms of elementary particles. The first class of elementary particles are point-like spin-$\frac{1}{2}$ fermions, which describe the matter part of the theory. The second class are spin 1 bosons, also called gauge bosons, which mediate the fundamental interactions.

A matter particle experiences a fundamental force, if it carries the specific charge of the corresponding interaction, e.g. a particle interacts via the electromagnetic interaction if it is electrically charged. The interactions or forces of the standard model are the electromagnetic force, the weak force and the strong force. Gravitation could not yet be included in this theoretical framework. A priori this is not a problematic issue since gravitation is weaker by 40 orders of magnitude and hence it can be neglected in small scale physics. Fermions, which can interact via the strong force, are called quarks; all other fermions are called leptons.

The mathematical concept, which describes the behavior of elementary particles, must obviously be a quantum theory, but it is also clear that the Schrödinger Equation, which describes atomic physics at a very high accuracy, is not sufficient for elementary particle physics, since for example the decay or the creation of particles cannot be explained. A first step in the right direction was done by Paul Dirac [9] by formulating a Lorentz-invariant version of the Schrödinger Equation. It can be expressed by the Lagrange density

[1] Without doubt, one of the most popular physicists ever was Richard Phillips Feynman, born 1918 in New York and died 1988 in Los Angeles. His popularity was not only due to his major contributions to Quantum Electrodynamics but also to his famous and illustrative lecture series. Every physicist should have read "Surely you are joking, Mr. Feynman". Despite his great talent for teaching he had very few PhD students.

$$\mathscr{L} = i\bar{\Psi}\gamma_\mu \partial^\mu \Psi - m\bar{\Psi}\Psi \tag{2.1}$$

The application of the Euler Lagrange formalism on (2.1) leads to the free Dirac Equation

$$\left(\gamma^\mu p_\mu - m\right)\Psi(x) = 0 \tag{2.2}$$

where Ψ are four dimensional vectors, called spinors, γ^μ are the Dirac matrices and p_μ is the momentum operator $i\partial_\mu$ [1] [10]. The Dirac equation has two essential properties: Firstly it allows describing relativistic spin-$\frac{1}{2}$ particles naturally, secondly it predicts anti-matter. In order to allow the creation and annihilation of particles, a quantization of the field Ψ is needed. This leads to a first quantum field theory of free fermions, i.e. fermions which do not interact.

The last ingredient for a meaningful physical theory is the inclusion of interactions. It is believed nowadays that the so-called gauge-theories build the basis of the connection between particles and their interactions. Requiring, that the Lagrange density in equation (2.1) is invariant under the transformation

$$\Psi(x) \rightarrow e^{i\alpha(x)}\Psi(x) \tag{2.3}$$

leads to

$$\mathscr{L} = \bar{\Psi}(i\gamma_\mu \partial^\mu - m)\Psi + e\bar{\Psi}\gamma_\mu A^\mu \Psi - \frac{1}{4}F_{\mu\nu}F^{\mu\nu} \tag{2.4}$$

with $F_{\mu\nu} = \partial_\mu A_\nu - \partial_\nu A_\mu$. A vector field A_μ had to be introduced to achieve this invariance, i.e. the local gauge symmetry. The term $e\bar{\Psi}\gamma^\mu A_\mu \Psi$ represents the interaction of the fermion field Ψ with the vector field A_μ. The term $F_{\mu\nu}F^{\mu\nu}$ is the kinetic energy of the vector field and has the same structure as in Maxwell's equations. The requirement of (2.3) corresponds to a local $U(1)$ group symmetry and hence the Lagrange density in equation (2.4) is called to be locally $U(1)$-gauge invariant. The second quantization of the fields Ψ and A_μ leads to a theory, called Quantum Electrodynamics, which describes the interaction of fermions via the exchange of the quanta of the electromagnetic field A_μ. These quanta are known as photons. Since no mass term $m^2 A_\mu A^\mu$ appears, the photon must be a massless gauge boson. A more detailed description can be found in [10, 11].

The theory of strong interaction, called Quantum Chromo Dynamics (QCD) is based on an local $SU(3)$-gauge invariant Lagrange density [10]. Hence, each quark is a triplet of the QCD gauge group, which implies three kinds of charges, called red (r), blue (b) and green (g), corresponding to the three primitive colors. The gauge bosons of QCD are called gluons and form the octet representation and hence carry color charges themselves (Table 2.1), since the $SU(3)$ is a non-Abelian group. As a consequence, the gluons do not only interact with quarks, but also among themselves. It is believed nowadays, that the self-interaction can explain, what is commonly known as confinement. Confinement describes the fact, that color charged objects cannot be observed individually but only in combinations, which are color-neutral, i.e. quarks are confined by gluons. Colorless objects, which consist of one quark and one anti-quark are called mesons, objects, which consist of three quarks are called baryons.

One of the most remarkable achievements in the past 50 years, was the unification of the theories of the electromagnetic and the weak force by S.Glashow, S.Weinberg and A.Salam

[1] The Einstein sum convention is used. Moreover, $\hbar = 1$ and $c = 1$ are used.

$r\bar{g}$	$r\bar{b}$	$g\bar{b}$	$g\bar{r}$	$b\bar{r}$	$b\bar{g}$	$\sqrt{\frac{1}{2}}(r\bar{r}-g\bar{g})$	$\sqrt{\frac{1}{6}}(r\bar{r}+g\bar{g}-2b\bar{b})$

Table 2.1: Represenation of $SU(3)$ color octet, i.e. the basis of the gauge boson color-charges.

[12]. Requiring a $SU(2) \times U(1)$ invariant Lagrange density, leads to isotriplet of vector field W_μ^i with a coupling strength g and a single vector-field B_μ with a coupling strength g'. The first two components of $\vec{W}$ imply the existence of two charged bosons, which are known as W^+ and W^-. The two neutral fields are mixed in such a way that their mass eigenstates are

$$A_\mu = B_\mu \cos\theta_W + W_\mu^3 \sin\theta_W, \qquad Z_\mu = -B_\mu \sin\theta_W + W_\mu^3 \cos\theta_W,$$

where θ_W is the so-called weak mixing angle. Hence, the photon field A_μ and the Z boson field Z_μ can be interpreted as an orthogonal combination of the two neutral gauge fields W_μ^3 and B_μ. The corresponding charge of the $SU(2)$ group is called weak isospin and labeled with T. The charge of the $U(1)$ group is called weak hypercharge and labeled with Y. The electric charge can be defined by these terms as $Q = T^3 + \frac{Y}{2}$. A more detailed discussion can be found in [11]. In contrast to photons and gluons, it is known from experiment [13] that the gauge bosons $W^\pm$ and Z of the weak interaction have a large mass of $80.403 \pm 0.029\,GeV$ and $91.1875 \pm 0.0021\,GeV$. It should be noted that also the gauge bosons of the weak interaction carry a weak-charge. Their self interaction is drastically reduced in contrast to the strong force, because of their large masses and hence no confinement can be observed due to the weak interaction.

The masses of the gauge bosons of the weak interaction introduce a theoretical problem, since writing a mass term like $m^2 A_\mu A^\mu$ in the Lagrange density in equation 2.4 would break its gauge invariance, which is an essential feature of the theory. A solution to this problem was formulated by Higgs [14] and Kibble [15], which is based on a spontaneous symmetry breaking of the electroweak gauge symmetry. The predicted Higgs-field, i.e. Higgs boson, leads to a dynamical mass generation of the W and Z boson. The masses of fermions can be interpreted as Yukawa-coupling to the Higgs field, where the couplings are proportional to the masses of the fermions. With this theoretical background the Lagrange density of the Standard Model can be written as [11]

$$\begin{aligned}
\mathscr{L} = \quad & -\tfrac{1}{4} W_{\mu\nu} W^{\mu\nu} - \tfrac{1}{4} B_{\mu\nu} B^{\mu\nu} - \tfrac{1}{4} G^\alpha_{\mu\nu} G^{\mu\nu}_\alpha && : \text{Kinetic energies and self-interactions of } W^\pm, Z, \gamma \text{ and gluons} \\
& + \bar{L}\gamma^\mu \left(i\partial_\mu - \tfrac{1}{2} g \tau_i W_\mu^i - g' \tfrac{Y}{2} B_\mu \right) L && : \text{kinetic energies and interactions of leptons and quarks with } W^\pm, Z, \gamma \\
& + \bar{R}\gamma^\mu \left(i\partial_\mu - g' \tfrac{Y}{2} B_\mu \right) R && \\
& + g_s \left(\bar{q}\gamma^\mu T_\alpha q \right) G^\alpha_\mu && : \text{Interactions of all quarks } q \text{ with gluons} \\
& + \left| \left(i\partial_\mu - g \tfrac{1}{2} \tau_i W_\mu^i - g' \tfrac{Y}{2} B_\mu \right) \Phi \right|^2 - V(\Phi) && : \text{Masses and coupling of } W^\pm, Z, \gamma \text{ and the Higgs-boson} \\
& - \left(G_1 \bar{L} \Phi R + G_2 \bar{L} \Phi_C R \right) + \text{hermitian conjugate} && : \text{Lepton and Quark masses and coupling to Higgs}
\end{aligned}$$

Name	Mass	$color_{L,R}$	T_L^3	Y_L	T_R^3	Y_R	$Q = T^3 + \frac{Y}{2}$
up-quark (u)	$1.5 - 3.0\,MeV$	$3, \bar{3}$	$+\frac{1}{2}$	$+\frac{1}{3}$	0	$+\frac{4}{3}$	$+\frac{2}{3}$
down-quark (d)	$3 - 7\,MeV$	$3, \bar{3}$	$-\frac{1}{2}$	$+\frac{1}{3}$	0	$-\frac{2}{3}$	$-\frac{1}{3}$
charm-quark (c)	$1.25 \pm 0.09\,GeV$	$3, \bar{3}$	$+\frac{1}{2}$	$+\frac{1}{3}$	0	$+\frac{4}{3}$	$+\frac{2}{3}$
strange-quark (s)	$95 \pm 25\,MeV$	$3, \bar{3}$	$-\frac{1}{2}$	$+\frac{1}{3}$	0	$-\frac{2}{3}$	$-\frac{1}{3}$
top-quark (t)	$174.2 \pm 3.3\,GeV$	$3, \bar{3}$	$+\frac{1}{2}$	$+\frac{1}{3}$	0	$+\frac{4}{3}$	$+\frac{2}{3}$
bottom-quark (b)	$4.2 \pm 0.07\,GeV$	$3, \bar{3}$	$-\frac{1}{2}$	$+\frac{1}{3}$	0	$-\frac{2}{3}$	$-\frac{1}{3}$
electron (e)	$0.511\,MeV$	$1, \bar{1}$	$-\frac{1}{2}$	-1	0	-2	-1
e-neutrino (ν_e)	$< 3\,eV$	$1, \bar{1}$	$+\frac{1}{2}$	-1			0
muon (μ)	$105.7\,MeV$	$1, \bar{1}$	$-\frac{1}{2}$	-1	0	-2	-1
μ-neutrino (ν_μ)	$< 0.19\,MeV$	$1, \bar{1}$	$+\frac{1}{2}$	-1			0
tau (τ)	$1777\,MeV$	$1, \bar{1}$	$-\frac{1}{2}$	-1	0	-2	-1
τ-neutrino (ν_τ)	$< 18.2\,MeV$	$1, \bar{1}$	$+\frac{1}{2}$	-1			0

Table 2.2: Overview of masses and gauge quantum numbers of all fermions in the standard model, grouped by quarks (upper part) and leptons (lower part) and the three generations, only differing by its masses. T is the weak isospin, and T^3 its third component. Y is the $U(1)_Y$-hypercharge and Q the electric charge. The subscript L described left-handed, the subscript R right-handed Dirac spinors.

where $G^\alpha_{\mu\nu}$ are the gluon gauge fields, g_s their couplings and $G_{1,2}$ the Yukawa coupling of the Higgs-field to the fermions, i.e. the masses of the fermions. The quantities $\vec{\tau}$ and T_α are the generators of the $SU(2)$ and $SU(3)$ group, respectively. It should be noted that the electroweak force distinguishes between left-handed and right-handed fermions and therefore these fermion fields are denoted with R and L, while the QCD part simply acts on all quark fields q, i.e. some fields are denoted with R, L in the electroweak part and q in the QCD part.

The fermions of the standard model are classified into six quark and six leptons plus the corresponding anti-particles. They can be grouped in three generations, which transform identical under the gauge groups but differ in mass. The particles of the second and third generation decay via the weak interaction in particles of the first generation. The quantum numbers of the quarks and leptons and their masses are shown in Table 2.2. The top-quark is special in a certain sense, since it is the only quark whose mass is on the electro-weak scale. All other quarks have significantly lower masses, which cannot be explained by the present theory.

One approach to describe the interaction of particles is the application of perturbation theory. The expansion parameters for the perturbation theory are the coupling constants of the chosen interaction.

The interaction and the decay of the elementary particles of the standard model can be interpreted in lowest order perturbation theory via the exchange of a single gauge boson. Figure 2.1 and 2.2 schematically illustrate the scattering of two electrons via the exchange of a photon and the decay of Z boson into two muons[2]. As each vertex represents an interaction, the probability of a certain process is always connected with the strength of the interaction, which is involved.

Perturbation theory can be applied with an enormous success to the electroweak part of the theory. This is in general not justified for QCD due to its large coupling constant $\alpha_s = \frac{g_s^2}{4\pi}$. In particular, the confinement effect cannot be described by perturbation theory and so far no other approach has been proven to result in a successful theoretical description of this effect.

[2]This form of illustrating processes in particle physics was introduced by Richard Feynman and, called Feynman diagrams [16]

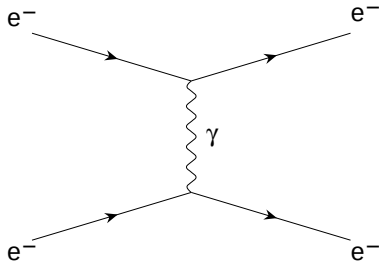

Figure 2.1: Feynman diagram of the scattering of two electrons via the exchange of a photon.

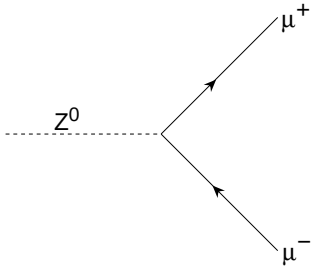

Figure 2.2: Feynman diagram of a Z boson decay into two muons.

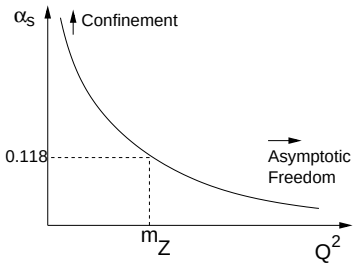

Figure 2.3: Schematic illustration of the dependence of the strong coupling α_s on Q^2.

A further interesting property of Quantum Field Theory is the dependence of the coupling constants on the energy scale Q^2 of the interaction[3] as shown in Figure 2.3 for the QCD coupling constant[4]. In contrast to QED, the coupling strength rises with smaller Q^2 values, i.e. larger distances between the interacting particles. In the region of large momentum transfers ($\gg 300\,MeV$), α_s becomes small and perturbation theory can be applied. This behavior is known as asymptotic freedom [17]. For larger distances, the α_s rises and the effect of confinement occurs.

Soon after the formulation of QED in the 1960s it was discovered that divergent integrals appear in pertubative calculations. A theory with divergent integrals has no predictive power and hence this is a crucial problem for any meaningful theory. A solution to that problem is a technique called renormalization, i.e. physical quantities can be defined in a way that emerging infinities are canceled by appropriate counter terms. It was proven by 't Hooft that this procedure can be successfully applied in all gauge theories [18]. This is the reason why it is crucial that the mass of the weak vector bosons is generated dynamically and not by just inserting their masses in the corresponding Lagrangian, which would destroy the gauge invariance.

The standard model has been extensively tested in many experiments [19]. Not a single serious contradiction has been discovered so far and hence it is the most successful theory in the history of physics. Nevertheless, it is believed that the standard model cannot be the final theory of particle physics, because of several questions and problems, e.g.

- **Fine Tuning Problem:** The mass of the Higgs-boson is on the electroweak scale, while quantum corrections to its mass are quadratically divergent with the cut-off value of the regularization scheme. A natural choice of this cut-off value is the Planck scale and hence a Higgs-boson mass at the Planck scale is expected, when no extreme fine-tuning of the quantum corrections to the bare Higgs mass is performed. Such a precise fine-tuning is unnatural, as absent in other physical quantities.

- **Gravitation:** Why is gravitation so much weaker than all other interactions? How can a meaningful quantum field theory of gravitation be formulated?

- **Dark Matter:** From cosmological observation it is concluded that more than 90 % of the universe is made of matter and energy, which is not included in the standard model.

[3] The energy scale of the interaction Q^2 is given by the momentum transfer q of the interacting particles: $Q^2 = -q^2$

[4] This effect is due to the non empty vacuum structure of quantum field theories.

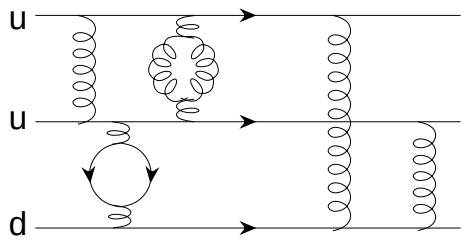

Figure 2.4: Schematic illustration of three valence quarks forming a proton and interacting via the exchange of gluons.

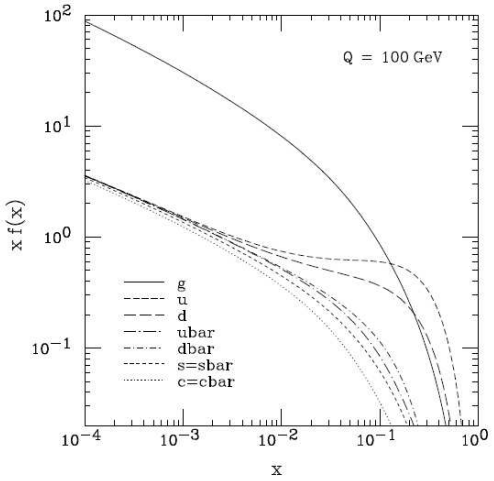

Figure 2.5: Structure functions of the proton (CTEQ working group [24]).

Several models provide solutions to one or more of these problems. These are commonly called models beyond the standard model (BSM) [20–22].

So far, no evidence could be found for BSM physics, but it is hoped, that this will change by the experimental results at the Large Hadron Collider.

2.2 Theory of Proton-Proton Collisions

A proton-proton collision at very low energies can be approximated as an elastic scattering of two electrically charged extended objects. At higher energies, the structure of the proton becomes visible and plays an important role in the scattering process. Therefore one is forced to introduce structure functions of the proton, which represent its internal structure, i.e.

$$F(x) = \sum_i f_i(x)x \tag{2.5}$$

where x is a fraction of the total momentum of the proton carried by the parton and $f_i(x)$ denotes the momentum distribution of the i-th type of parton, also called parton density function (PDF). The interaction between the partons is dominated by the strong interaction, which leads to an additional production of gluons and quark anti-quark pairs during the interaction of two valence quarks (see Figure 2.4). Hence, the proton consists not only of three valence quarks, but also of a 'sea' of further gluons and quarks. It was yet not possible to calculate the PDFs for the proton and hence the knowledge of the PDFs relies on (mainly) deep inelastic scattering experiments [23]. An illustration of the actual understanding of the PDFs for the proton is shown in Figure 2.5.

This ignorance is not the only problematic issue for the calculation of matrix elements, as already mentioned in section 2.1, since higher orders in perturbation theory have not yet been calculated for all QCD processes. In fact, even the calculation of lower orders is mathematically very demanding and only a few processes have been calculated so far to second order perturbation theory. Hence, several simplifications and approximations must be applied to describe QCD interactions. The basis for a theoretical description is the so-called

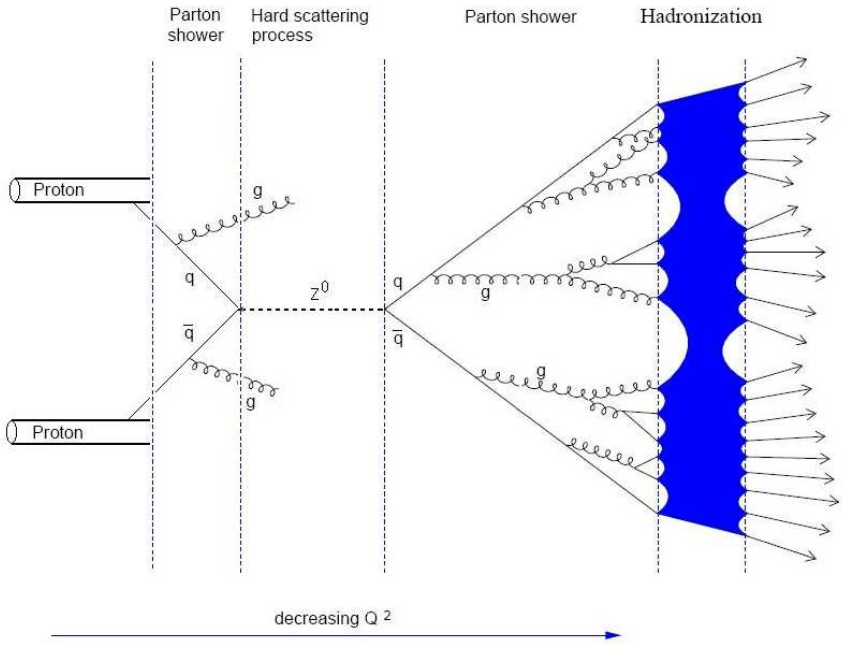

Figure 2.6: Hard scattering process of two partons, producing a Z boson and its decay into two quarks, which are decaying into color-neutral hadrons (hadronization).

factorization theorem. In a naive interpretation, the theorem states that the hard QCD interaction of two protons can be split up in several stages, as illustrated in Figure 2.6.

The hard scattering describes the actual sub-process between two partons. The calculation of this process is at least available at tree-level, i.e. in leading order perturbation theory, for few cases also for higher orders.

All those orders of perturbation theory, not included in the calculation of the hard scattering process, must be approximated for the initial state and final state partons. Since the partons are electrical and/or color charged, they are accompanied by the emissions of gluons and photons. The emission of gluons dominates for hadronic interactions. These perturbative corrections are approximated by the so called parton shower approach. Each radiation process is simulated by the branching of a parton into a parton with lower energy plus an emitted gluon, i.e. $q \rightarrow qg$. The energy distribution between the two daughter particles can be modeled with the Altarelli-Parisi splitting function [25]. The two newly created particles might again undergo a branch. The shower evolution is stopped when reaching a fixed energy scale of the branching parton, which is usually around $1\,GeV$, i.e. well above the confinement regime.

So far, the above description of the scattering process leaves colored objects in the final state, which obviously cannot be the final answer. The process in which colorless hadrons are formed from colored objects is called hadronisation and involves non-perturbative processes which cannot be described analytically. Two different phenomenological approaches are used to describe the hadronization and thus the confinement of colored objects.

- **String model:** This model is inspired by the string model [26] of strong interaction. It was formulated prior to the quark and QCD models as well as modern lattice QCD calculations [27], which predict a linear rising potential between a quark q and an anti-quark $\bar{q}$ with increasing distance, caused - in a naive physical picture - by a colored flux

tube or string due to the self interaction of gluons. If the energy stored in the string is large enough a second pair of quarks q' and $\bar{q}'$ is produced, which form two color singlets $q\bar{q}'$ and $q'\bar{q}$. The breaking up of strings stops, if only on-mass-shell hadrons remain. It should be noted, that the diquark anti-diquark pair-production allows also the production of baryons in this picture.

- **Cluster model:** In a first step, all gluons of the parton showers are split into light quark-antiquark or diquark-antidiquark pairs. In a second step, all quarks are combined with their nearest neighbors to form color singlet clusters. Basically, the mass of these clusters is used to determine in which hadrons they will decay finally [28].

2.3 Monte Carlo Generators

The purpose of Monte Carlo event generators is to describe the theoretical prediction of physics processes, e.g. the production of a Z boson in a proton-proton collision and its decay into two muons. Such a theoretical prediction is crucial to understand the measured data and to tune physics analyses. In the present phase of the ATLAS experiment, where no real data is available, Monte Carlo simulations are used to study the expected sensitivity for various measurements and to tune the present algorithms to achieve an optimal preparation for the analysis of data.

The factorisation scheme, which was introduced in section 2.2, is the basis of Monte Carlo event generators, which rely at least partially on QCD. In case of LHC, Monte Carlo generators must describe the structure of hadrons, the parton showers, the actual hard scattering process, and the hadronization. Various Monte Carlo event generator programs use different approximations during the different steps and therefore the theoretical prediction relies at least partially on the choice of the underlying Event Generator. Some event generator programs, which have been used in this thesis, are outlined in the following:

- PYTHIA**:** PYTHIA is a general purpose event generator [29], which is commonly used in high energy physics, because of its easy handling and relatively large predictive power. It can simulate lepton-lepton, lepton-hadron and hadron-hadron interactions with a broad field of theoretical models, including supersymmetric models or models with leptoquarks. The hard scattering process is calculated in leading order approximation. The higher order corrections are approximated with the parton shower approach. The hadronization process is based on the String-Model as introduced briefly in the previous section.

- HERWIG**:** The Hadron Emission Reactions With Interfering Gluons (HERWIG) program is also a general purpose event generator [30], which is quite similar to PYTHIA. The main differences are the modelling of the parton shower and the hadronization process. HERWIG is based in the clusterization model.

- **MC@NLO:** This Monte Carlo event generator includes full next-to-leading-order calculations of rates for QCD processes during the hard scattering process [31]. The output of the simulation is further processed by the HERWIG Event generator, which adds higher order approximations of the parton shower[5] and simulates the hadronization step.

[5]Only those additional parton showers are approximated, which are not described within the next-to-leading-order calculation of MC@NLO

- RESBOS: Among other things, the RESBOS event generator [32,33] computes the fully differential cross section

$$\frac{d\sigma}{dp_T^B\, dy_B\, d(p^B)^2\, d\Omega}$$

for processes $pp \to B \to l^+l^-$ with next-to-leading initial state QCD corrections. The label B indicates a boson, p_T its transversal momentum and y its rapidity. The calculation is based on the CSS resummation formalism [34] and contains the exact matrix element, including initial state soft gluon resummation effects, for the production of the specified boson. The hadronization is then modeled by the HERWIG generator.

The prediction of Monte Carlo event generators has several uncertainties, arising from various sources. The cross-section of the majority of low energetic QCD-processes has uncertainties in the order of one hundred percent. Moreover, the modeling of parton showers, i.e. initial and final state radiation and the hadronization can only be described within certain approximations. A further point are the uncertainties on the PDFs of the proton or in general of hadrons at large energies, which obviously have a large impact on the predicted cross-sections and kinematics properties of the produced final state objects. Hence, predictions of Monte Carlo event generators must not be trusted in detail, they should only be used as a guideline for the physics analysis of real data.

2.4 The Production of Z Bosons at the LHC

The mass and the width of the Z boson were measured by the LEP experiments to highest precision [35]. The world average values are $91.1875 \pm 0.0021\,GeV$ and $2.4952 \pm 0.0023\,GeV$ respectively. The branching ratios of its decay channels are given in Table 2.3.

Decay mode	Probability
e^+e^-	3.363 ± 0.004
$\mu^+\mu^-$	3.366 ± 0.007
$\tau^+\tau^-$	3.370 ± 0.008
Invisible	20.00 ± 0.06
Hadrons	69.91 ± 0.06

Table 2.3: Experimental determined decay modes of the Z boson [35].

The production of Z bosons at the LHC is due to the Drell-Yan process [36]. The dominating processes at the LHC are $q\bar{q} \to Z/\gamma^* \to \mu^+\mu^-$ (65%) and $qg \to q\gamma^*/Z \to q\mu^+\mu^-$ (35%) which are illustrated in Figure 2.7 and 2.8. The dominant higher order correction of the first process is the scattering of a quark with a gluon, which contributes roughly 1/3 to the overall cross-section of this process.

The x-value of the initial partons can be estimated with a simple calculation. The total energy in the center of mass frame of two colliding protons with four momenta P_1 and P_2 is determined by

$$S = (P_1 + P_2)^2 \approx 2P_1P_2$$

when neglecting the rest mass of the protons. The square of the total energy in the center of mass frame of the two partons with the momenta p_1 and p_2 is then given by

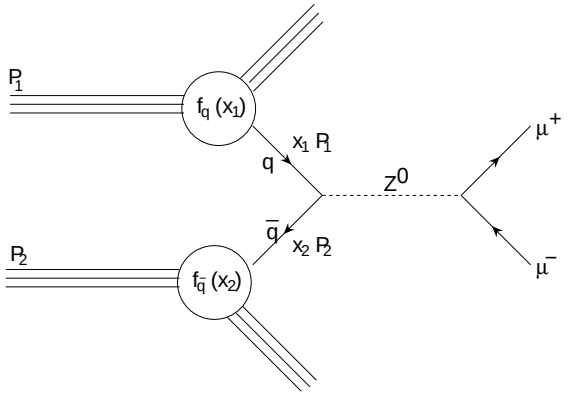

Figure 2.7: Leading order diagram of the Drell-Yan process

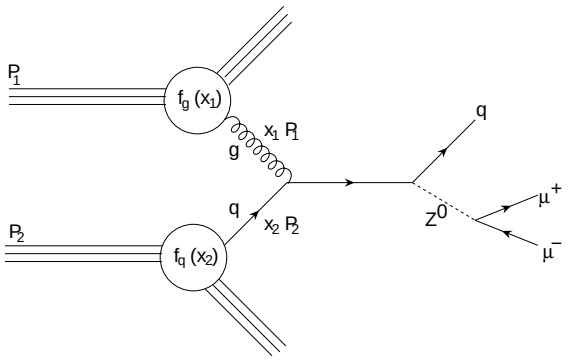

Figure 2.8: One next to leading order diagram of the Drell-Yan process

$$s = (p_1 + p_2)^2 = (x_1 P_1 + x_2 P_2)^2 \approx 2 x_1 x_2 P_1 P_2 = 2 x_1 x_2 S$$

where x_i denotes the fraction of the proton's four-momentum. This energy s must be at least m_Z and therefore

$$x_1 x_2 > \frac{m_Z^2}{S}$$

For an average typical value $x \approx x_1 \approx x_2$ it follows

$$x \approx \frac{m_Z}{\sqrt{S}} \approx 0.01$$

for the expected collision energy at the Large Hadron Collider of $14\,TeV$. Comparing this small value with the structure functions of the proton shown in Figure 2.5 it becomes obvious that gluons are the dominating partons. Hence this raises the question, why the process $qg \to qZ/\gamma^*$ is not dominating. This can be explained by two facts: at these high energies, the assumption $x_1 \approx x_2$ may not be valid; moreover, the annihilation of $q\bar{q}$ leads to a resonant production of the Z boson which is enhanced by many orders of magnitude.

A next-to-next-to-leading order calculation of the total cross section of the process $pp \to Z$ at a center of mass of $14\,TeV$ yields[6] $1880\,nb \pm 70\,nb$. The systematic theoretical uncertainty of the cross section arises from the uncertainties of the CTEQ 6.2 PDF functions, which have been used [24].

[6]It should be noted that this cross section does not include the photon mixing contribution

"Mathematics began to seem too much like puzzle solving. Physics is puzzle solving, too, but of puzzles created by nature, not by the mind of man."

Maria Goeppert Mayer[1]

Chapter 3

The Large Hadron Collider

The head-on collisions of particles provide the largest center of mass energy, which is available for the creation of new particles. The Large Electron Positron (LEP) collider, which was in operation at CERN from the year 1989 to 2000, accelerated electrons and positrons to an energy of $\sim 105\,GeV$, which results in an available collision energy of $\sim 210\,GeV$ [37]. The reachable energy of the electron and positron colliders is limited by the synchrotron radiation which is emitted by the accelerated charged particles.

The acceleration of protons overcomes this problem, since the radiated power is proportional to $\frac{1}{m^4}$, where m is the mass of the accelerated particle. The prize to pay are the QCD interactions during a collision of protons, which lead to large background processes and no clean final states. Moreover, the initial energy and the momentum of the colliding partons is unknown. Thus hadron colliders reach higher energies and, therefore, may create new particles, but precision measurements are extremely demanding.

The difference between proton and anti-protons becomes smaller for the small x-values of the interaction partons, which are expected at large energies ($\sim 10\,TeV$), as already mentioned in section 2.2[2]. Moreover, it is technically much easier to produce and accelerate a large number of protons, than an equal amount of anti-protons. Hence, colliding protons at high energies offers high luminosities ($\mathscr{L}$), i.e. the expected rate of proton-proton collisions per second and per square centimeter, at high energies, which were the basic arguments for the design of the successor at the LEP collider: the Large Hadron Collider (LHC) [39].

The LHC, which is currently being installed at CERN, is a proton-proton collider with a center of mass energy of $14\,TeV$. It is built in the tunnel of the former LEP collider, which has a circumference of $26.7\,km$ (Figure 3.1). Super conducting magnets are the basic technology of the LHC and are used for bending and focusing the counter rotating proton beams. An

[1] Maria Goeppert-Mayer, born 1906, grew up in Göttingen. After her graduation from school, she started to study mathematics, but changed to physics after three years. After her studies she emigrated to the United States together with her husband. Goeppert-Mayer worked at the Manhattan project and became full physics professor at the University of Chicago in 1946. 1963, she received a Nobel prize in physics together with Paul Wigner for the discovery of nuclear shell structure.

[2] The underlying theorem is called Pomerantschuk Theorem [38].

instantaneous luminosity $1 \times 10^{34}\, cm^{-2}s^{-1}$ is reached, by accelerating of 2835 proton bunches per direction, consisting of 1×10^{11} particles, with a bunch length of $7.5\, cm$ and a time between the collisions of $25\, ns$. The luminosity lifetime is expected to be in the order of ten hours.

The beam-pipe of the LHC (Figure 3.2) contains two separate beam-lines for the opposite direction of the two proton beams, which also makes an opposite magnetic field for both beam-lines necessary. The solution to this technical problem are so-called twin-bore magnets, which consist of a set of coils. The advantage of this approach is that the whole structure can use the same cooling infrastructure within the same beam-pipe (Figure 3.2). The cooling of 1232 magnets with a field strength of 8.33 Tesla and 392 quadrupoles is achieved by super-fluid Helium at a temperature of $2^\circ\, K$.

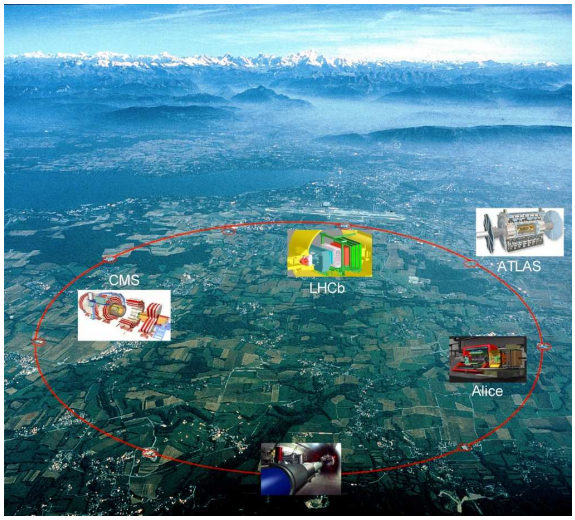

Figure 3.1: Overview of the CERN area. The LHC ring and its four experiments are schematically indicated.

Before injecting the proton beams into the LHC, they traverse several other acceleration steps. The protons are extracted from hydrogen gas and accelerated in bunches of $\sim 10^{11}$ protons by the Linac-accelerator to $50\, MeV$. These bunches are further accelerated by the PS booster to $1.4\, GeV$, followed by the Proton Synchroton (PS) and the Super Proton Synchroton (SPS) which accelerate the proton bunches to $26\, GeV$ and finally up to an injection energy of $450\, GeV$, respectively.

Figure 3.2: Illustration of the $15\, m$ long LHC cryodipole.

It is planed for later periods of the LHC running, also to inject lead nuclei and accelerate them to an energy of $1150\, TeV$ with a luminosity of $\mathscr{L} = 10^{27} cm^{-2}s^{-1}$.

Four particle detectors are currently installed at the LHC: ATLAS (A Toroidal LHC ApperatuS) and CMS (Compact Muon Solenoid) are general purpose detectors, which cover a broad field of experimental studies. The ALICE (A Large Ion Collider Experiment) experiment is designed to study the quark gluon plasma, i.e. a state of matter in which the quarks and gluons can be considered as free particles. The LHCb experiment is dedicated to B-meson physics and will study CP-violation to high precision.

"What we learn about is not nature itself, but nature exposed to our methods of questioning."

Werner Heisenberg[1]

Chapter 4

The ATLAS Experiment

ATLAS (A Toroidal LHC ApparatuS) is a collaboration of roughly two thousand physicists from more than thirty nations, who gathered to built one of the largest experiments in the history of mankind. The ATLAS Experiment was designed to exploit the full physics potential of LHC and it supposed to be in operation for roughly two decades [40]. This implies basic design requirements, which satisfy a broad field of specifications. The detector and its electronics must work reliably in high radiation environment and provide precise measurements of various physical quantities, e.g. charge, transverse momentum and energy of leptons, photons and jets as well as the missing transverse energy. These quantities are crucial to discover and study new and interesting physics signatures and processes.

To reach such a high precision further design constraints must be respected, e.g. the detector must be built with as less material as possible. All material, such as support structures, cables, gas-pipes or even detector elements themselves, enhance multiple Coulomb scattering, hadronic interactions or energy loss fluctuations of final state objects. These effects lead therefore to changes of the measured energy and thus have a crucial impact on the detector performance.

Moreover, the detector must deal with extremely high event- and collision-rates, i.e. more than 10^9 proton-proton interactions per second are expected during the high luminosity phase of LHC. Each interesting physics event is accompanied on average by further 22 soft hadronic interactions. This introduces further problematic issues such as pile-up. Pile-up is the effect that there are physical objects, e.g. pion, from previous bunch crossings still in the active part of the detector. This makes an exact timing of all measurements indispensable since all measured final state objects should be associated to the corresponding proton-proton interaction.

So far not mentioned at all have been man-power or financial constraints on the available technology or time-constraints in general. Thus it has become obvious that ATLAS is a

[1] By the age of 26 year, Werner Heisenberg, born 1901 in Würzburg, was professor for physics in Leipzig. He received the Nobel Prize at age of 31 for the quantitative explanation of the spectra of the hydrogen atom. It is said that Heisenberg nearly failed his PhD exam, since one of his examiner blamed him for "exceeding ignorance" in experimental physics. Only due to the strong support of his supervisor Arnold Sommerfeld he did finally pass his exams.

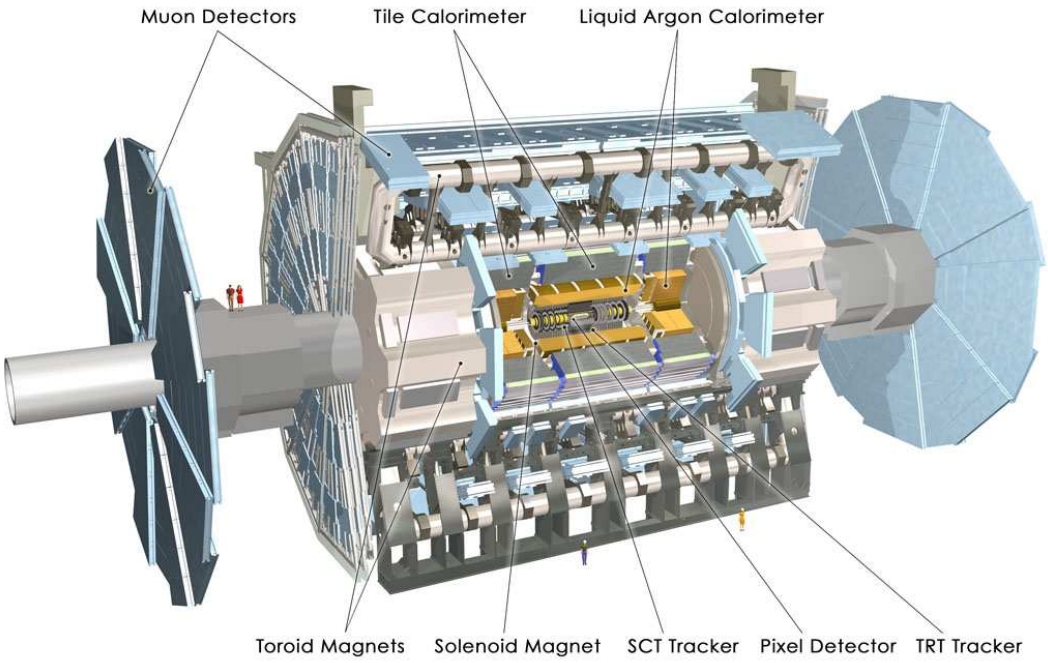

Figure 4.1: Schematic illustration of the ATLAS Detector

highly complex experiment with various critical aspects which had to be solved. The basic design of the ATLAS detector is described in the following sections.

4.1 The ATLAS Detector

A schematic drawing of the ATLAS detector is shown in Figure 4.1. As most colliding beam experiments, the ATLAS detector has a cylindrical shape, which is centered around the beam-pipe. As already mentioned in chapter 2.1, heavy particles are expected to decay into stable particles shortly after their production. Therefore it is not possible to prove the existence or measure the properties of heavy particles directly, but instead to measure their stable decay products. These stable decay particles are electrons, photons, muons and hadrons. Since quarks are colored objects, they are hadronizing shortly after their production and appear as concentrated shower of mesons and hadrons in the detector, which are called jets. Neutrinos cannot be detected within the ATLAS detector due to their small interaction cross-section with any matter. Their existence in an event can be concluded by a quantity called missing energy, which is the amount of energy which is needed to balance the energy in one event. Therefore the detector must cover a hermetically closed area around the interaction to ensure that no stable particles can escape without being detected.

ATLAS has three sub-detectors, which provide these necessary measurements of stable objects, starting from the inner to the outer,

- **Inner Detector (ID)**: Tracking and measurement of the charge and the transverse momentum of charged particles,
- **Calorimetric system (CS)**: Identification of electrons, photons and hadrons and measuring of their energy,
- **Muon Spectrometer (MS)**: Identification, tracking and the measurement of charge and momentum of muons.

θ	7.7°	15°	30°	45°	75°	90°
η	~ 2.7	~ 2.0	~ 1.32	~ 0.88	~ 0.26	$= 0$

Table 4.1: Various values of angle θ and the corresponding pseudo-rapidities η

These subdetectors are described briefly in the following subsections. Each sub-detector can be divided into three parts: the barrel region and two end-cap regions. The barrel region has usually a cylindrical form, while the endcap-region consists of one or more discs which close the barrel region from both ends.

The shape of the detector already implies a coordinate system. The center of the experiment, i.e. the collision point, is chosen as origin, the beam-direction is defined as the z-axis, the azimuthal angle in the x- and y-plane[1] is labeled as ϕ. The polar angle θ, is defined by $atan\left(\frac{r}{z}\right)$, where $r = \sqrt{x^2 + y^2}$ is the minimal distance to the z-axis.

An important quantity in high energy physics is the so-called rapidity, which is defined by

$$Y = \frac{1}{2} \log \frac{E + p_z}{E - p_z},$$

where E is the overall energy of the particle and p_z is the momentum of the particle in z-direction. The rapidity Y is a Lorentz-invariant quantity and particle multiplicity is approximately constant vs. y. In the limit of vanishing masses, the rapidity simplifies to

$$\eta = -\log(\tan(\frac{\theta}{2}))$$

which is called the pseudo-rapidity. An overview of various η-values and the corresponding θ-values is given in Table 4.1.

Note that the physical relevant quantity for hadron collider experiments is not the momentum of particles but the transverse momentum, i.e. the momentum in the xy-plane. This is due to the fact that the initial momentum in z-direction of the interacting partons of the two protons is unknown, while the momentum in x- and y-direction can be assumed to be zero. This applies not only for the momentum but also for the energy. Hence, the overall transverse energy balance is expected to be zero if all particles are considered.

4.1.1 Magnet System

Magnetic fields bend the trajectory of charged particles proportional to their field strength. A stronger magnetic field implies a stronger bending of the particle tracks, which enhances the precision of the momentum measurement. Hence a powerful magnet system is installed within the ATLAS detector [41]. The Magnet System is separated in two parts: The central solenoid magnet system and the toroid magnet system.

Central solenoid magnet system

The central solenoid magnet system provides a magnetic field for the Inner Detector. The magnet system is based on superconducting NbTi/Cu-magnets and cooled down to $4.5^\circ K$ in a cryostat, which is shared with the calorimeter to minimize the usage of material. The magnet system has a diameter of 2.5 meters and is 5.3 meters long. It is shorter by $80\,cm$ than the Inner Detector, which leads to an inhomogeneous magnetic field. The field strength is $2\,T$ at

[1]The ATLAS coordinate system is right-handed; the x-direction points to the center of the LHC ring.

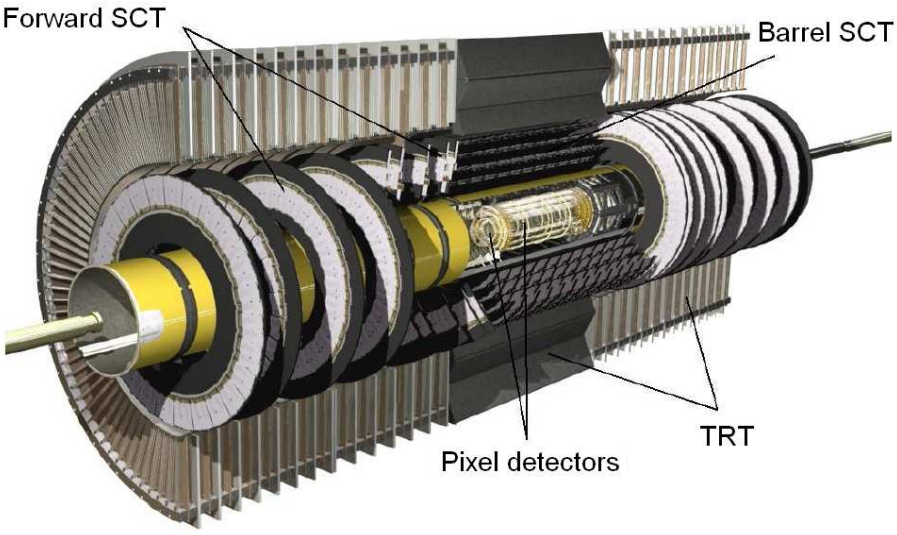

Figure 4.2: Schematic illustration of the ATLAS Inner Detector

the interaction point and $0.5\,T$ at the end of the Inner Detector. A precise knowledge of the field distribution is necessary to provide a precise measurement of the transverse momentum.

Air-core toroid magnet system

The toroid magnet system provides the magnetic field for the Muon Spectrometer. It covers an η-range up to 2.7 and has an average magnetic field strength of $0.5\,T$. The magnetic field lines are toroidial, which suggests also the name of the magnet system, and are perpendicular to the magnetic field of the solenoid magnet system.

The magnetic field is created by eight superconducting coils in the barrel and by two toroids with eight coils each in the end-cap- region. The inner radius in the barrel region is $5\,m$, the outer radius is $10.7\,m$. These large extensions of the magnetic field allow a track measurement with a long lever arm and hence also improve the precision of the momentum measurement. The magnet coils are not placed in iron, which would increase the magnetic field strength, but are surrounded by air to minimize multiple scattering effects. This is the reason, why the toroid magnet system is also labelled as air-core toroid system.

4.1.2 Inner Detector

The Inner Detector is the closest subsystem to the interaction point and therefore has high importance [42]. Its primary task is the precise reconstruction of the trajectories (tracks) of charged particles. Knowing the trajectory and the magnetic field in the Inner Detector, one can calculate the charge, the initial momentum, the direction of flight and the impact parameter of charged particles. The impact parameter describes the point of closest approach of the trajectory to the beam line.

The design of the Inner Detector must fulfill several requirements to allow an optimal search for rare physics processes. The track reconstruction efficiency of the Inner Detector must be larger than 90%. The design of the Inner Detector ensures a coverage in $|\eta|$-direction up to 2.5 and a full ϕ-coverage. The transverse momentum resolution is supposed to be better than 30% for charged particles with a transverse momentum of $500\,GeV$. Moreover, the Inner Detector must provide a precise primary and secondary vertex reconstruction, which is important for the identification of B-mesons and converted photons.

The resolution of the Inner Detector can be parameterized by [43]

$$\frac{\Delta p_T}{p_T} \approx 0.00036 p_T[GeV] \oplus \frac{0.013}{\sqrt{\sin\phi}}$$

The first term corresponds to the intrinsic resolution, while the second term parameterizes the multiple scattering effects due to more material in the forward region.

A rather large problem of the Inner Detector is the high multiplicity of charged particles per collision, which leads to many overlapping tracks and therefore introduces ambiguities in the track reconstruction. The idea to minimize this problem is the combination of a high precision measurement of few points and a nearly continuous low precision measurement of many points along the particle trajectory. The Inner Detector is built of three subsystems to achieve this combination.

- The pixel detector has a very high granularity and allows a high precision measurement of three dimensional interaction points along the particle trajectory
- The silicon strip detector, or semi conducting tracker (SCT), measures at least four three dimensional space-points along the trajectory also to high precision.
- The straw tracker, or transition radiation tracker (TRT), provides on average 36 measurements in the bending plane of the particle.

These three subsystems are discussed in the following.

Pixel Detector

The active material of the pixel detector is silicon, which is structured in rectangular cells with a size of $40 \times 400 \mu m^2$. These cells are called pixels and can be compared to the pixels of a usual digital camera. Charged particles which pass through silicon produce electron hole pairs. A bias voltage, which is applied to each cell, causes the electrons and holes to drift to the readout-side of the cell. The threshold on single cell-level is a charge corresponding to $3000\, e^-$. The amount of charges, which was deposited in one cell, is stored above this threshold.

The cells are placed in three cylindrical layers in the barrel region, with distances to the beam-line of $r = 5.05\, cm$, $r = 8.85\, cm$ and $r = 12.25\, cm$. The endcap-region is covered by three disks of cells on each side. The pixel detector has in total 80 million cells, with an efficiency of nearly 100%, which was tested in the H8 test-beam setup [44]. The test-beam measurements revealed a resolution of $12 \mu m$ in the $r\phi$-plane and a resolution of $110\, \mu m$ in z-direction. This high precision of the pixel detector drives the measurement of the impact parameter of each reconstructed track.

Silicon Strip Detector

The SCT is responsible for the tracking at radii from $30\, cm$ to $60\, cm$. It is important for the determination of the z-position of the vertex, the momentum resolution and also for the pattern recognition of the reconstruction algorithms.

Silicon was also used here as active material, but in contrast to the pixel detector, the silicon is not structured in cells but in strips with a width of $80\, \mu m$. A sensor is formed of 768 strips and covers an area of $6 \times 12\, cm^2$.

A SCT module is a combination of the readout-electronic and two sensors, which are glued together with a relative angle of $40\, mrad$. The readout-electronics for one module allows only

a binary information from each strip, in contrast to the pixel detector, where also the amount of charges is accessible. This limits the spatial resolution to $23\,\mu m$ per module. The relative angle between the two sensors allows the measurement of the second coordinate of the sensor's plane to a precision of $800\mu m$. The 2112 SCT modules are placed in four cylindrical layers in the barrel region and 988 modules in four disks in each endcap-side.

Transition Radiation Tracker

The number of precision layers is constrained by the high cost per unit area of semiconductor layers and their relative high radiation length. Hence it was decided to use a third sub-detector type, for radii larger than $60\,cm$, which consists of straw tubes with a diameter of $4\,mm$. These tubes are filled with a gas mixture of $70 : 27 : 3\ Xe : CO_2 : O_2$ and have a gold-plated tungsten wire in the middle. Charged particles, which traverse trough the tube, lead to a ionization of the gas mixture.

In addition, the walls of the straw tubes contain radiator material (polyethylene) which enhances the production of transition radiation photons. These photons can be detected in Xe-gas. The number of produced photons by a particle is proportional to the relativistic correction factor $\gamma = \frac{E}{m}$ of the particles [45]. Electrons produce most of these photons due to their small mass. This allows an additional identification of electrons.

The roughly 50,000 tubes of the TRT, which are arranged in 73 cylindrical layers, provide roughly 36 track points for the track reconstruction. The expected occupancy of 50% of the TRT tubes is challenging for the pattern recognition. Nevertheless, the track points are rather important for the resolution of the Inner Detector, since they are positioned along a relative large level arm.

4.1.3 Calorimetric System

The calorimetric system of ATLAS measures the energy and position of particles by sampling the energy deposit in the calorimeter [46]. The main goal is the identification of photons, electrons and jets with energies from $10\,GeV$ to $1\,TeV$. Moreover it is used for the determination of missing energy. This requires a large η-coverage of the calorimetric system. The main calorimetric system consists of one barrel and two endcap parts which cover the area up to $|\eta| < 3.2$. A special forward calorimeter is placed at $3.1 < |\eta| < 4.9$, which is resistant against hard radiation coming directly from the proton beam and is used to improve the measurement of the missing transverse energy.

The calorimetric system itself has two basic components: The inner component is the electromagnetic calorimeter for the measurement of electrons and photons, the outer component is the hadronic calorimeter for the measurement of hadrons.

Electromagnetic Calorimeter

The Electromagnetic Calorimeter (EC) makes use of the interaction of electrons and photons with matter. The most important effect for electrons at high energies ($E \gg m_e c^2$) is bremsstrahlung which leads to the production of an additional photon. The probability of interaction depends on the square of the number of protons of the nucleus Z, i.e.

$$\sigma_b \sim Z^2 E_e,$$

where E_e is the energy of the incident electron. The photons themselves produce electron pairs via pair production, which is the dominant process for high energetic photons. Its cross-section depends also on Z^2, via

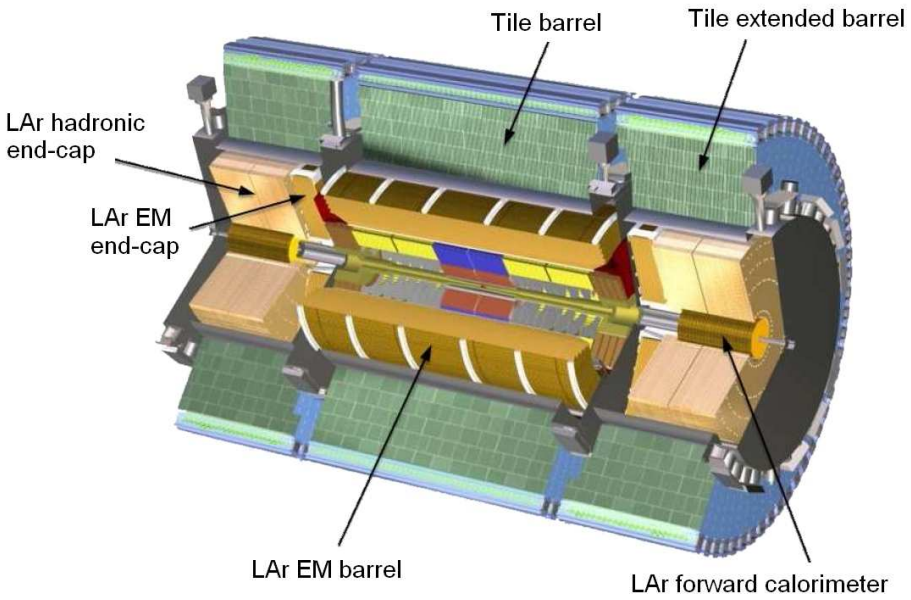

Figure 4.3: Schematic illustration of the ATLAS Calorimeteric System

$$\sigma_p \sim Z^2 \ln E_\gamma$$

where E_γ is the photon's energy [45]. This leads to a cascade of electrons and photons as schematically shown in Figure 4.4. The ATLAS Electromagnetic Calorimeter uses lead absorber plates as passive medium, due to the high Z-number of lead, for the shower production of photons and electrons. Liquid argon acts as a simple ionisation chamber. The corresponding readout electrodes are made of copper and kapton.

The accordion shape of the lead plates (Figure 4.5) was chosen to prevent cracks in azimuthal angle ϕ and hence allow a full ϕ-coverage. Moreover, this design ensures that approximately all tracks transverse the same amount of material [45].

This method is called sampling technique, since not all tracks of the electron shower are detected. The liquid argon is kept in the same cryostat as the Inner Detector solenoid to save additional material of the Electromagnetic Calorimeter.

The energy of incident electron or photon can be determined in this way, since the number of produced electrons is proportional to the energy of incident electrons or photons. Testbeam measurements showed, that the energy resolution of the ATLAS EC can be parameterized roughly by [47]

$$\frac{\Delta E}{E} = \frac{11.0\%}{\sqrt{E[GeV]}} \oplus 0.4\%$$

The first term describes the statistical fluctuations of the method, the second term stands for systematic uncertainties, which arises from inhomogeneities in the response of the calorimeter.

The barrel region of the EC covers an η-range up to ± 1.475, the endcap region is covered to $1.375 < |\eta| < 3.2$. An important aspect for the performance is the material budget in front of the EC because a significant fraction of the particles energy is lost in the inactive material in front of the EC thus causing a systematic uncertainty. The radiation length of material

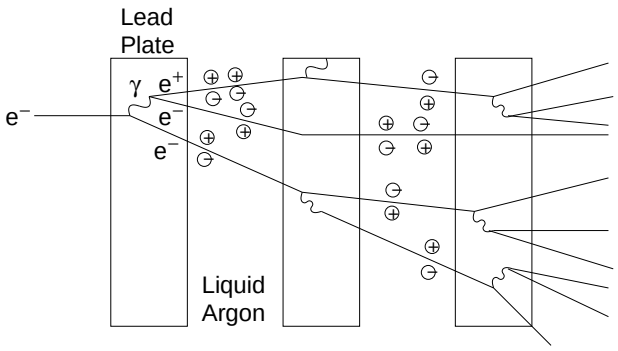

Figure 4.4: Illustration of an electron cascade in a liquid argon sampling calorimeter

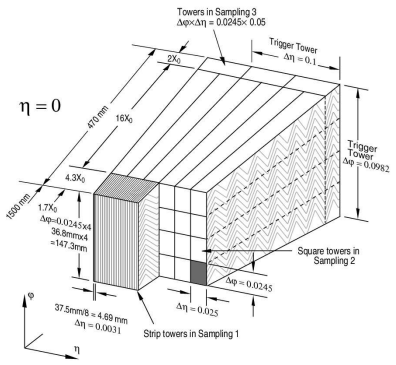

Figure 4.5: The layout of an Electromagnetic Calorimeter module with the accordion shape of the lead plates

in front of the EC at $\eta = 0$ is $2.3\,X_0$. The Electromagnetic Calorimeter is preceded by a presampling detector to correct for energy loss effects, in those regions which have a too large radiation length. In the overlap region between barrel and endcap, the material length is in the order of $7\,X_0$, which makes the insertion of a scintillator slab between barrel and endcap cryostat necessary.

Hadronic Calorimeter

The purpose of the Hadronic Calorimeter (HC) is the identification, reconstruction and energy measurement of particle jets, which result from the hadronization of quarks and gluons, and the measurement of the missing transverse energy in an event. Hadronic jets are longer than electromagnetic jets since the interaction length[2] λ is ten timer larger than for electromagnetic jets.

The major difference of the Hadronic Calorimeter to the Electromagnetic Calorimeter is that the hadronic showers are produced via strong interactions. The incoming hadrons interact with the atomic nuclei and produce further neutrons, protons and primarily π^0- and $\pi^{\pm}$-mesons, which themselves start interacting with further nuclei. Roughly 20% of the incoming energy of the hadrons is used for breaking up the nuclear binding. This is one of the reasons for the worse energy resolution of the Hadronic Calorimeter compared to the Electromagnetic Calorimeter. The decay of π^0 into photons induces also an electromagnetic shower, which accompanies the hadronic counterpart. These hadronic interactions leave highly excited nuclei behind, which undergo fission or radiate to lower their energy state. These effects lead to a hadronic shower, which is measured again by a sampling technique. Due to the larger interaction length of hadrons, more material is needed in the Hadronic Calorimeter.

The ATLAS Hadronic Calorimeter is positioned around the Electromagnetic Calorimeter from the radius $2.28\,m$ to $4.23\,m$. The central barrel part, also called Tile Calorimeter, covers an η-region up to 1.0. An extend barrel region is responsible for the η-coverage from 0.8 to 1.7. Iron plates are used as absorber material and are also used as return yoke for solenoid magnet field. Scintillator plastic tiles are used as an active medium. The read out of the tiles is achieved with optical fibers. Readout Cells are formed by a cluster of tiles and are projective to the interaction point. They provide a granularity of $\delta\eta \times \delta\phi = 0.1 \times 0.1$ which corresponds to roughly 10,000 individual channels. The endcap part of the Hadronic Calorimeter uses copper plates as absorber material and liquid argon as ionization material.

[2]length of the mean free path of a hadron between two interactions

The barrel as well as the endcap part is segmented into three independent layers. The readout cells provide a three dimensional measurement of the deposited energy, which is needed for the reconstruction and the triggering of jets. The energy resolution of the Hadronic Calorimeter in the barrel region can be parameterized as [48]

$$\frac{\Delta E}{E} = \frac{50\%}{\sqrt{E[GeV]}} \oplus 3\%$$

The Hadronic Calorimeter is a possible source of background, called cavern background, for the muon detector. This background is mainly due to thermalized neutrons and low-energy photons. Moreover, the Hadronic Calorimeter must prevent hadrons from proceeding into the muon system[3] and provide a good containment for hadronic showers. This is achieved by a total thickness of 11 interaction lengths of the Hadronic Calorimeter.

4.1.4 Muon Spectrometer

Muons with a minimal energy of roughly $6\,GeV$ are the only particles which pass the Inner Detector and the calorimeters with little interaction, while all other particles have been absorbed before. Hence, the outermost part of the ATLAS detector is the so-called Muon Spectrometer [49]. The goal of the ATLAS Muon Spectrometer is not only the identication of muons but primarily a precise stand-alone measurement and triggering of high energetic muons. This independence of the Muon Spectrometer from the other sub detectors provides good discovery potential even in the case of unexpected backgrounds at the TeV scale.

Before introducing the actual layout and design of the Muon Spectrometer, the basic principle of the momentum measurement in the Muon Spectrometer will be discussed briefly. A homogeneous magnetic field is assumed for this discussion of the main principles of the momentum measurement. Obviously, this assumption does not hold for the toroidal magnetic field, since this has large inhomogeneities around the coils, but the assumption is sufficient to introduce some of the main concepts.

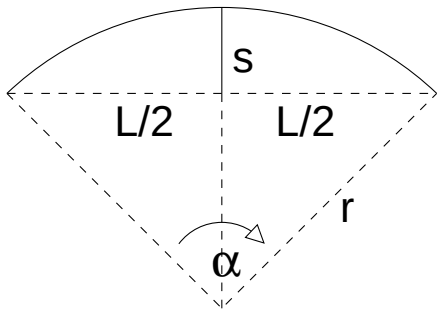

Figure 4.6: Definition of sagitta.

Since muons, which are perpendicular to the magnetic field, are bent on circles, it is sufficient to measure the radius of the circle to determine the muon's momentum. The radius r of a circle is correlated with its sagitta s, via

$$s = r(1 - \cos\frac{\alpha}{2}) \approx r\frac{\alpha^2}{8} \tag{4.1}$$

and hence the sagitta of a trajectory is defined through a segment of a circle as shown in Figure 4.6. The dependence of the sagitta s on the transverse momentum p_T of a particle in a magnetic field is given by

$$s \approx \frac{1}{8}\frac{L^2 B}{p_T} \tag{4.2}$$

where B is the strength of the magnetic field and L the length of the muon trajectory. From this equation follows that the measurement of sagitta is equivalent to the measurement of the transverse momentum of a charged particle. The sagitta could be determined by measuring three points along the trajectory of the muon.

[3] The related effects are called punch-through, sail-through or sneak-through

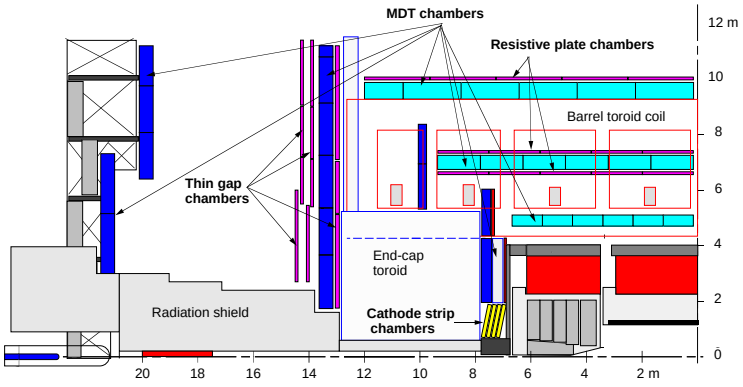

Figure 4.7: Profile of one side of the Muon Spectrometer in the *yz*-plane.

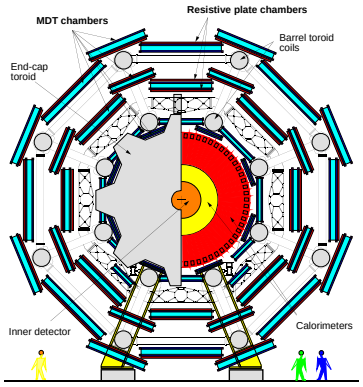

Figure 4.8: Profile of the Muon Spectrometer in the *xy*-plane.

The design of the ATLAS Muon Spectrometer is to reach a momentum resolution of 10 % for $1\,TeV$ muons. Assuming a magnetic field strength of $0.5\,T$, which is roughly the average of the ATLAS torodial magnetic field and an average trajectory length of $5\,m$, this leads to a required precision of $50\mu m$ of the sagitta measurement.

This required precision is achieved by four chamber technologies, i.e.

- Monitored Drift Tube (MDT) chambers: Precise muon tracking
- Cathode Strip Chambers (CSCs): Precise muon tracking in the very forward region
- Resistive Plate Chambers (RPCs): Trigger chamber is the barrel region
- Thin Gap Chambers (TGCs): Trigger chambers in the endcap region.

Before discussing the operation principle of these chambers, the actual layout of the Muon Spectrometer is introduced, which is shown in Figure 4.7 for the rz-plane and in Figure 4.8 for the *xy*-plane of the ATLAS detector. The layout of Muon Spectrometer was designed as a most hermetic system as possible and cover an η-range up to 2.7. The core element of the Muon Spectrometer are the roughly 1.200 MDT chambers, which are responsible for a precise muon tracking and hence for a precise momentum measurement. The MDT chambers are positioned in such a way that all particles coming from the interaction point of the detector should intercept at least three MDT chambers to provide a precise sagitta measurement. Such a combination of three MDT chambers, which is projective to the interaction point, is called tower in the following.

The MDT chambers are placed in three layers in the barrel region at radii of about $5\,m$, $7.5\,m$ and $10\,m$. In the barrel, particles are measured near the inner and the outer magnetic field boundaries, and inside the field volume, in order to determine the momentum from the sagitta of the trajectory.

There are also three layers of MDT-chambers in the endcap region, concentric around the beam axis at $7\,m$, $10\,m$, $14\,m$ and $21\,m$ from the interaction point. In the end-cap regions, for $\eta > 1.4$, the magnet cryostats do not allow the positioning of chambers inside the field volume. Therefore the chambers in this region are arranged to determine the momentum with the best possible resolution from a point-angle measurement (Figure 4.9). A relatively large background rate is expected in the very forward region of the Muon Spectrometer. Hence, CSCs are used instead of the MDT chambers in the inner-most ring of the inner-most endcap layer, because of their finer granularity and less occupancy.

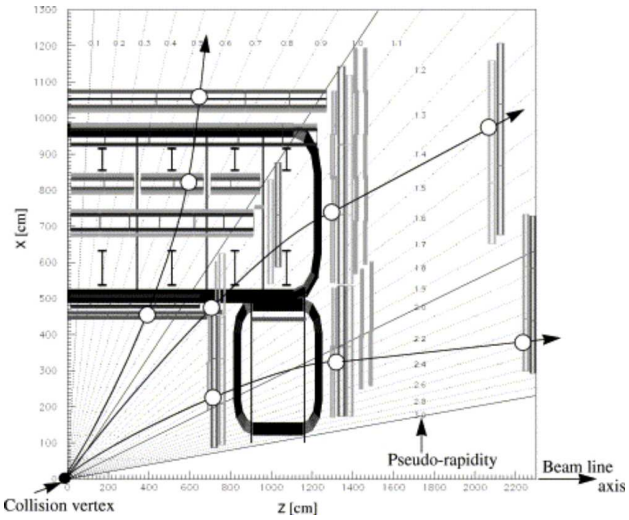

Figure 4.9: Longitudinal profilee in the bending plane (yz) of the spectrometer showing the barrel and end-cap magnet air-coil toroid configuration. It shows the pseudo-rapidity coverage of the muon spectrometer from 0 to 2.7 and a sketch of the layout principle of the three detecting muon stations showing the trajectories of a few GeV/c positively and negatively charged particles.

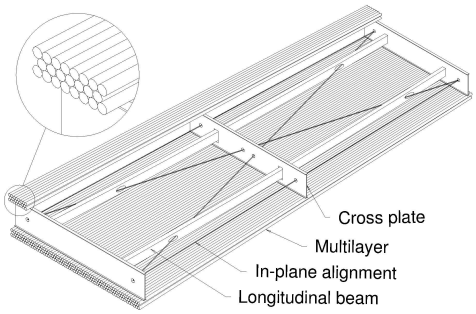

Figure 4.10: Scetch of a monitored drift tube chamber, with six layers of tubes, ordered in two multi-layers.

The huge size of the Muon Spectrometer and the required precision of the sagitta measurement of $50\,\mu m$, makes a precise alignment of the MDT chambers necessary. The MDT chambers are monitored by an optical alignment system, which is designed to provide a relative precision, i.e. the positioning of MDT chambers within one tower relative to each other, of $30\,\mu m$ and an absolute precision, i.e. the positions of MDT chambers in the ATLAS coordinate system, of $300\,\mu m$. The label 'monitored' of MDT reflects the fact, that these chambers are monitored by an optical alignment system. It should be noted, that the relative precision has the dominant impact on the sagitta measurement. The optical alignment system will monitor the relative movement of the MDT-chambers due to e.g. thermal effects, and provide the information for the muon trajectory reconstruction.

As already mentioned, the MDT chambers are the core element of the Muon Spectrometer and, therefore, it is justified to discuss them in more detail. A schematic sketch of an MDT-chamber is shown in Figure 4.10. An MDT-chamber consists of six to eight drift tube layers, which are arragened in two so-called multi layers with a spacing of $200\,mm$. The aluminum drift tubes have diameter of $30\,mm$ and are filled with $Ar : CO_2$ gas mixture $97 : 3$ at 3 bar absolute pressure. A central wire is positioned in the middle of the tube. A high energetic muon, which passes through a tube, ionizes the gas, i.e. separates electrons from the gas atoms. An applied potential difference between wire and tube of $3080\,V$ leads to an electric field, which lets the electrons drift towards the wire, while the positive ions drift towards the tube wall. When the drifting electrons reach some critical velocity, i.e. energy, they can ionize further gas molecules around them. This creates an avalanche of further electrons and leads to a so-called Townsend avalanche, which consists of electrons and positive charge ions. The ions drift through the whole potential difference to the tube wall and induce a measurable signal in the electrodes [45]. By measuring the so-called drift-time, i.e. the time which is needed for the ionization cluster to reach the wire, one can determine the so-called drift-radius, i.e. the minimal distance of the muon trajectory to the central wire. Figure 4.11 shows the precision of the drift-radii determination in dependence of the drift-radius itself. A

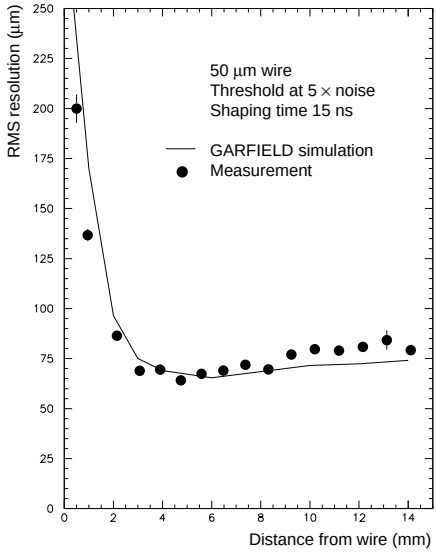

Figure 4.11: Resolution of the drift-radius measurement in dependence of the distance to the central wire.

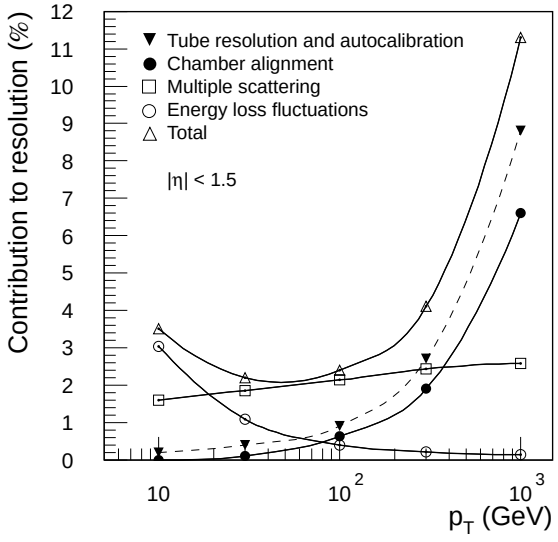

Figure 4.12: Expected contributions to the momentum resolution of the Muon Spectrometer in the barrel region.

relatively bad resolution is expected for small drift-radii since the muon does not necessarily interact at the point of closest approach to the wire with the gas molecules. On average a precision of $80\,\mu m$ is expected. Having measured the drift-radii for all tubes which have been hit, one can fit a tangential line to the drift-circles, which approximates the muon trajectory within one MDT-chamber. These fitted straight lines are called segments in the following.

The CSC's are multiwire proportional chambers which are used in the very forward region of the Muon Spectrometer instead of the MDT chambers. They have an expected single track resolution of $\lesssim 60\mu m$. This good resolution is achieved by a cathode strip readout which measures the charge induced on the segmented cathode by the electron avalanche formed on the anode wires. The transverse coordinate can be calculated via the measurement of the orthogonal strips on the second cathode of the chamber. The chambers have a small sensitivity to photons ($\sim 1\%$) and also a small neutron sensitivity ($\lesssim 10^{-4}$). The small neutron sensitivity is achieved by the small gas volume used and the absence of hydrogen in the operating gas, which is a $Ar/CO_2/CF_4$ mixture.

The RPCs are the trigger elements for the barrel region, which provide a fast momentum estimation of muons for the hardware based trigger and also the necessary timing information for the drift-time measurement of the MDT-chambers. They have a spatial resolution of 1cm and timing resolution of $2\,ns$. The RPCs are made of two bakelite plates which form a narrow gap. The gap is filled with $C_2H_2F_4$ gas. Incident muons lead to ionization of the gas, which leads to a streaming discharge caused by the high electric field between the bakelite plates. The two bakelite plates are covered with read-out strips on their back, which are orthogonal with respect to each other. This allows an η- and ϕ-measurement of the muon track.

The TGCs are the trigger elements for the endcap region. They consist of two cathode plates with a distance of $1.4\,mm$. The gap between the plates is filled with a gas mixture of C_5H_{10} and CO_2. Evenly spaced anode wires ($1.8\,mm$ spacing distance) are placed in between the plates and a high voltage of $3.1kV$ is applied across the wires. Each wire collects a certain number of ionization electrons caused by an incident muon. The measured ionization electron distribution across all wires is used to identify the path of an incident muon. These chambers are combined to two or three layers to provide also a spatial coordinate measurement.

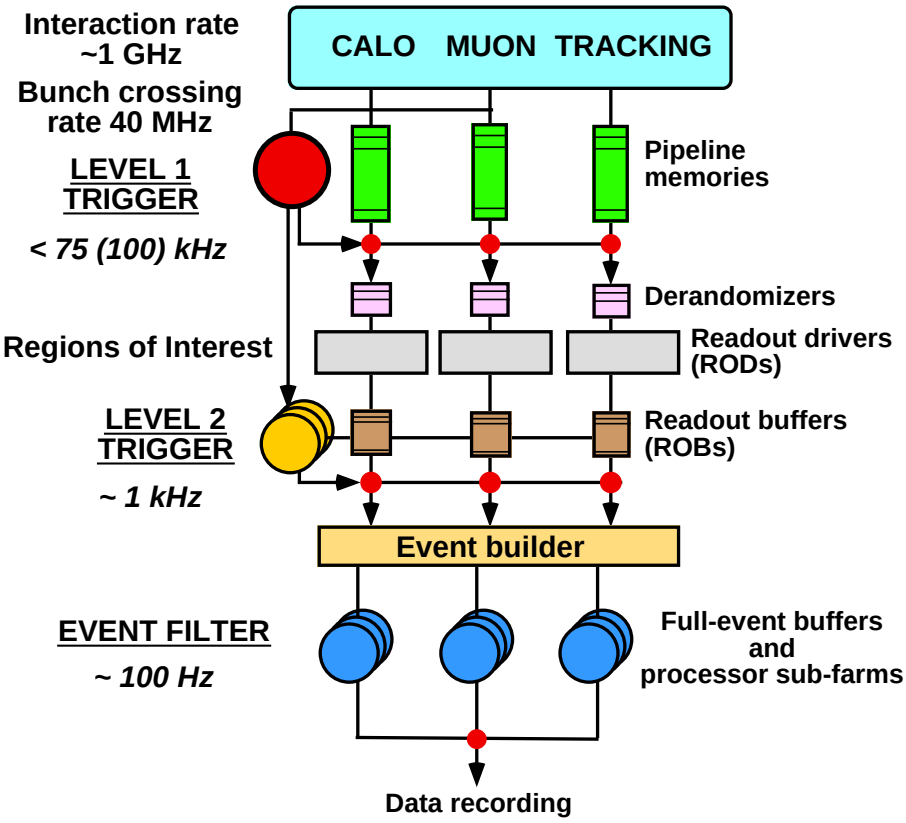

Figure 4.13: Overview of the trigger system of ATLAS.

It should be noted, that the choice of the torodial magnetic field determines that the Muon Spectrometer measures the momentum p of the muons and not the transversal momentum p_T. Obviously, these two quantities can be converted in each other via $p_T = p \sin\theta$. The design value of the transverse momentum resolution and its various contributions of the ATLAS Muon Spectrometer is shown in Figure 4.12. The muon spectrometer is designed for a transverse momentum resolution of about $2-3\%$ for muons with a $p_T = 50\,GeV$ and 10% for muons with $p_T = 1\,TeV$. The contribution of multiple scattering to the resolution is relatively small for low and high energetic muons due to the choice of air-core magnetic field configuration, which minimizes the use of material. The resolution is dominated by energy loss fluctuations on the calorimenters for low energetic muons ($\lesssim 20\,GeV$) and by the precision of the drift-radii measurement for high energetic muons ($\gtrsim 300\,GeV$).

4.2 Trigger System and Data Acquisition

The data-size of one recorded collision is in the order of $1\,MB$. Since bunch crossings occur with a rate of 40 MHz, this would result in data volume, which cannot be stored with today technologies. To be handled by the ATLAS computing system a reduction to 100 MB/s is needed. The goal of the ATLAS trigger system is to reduce the rate of candidate collisions from $40\,MhZ$ to $100\,Hz$ without a loss of interesting physics events, e.g. events which contain the production a Higgs boson or even a W/Z boson [50]. The trigger system has three levels and is schematically illustrated in Figure 4.13.

The level one (LVL1) is hardware based. It uses information from the calorimeters with

reduced granularity and from the muon-trigger chambers, i.e. RPC- and TGC-stations, which fire for muons with sufficiently high energy. The latency[4] of the level one trigger is $2\,\mu s$, which leads to a target rate of $75\,kHz$. A further important task of LVL1 is to define the so-called region of interests (RoI) for each event. The RoIs are regions in the detector, where possibly interesting objects might be present, e.g. a high energetic muon. The LVL1 trigger passes the event information within the RoIs from the read-out buffers (ROBs) to the LVL2-trigger.

The level two (LVL2) trigger is software based and uses the full granularity in the RoIs of the detector and also the Inner Detector. The target rate is $1\,kHz$, with a latency of $1\,ms$ to $10\,ms$, depending on the complexity of the event. The full access of the LVL2 trigger on the event would exceed the required maximal latency and hence the concept of RoIs had to be introduced. The disadvantage of this approach is, that interesting objects, which have failed the LVL1-trigger, cannot be found by level 2. If an event passes the LVL2-trigger requirements, all information of one event is collected from the ROBs by the so-called Event Builder and passed to the third trigger level, which is called Event Filter (EF).

The Event Filter makes the final decision if an event is recorded for further analysis. Its target rate is $100\,Hz$. The Event Filter is software based and runs on a computer farm near the ATLAS pit. This allows for a relatively long decision time in the order of one second. As a consequence, the EF has access to the full event with full granularity. More sophisticated reconstruction algorithms can be applied. Events which are accepted by the EF are written to mass-storage devices and available for further offline-analysis.

Even with this output rate, the total storage space needed by the ATLAS experiment is in the order of 1 PetaByte (10^{15} bytes) per year. This makes a powerful computing environment necessary, which is introduced in section 4.4.

The ATLAS trigger menu defines the operation of the trigger system and its conditions. A condition is a combination of an object, e.g. an electron, and a certain threshold, e.g. $p_T > 20\,GeV$. Table C.2 shows the planned trigger menu for the low luminosity phase of LHC.

Selection signature	**Expected Trigger rate [Hz]**
One isolated electron with $p_T > 25\,GeV$	40
Two isolated electrons with $p_T > 15\,GeV$	< 1
One isolated photon with $E_T > 60\,GeV$	25
Two isolated muons with $E_T > 60\,GeV$	2
One isolated muon with $p_T > 20\,GeV$	40
Two muon with $p_T > 10\,GeV$	< 10
One jet with $E_T > 400\,GeV$	10
Three jets with $E_T > 165\,GeV$	10
Four jets with $E_T > 110\,GeV$	10
One jet with $E_T > 70\,GeV$ and $\not{E}_T > 70\,GeV$	20
One isolated tau with $p_T > 35\,GeV$ and $\not{E}_T > 45\,GeV$	5
Further Trigger Requirements	20

Table 4.2: Selection of expected trigger rates for the low luminosity phase ($\mathscr{L} = 10^{33} cm^{-2} s^{-1}$) of the ATLAS experiment.

[4]The latency is defined as the time in which data of all sub-detectors can be stored in a pipeline

4.3 Physics Program

The benchmark test of the ATLAS detector design is its discovery potential for the Higgs-boson, however the high luminosity and the large center of mass energy of the LHC proton-proton collisions allow also a test of various theoretical models, e.g. supersymmetry.

In each second the production of one $t\bar{t}$-pair, five Z bosons, which decay into lepton pairs, 50 W bosons, 100 QCD jets with a transverse momentum larger than $200\,GeV$ and half a million $b\bar{b}$-pairs are expected within the ATLAS detector during the low luminosity phase of LHC, which corresponds to a instantaneous luminosity of $10^{33} cm^2 s^{-1}$. These large rates of physics processes provide not only a good opportunity for high precision tests of the standard model, but are also a huge background to many hypothetic physics channels. Some of these physics channels are shortly discussed in the following [43].

4.3.1 The Higgs Boson

The production cross-section of a Higgs boson with a mass of $1\,TeV$ is expected to be more than $100\,fb$, which corresponds to roughly 1,000 events in one year during the low luminosity phase. The width of the Higgs boson Γ_H depends on its mass m_H, i.e.

$$\Gamma_H \sim (m_H)^3$$

and is expected to be in the order of a few MeV for $m_H \approx 100\,GeV$ and rises up to $100\,GeV$ for $m_H \approx 600\,GeV$. Therefore, Higgs-bosons with large masses cannot be identified as a clear peak. As shown in section 2.1, the couplings of the Higgs boson to fermions are proportional to the fermion masses. This implies different dominating decay modes for different m_H- scenarios (Figure 4.14). For the search of the Higgs-boson, three mass-ranges are distinguished:

- **Low mass region:** $m_H < 130\,GeV$: The decay into two b-quarks will dominate in this region since these quarks are the most massive fermions, which are kinematically accessible. Due to the overwhelmingly large QCD-background, it is extremely difficult to discover the Higgs-boson in this channel. The decay $H \rightarrow \gamma\gamma$ is more promising, but even here, the irreducible background has a cross section which is 60 times larger than the signal one.

- **Intermediate mass region:** $130\,GeV < m_H < 180\,GeV$: The decay into vector gauge bosons $H \rightarrow ZZ^* \rightarrow 4l$ and $H \rightarrow WW^* \rightarrow l\nu l\nu$ becomes dominating in this regime[5]. For $m_H \approx 170\,GeV$ the four lepton decay gets suppressed, once the decay mode into two real W bosons opens up. In this case, it is crucial to understand the background. The signal significance exceeds 5σ, assuming a relative uncertainty on the background contribution of 5%. This is the most promising mass regime for the discovery of the Higgs-Boson.

- **High mass region:** $180\,GeV < m_H$: In this mass regime the decay in two real Z bosons is dominating, which is the most clear channel for the Higgs-boson search. The dominating background is the continuum production of Z boson pairs.

Figure 4.15 illustrates the overall sensitivity for a standard model Higgs-boson for an integrated luminosity of $100\,fb^{-1}$, which corresponds to a few years of running at low luminosity.

[5]the letter l indicates the decay into a lepton, i.e. a muon or an electron

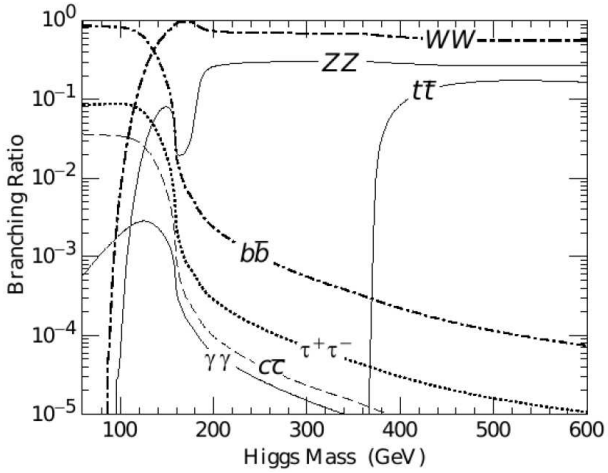

Figure 4.14: Branching ratio of the Higgs boson as a function of the Higgs mass.

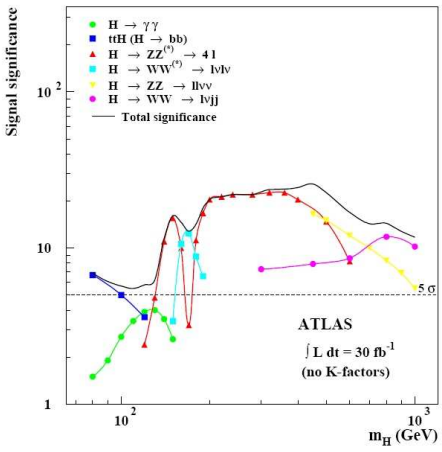

Figure 4.15: The ATLAS sensitivity for the discovery of the standard model Higgs boson. The statistical significance is plotted for various decay channels.

It can be seen that a signal significance of 5 standard deviations can be achieved. It is expected that higher integrated luminosities in the range of 300 fb^{-1} allow for a determination of the Higgs boson mass to a precision of 0.1% for a $120\,GeV < m_H < 400\,GeV$ and its cross section to a precision of roughly 10%. It should be also noted that ATLAS provides good possibilities to discover a Higgs-sector within the minimal supersymmetric standard model (MSSM) [51].

4.3.2 Supersymmetry

The discovery of supersymmetric particles [20], which exists at the electro-weak scale, should be relatively easy compared to the discovery of the Higgs-boson. The cross-sections of the production of gluinos and squarks are comparable with the relevant standard model background processes at the same Q^2. 10,000 events containing supersymmetric particles with a mass around $1\,TeV$ are expected during one year of running at low luminosity.

The actual decay modes of supersymmetric particles are model dependent. Usually, final state objects with high transverse momenta are expected, since they stem from heavy particles. A very significant feature of the decay of supersymmetric particles is a relative large amount of missing transverse energy, which is due to the lightest supersymmetric particle the so called neutralino. The neutralino cannot decay further, since it is already the lightest particle with a supersymmetric quantum number. Moreover it should be a weakly interacting particle and hence escapes the detector without any further interaction. These signatures are therefore easy to discriminate from the Standard Model background processes.

4.3.3 Beyond the Standard Model

The supersymmetric extension has some pleasant theoretical features, but is not the only possible theoretical scenario, which could be discovered by the ATLAS detector. The discovery potential of ATLAS covers also:

- New vector bosons, which are usually labelled as W' and Z' up to a mass scale of $5\,TeV$

- Leptoquarks up to a mass scale of $1.5\,TeV$
- Excited quarks up to masses of $6\,TeV$
- Technicolor resonances up to a mass limit of $1\,TeV$
- Signature of extra-dimension models
- New particles, predicted by Little Higgs-models

4.3.4 Precision Measurements

The statistical uncertainty on measurements scales as $\frac{1}{\sqrt{N}}$, where N is the number of signal events. Hence, the error on most measurements is dominated by systematic uncertainties, since the statistical contribution can be usually neglected due to the enormous luminosity of LHC. Some systematic uncertainties can be also reduced with high statistic calibration samples, e.g. the decay of the Z boson into two leptons. This decay was studied in detail in this thesis to determine reconstruction efficiencies, momentum scales and momentum resolutions of various parts of the detector (see section 8.3.3).

Moreover, the high statistic in most channels allows a clean cut-based selection of signal processes. An example is the determination of top quark mass. While the experiments at the Tevatron collider have a few hundred recorded top quark events [52], which require sophisticated methods for the signal selection and mass determination, the ATLAS detector is expected to record thousands of top quark events during a single day in the low luminosity phase. This large statistics allows simple hard cuts, which ensure a very clean and well understood event sample.

The precise measurement of the top-quark mass is interesting not only because it is the only quark with mass at the electroweak scale, but also because it constrains the Higgs boson mass through loop corrections. A Higgs-boson discovered with a mass, which is predicted by precision top-quark measurements, would be a very remarkable result of the standard model. The mass of the top-quark will be measured in the semi-leptonic decay mode of a top-quark pair (Figure 4.16). The lepton, stemming from W boson decay, is used to tag the event, while the jets resulting from the decay of the second top-quark, are used for the mass determination. This process can also be used for the determination of the jet-energy scale, i.e. the precision to which the average energy of particle jets can be reconstructed in the detector. Assuming an uncertainty of 1% on the jet energy scale in ATLAS, a precision of $\Delta m_{top} \approx 1 - 1.5\,GeV$ can be reached.

In order to predict the mass of a standard model Higgs boson, also the mass of the W boson must be measured to high precision. Figure 4.17 illustrates the expected Higgs boson mass, constrained by higher order corrections in dependence of the measured top quark and W boson mass [53]. The mass of the W boson is known to $\sim 30\,MeV$. The measurement of the W boson mass in hadron colliders is achieved by measuring the invariant mass of the decay products of the W boson in the plane transverse to the beam axis. The expected dominant systematic contributions of this measurement are the absolute calibration of the lepton energy scale and various theoretical uncertainties. It is expected that this measurement is one of the most complex measurements at ATLAS and will take several years to reach the precision of todays experiments.

The last aspect of precision measurements at ATLAS mentioned here is B-physics, which includes

- Precision measurements of CP-violaton in B-mesons

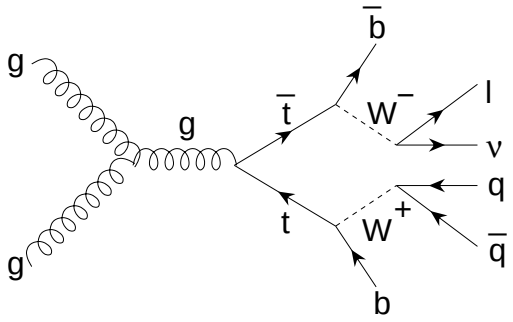

Figure 4.16: Feynman diagram of a semileptonic decay of a top-quark pair.

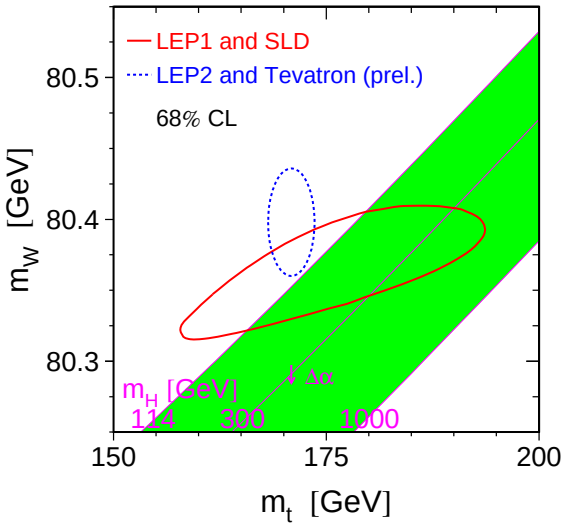

Figure 4.17: Dependence of the Higgs boson mass on the masses of the W boson and the top quark. The latest measurements of these W and top mass suggest a light Higgs mass, i.e. below 300 GeV.

- Measurement of rare decays which a strongly suppressed in the Standard Model
- Overconstraining the CKM matrix by a precise measurement of flavor oscillations in B_s^0 and B_d^0

It is expected that ATLAS delivers several more precise results on B-physics than the present lower energy colliders. Some measurements are even comparable to the LHCb-experiment. For these measurements an optimal performance of the Inner Detector is necessary, since it is responsible for the reconstruction of a second vertex and therefore for the identification of b-quarks.

4.4 ATLAS Computing

4.4.1 The ATLAS Software Framework

The software for the experiment is developed by a working group, comparable in manpower to a subdetector working group in hardware. The complexity of the detector also implies the complexity of the underlying software and hence it requires to develop a common software framework for the experiment which is called ATHENA [54].

ATHENA provides several features. First of all, it allows an integrated communication between various software applications - called algorithms - within the framework. All algorithms have access via the so-called STOREGATE to data of other algorithms, e.g. the event information[6] or the detector description. Moreover, a common framework ensures a common approach

[6] the information of one proton-proton collision

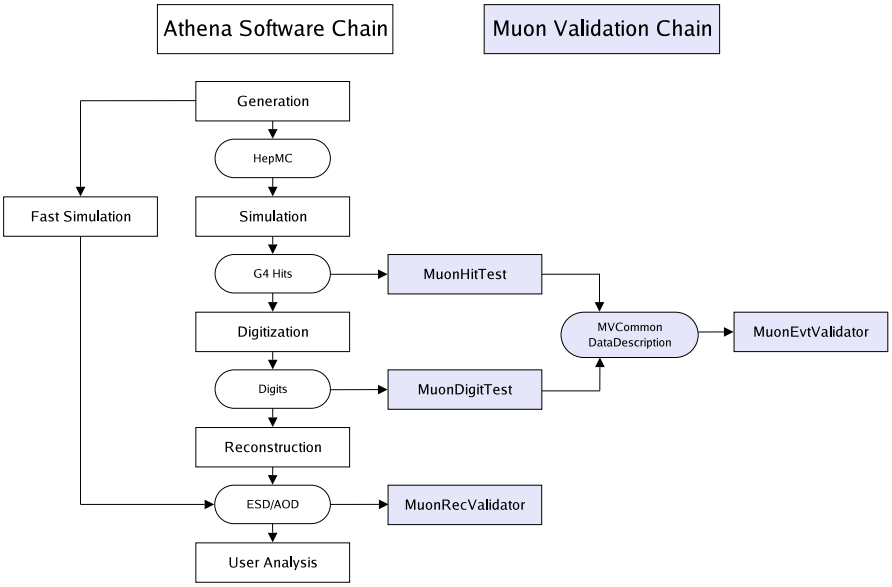

Figure 4.18: Illustration of the ATHENA Monte Carlo software chain and the corresponding Muon Software validation chain, which is discussed in detail in appendix A.

of software developing, e.g. messaging or access on disk and re-use of already written code-segments, i.e. a common underlying design of the software packages. The ATHENA framework allows a dynamic loading of libraries and is organized in form of plug-in modules and allows a flexible configuration of various algorithms which should be executed. The configuration is done via the so-called JOBOPTION file which allows a user specification of the algorithms via PYTHON scripting.

The main purposes of the ATLAS software is to generate, simulate, digitize and reconstruct proton-proton collisions, i.e. events, in the LHC environment. This ATHENA software chain is illustrated in Figure 4.18. Thus the advantage of the modular approach becomes obvious at this stage since the simulation, digitization and reconstruction algorithms for the sub-detector systems, i.e. Inner Tracker, Electromagnetic Calorimeter, Hadronic Calorimeter and Muon Spectrometer, can be implemented by the corresponding development teams independently from each other.

The generation step includes the proton-proton collision itself, i.e. calculating the position and momentum four-vectors of all particles which are produced in the collision[7]. The generation is based on various Monte Carlo generator programs, which are briefly discussed in section 2.3.

The second part is the tracking of the produced particles through the detector using the GEANT4 toolkit [55]. GEANT4 simulates the impact of the magnetic field and the interactions with the material, e.g. multiple scattering, energy loss, photon conversions and further decays of unstable particles. Each interaction of a particle with an active, i.e. sensitive, detector element is stored in a so called hit-object, which represents the position and type of the interaction.

During the digitization step, the response of the detector and its electronics on the various

[7]The four-vector information, coming from the Monte Carlo generator programs, is called Monte Carlo truth information in the following

hit-objects is simulated. As an example the interaction between a final state muon in the gas-volume of an MDT-chamber is discussed. The muon interacts with the gas at several positions and hence these positions are stored in hit-objects. During the digitization, the hit-object with the closest distance to the wire is used for the calculation of the drift-radius, which is converted to a measured drift-time, assuming a certain resolution for a single MDT-tube. The drift-time information is stored in a so-called digit-object, which also stores the information about the associated tube and MDT-chamber.

The reconstruction part is based on the digitized information, i.e. in the above example on the simulated drift-time or in case of data on the measured drift-time for each tube. The reconstruction includes various algorithms, e.g. for pattern recognition, track fitting, vertex determination and energy measurements. It should be noted that the digitized information and the real data are equivalent from a data representation point of view.

The output of the reconstruction part are so-called event summary data (ESD) and analysis object data (AOD) files. While the first include a more detailed description of an event, e.g. the drift-radius information which was used for the track reconstruction, the latter one, only include information which is of primal interest for physics analysis, e.g. the charge or the momentum of particles.

The last step in a standard Athena chain is the actual physics analysis, where several analysis techniques can be applied to study a particular physics process.

It should be also mentioned, that ATLAS software provides an event display, called Atlantis, which presents an event graphically. Such a tool is useful not only for the visualization of events but also for the validation of the reconstruction algorithms and detector geometry description.

The simulation and reconstruction step require a common basis of the detector description, which should include a description of the geometry, the positioning and the material of the detector elements. This common source of the detector description is called GeoModel [56]. This ensures that each step is based on the same detector information which prevents the algorithms from inconsistencies. The corresponding data of the GeoModel are stored in a database. A crucial point is that all alignment algorithms are also based on the GeoModel description. Hence, applying alignment algorithms on real data, will lead to an adjusted database, which is a new basis for the reconstruction of data.

All objects in GeoModel are recursively defined by adding or subtracting geometric primitives, e.g. cubes or cylinders. The description of a part of the torodial magnet system is shown in reality and in the GeoModel description as an example in Figure 4.19. A material description is assigned to each component within GeoModel, which is accessible for the reconstruction and the Geant4 simulation. GeoModel allows also the handling of time-dependent positioning of all detector-elements, which is especially important for the alignment of 1.200 MDT-chambers in the Muon Spectrometer.

It is obvious, that a valid description of the detector within GeoModel and the validation of the Athena software chain, starting from generation to reconstruction, is crucial for all physics analysis. A significant part of this thesis was to provide a corrected description and tools for the validation of the software chain. A brief overview is given in Appendix A, a more detailed description has been published in [3, 8].

4.4.2 Grid Computing

One year of data taking at the LHC results in 15 Petabytes (15 million Gigabytes) of data, produced by the four experiments, which has to be carefully analyzed by physicists worldwide

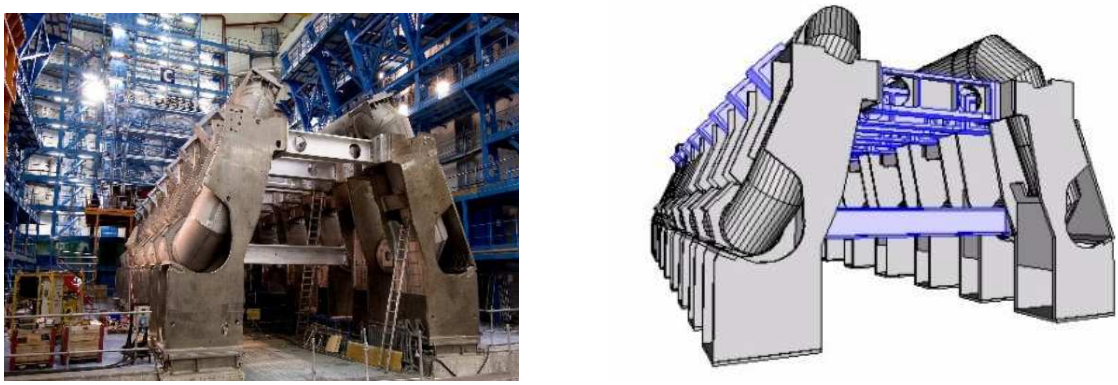

Figure 4.19: Two magnetic coils and their support structures during the building phase of ATLAS (left) and their GeoModel description (right).

to discover new physics processes. Moreover, billions of complex theoretical simulations of the proton-proton collision must be calculated.

In the former LEP experiments, the computer processing was done at a computer farm, near to the experiment itself. For LHC, storage and processing requirements exceed by far the capacities available at a single site and hence a new approach was chosen, which is commonly known under LHC Computing Grid (LCG) project [57]. This computing grid provides to infrastructure for the storage of data and the necessary computing power for the physics analyses and simulations.

The data distribution follows a so-called Tier-structure (Figure 4.20). The LHC data is recorded in a first step on tape at so called Tier-0 center at CERN. From there, it is further distributed to worldwide Tier-1 centers (e.g. GridKa@FZK), which store also a large part of data and provide a twenty-four hour support. The Tier-2 centers like the computer cluster at the LMU Munich (LRZ) store only a small part of data since they are designated for user specific physics analysis and simulation. The Grid is accessed via the lowest hierarchy level (Tier-3), which are small computer clusters or individual PCS of physicists. The Tier-structure has several advantages. First of, several copies of data exists, which ensures that data safety. The single Tier centers are independent from each other which minimizes the critical points in the infrastructure. A further advantage is the cost sharing for maintenance and support through the several national computer centers.

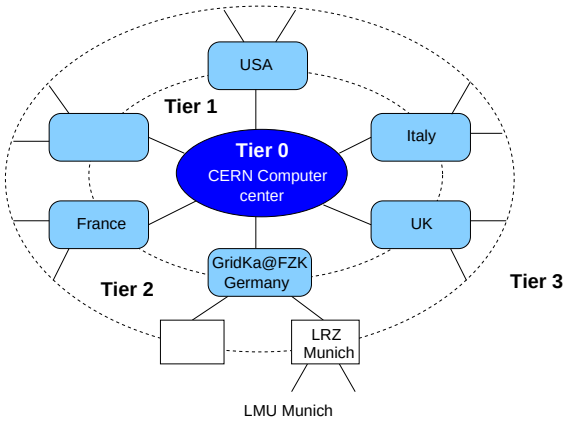

Figure 4.20: Illustration of Tier-structure of the LCG.

The LCG project involves dedicated hardware and software developments. Obviously, an adequate bandwidth is needed for the data distribution within the grid. The grid-software must be compatible with heterogeneous hardware and must also ensure coherent software at all connected computers. Distributed data must be identifiable by the user and stored redundantly. Moreover a fair access to all resources for all users (load balancing) must be guaranteed and a secure access to more than 100 sites without local accounts must be

provided.

Several tests of the grid infrastructure called data challenges have been performed during the last years to ensure the full functionality of the grid with the start of the data taking.

Part II

Muon Spectrometer Performance

"We haven't got the money, so we've got to think!"

Ernest Rutherford[1]

Chapter 5

Expected Performance of an Ideal Muon Spectrometer Setup

The Muon Spectrometer, one of the biggest and most complex detectors ever designed, requires a detailed and flexible simulation to deal with questions related to design optimization and detailed physics studies which will lay the basis for the first discoveries of new physics. Hence it is crucial also for this thesis to understand the Muon Spectrometer and its simulation in detail in order to give meaningful predictions of physics analysis on first data.

The simulation of the Muon Spectrometer includes a detailed description of several thousand detection chambers, a detailed material description of support structures and a precise model of the expected torodial magnetic field. A short survey of the simulation side of the ATLAS Muon Spectrometer can be found in [8]. The validation and the development of the Muon Spectrometer software was crucial to prepare the physics analysis of this thesis. A more detailed discussion can be found in appendix A.1.

The results of the expected performance of an ideal Muon Spectrometer, gained from the developed validation algorithms, are discussed in this chapter. The label 'ideal' means that all parts of the Muon Spectrometer are fully functional, calibrated, placed at their nominal positions and operate with nominal resolutions. The following study is mainly based on a single muon sample, containing 10,000 events, with a transverse momentum of $50\,GeV$, fully simulated and reconstructed within ATHENA software release 12.0.6. The transverse momentum of $50\,GeV$ was chosen, because the Muon Spectrometer is expected to have its best performance at these energies. Moreover, standard physics processes like the decay of the W or Z boson, which play an important role already in the first phase of LHC, have final state muons in this energy-regime.

[1] Sir Ernest Rutherford, born 1871 in New Zealand, was the first physicists who distinguished between α, β and γ radiation and introduced the term "half life". After receiving the Nobel prize in chemistry in 1908, he postulated the so-called Rutherford atomic model, which he derived from his famous experiment of the deflection of α particles from a thin gold film.

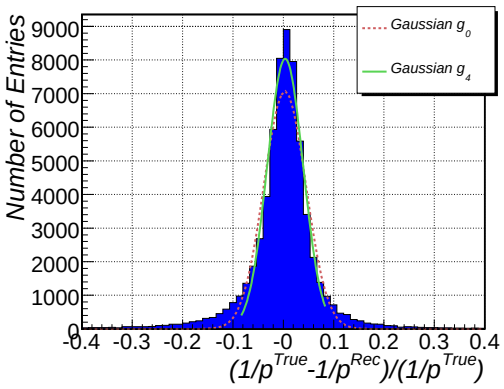

Figure 5.1: Definition of the transverse momentum (p_T) resolution. g_0 is the fitted Gaussian of iteration step 0, g_4 is the fitted Gaussian of iteration step 4.

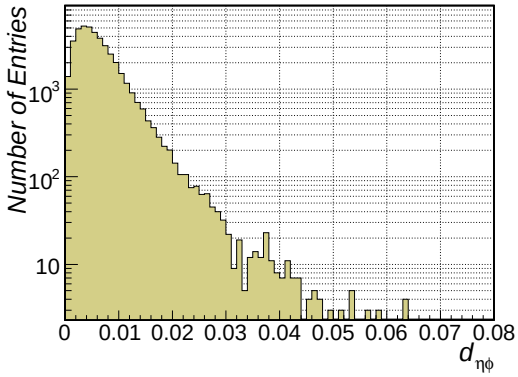

Figure 5.2: Distribution of the distance $d_{\eta,\phi}$ for tracks reconstructed by the ATLAS Muon Spectrometer to Monte Carlo generated muons in a $50\,GeV$ single muon Monte Carlo Sample.

5.1 Definitions

The performance of the Muon Spectrometer is evaluated in terms of *efficiency*, *fake-rate* and *resolution*. Efficiency is defined as

$$\varepsilon := \frac{N_{\text{Correctly Reconstructed Track}}}{N_{\text{Monte Carlo Truth Muons}}} \tag{5.1}$$

where a track is defined as correctly reconstructed if its transverse momentum p_T and its η- and ϕ-coordinates[1] fulfill the condition

$$d_{\eta\phi} = \sqrt{\omega_1 \cdot (\eta - \eta^{Truth})^2 + \omega_2 \cdot (\phi - \phi^{Truth})^2} \leq r_c \tag{5.2}$$

where ω_1 and ω_2 are weights for the two coordinates and r_c is the maximal threshold value. It was chosen to set $\omega_1 = \omega_2 = 1$ for this thesis.

Figure 5.2 shows the distances defined by Equation (5.2) of generated muon tracks to reconstructed tracks in a $50\,GeV$ single muon sample, requiring that the reconstructed transverse momentum does not differ by more than $10\,\%$ from the corresponding truth value. Figure 5.2 suggests to choose a threshold value of $r_c = 0.05$ for the definition of matched reconstructed muon tracks. This chosen condition in Equation (5.2) requires that the reconstructed particle track lies within a cone radius of 0.05 around the truth muon track.

Having defined a matched track, also a first simple definition of a fake track can be introduced. A fake track is defined as a track which cannot be associated to a truth muon, and hence fails the condition 5.2. In this context, the fake rate ζ is defined as:

$$\zeta := \frac{N_{\text{Fake Tracks}}}{N_{\text{Monte Carlo Truth Muons}}} \tag{5.3}$$

The common meaning of fake tracks is only partly covered by the above definitions. In general understanding, a fake track is a track, which is not caused by a real muon. Within the definition in Equation (5.3) not correctly reconstructed tracks, which are caused by a

[1] The pseudo-rapidity η and the azimuthal angle ϕ are defined at the interaction point

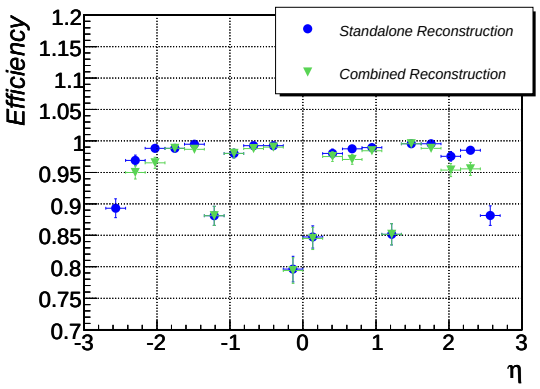

Figure 5.3: Muonboy Spectrometer reconstruction efficiencies for various reconstruction algorithms vs. η.

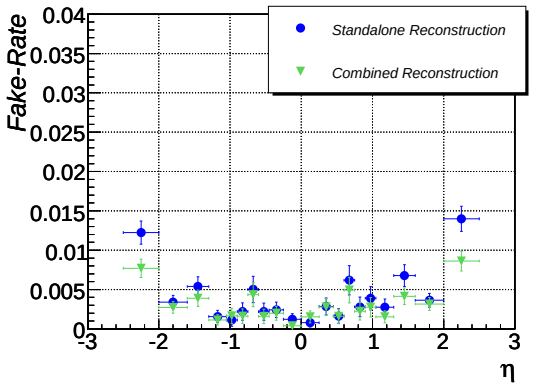

Figure 5.4: Muonboy Spectrometer fake-rates for various reconstruction algorithms vs. η.

muon, are also classified as fake tracks. Nevertheless, this definition allows a first study of this quantity.

Another important variable for the Muon Spectometer performance is the transverse momentum (p_T) resolution, which is defined in the following. The normalized p_T deviation for each correctly identified track is given by

$$\rho := \frac{\frac{1}{p_T^{Truth}} - \frac{1}{p_T^{Reconstructed}}}{\frac{1}{p_T^{Truth}}} = 1 - \frac{p_T^{Truth}}{p_T^{Reconstructed}} \tag{5.4}$$

and is plotted for each track in a histogram as it is shown for example in Figure 5.1. Note, that we expect a Gaussian distribution of $\frac{1}{p_T}$, but not for p_T itself, since the momentum measurement derives from the inverse of the sagitta s measurement

$$p \sim \frac{1}{s}$$

which is subject to gaussian uncertainties. The p_T-resolution itself is defined in the following manner. In a first step, a Gaussian g_0 is fitted to the distribution. In a next step i a Gaussian g_i is fitted to the data between the $x_{m,i-1} \pm 2 \cdot \sigma_{g_{i-1}}$, where $\sigma_{g_{i-1}}$ is the width of g_{i-1} and $x_{m,i-1}$ its mean. This iterative procedure is repeated n times. It turns out that $n = 2$ are already enough steps for a stable result. The width of g_2 is then defined as p_T resolution. The mean of g_2 is referred to as the *momentum-scale*, which is a measure for a systematic shift of measured muon momenta.

5.2 Results

The track reconstruction of muons can be achieved stand-alone by the Muon Spectrometer, i.e. no information of the Inner Detector is used, or in the so-called combined mode, where the track-information of the Muon Spectrometer and the information from the Inner Detector is combined. For this study, it was chosen to use the reconstruction algorithm called *Muonboy* [58] for the stand-alone reconstruction and the so-called *STACO*-algorithm [59] for combined reconstruction.

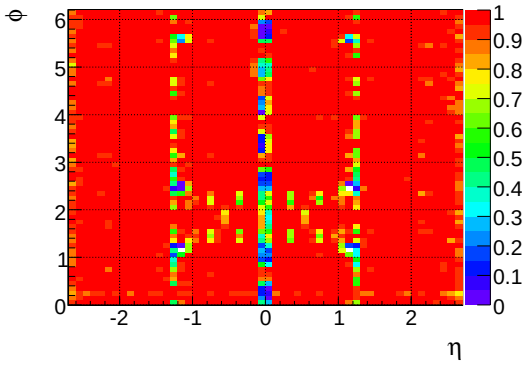

Figure 5.5: Standalone Muonboy Spectrometer reconstruction efficiencies for vs. η and ϕ.

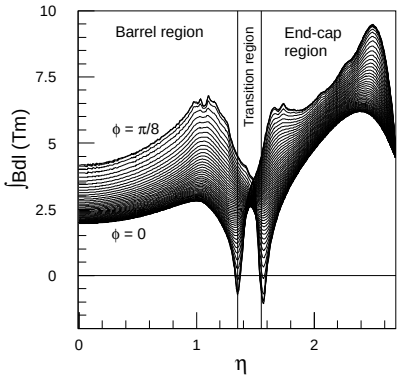

Figure 5.6: Bending power of the magnetic field in the ATLAS Muon Spectrometer vs. η.

The reconstruction efficiency and the fake-rate distribution versus η for standalone and combined reconstruction is shown in Figure 5.3 and 5.4. *Standalone reconstruction* refers to a muon track reconstruction which is exclusively based on Muon Spectrometer information. The efficiency for both reconstruction methods is expected to be roughly equivalent, with a slightly higher reconstruction efficiency of the standalone reconstruction. The drop of efficiency at $\eta \approx 0$ is due to holes for service passages in this region. Some MDT-chambers, the so-called EE type, are missing in the η-region $1.1 < |\eta| < 1.3$ foreseen in the initial layout of the Muon Spectrometer, which was used for this study [60]. This η-region corresponds to the transition between the Muon Spectrometer's barrel and the endcap region and explains the drop of efficiency at $|\eta| \approx 1$.

Figure 5.5 shows the standalone reconstruction efficiency vs. η and ϕ. The ϕ-region from $1.0 < \phi < 2.5$ corresponds to the feet region of the Muon Spectrometer, where a large amount of support material is present and therefore the loss of efficiency in this region can be explained.

The p_T-resolution is roughly ϕ-symmetric, but has a relatively strong η-dependence due to several design aspects of the Muon Spectrometer, which are discussed in the following. Hence it is usually sufficient to study the η-dependence of the transverse momentum (p_T) resolution. The p_T-resolution versus η is shown in Figure 5.7. The resolution of the combined reconstruction is significantly better than the standalone reconstruction for the studied muon energy of $50\,GeV$. Large differences can be observed in the Barrel/Endcap transition region of the Muon Spectrometer. Indeed in this region the absence of the EE type chambers imposes an p_T measurement via the deflection angles which leads to a severe degradation of the Muon Spectrometer momentum resolution [60]. Moreover, the expected magnetic field in this region is relatively weak as illustrated in Figure 5.6. The combined reconstruction resolution is driven by the Muon Spectrometer performance for $|\eta| > 2$. Note, that the inner tracker covers an η-region from -2.5 to $+2.5$, while the Muon Spectrometer covers a region up to $|\eta| = 2.7$.

The p_T-dependence of the resolution is shown in Figure 5.8. While we observe a linear degrading of the combined reconstruction resolution, a more complicated behavior is seen for the standalone reconstruction. The resolution improves up to an energy of roughly $50\,GeV$. After that, the resolution degrades also for the Muon Spectrometer. This can be explained by the different effects which have an impact on the p_T-resolution. Multiple scattering effects on the p_T-resolutions are independent of p_T itself and are dominating the resolution at around $100\,GeV$. For low p_T muons, the energy loss in the calorimeter is the leading contribution to

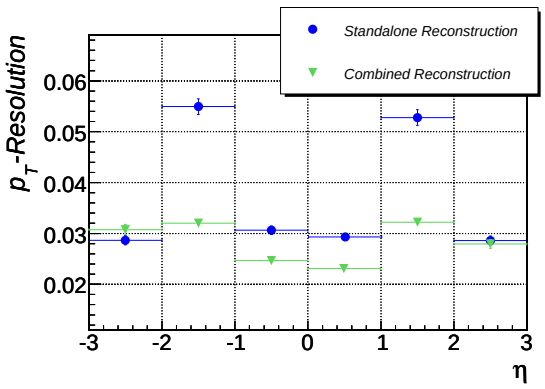

Figure 5.7: Muonboy Spectrometer p_T-resolution for various reconstruction algorithms vs. η.

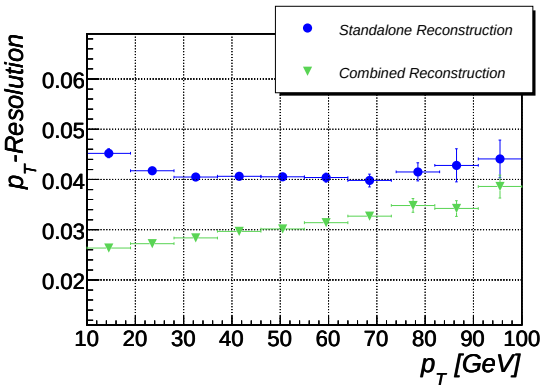

Figure 5.8: Muonboy Spectrometer p_T-resolution for various reconstruction algorithms vs. p_T of muons (Based on an $Z \rightarrow \mu\mu$ sample).

the resolution. It is roughly 3% at 10 GeV but only 0.5% at 100 GeV. The contribution of the intrinsic resolution of the precision chambers and their alignment is small at low momenta. However, above a p_T of around 100 GeV it starts to rise sharply and quickly dominates the resolution. For muons with p_T above 100 GeV, the spectrometer provides a better resolution than the inner detector and it becomes the dominant component for combined reconstruction.

"An expert is a man who has made all the mistakes which can be made in a very narrow field."

Niels Bohr[1]

Chapter 6

Validation of the MDT Chamber Simulation with Cosmic Rays

So far, the Muon Spectrometer performance was primarily tested within Monte Carlo simulations based on the Geant4 toolkit as discussed in Chapter 5. The cosmic ray measurement facility in Garching, Germany, provides a good environment to study the agreement of a Geant4 simulation of the MDT-chambers with real cosmic muon data. Such a test is an important input for the ATLAS Muon Spectrometer performance, which is based on pure Monte Carlo simulations.

The cosmic ray measurement facility is designed for measurement, commissioning and calibration of ATLAS MDT chambers (see Figure 6.1). The measurement facility consists of three MDT chambers, which are positioned one on top of the other. The upper and the lower chamber are used as reference chambers. The properties of these two chambers are known to a very high precision from tomography measurements made at CERN [61]. The so-called *test chamber* is sandwiched between the two reference chambers. Furthermore, an iron absorber is placed below the lower reference chamber to cut off low energy muons in the trigger. Since no magnetic field is applied at the cosmic ray measurement facility, the track of an incident cosmic muon is expected to be a straight line. With this assumption the rt-relation, the wire positions and the geometry of the test-chamber can be determined. Detailed information is given in [61, 62].

The measured track positions may not perfectly fit to a straight line, because of the finite resolution of the tubes, multiple scattering effects on the material of the MDT-chambers or δ-electron emissions which may mask or displace the signal of the muon. Even though, the muon trajectory can be described by a parabola which parameterizes the limited sagitta resolution: The opening parameter of the parabola is expected to be zero for a straight line and a deviation from zero is a measure of the sagitta resolution.

[1] Niels Henrik David Bohr was born 1885 in Kopenhagen and is the only Danish physicist who received a Nobel Prize (1922). Bohr formulated a new theoretical model for atoms in 1913. His model was one of the major steps in physics, since it assumed for the first time the quantization of electron orbits. 1922 Bohr and Sommerfeld delivered an explanation for the structure of the periodic table of elements.

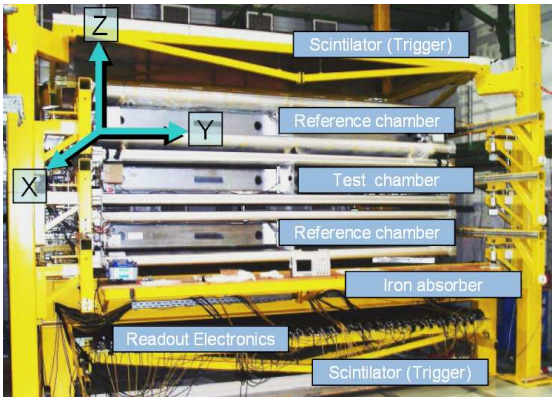

Figure 6.1: The cosmic ray measurement facility in Garching and the appropriate coordinate system.

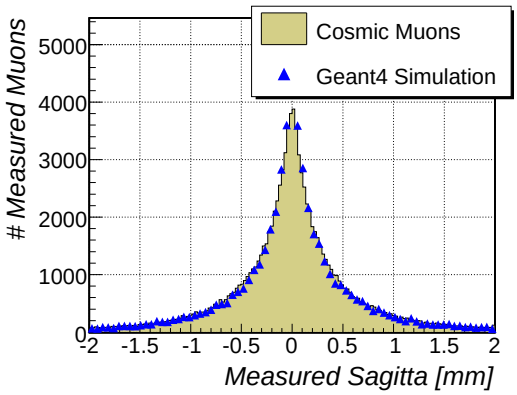

Figure 6.2: Comparison of the sagitta distribution of measured and simulated cosmic muons.

The simulation of the cosmic ray measurement facility (CMF-Simulation) is based on Geant4 and was fully implemented within the ATHENA framework. It also this includes an implementation of the GEOMODEL description [56] of the measurement facility. The ATHENA package COSMIC GENERATOR was used to generate cosmic muons with the correct energy and momentum spectrum.

Figure 6.2 shows the comparison of the measured sagitta of 100.000 recorded cosmic muon tracks as well as the predicted distribution based on the Monte Carlo simulation of the cosmic ray measurement facility. The width of both distributions agrees within a relative difference of 5% and also the shapes of the distributions agree well. This is a strong indication that the GEANT4 simulation describes well the response of MDT chambers to cosmic muons.

It is a useful exercise to use the simulation validated by the cosmic ray measurement facility and to extend the setup of the MDT chambers to the ATLAS Muon Spectrometer. To modify the CMF-Simulation according to the ATLAS geometry the distances between the chambers where chosen to be 2580 mm and 3550 mm. Multiple scattering effects due to the RPC chambers of the Muon Spectrometers could not be neglected. Therefore blocks with the dimensions of the RPCs which consist out of the respective materials were introduced in the simulation. This setup approximates one sector of the ATLAS Muon Spectrometer and allows for assessing its performance.

The reconstructed sagitta resolution in the modified CMF-Simulation versus muon energy is shown in Figure 6.3. The energy dependence of the sagitta resolution in the case of a perfect single tube resolution is presented in Figure 6.4. It is clearly visible that the single tube resolution starts to dominate multiple scattering effects at a muon energy of roughly 80 GeV in agreement with the TDR [49].

Using Equation 4.1 the sagitta resolution can be translated into the momentum resolution. For simplicity we assume a constant magnetic field with a field-strength of 0.5 T. Using this value the energy dependent momentum resolution of the modified CMF-Simulation can be calculated, which is shown in Figure 6.5. One should note that this study does not include energy loss fluctuations, which dominate the resolution at small energies at the ATLAS Muon Spectrometer. Furthermore, a perfect alignment of the detector was assumed.

In spite of these idealizations, the resolution of the ATLAS Muon Spectrometer due to the single tube resolution and due to multiple scattering effects can be compared with the values given in the TDR [49]. The high energy regime provides a possibility to compare the single

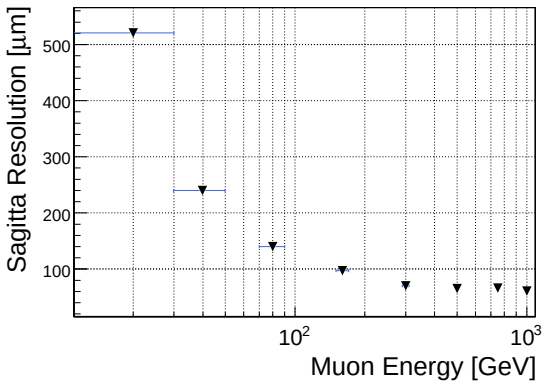

Figure 6.3: Sagitta resolution of the simulated ATLAS Muon Spectrometer setup in dependence of the muon energy with an average single tube resolution of about $100\,\mu m$

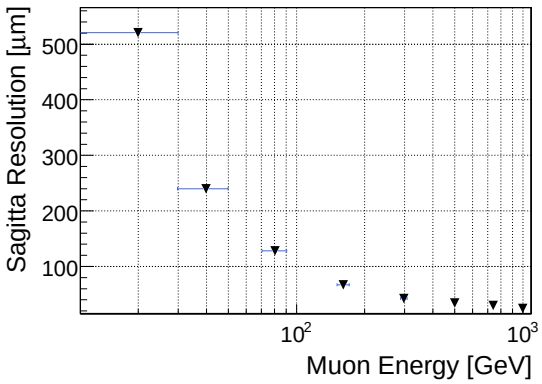

Figure 6.4: Sagitta resolution of simulated ATLAS setup in dependence of the muon energy with infinite single tube resolution

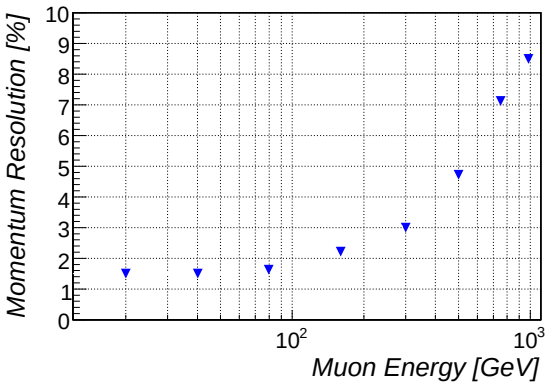

Figure 6.5: Momentum resolution of simulated ATLAS setup in dependence of the muon energy

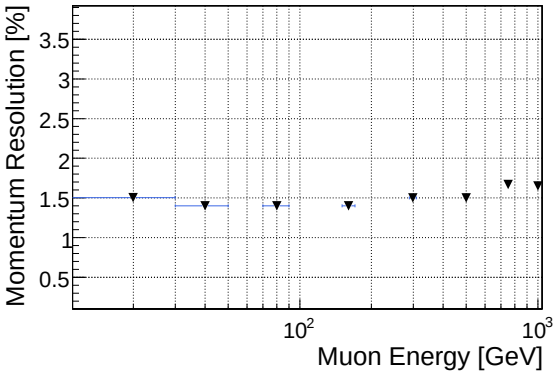

Figure 6.6: Momentum resolution of simulated ATLAS setup in dependence of the muon energy with infinite single tube resolution

tube resolution since this is the dominating effect at these energies. For 1 TeV a momentum resolution of $\sim 10\%$ is expected in the ATLAS detector. The simulation in this study predicts a momentum resolution of $\sim 9\%$ for muon energies of 1 TeV, which is a good agreement, given the differences in the details of simulation, digitization and magnetic field between the CMF-simulation and the TDR studies [49].

At lower energies multiple scattering becomes the dominating effect for the momentum resolution. In order to investigate them in detail the simulation was run with the assumption of a perfect single tube resolution. This leads to the momentum resolution shown in Figure 6.6, which only includes multiple scattering effects. We obtain a resolution due to multiple scattering effects of about 1.5%. The results of the TDR [49] range from $1.6 - 2.2\%$.

A more detailed discussion of this study can be found in [6] and in appendix B.

"This isn't right, this isn't even wrong."

Wolfgang Pauli[1]

Chapter 7

Impacts of Random Misalignment on the Muon Spectrometer Performance

After having discussed the expected performance of an ideal Muon Spectrometer in chapter 5 and validated this simulation via cosmic data in chapter 6, the last aspect to study are various discrepancies of the simulation to the real Muon Spectrometer, which might be present in the first phase of the experiment. These discrepancies are for example misalignments, miscalibrations, an imperfect material description of the ATLAS detector or, in particular, an imprecise knowledge of the magnetic field.

The latter two aspects have been studied in [63] and [64] and no large degradation of the Muon Spectrometer performance is expected, assuming conditions which are expected at the startup phase of ATLAS. Large experience in the calibration of MDT-chambers has been gathered [65] at the various cosmic ray test facilities, e.g. the cosmic ray measurement facility in Garching, which was introduced in chapter 6.

A less extensively studied aspect is the alignment of the ATLAS Muon Spectrometer chambers, which will be a long and challenging task. The correct alignment of the ATLAS Muon Spectrometer is crucial to ensure its design performance. It is thus worth to investigate the impact of imperfect knowledge of the geometry on the performance. The impact of various misaligned Muon Spectrometer layouts on the performance have been studied and are discussed in this chapter; they are published in [2,7]. This study is also based on a single 10,000 muon sample, with a transverse momentum of $50\,GeV$, simulated and reconstructed within ATHENA software release 12.0.6.

The position of each Muon Spectrometer chamber can be described by 6 parameters, three spatial parameters and three rotations: Each position and angle is expected to deviate from

[1] Wolfgang Ernst Pauli was born in 1900 in Vienna. His godfather was the famous physicists Ernst Mach. Shortly after his graduation from school he published his first work based on the Weyl's extension of the theory of general relativity. In 1925 he introduced a new degree of freedom into quantum mechanics, which is now known as the spin of the electron and formulated the Pauli exclusion principle. In 1930 he postulated the existence of the neutrino. After the world war two, Pauli was involved in the foundation of CERN.

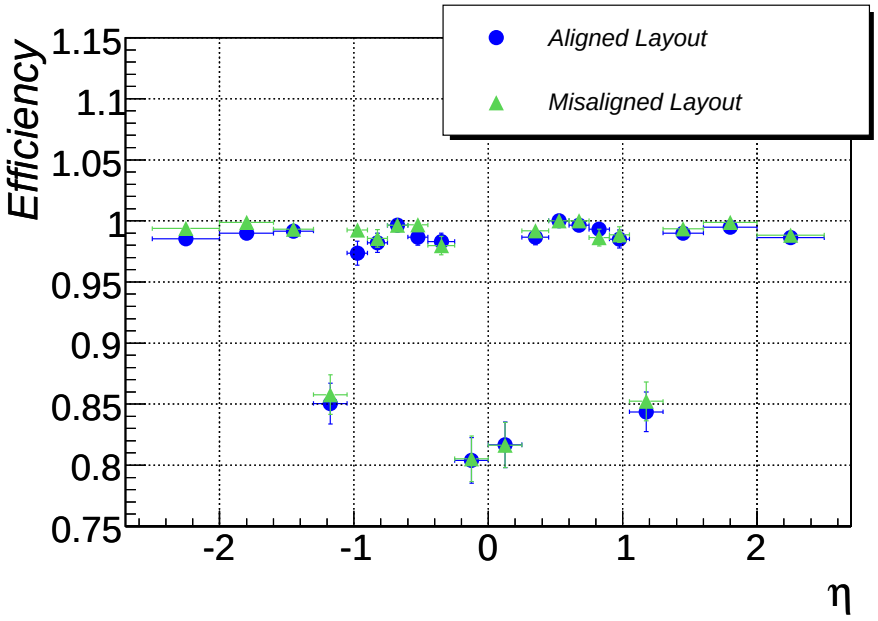

Figure 7.1: Comparison of reconstruction efficiency for an aligned Muon Spectrometer and a misaligned Muon Spectrometer with $\sigma_m^{All} = 1mm$.

its nominal value by a certain amount. In order to model these displacements we introduce a dimensionless variable called *misalignment parameter* σ_m^{All}. The value of this parameter corresponds to the width of a Gaussian function which is centered around zero. Each position parameter and rotation angle of all MDT-chambers is smeared independently by this Gaussian multiplied by $1000\mu m$ in case of translations or $1\,mrad$ in case of rotations. The ATLAS Muon Spectrometer working group has chosen one standard misaligned Muon Spectrometer layout, which was generated with $\sigma_m^{All} = 1$, e.g. all chambers are randomly shifted in mean by $1\,mm$ in all directions and are additionally rotated by a mean of $1\,mrad$[1]. New survey measurements in the Endcap-region of the Muon Spectrometer have shown that these misalignments are in the right order of magnitude, but might be underestimated within the current implemented misaligned layout[2].

Note, that an MDT-chamber can also be internally misaligned, i.e. the two multi-layers can be rotated and shifted with respect to each other and even the layers within the multilayers might be affected by distortions [62]. This aspect of misalignment has not been studied here.

Several aspects of misalignment effects have to be studied. The most important aspect is the difference of the Muon Spectrometer performance of a perfectly aligned Muon Spectrometer layout and an uncorrected misaligned layout. In other words: To which precision must the Muon Spectrometer be aligned, to achieve a certain momentum resolution.

In order to study these effects, an ideal Muon Spectrometer layout was used during the simulation step of the ATHENA software chain, but a misaligned layout was used during the reconstruction phase. This leads to simulated samples, which are based on an uncorrected misaligned Muon Spectrometer [3]. Figure 7.1 illustrates the comparison of the stand-alone

[1] A discussion of the effect of an independent translation and rotation of the 6 parameters can be found in appendix C.1.2

[2] Translations and rotations of the nominal positions of MDT-chambers in the order of $2-4\,mm$ and $2-4\,mrad$ have been measured

[3] A corrected misaligned Muon Spectrometer, i.e. in the case where the 6 parameters of all chambers are

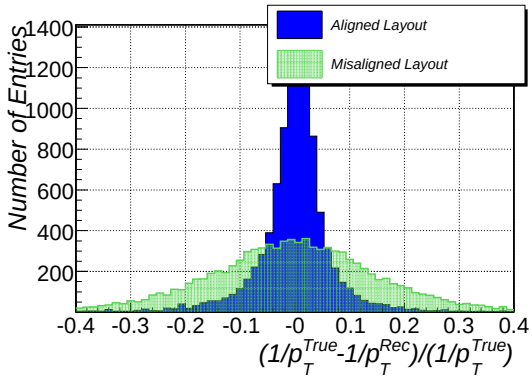

Figure 7.2: Comparison of p_T-resolution distribution for an aligned Muon Spectrometer and a misaligned Muon Spectrometer with $\sigma_m^{All} = 1$.

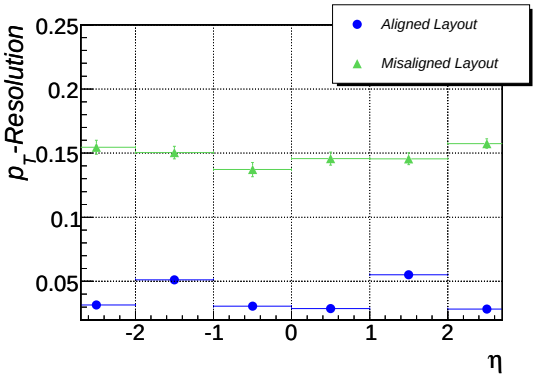

Figure 7.3: Comparison of p_T-resolution width for an aligned Muon Spectrometer and a misaligned Muon Spectrometer with $\sigma_m^{All} = 1$.

track reconstruction efficiency for the ideal and the misaligned case using $\sigma_m^{All} = 1$. No significant decrease in the reconstruction efficiency can be observed. This has the consequence that even a largely misaligned Muon Spectrometer can still be used for muon identification of inner tracks during the very first phase of the ATLAS experiment, without applying any further corrections.

Figure 7.2 and 7.3 show the impact of a misaligned Muon Spectrometer on the transverse momentum resolution. A strong degradation of the resolution can be observed. The overall observed Muon Spectrometer resolution σ_{All} can be expressed as the quadratic sum of the p_T-resolution at the ideal geometry (σ_{ideal}) and the resolution due to the misaligned geometry ($\sigma_{Alignment}$).

$$\sigma_{All} = \sqrt{\sigma_{Alignment}^2 + \sigma_{ideal}^2}$$

This leads to $\sigma_{Alignment} \approx 0.14$ for muons with $p_T \approx 50\,GeV$. The impact on the momentum scale is relatively small for the overall Muon Spectrometer, since random misalignments cancel to a certain extend. In physics signatures, such as the decay of a Z boson into to muons, the impact is even less, since a misaligned geometry has the opposite effect for opposite charged muons to first order (See appendix C.1.1).

The behavior of the p_T-resolution with increasing muon p_T reveals a strong linear correlation, which is illustrated in Figure 7.4[4]. This linear worsening of the resolution can be explained by the dependence of the measured sagitta s on the corresponding momentum as $s \sim \frac{1}{p}$ and hence it follows that

$$p \cdot \Delta s \sim \frac{\Delta p}{p}.$$

The uncertainty on the measured sagitta has several contributions, e.g. multiple scattering effects, which scale as $1/p$. However, the impact of relative large misalignments, considered here, is dominating the overall uncertainty of sagitta and hence it can be assumed, that Δs is approximately independent of the track momentum even for small momenta.

known to high precision, is nearly equivalent to the ideal case (see appendix C)

[4]The measured points of the misaligned layout have not been corrected for the p_T-distribution of muons resulting from a Z boson decay. An exception is the point at $100\,GeV$ which was determined with a single muon sample at this energy.

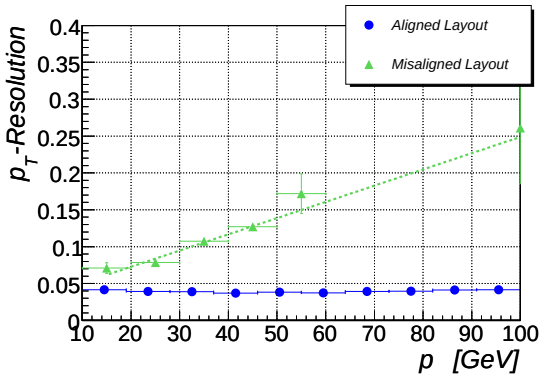

Figure 7.4: Comparison of p_T-resolution width for an aligned Muon Spectrometer and a misaligned Muon Spectrometer with $\sigma_m^{All} = 1mm$ vs. p_T (Based on an $Z \rightarrow \mu\mu$ sample).

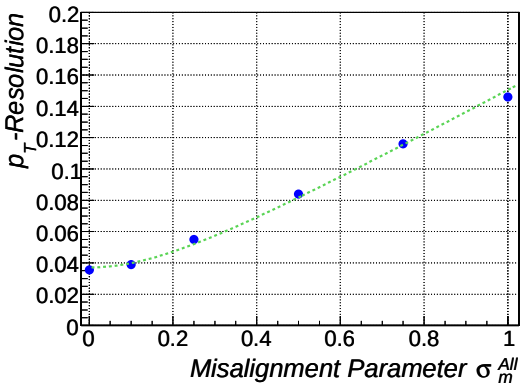

Figure 7.5: Width of p_T-resolution vs. misalignment parameters σ_m^{All} for a $50\,GeV$ muon sample.

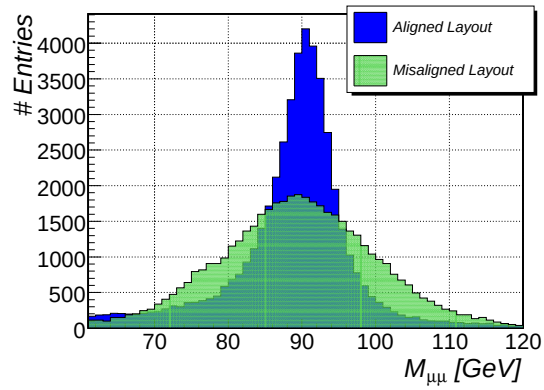

Figure 7.6: Reconstructed Z boson mass distributions for an aligned and a misaligned ($\sigma_m^{All} = 1$) Muon Spectrometer layout.

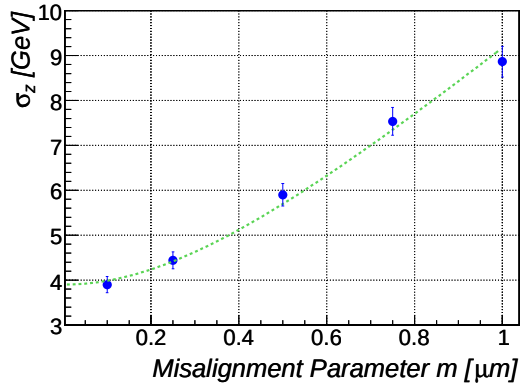

Figure 7.7: Width of smearing Gaussian σ_g vs. misalignment parameter σ_m^{All}.

The impact of Muon Spectrometer layouts with various values of the misalignment parameter σ_m^{All} on the p_T-resolution for $50\,GeV$ muons is shown in Figure 7.5. The muon p_T-resolution width increases with increasing misalignment parameter. The increasing behavior can be parameterized by the function:

$$\sigma_{res} = \sqrt{\left(\sigma_{MS}^2 + a \cdot (\sigma_m^{All})^2\right)} \tag{7.1}$$

where σ_{MS}^2 corresponds to the Muon Spectrometer resolution width σ_{res} if no misalignment is present. Fitting Equation 7.1 to the measured resolution leads to $a \approx 0.021$ and $\sigma_{MS} \approx 0.037$. A misalignment parameter of 0.05 leads only to a relative decrease by 2% of the p_T-resolution for $50\,GeV$ muons, which is negligible to a good extent.

So far, only the results of a single muon sample have been discussed. The impact of a misaligned Muon Spectrometer layout ($\sigma_m^{All} = 1$) on the Z boson resonance is shown in Figure 7.6. It is expected that the mean of the invariant mass distribution does not change significantly, since the momentum scale of the reconstructed muon p_T is hardly affected by misalignment (see appendix C). On the other hand a large broadening of the distribution due to the degradation of the p_T-resolution of the muons is expected, which is shown in Figure 7.6. The dependence of the reconstructed width of the Z boson mass distribution on σ_m^{All} is

shown in Figure 7.7. The observed dependence is the basis for the determination of the Muon Spectrometer resolution with data, which is discussed in section 8.4. Moreover, the decay of $Z \rightarrow \mu\mu$ offers a possible alignment approach for the ATLAS Muon Spectrometer as briefly discussed in section C.3.

Part III

Production of the Z boson at LHC

"It is not the possession of truth, but the success which attends the seeking after it, that enriches the seeker and brings happiness to him."

Max Planck[1]

Chapter 8

Cross-Section $\sigma\left(pp \to Z/\gamma^* \to \mu^+\mu^-\right)$ Measurement

The measurements of cross section and transverse momentum spectrum (p_t) of the Z boson at ATLAS provide additional tests of the standard model and may be sensitive to exotic physics processes. The Z boson production is also a common background process for many other physics analyses and must be understood very well. Moreover, the decay of Z bosons in two muons is a very important calibration channel for the ATLAS Muon Spectrometer.

The achievable precision of the cross section $\sigma(pp \to Z/\gamma^* \to \mu^+\mu^-)$ with first data of LHC (corresponding to an integrated luminosity of $50\,pb^{-1}$) at the ATLAS detector is discussed in this chapter. This includes also a detailed study of the in-situ determination of the Muon Spectrometer performance. An integrated luminosity of $50\,pb^{-1}$ is expected to correspond roughly to 30,000 reconstructed $Z \to \mu^+\mu^-$-events, which corresponds to a statistical uncertainty of $\sim 0.5\%$. This number should be recalled during the discussion of the following analysis, since it is a measure for the importance of various systematic effects.

An important goal of this analysis was to minimize the dependence on Monte Carlo simulation. Therefore various methods, like 'tag and probe' for various efficiency determinations or for background estimation within data were studied and are discussed.

The chapter is structured as follows. The signal selection is discussed in section 8.1, the estimation of the remaining background events, after the selection process, is introduced in section 8.2. Various methods for the determination of the ATLAS Muon Spectrometer performance within data are explained and discussed in section 8.3 and 8.4. An estimation of further systematic uncertainties regarding the cross-section measurements is given in section 8.5. The final result of the expected precision of this measurement is discussed in section 8.6.

[1] Max Karl Ernst Planck, born 1858 in Kiel, was one of the most famous students in Munich, where he started studying physics in 1874. His physics professor Jolly dissuaded Planck from studying physics, since he believed that physical science was more or less completed. Planck was one of the founders of quantum theory by postulating quantized energies in order to explain the black body radiation spectrum.

8.1 Event Selection

8.1.1 Relevant Background Samples

The event topology of $pp \to Z/\gamma^* \to \mu^+\mu^-$ has a very characteristic signature: two high energetic and isolated muons in the final state are produced. A significant contribution of QCD-background due to the overwhelming cross section of QCD processes is expected. Moreover, the decay of a $W^{\pm}$-Boson into one high energetic muon and a neutrino plus an additional muon from a QCD-jet and the process $Z \to \tau^+\tau^- \to \mu^+\nu_\tau\bar{\nu_\mu}\nu_\tau\nu_\mu$ were studied as possible background processes in this analysis.

Due to the high collision energy of LHC, the production of top-quark pairs has a cross section in the order of the signal cross section. The top-quarks mostly decay into a W boson and b-quark. The W boson and the b-quark can decay further into muons, which also might fake the signal process.

The cross section of QCD-processes is far too large to be simulated within a full Monte Carlo simulation of the ATLAS detector. Hence it is assumed, that the dominating contribution of high energetic muons is due to the decay of $b\bar{b}$-mesons. To support this assumption, the origin of high energetic muons was studied in a $b\bar{b}$-sample and an inclusive lepton QCD sample. The results are shown in Table 8.1, where two muons with a minimal p_T of $10\,GeV$ were required. The origin of high energetic muons agree to a very high extend in both samples and hence the above assumption is justified. The QCD-sample is therefore labeled as $b\bar{b} \to \mu\mu$ in the following.

Sample	**Fraction of mesons, with $\geq$ one b-quark**	**Fraction of mesons, with $\geq$ one c-quark**	**Fraction of other origin**
Incl. lepton sample	0.73 ± 0.15	0.23 ± 0.08	0.04 ± 0.04
$b\bar{b}$-sample	0.734	0.243	0.023

Table 8.1: Overview of origin of two muons with $p_T > 10\,GeV$

The Monte Carlos sample for signal and background processes were generated with PYTHIA and ATHENA version 11.0.4. An overview of the relevant Monte Carlo samples is given in Table 8.2. Note, that the analysis is mainly based on ATHENA version 11.0.4. The signal sample produced with ATHENA version 12.0.6 was only used for cross checks to ATHENA version 11.0.4 and for the muon LVL2-trigger studies. Another exception is the $t\bar{t}$-background sample which was generated with MC@NLO and simulated and reconstructed with ATHENA version 12.0.6.

Sample	Software Version	Cuts	Cross-section $[pb^{-1}]$	Number of simulated Events
$Z \to \mu\mu$	11.0.4	$M_{\mu\mu} > 60\,GeV$ $1\mu : \lvert\eta\rvert < 2.8, p_T > 5\,GeV$	1497	106,000
$Z \to \mu\mu$	12.0.6	$M_{\mu\mu} > 60\,GeV$ $1\mu : \lvert\eta\rvert < 2.8, p_T > 5\,GeV$	1497	87,800
$b\bar{b} \to \mu\mu$	11.0.4	$2\mu : p_T > 6GeV, \lvert\eta < 2.5\rvert$ $1\mu : p_T > 15\,GeV$	9450	10,030
$W \to \mu\nu$	11.0.4	$1\mu : \lvert\eta\rvert < 2.8, p_T > 5\,GeV$	11946	84,100
$t\bar{t} \to W^+bW^-b$	12.0.6	no all hadronic decay	461	60,000
$Z \to \tau\tau$	11.0.4	$\tau\tau \to ll, M_{\mu\mu} > 60\,GeV$ $1\mu : \lvert\eta\rvert < 2.8, p_T > 5\,GeV$	77	29,050

Table 8.2: Overview of Monte Carlo samples used for this study

8.1.2 Cut Based Selection

ATLAS data which will be triggered by a $6\,GeV$ or $20\,GeV$ single muon trigger is the basic sub-sample for the following analysis. The $6\,GeV$ trigger is supposed to be in operation for the start-up period of LHC and is supposed to be replaced by a $20\,GeV$ single muon trigger for higher luminosities. The impact of this replacement on the cross-section measurement and its uncertainties is expected to be small, since large p_T-cuts are applied on the reconstructed muons as discussed in the following.

The triggered data sample can be further reduced by requiring at least two reconstructed muon tracks. As already mentioned in Chapter 5 there are two standard procedures for the muon track reconstruction in ATLAS: A standalone reconstruction by the ATLAS Muon Spectrometer and a combined reconstruction together with the inner tracker. In the start-up phase of ATLAS both sub detectors must be calibrated and aligned and therefore one might want to compare measurements based on both possible reconstruction methods. It will be shown that the expected impact of this choice on the cross-section measurement is small. Figure 8.1 shows the expected behavior of signal and background events for the basic detector acceptance requirements[1]. The relatively large drop of events caused by the requirement of two reconstructed muons can be explained by the geometric acceptance of the detector. The inner tracker has an η coverage of -2.5 to 2.5, while the muon system itself has an η-coverage from -2.7 to 2.7. We require that the η of the reconstructed muon tracks is smaller than 2.5 since it is difficult to determine the efficiency of the ATLAS Muon Spectrometer beyond the η acceptance of the inner detector as will be discussed in section 8.3.

Two further basic requirements have been chosen for the analysis. The reconstructed charges must be opposite and the invariant mass of the muons

$$M_{\mu\mu}^2 = \left[\begin{pmatrix} E_1 \\ \vec{p}_1 \end{pmatrix} + \begin{pmatrix} E_2 \\ \vec{p}_2 \end{pmatrix} \right]^2 \approx 2p_1p_2(1 - \cos\alpha)$$

is required to fulfill $60\,GeV < M_{\mu\mu} < 120\,GeV$. The impact on the ratio of signal and background processes is also shown in Figure 8.1. A large background contribution in the chosen data can already be reduced even with these basic requirements. The expected invariant

[1]Note, that all figures containing a comparison of signal and background processes are normalized to the same integrated luminosity

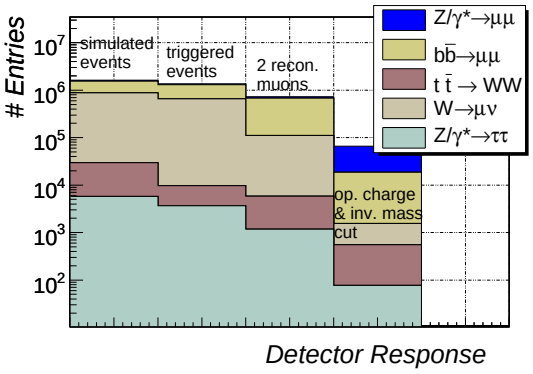

Figure 8.1: Detector Acceptance: (0) Number of simulated events for an integrated luminosity of $50\,pb^{-1}$, (1) Number of triggered events, (2) Number of events with two reconstructed muon tracks, (3) Basic Cuts: $|\eta(\mu)| < 2.5$, opposite charge, $|M_{\mu\mu} - M_Z| < 30\,GeV$.

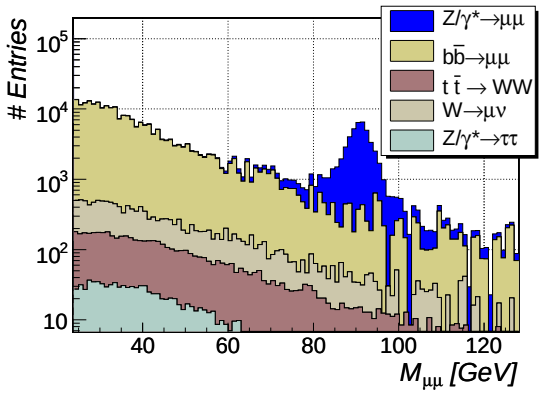

Figure 8.2: Reconstructed invariant di-muon mass for different processes, requiring two reconstructed muon tracks with opposite charge and no further cuts.

mass spectrum is shown in Figure 8.2. The peak of Z boson can already be identified clearly even with a standalone Muon Spectrometer reconstruction.

To discriminate between signal and background processes various other selection variables have been investigated: Two selection variables account for the transverse momenta p_T of the two muons and are defined by

$$p_T^{\max} = max(p_T^{\mu_1}, p_T^{\mu_2}), \qquad p_T^{\min} = min(p_T^{\mu_1}, p_T^{\mu_2}). \tag{8.1}$$

The distribution for these two variables for signal and background processes normalized to their cross sections is shown in Figure 8.3. Muons resulting from a decay of the Z boson tend to be highly energetic, while muons from QCD events are low energetic. This is different for events containing a W boson. One reconstructed muon results directly from the W decay, while the other muon is mainly due to a QCD-process in this event. Hence, a relatively similar $p_T^{\max}$ distribution but a largely different $p_T^{\min}$ distribution for W and Z processes is expected. The $t\bar{t}$-background is special. The high energetic muon results from the decay of a W boson into a muon, while the muon with the lower momentum might also come from the decay of one b-quark. Hence, we expect also a relatively broad distribution of $p_T^{\min}$.

Moreover, it is expected that signal muons are produced mainly back to back in the ϕ-plane of the detector as shown in Figure 8.5 for signal and background processes normalized to their cross sections. Hence, $\Delta\Phi$ is another possible cut variable.

Muons resulting from QCD interactions tend to be produced within a large decay cascade of further particles and therefore should not appear isolated in the detector in contrast to the leptonic decay of the Z and W boson. The following isolation variables have been chosen for this analysis.

- number of reconstructed tracks in the ATLAS Inner Detector within a hollow cone around the candidate muon: $N^{\text{ID Tracks}}_{r_1<r<r_2}$
- sum of the p_T's of reconstructed tracks in the ATLAS Inner Tracker within a hollow cone around the candidate muon: $\sum_{r_1<r<r_2} p_T^{\text{ID Tracks}}$

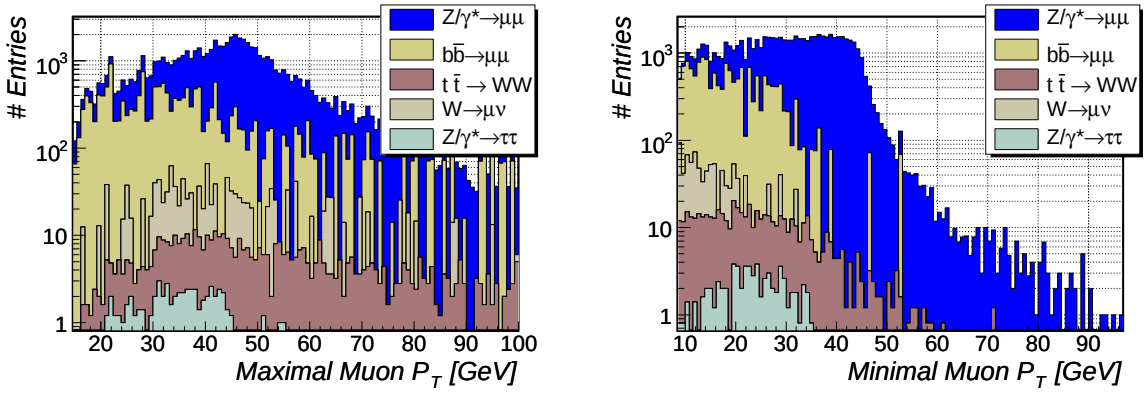

Figure 8.3: Reconstructed p_T distributions for signal and background processes for $max(p_T^{\mu_1}, p_T^{\mu_2})$ (left) and $min(p_T^{\mu_1}, p_T^{\mu_2})$ (right), without any further cuts, i.e. only requiring two reconstructed muons with opposite charge and $|M_{\mu\mu} - M_Z| < 30\,GeV$

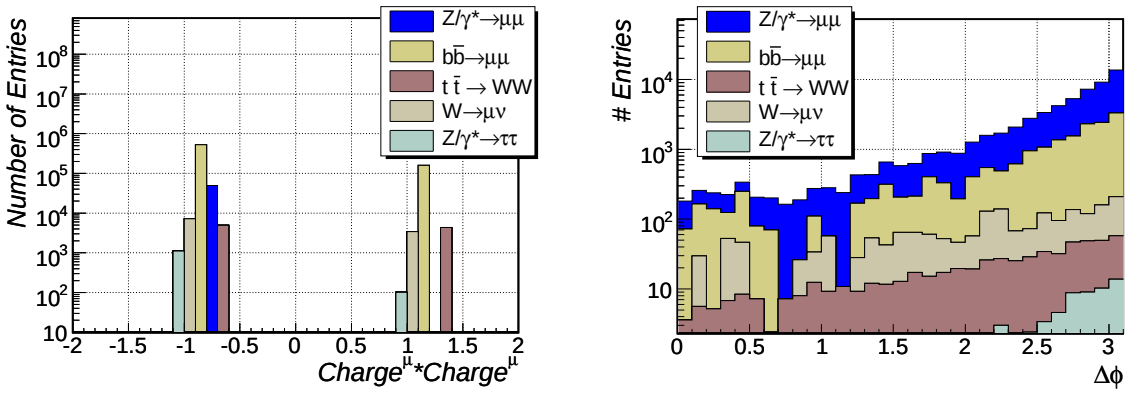

Figure 8.4: Reconstructed charge of first muon multiplied with reconstructed charge for second muon for signal and background process normalized to signal cross section without any further cuts, i.e. only requiring two reconstructed muons with opposite charge and $|M_{\mu\mu} - M_Z| < 30\,GeV$

Figure 8.5: Reconstructed $\Delta\Phi$ for signal and background process normalized to signal cross section without any further cuts, i.e. only requiring two reconstructed muons with opposite charge and $|M_{\mu\mu} - M_Z| < 30\,GeV$

- sum of reconstructed energy in the cells of the Calorimeter within a hollow cone around the candidate muon: $\sum_{r_1<r<r_2} E_T$
- energy of a possible reconstructed jet within a hollow cone around the candidate muon: $E_{r<r_2}^{\text{Jet Energy}}$

These isolation variables are defined within a hollow cone in the $\eta-$ and $\phi-$plane of the reconstructed muon track,

$$r_1 < \sqrt{\left(\eta_\mu - \eta_{ic}\right)^2 + \left(\phi_\mu - \phi_{ic}\right)^2} < r_2 \tag{8.2}$$

where r_1 and r_2 is the inner and the outer radius of the hollow cone. The index μ stands for the reconstructed muon track while the index ic stands of the isolation criteria. The smaller radius is set to $r_1 = 0.05$ and is introduced to exclude the candidate muon track itself from isolation quantity calculations. The specific value of the outer radius r_2 has only

a minor effect on the signal and background separation, as long it is large enough to contain a significant amount of data for the definition of isolation variables, i.e. $r_2 > 0.3$. Along with other studies in the ATLAS Standard Model working group, it was chosen[2] that $r_2 = 0.5$. The distributions of these isolation variables for signal and background processes normalized to their cross sections is shown in Figure 8.6. The high and low isolation criteria for both muons

$$\begin{aligned} \mathrm{Iso}^{\mathrm{max}}_{\mathrm{Criteria}} &= \max(\mathrm{Iso}^{\mu_1}_{\mathrm{Criteria}}, \mathrm{Iso}^{\mu_2}_{\mathrm{Criteria}}) \\ \mathrm{Iso}^{\mathrm{min}}_{\mathrm{Criteria}} &= \min(\mathrm{Iso}^{\mu_1}_{\mathrm{Criteria}}, \mathrm{Iso}^{\mu_2}_{\mathrm{Criteria}}) \end{aligned} \tag{8.3}$$

have been studied separately since a similar behavior of W boson background is expected as seen in the cut variables p_T^{max} and p_T^{min}.

The cuts on the kinematic variables p_T^{max}, p_T^{min} and $\Delta\Phi$ and on the isolation criteria are chosen to minimize the expected uncertainty on the cross-section measurement. To calculate this uncertainty, we introduce the efficiency ε and the purity p as

$$\varepsilon = \frac{N_m - N_b}{N_0} \qquad p = \frac{N_m - N_b}{N_m} = \frac{\varepsilon N_0}{N_m}, \tag{8.4}$$

where N_m stands for the number of events passing the selection cuts, N_b for the number of background events and N_0 for the number of all $Z \to \mu\mu$ events. The uncertainty on the cross section is given by

$$\frac{\Delta\sigma}{\sigma} = \frac{\Delta(N_0)}{N_0} = \frac{\Delta(\frac{N_m - N_b}{\varepsilon})}{N_0}, \tag{8.5}$$

where the relation $N_0 = (N_m - N_b)/\varepsilon$ was used. If the background is well understood it can be assumed that the uncertainty of N_b is negligable. This leads to

$$\frac{\Delta\sigma}{\sigma} = \frac{\sqrt{N_m}}{\varepsilon N_0} = \frac{1}{\sqrt{\varepsilon p N_0}}, \tag{8.6}$$

which is a pure statistical contribution on the cross section uncertainty. A large part of background processes in this study depend on QCD processes for which the behavior, e.g. cross section, is not known with high accuracy. As a general, conservative error estimate it is assumed that the uncertainty on the number of background processes is 100%, which leads to the following expression of the expected uncertainty of the cross-section measurement:

$$\frac{\Delta\sigma}{\sigma} = \frac{\sqrt{N_m + N_b^2}}{\varepsilon N_0} = \sqrt{\frac{\varepsilon N_0 (p-1)^2 + p}{p^2 \varepsilon N_0}} \tag{8.7}$$

[2]This value might change when also including pile-up and minimum bias effects in the simulation. Nevertheless, this impact is expected to be relatively small [66].

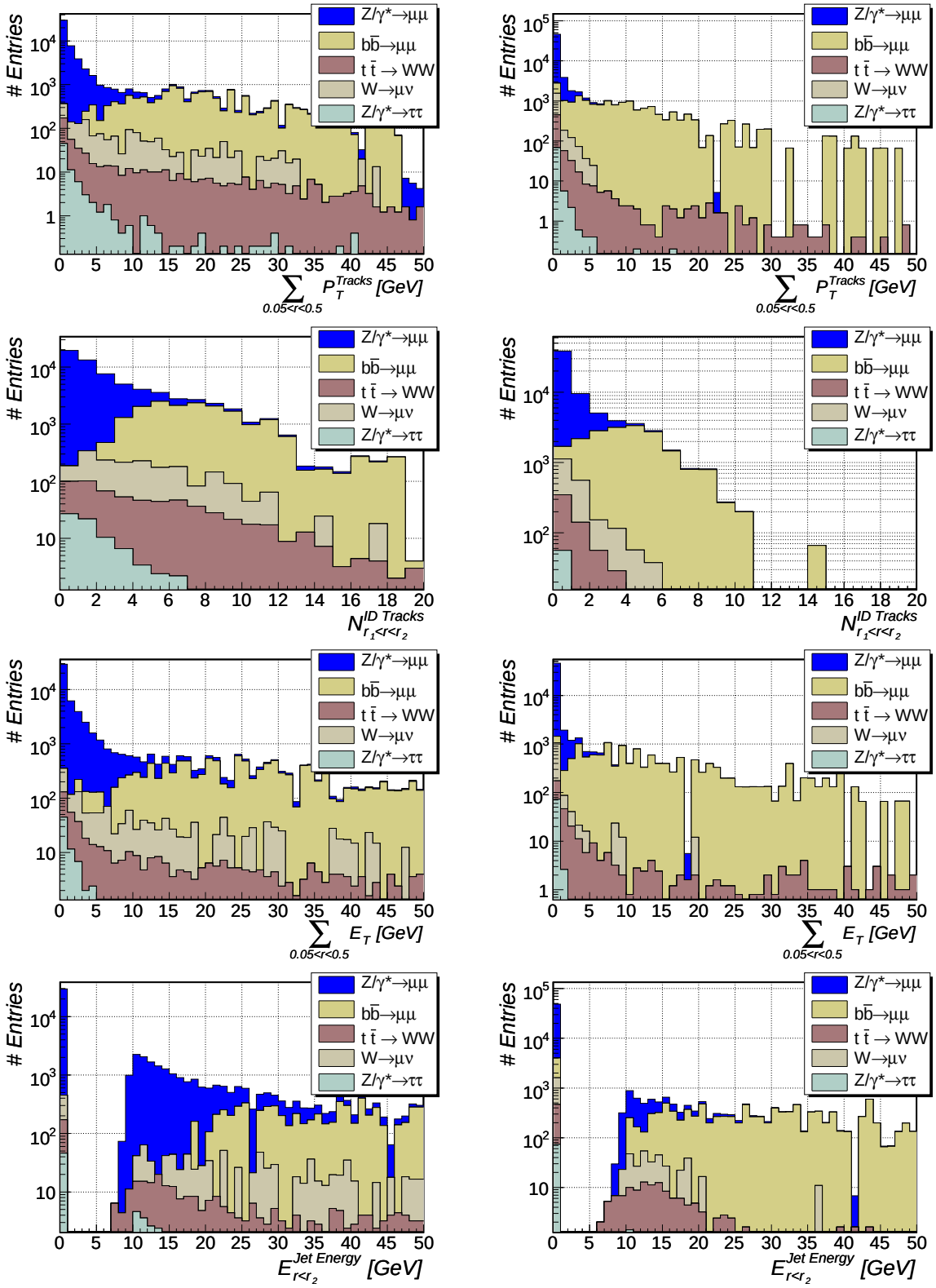

Figure 8.6: Distributions for various muon isolation criteria for signal and background processes without any further cuts, i.e. only requiring two reconstructed muons with opposite charge and $|M_{\mu\mu} - M_Z| < 30\,GeV$. Left-side: $max(Iso^{\mu_1}_{\text{Criteria}}, Iso^{\mu_2}_{\text{Criteria}})$, right-side: $min(Iso^{\mu_1}_{\text{Criteria}}, Iso^{\mu_2}_{\text{Criteria}})$

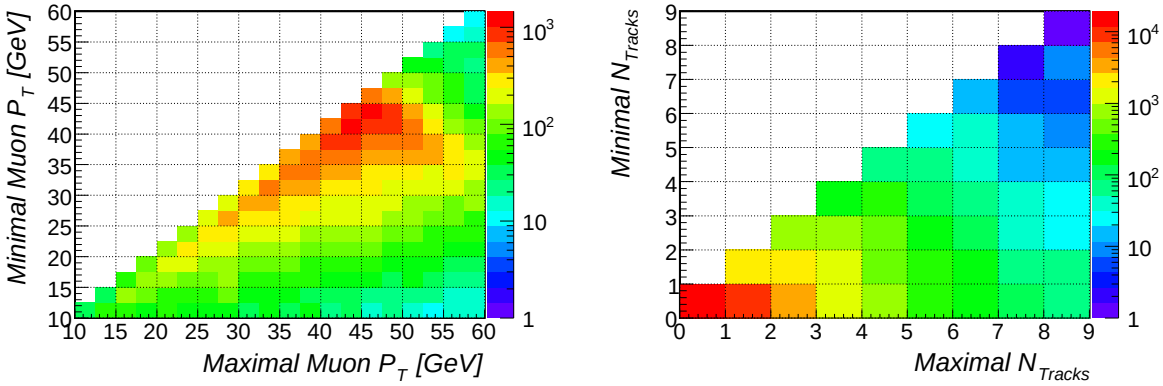

Figure 8.7: 2-dimensional distributions for lower and higher values for the muon's p_T and the number of reconstructed tracks around the muon track

Two limits are important in Equation (8.7). For small integrated luminosities, i.e. small N_0, we recover Equation (8.6). For large integrated luminosities, i.e. large N_0, we get

$$\frac{\Delta\sigma}{\sigma} \approx \frac{1-p}{p}, \tag{8.8}$$

which can be also understood, since we expect only a dependence on the purity p. It is useful to know, which purity is needed so that the background contribution is not dominating the overall uncertainty, for an integrated luminosity of $50\,pb^{-1}$, i.e. $N_0 \approx 50,000$. Assuming a selection efficiency of $\varepsilon \approx 0.5$ and using Equation (8.8) and (8.6), it follows that a required purity of $p \approx 0.994$ is needed. With an assumed efficiency of $\varepsilon \approx 1.0$ a purity of $p \approx 0.996$ is required. It can be concluded that the uncertainty is not sensitive on the selection efficiency, but that the purity contribution to the overall uncertainty is dominating for high integrated luminosities[3].

The cut optimization is done with the following iterative procedure:

- *Step 1*: Each cut variable is minimized with respect to Equation (8.7) separately.
- *Step 2:* Choose one cut-variable. Apply all cuts of the previous step on the Monte Carlo samples except the cut on the variable which should be optimized. Calculate the new optimal cut for this variables with respect to Equation (8.7). Repeat for all variables
- *Step 3:* Repeat *Step 2* two times
- *Step 4:* Calculate the average of the calculated cut-variables in step n and $n-1$

It should be noted, that this procedure is only appropriate in case of independent cut variables. This does not apply in the present case, e.g. when $p_T^{\max}$ and $p_T^{\min}$ depend on each other by construction. A search for optimal cuts should therefore be performed in an N-dimension space, where N is the number of cut variables. Yet, this is not applicable as the dimensionality is too high compared to the available statistics of full simulated Monte Carlo samples. Instead, the optimization was done for those two variables, which depend most on

[3]Remark: Equation (8.8) does not represent the full uncertainty of the cross-section measurement. The efficiency ε itself has an uncertainty which depends on the luminosity (see section 8.3). Nevertheless, it can be shown, that this impact can be neglected for the calculation of the required purity.

each other, in a two dimensional space. These variables are $p_T^{\max}$ and $p_T^{\min}$, and $\mathrm{Iso}^{\max}_{\mathrm{Criteria}}$ and $\mathrm{Iso}^{\min}_{\mathrm{Criteria}}$ (Figure 8.7).

Theoretically, this algorithm converges to the optimal cuts. In a first step very hard cuts are chosen, because each cut is applied standalone with no other cuts at all. In the second step each cut gets relaxed again significantly when the other hard cuts from step one are applied. The next iteration leads again to more tight cuts. Hence the calculated cut values oscillate around the optimal values within the chosen dimensionality. In practice, three iterations are sufficient for the cut optimization since the limited Monte Carlo statistics of the background samples lead to no further improvement. Note, that the cut-optimization was applied only for the QCD- and $W \to \mu\nu$-background samples. This is due to the fact that the Monte Carlo description of the $Z \to \tau\tau$- and $t\bar{t}$-background is relatively good and no 100% uncertainty on the expected background contribution must be applied.

Figure 8.8 shows several distributions of cut-variables for signal and background processes, where all calculated cuts have been applied except the cut on the variable shown. It can be seen, that background contributions from $Z \to \tau^+\tau^- \to \mu^+\nu_\mu\nu_\tau\mu^-\nu_\mu\nu_\tau$ and $t\bar{t}$-background cannot be easily reduced by further cuts, since the topology of the processes is quite similar to the signal. The background contribution from muons, which result from QCD processes, can strongly be reduced by requiring the isolation cuts.

The cut optimization procedure leads to cuts shown in Table 8.3. The loose cuts apply to $p_T^{\min}$ and $\mathrm{Iso}^{\max}_{\mathrm{Criteria}}$, the tight cuts to $p_T^{\max}$ and $\mathrm{Iso}^{\min}_{\mathrm{Criteria}}$, respectively. The cut selection implies that the efficiency of each cut must be known and/or be determined within data to high precision, since the dependence on Monte Carlo predictions should be avoided. This is not a problem for the kinematic cuts like the p_T-cut or the cut on the invariant mass, but far from trivial for the eight isolation cuts. A 'tag and probe' approach for the efficiency determination (see section 8.3.6) cannot be applied by simple means, since the isolation cuts are strongly correlated.

A possible solution is to include this strong correlation in the definition of loose and tight muons, i.e. using the fact that a muon which passes one isolation cut is highly probable to pass also another isolation cut. Hence, the following isolation properties for single muons are introduced:

- **loosely isolated**, if it passes three out of four loose isolation cuts,
- **tightly isolated**, if it is loosely isolated and passes all tight isolation cuts, except the electromagnetic calorimeter isolation cut,
- **very tightly isolated**, if it passes all tight isolation cuts.

This definition allows for having only one isolation criteria per muon, instead of having four. The advantage of this definition is that the 'tag and probe' method can be applied, since all correlations are absorbed in the definition of a loosely and tightly isolated muon.

A muon resulting from a Z boson decay might fail one loose isolation requirement due to detector noise or a background event by chance. In order not to reject these signal events it was decided to require only three out of four loose isolation requirements. This improves the signal selection efficiency by 3%.

The simulation of the ATLAS electromagnetic calorimeter is expected to be particularly critical in the first phase of LHC in terms of background noise and energy scale. Hence, the isolation cut based on this detector component is treated differently in case of the tight isolation requirement.

Cut Name	Cut range
Invariant mass cut	$61\,GeV < M_{\mu\mu} < 121\,GeV$
Opposite charge requirement	$c_{\mu_1} * c_{\mu_2} = -1$
$\Delta\Phi$	$> 0.3\,rad$

Cut name	loose cut	tight cut
p_T-cut	$> 15\,GeV$	$> 25\,GeV$
Number of inner track isolation: $N^{\text{ID Tracks}}_{r_1<r<r_2}$	≤ 6	≤ 4
Inner Track p_T isolation: $\sum_{r_1<r<r_2} p_T^{\text{ID Tracks}}$	$< 15\,GeV$	$< 8\,GeV$
Jet isolation: $E^{\text{Jet Energy}}_{r<r_2}$	$< 25\,GeV$	$< 15\,GeV$
Calorimeter isolation: $\sum_{r_1<r<r_2} E_T$	$< 20\,GeV$	$< 6\,GeV$

Table 8.3: Summary of optimized cuts for event selection

An event is defined to pass the isolation cut, if it contains at least two loosely isolated muon tracks of which one must fulfill the tight isolation requirement. It is clear that this new definition of loose and tight isolated muons does not reflect the optimized cuts in terms of Equation (8.7). Nevertheless, the difference is negligible in terms of purity within our statistics of fully simulated Monte Carlo events.

Figure 8.9 and Table 8.4 shows the cut-flow of signal and background processes. It is expected, that the cut on $p_T^{\max}$ has only a small impact on the background resulting from a W boson decay compared to the cut on $p_T^{\min}$, which directly affects the additionally produced muons. The isolation cut rejects all of QCD muons within our statistics. Note, that the requirement of one tightly isolated muon rejects only a small number of signal events but affects significantly the QCD contribution. The W boson background is not affected by this additional tight isolation requirement, since the muon resulting from $W \to \mu\nu$ is expected to appear highly isolated in the detector. The same applies for the muons resulting from $Z \to \tau^+\tau^- \to \mu^+\nu_\mu\nu_\tau\mu^-\nu_\mu\nu_\tau$, which are also expected to be isolated. The choice of cuts for the tight muon isolation requirements depends therefore only on the QCD background. Hence, it makes no sense to apply harder cuts for tight isolation once the QCD background is rejected. For the rare number of cases of more than two selected muons within one event, the two most isolated muons[4] are selected, since it is assumed that the additional muon results from a QCD process. Again, the $t\bar{t}$-background is special, since it has muons from two different sources. Muons stemming from the W boson, tend to be highly energetic and isolated, while muons stemming from the b-quark, tend to be low energetic and not isolated. This explains the relative large rejection after applying the cut on $p_T^{\min}$, while the cut on $p_T^{\max}$ has only a small effect. It is very probable that at least one of the two reconstructed muons results from the W boson and hence will pass the cut on $p_T^{\max}$. The cut on $p_T^{\min}$ rejects a large fraction of the muons resulting from a b-quark decay. The loose isolation requirement rejects all further remaining events, containing b-quark muons and hence the tight isolation requirement has again only a very limited impact, as it can be seen in Table 8.4.

The chosen selection cuts lead to an efficiency of 0.747 normalized to all $Z \to \mu\mu$ events

[4]Most isolated muon is defined as the muon with the smallest p_T-sum of tracks in the inner tracker within a maximal cone-distance of 0.5

Cut Name	**Number Of Events**				
Process	$Z \to \mu\mu$	$b\bar{b} \to \mu\mu$	$W \to \mu\nu$	$Z \to \tau\tau$	$t\bar{t} \to W^+bW^-\bar{b}$
Opposite charge requirement	33553	519882	6197	1028	4992
Invariant mass cut	32852	16566	815	72	472
$p_T^{\max}$-cut	31346	12210	765	62	446
$p_T^{\min}$-cut	30417	8052	131	54	285
Two loose isolated muons	29622	594	50	52	135
One tight isolated muon	28885	0	50	51	125

Table 8.4: Number of events for signal and background processes normalized to the signal cross section which passed different cuts

within $|\eta_\mu| < 2.5$ and $|M_Z - M_{\mu\mu}| < 30\,GeV$. The purity p of this selection is predicted to be $0.992 \pm 0.003(stat) \pm 0.003(sys)$ [5]. Figure 8.10 shows the expected mass peak including the background contribution of the Z boson, reconstructed with a combined tracking algorithm and all selection cuts applied. It illustrates the overwhelming purity of this signal.

[5]It has been assumed that the error on the QCD-background contribution is $0 + 60$, i.e. one event of the available background Monte Carlo sample remains after all selection cuts. This corresponds to a one σ uncertainty.

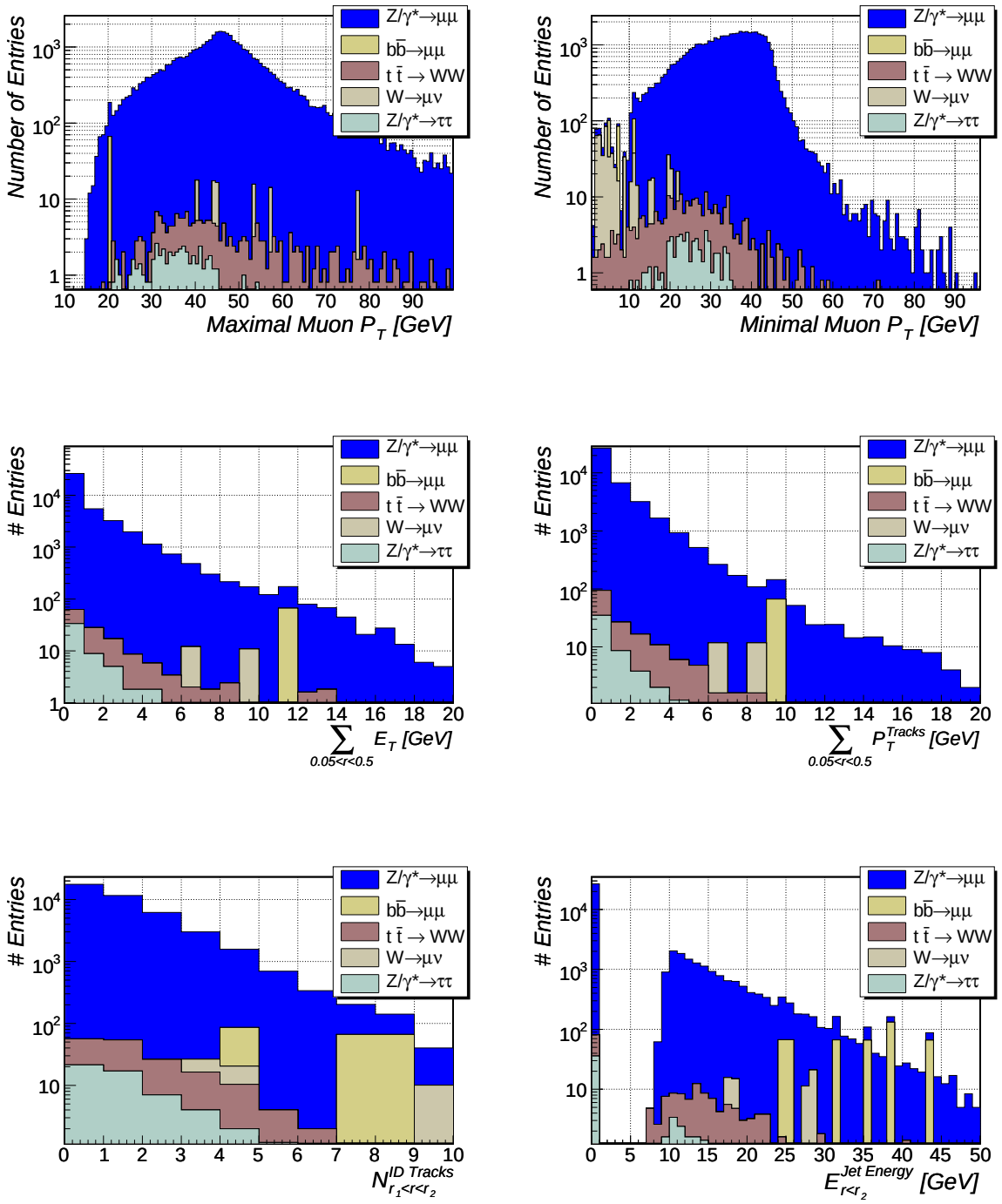

Figure 8.8: Distributions for several cut-variables for signal and background processes when cuts have been applied to all variables expect the one shown.

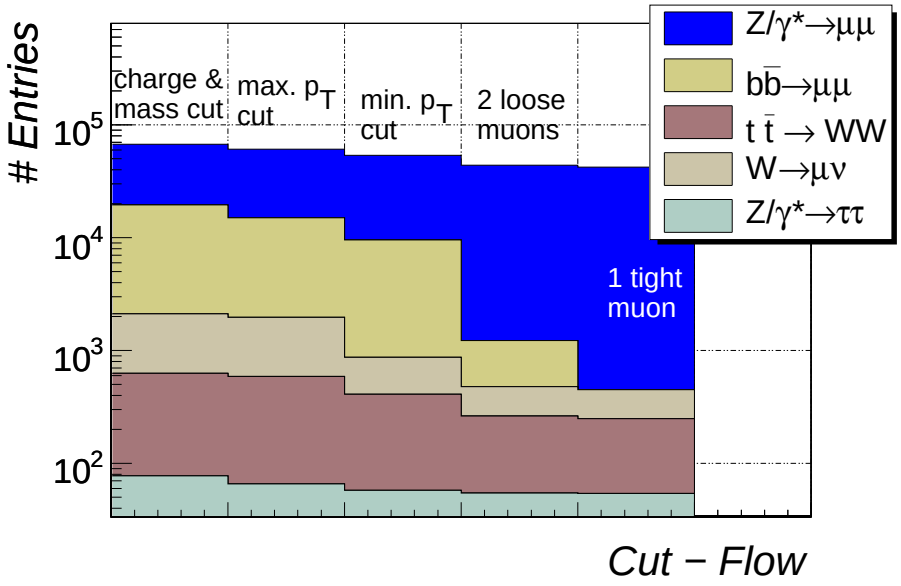

Figure 8.9: Number of Events for signal and background processes which passed charge and invariant mass cut (0), maximal p_T-cut (1), minimal p_T-cut (2), requirement of two loose isolated muons (3) and requirement of one tight isolated muon (4)

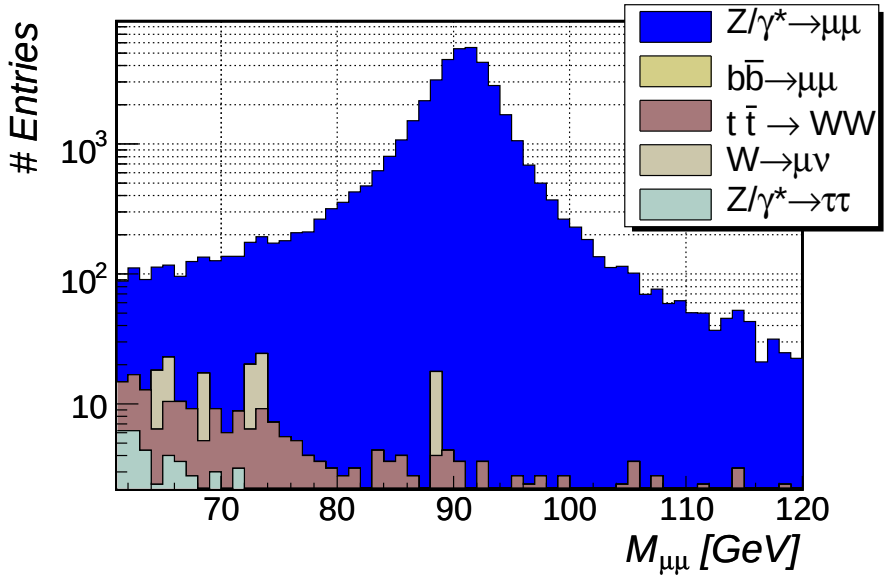

Figure 8.10: Expected reconstructed invariant mass spectrum $M_{\mu\mu}$ after cuts.

8.2 Background Estimation

8.2.1 $Z \to \tau\tau$-background Estimation

The decay of the Z boson into two τ-leptons and the further decay $\tau \to \mu\nu$ is understood very well in theory, since it is an electroweak process and higher order calculations of perturbation theory are available. Moreover, this process was studied in detail in the different LEP experiments [13]. Modern event generator programs like PYTHIA model this process with good precision. It was shown in section 8.1.2 that the background of $Z \to \tau\tau$ is mainly reduced by kinematic constraints and hardly affected by the isolation requirements. The impact of the detector response is therefore also small. Hence, we can estimate the background contribution due to this process with fully simulated Monte Carlo events. We expect a background contribution of

$$f_{Z\to\tau\tau} \approx 0.0018 \pm 0.0006\,(stat.).$$

8.2.2 $t\bar{t}$-background Estimation

As already mentioned in section 8.1.2, the remaining $t\bar{t}$-background is due to two muons, which stem from the decay of the two opposite charged W bosons. They appear isolated and highly energetic in the ATLAS detector. Their background contribution is limited by the kinematic cuts on the p_T of the muons, their invariant mass and the muon isolation criteria. The decay of a top-quark pair into two W bosons is understood theoretically very well. This also applies for the further decay of the W boson into one muon and one neutrino. The cross section of this process is known with a precision of $\sim 15\%$, which is mainly due to the uncertainties of the parton distribution functions of the proton at these high energies.

The $t\bar{t}$-background contribution is based on the Monte Carlo simulation predictions. The muon reconstruction and trigger efficiencies for muons originating from $t\bar{t}$ decays can be assumed to be equivalent to Z boson events. This does not apply for the isolation requirement, since $t\bar{t}$ events are expected to have a significant larger hadronic activity. It can be assumed, that the hadronic activity in a Z boson event with at least two reconstructed jets with a transverse energy above 50 GeV is comparable to a $t\bar{t}$ event with full leptonic decay. The isolation efficiency for these selected Z boson events can be determined in data (see section 8.3.6) and hence also be estimated for $t\bar{t}$ events. The probability for a tight isolated muon in the selected Z boson events is 0.858 while the full Monte Carlo simulation of $t\bar{t}$ events predicts an isolation probability of 0.765. The difference of roughly 10% is treated as further systematic uncertainty. This leads to an overall systematic uncertainty of $\sim$ 20% on the expected background contribution due to $t\bar{t}$ events. Hence, a $t\bar{t}$ background contribution of

$$f_{t\bar{t}} \approx 0.0043 \pm 0.0004\,(stat.) \pm 0.0010\,(sys.).$$

is expected.

8.2.3 QCD-background Estimation

A precise theoretical and experimental description as for the previous$t\bar{t}$ two background processes is not available for the QCD background. Hence, another method had to be developed to estimate this background contribution.

The main idea of the QCD background estimation is to use a sub-sample of the triggered data which is enriched of QCD events. Using a Monte Carlo prediction of the ratio between the size of the sub-sample and the number of expected QCD events in the signal-sample allows an indirect calculation of the QCD background contribution. The big advantage of this method is that it is independent of cross section assumptions of QCD processes which are not known with sufficient precision. Only a ratio between data samples based on the same physics process but different selection cuts must be predicted correctly by the full Monte Carlo simulation.

Two examples of possible choices of an QCD enriched data sample are shown in Figure 8.11 and Figure 8.12. Two reconstructed muons, passing the kinematic cuts but not being isolated, have been required. A further like-sign charge requirement on the two muons leads to a nearly pure QCD sub-sample.

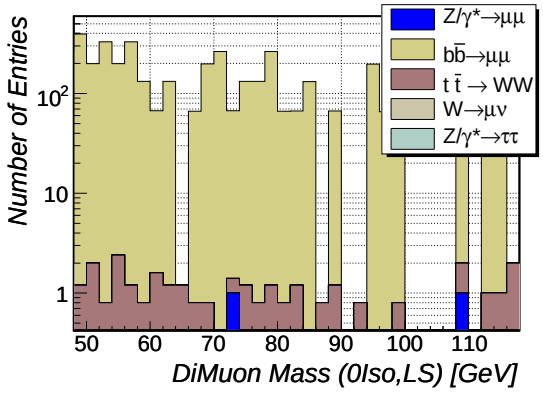

Figure 8.11: Expected invariant mass spectrum for signal and background process with two non-isolated, like-sign muons passing all kinematic cuts

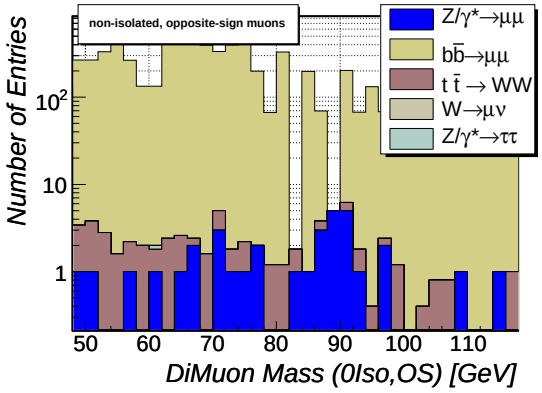

Figure 8.12: Expected invariant mass spectrum for signal and background process with two non-isolated, opposite-sign muons passing all kinematic cuts

Tevatron data suggests that the charges of muons coming from an $b\bar{b}$ decay are described in general reasonably well by Monte Carlo generator programs like PYTHIA. The situation becomes more complicated in the case of the isolation probability of these muons, since isolation is defined within the detector response which might not be modeled to high precision in the ATLAS detector simulation for the first phase of LHC. Hence it would be preferable to have a QCD enhanced data sample which does not depend on the detector simulation itself. One solution would be to require two muons which have passed all cuts but are like-sign. Monte Carlo studies suggest, that the sub sample defined with these cuts contains all types of background and signal events. In order to enhance the QCD background in the sub sample it is advantageous to apply looser isolation cuts and a like-sign requirement.

Cut name	**loose cut**	**tight cut**
Number of inner track isolation	$\leq ISF \times 6$	$\leq ISF \times 4$
Inner Track p_T isolation	$< ISF \times 15\,GeV$	$< ISF \times 8\,GeV$
Jet isolation	$< ISF \times 15\,GeV$	$< ISF \times 25\,GeV$
Electro Calorimeter isolation	$< ISF \times 6\,GeV$	$< ISF \times 20\,GeV$

Table 8.5: Impact of the *Isolation Safety Factor (ISF)* on the choosen isolation cuts.

A quantity called *Isolation Safety Factor (ISF)* is defined to describe the tightness of isolation cuts, as shown in Table 8.5. An *ISF* of 1.0 corresponds to the usual cuts, $ISF = 2.0$ relaxes all cuts by a factor of two. For example, a muon must have less than 12 reconstructed inner

tracks within a halo to pass the loose cut requirement for $ISF = 2.0$ instead of less than 6 reconstructed inner tracks as it was the case for $ISF = 1.0$.

As a first cross-check, the impact of the ISF is tested for single muons stemming from $b\bar{b}$-events. Figure 8.13 and 8.14 shows the fraction of loosely and tightly isolated $b\bar{b}$-muons vs. different ISFs. As expected, both distributions reach 0 for small values of ISFs and a saturation value for large ISFs. The distributions can be parameterized by

$$f_{ISF} = A \cdot \frac{e^{-x \cdot B}}{1 + e^{-C \cdot (x - D)}}, \tag{8.9}$$

where A, B, C and D are fitting variables. The fitted function f_{ISF} is also shown in Figures 8.13 and 8.14.

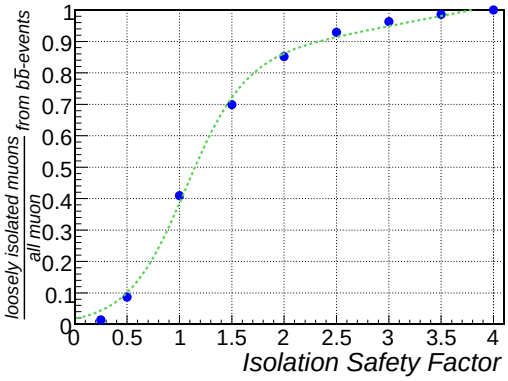

Figure 8.13: Fraction of loosely isolated muons stemming from $b\bar{b}$-events for different *Isolation Safety Factors*

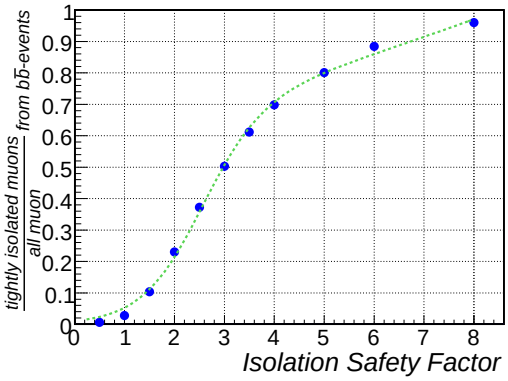

Figure 8.14: Fraction of tightly isolated muons stemming from $b\bar{b}$-events for different *Isolation Safety Factors*

A similar behavior as seen for the single muons, is also expected for the number of selected QCD background events. Figure 8.15 shows the number of selected events for several processes, predicted by full Monte Carlo simulation, for different values of ISF. Two things can be noted: First of all the QCD processes seem to dominate for $ISF > 2.5$. Secondly, Monte Carlo simulation predicts a similar behavior between the number of QCD events and the chosen ISF as shown in Figure 8.14 for single muons. These facts suggest the following procedure for QCD background estimation from data:

- Count the number of events, which pass all kinematic cuts for *Isolation Safety Factor* values of 2.5 to 10.0. It is expected that these samples are largely dominated by QCD-background
- Fit a function f_{ISF} to the measured values and extrapolate to $ISF = 1$. This will give an estimate of the number of QCD-events N_{LS}^{QCD} which have passed all cuts, but are like-sign.
- Multiply N_{LS}^{QCD} by the Monte-Carlo ratio $r_{LS,OS}^{MC}$ to get an estimation of the number of opposite-sign QCD-events N_{OS}^{QCD}.

It is crucial to note that N_{LS}^{QCD} does not depend on the simulation of the isolation probability but is determined exclusively within data. The ratio

$$r_{LS,OS}^{MC} = \frac{\text{Number of opposite-sign QCD events}}{\text{Number of like-sign sign QCD events}}$$

for events which pass all kinematic and isolation cuts must be determined within the Monte Carlo simulation. The limited statistics of the available QCD-sample forbids a direct calculation. Figure 8.16 shows the ratio for different values of *ISF* and two different invariant mass-ranges. Isolation Safety Factors below 2.5 lead to a background contribution from other processes and hence cannot be used. A linear extrapolation of the fitted function to $ISF = 1.0$ leads to an expected ratio $r_{LS,OS}^{MC} \approx 11 \pm 6$. The error on the ratio includes statistical and a conservative estimation of systematic uncertainties. The uncertainty will decrease significantly as soon a higher statistic sample of the QCD background is available.

The dependence of $r_{LS,OS}^{MC}$ on the isolation can be explained on physics grounds: A direct decay of $b\bar{b}$ would lead to two opposite charged muons. Like-sign $b\bar{b}$ muons come from the decay of a $b\bar{b}$-mixing state or from the cascade decay of one b-quarks

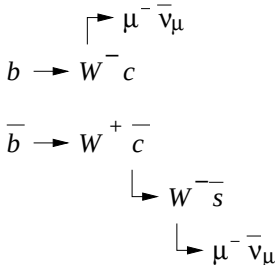

The probability of the second process has a stronger correlation with the isolation requirement than the direct decay of $b\bar{b}$.

Applying this method to the available Monte Carlo samples, we expect a QCD background contribution of $f_{b\bar{b}} \approx 0.002$. A systematic uncertainty of this method is the choice of Equation (8.9) as parameterization of f_{ISF}, since the structure of the function is not physically motivated. To get an estimation of the systematic uncertainty due to this special choice, it was also tested to use a simple parabola

$$f_{ISF} = Ax^2.$$

as a parameterization. The extrapolated value at ISF=1 using the parabola differs by 20% from the value using Equation (8.9), which should be treated as further systematic uncertainty. No $b\bar{b}$-events survives the selection cuts within the available Monte Carlo sample. As an estimation it can be assumed that one $b\bar{b}$-event survives the selection cuts, which corresponds to an uncertainty of 68 %. This would lead to a background contribution of $f_{b\bar{b}} \leq 0.0019$, which is in agreement with the above estimated value and is used in the following discussion.

8.2.4 $W \to \mu\nu$-background Estimation

The decay of $W \to \mu\nu$ and $Z \to \mu\mu$ are relatively similar from a theoretical point of view. The only large difference between the two processes is the ten times larger cross section of W production. It can be assumed that the probability having a high energetic, additional muon, resulting from a QCD interaction, is equal in both processes[6]. Hence, the number of

[6]It should be noted, that the QCD interaction responsible for the additional muon, is the reason, why this background contribution is also estimated from data and not from Monte Carlo prediction

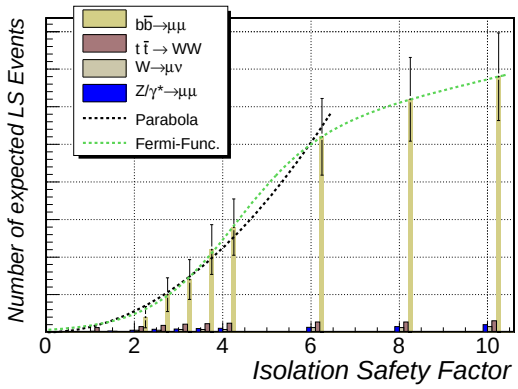

Figure 8.15: Comparison of expected events passing all cuts with like-sign requirement for different processes vs. the isolation Safety-factor is shown.

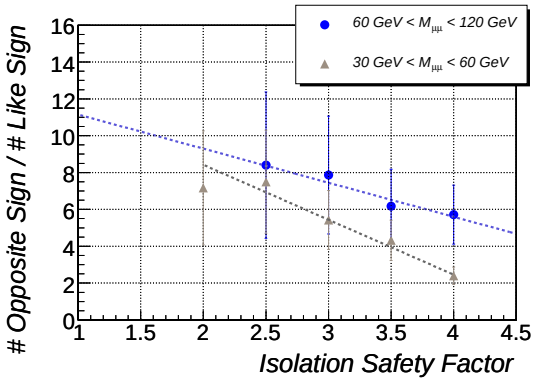

Figure 8.16: All cuts have been applied on reconstructed muons within the $b\bar{b}$-sample except the opposite-charge requirement. The ratio of events passing a like-sign requirement to events passing the opposite-sign requirement is shown for different isolation Safety-factors.

$Z \to \mu\mu$ with two tight and one loose isolated candidate muons	$Z \to \mu\mu$ with three tight isolated muons	$W \to \mu\nu$ with one tight and one loose isolated muon	$W \to \mu\nu$ with two tight isolated muons
4 ± 2	0	60 ± 24	0

Table 8.6: Overview a $W \to \mu\nu$- and $Z \to \mu\mu$-events, with more than one or two isolated muons, respectively. The number of events are normalized to the same integrated luminosity.

$W \to \mu\nu$ events, which pass all selection cuts should be ten times higher, than the number of $Z \to \mu\mu$ events, where three instead of two muons pass all cuts, i.e. two Z boson candidates are found.

A possible systematic uncertainty of this approach are di-boson events. These events could have also a third muon which passes all selection cuts. All muons resulting from a di-boson event are expected to fulfill the tight isolation requirement, while it is more probable for an additional muon from QCD process to pass only the loose isolation requirement. Hence, the number of events with three tightly isolated muons must be subtracted.

This method was tested on simulated data with results shown in Table 8.6. As expected, no events with three tight isolated muons were found within the $Z \to \mu\mu$ sample, but four events with two tight and one loose isolated muon. Considering the statistical uncertainty, the prediction of $W \to \mu\nu$ background contribution agrees well with the direct Monte Carlo measurement. The difference of the number of predicted W events and the true number of W events is treated as systematic uncertainty, which is expected to get smaller with increasing size of the relevant Monte Carlo simulation samples. Hence, the background contribution in this channel is expected to be $f_{W\mu\nu} \approx 0.002 \pm 0.001(sys)$.

8.2.5 Cosmic Muons

High energetic cosmic ray muons are also expected to fake the signal process, when traversing the ATLAS detector. The problematic issue about a cosmic muons track is that it appears as two opposite charged and isolated tracks in the detector. Obviously only those cosmic muons might fake the signal which are reconstructed by the Muon Spectrometer and the

inner detector with a relatively close distance of closest approach to the interaction point. A rate of $0.7\,Hz$ is expected for cosmic muons with an energy above $20\,GeV$ and a maximal distance of $60\,cm$ from the ATLAS origin in z-direction and $20\,cm$ in the radial direction [67]. A smaller area around the interaction point with $\delta z \approx 10\,cm$ and $\delta r \approx 10\,cm$ lowers the expected rate to $0.05\,Hz$ of possible reconstructed and triggered events.

Three cuts can be applied to reject the background due to cosmic muons. The first and expectedly most efficient cut uses the timing information of the associated muon hits in the RPC trigger chambers in the upper half of the ATLAS Muon Spectrometer. If the hits in the outer most RPC chamber are recorded before the hits in the inner RPC station, it can be concluded that this muon was coming not from the interaction point, but from outside the Muon Spectrometer and hence this event is rejected. A further cut can be applied on the distance of closest approach, i.e. only considering events, which are close to the interaction point. A third cut can be applied on the opening angle $\alpha_{\mu\mu}$ between the two muons, which is expected to be exactly 180°. This is not necessarily true for muons stemming from Z boson decay, because their pseudorapidity sum is usually not zero, i.e. $\eta_\mu^1 + \eta_\mu^2 \neq 0$.

The selection efficiency of these cuts can also be studied in data. Selecting only those events, which fulfill $\eta_\mu^1 + \eta_\mu^2 \approx 0$ to high accuracy and moreover have a relative large distance of closest approach to the interaction point is expected to result in a clean cosmic sample. In this sample, the efficiency of the first cut can be tested.

It is expected from Tevatron experience that the cosmic background can be neglected for similar studies [68]. This is also a conservative estimation for the ATLAS experiment, since the Tevatron experiments are built close to the surface, while the ATLAS detector is $\sim 100\,m$ underground.

8.3 Determination of Trigger-, Reconstruction- and Cut- Efficiencies with Data

8.3.1 Tag and Probe Method

The full simulation of the ATLAS Detector might not describe all details to highest accuracy for the start-up period of LHC. Therefore it is necessary to determine all efficiencies which are important for this study with data in order not to rely on the simulation.

The so-called 'tag and probe' method is one possible way to determine these efficiencies with data. The basic idea of this method will be explained using the determination of the reconstruction efficiency of the Muon Spectrometer as an example. The decay of the Z boson into two muons will lead to reconstructed tracks in the ATLAS Inner Tracker as well as in the ATLAS Muon Spectrometer. These two measurements are in principal independent, though not necessarily uncorrelated. We require two reconstructed tracks in the ATLAS Inner Tracker, at least one associated track in the Muon Spectrometer and an invariant mass of the two muons which is close to the mass of the Z boson. The last requirement ensures that the reconstructed tracks result from the decay of a Z boson. The inner track which could be associated to the track in the Muon Spectrometer is therefore a muon and called 'tag' muon. The 'tag' muon ensures that the event stems from a $Z \rightarrow \mu\mu$ decay and therefore the second inner track must be also a muon, which is called 'probe' muon (Figure 8.17). The 'probe' muon is used to test the association of a reconstructed track in the Muon Spectrometer. In this way the efficiency of the Muon Spectrometer can be determined.

It is obvious that this technique can be as well applied for the efficiency determination of other

quantities such as the Inner Tracker efficiency or the trigger efficiency. The basic principle is to define a suitable *Probe-Object*.

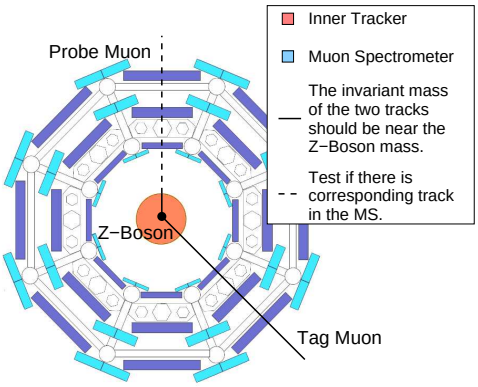

Figure 8.17: Schematic Illustration of the 'tag and probe' method

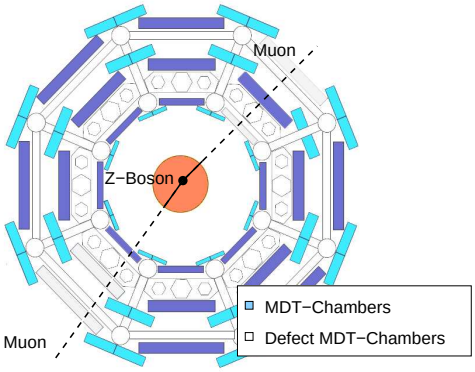

Figure 8.18: Illustration of possible systematic effects of the 'tag and probe' method

Some systematic uncertainties of this method must be considered. As shown in Figure 8.5 it is most likely that muons resulting from the Z boson decay are back to back in Φ. This implies that inefficiencies which are symmetric in $\Delta\Phi \approx \pi$ may not be detected with this method as illustrated in Figure 8.18. Such symmetric reconstruction problems are not unexpected since the ATLAS Detector is built in general in a Φ-symmetric way. A further systematic uncertainty arises from the assumption that the measurement of the 'tag' muon is independent from the measurement of the 'probe' muon. This assumption is in general fulfilled for the determination of reconstruction efficiencies but not for the determination of isolation efficiencies as will be discussed in section 8.3.6. Most important, it must be ensured, that the 'tag' and 'probe' muon result from a Z boson decay. A background process which leads to two isolated tracks in the Inner Detector of which only one is a real muon will reduce the measured efficiency. Hence, hard selection cuts are required to have a clean signal sample[7]. The choice of the selection cuts is discussed in the following section.

Figure 8.19 shows a comparison of the Muon Spectrometer reconstruction efficiencies for a single muon sample and a $Z \rightarrow \mu\mu$-sample including pile-up. The two distributions coincide within their statistical uncertainty. As a consequence, the 'tag and probe' method can be used not only for the determination of reconstruction efficiencies for a specific physics process but also for the extrapolation to single muon reconstruction efficiencies.

8.3.2 Selection of Candidate Tracks

The selection of tracks for the 'tag and probe' method differs from the selection for the cross-section measurement, since the selection cuts must be applied on Inner Detector tracks, which are not necessarily muon tracks. This has a large influence on the selection variables as is illustrated in Figure 8.20 for some chosen processes. The number of reconstructed tracks from background-processes increases, while the p_T-spectra is shifted to much lower values. The Z boson peak can still be identified clearly, but the background contribution has increased by some orders of magnitude.

The following cuts have been applied to get a clean track selection. Both muon tracks must have an invariant mass $M_{\mu\mu}$ between $81\,GeV$ and $101\,GeV$ and must have a reconstructed

[7] An alternative approach is discussed in Appendix D.1

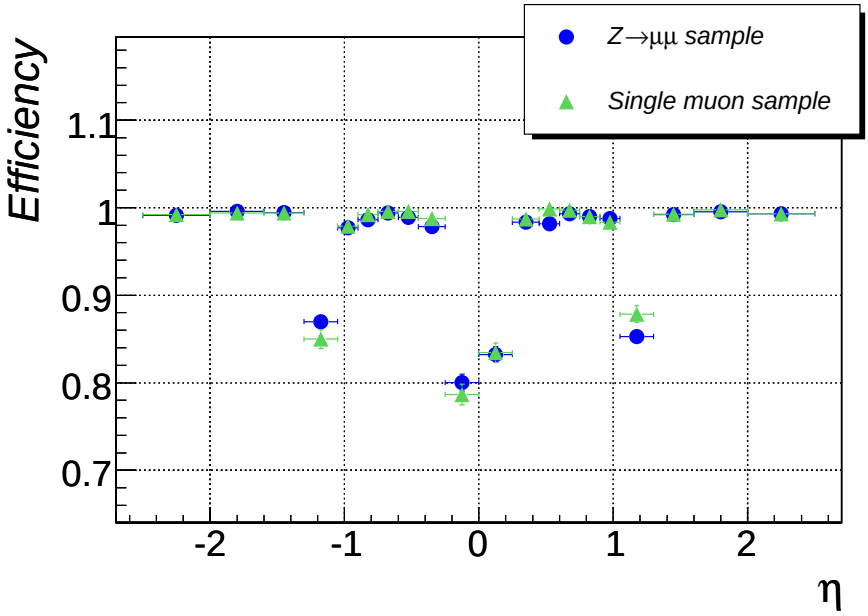

Figure 8.19: Comparision of Muon Spectrometer efficiency for a single 50 *GeV* muon sample and a $Z \rightarrow \mu\mu$-sample for muons with $p_T > 25\,GeV$

p_T above 20 *GeV*. The $\Delta\phi$ value of both tracks is required to be above 2.0*rad* and opposite reconstructed charges are required. Moreover, the very tight isolation cuts defined in section 8.1.2 are applied to both tracks. At least one of the two tracks must be matched to a Muon Spectrometer track to define a 'tag' muon.

The relatively high p_T-cuts have the disadvantage that the efficiency for muons with a p_T between 15 *GeV* and 20 *GeV* cannot be determined. A lower limit of the required minimal p_T would lead to an increased background contribution. Nevertheless, Monte Carlo studies showed that the efficiency of the Muon Spectrometer does not depend significantly on p_T for muons above 15 *GeV*.

The cut-flow diagram for 'probe' muons is shown in Figure 8.21. The QCD background can be rejected again by the isolation cuts. More problematic in this selection is the $W \rightarrow \mu\nu$

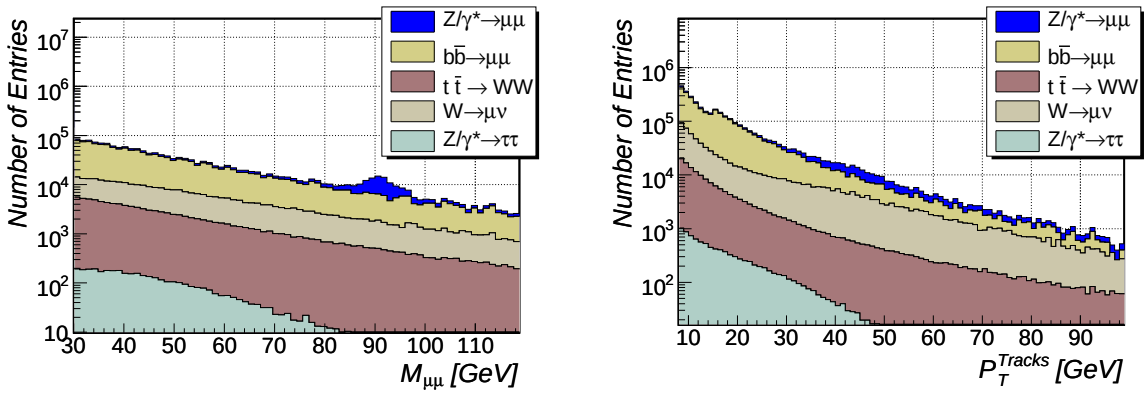

Figure 8.20: Reconstructed quantities only using Inner Detector tracks without any further cuts for signal and background processes: (a) Invariant mass of two tracks with opposite charge, (b) Transverse momentum distribution.

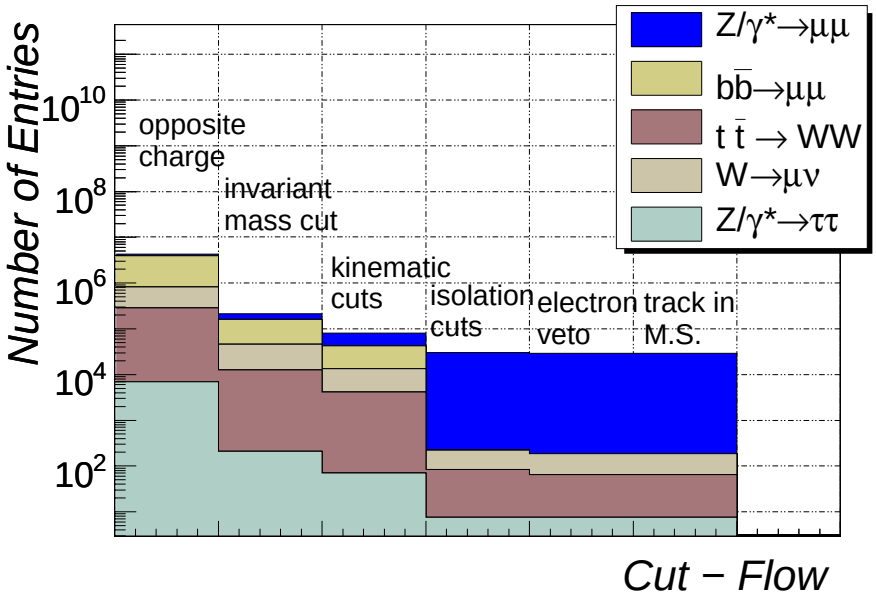

Figure 8.21: Cut-Flow Diagram for 'probe' muon tracks: (0) opposite charge requirement, (1) Invariant mass requirement, (2) Kinematic Cuts, (3) Isolation requirements, (4) Electron veto, (5) Found at least one track in the Muon Spectrometer

background and those $t\bar{t}$-events, where at least one W boson decays into a muon and a neutrino. These processes provide one high energetic isolated muon track which passes all selection cuts for a 'tag' muon. A further track in the inner detector which passes the other cuts and is not a muon will decrease the measured efficiency. Such a track is most likely caused by an electron, since it is expected that electrons also appear as isolated track in the Inner Detector. Therefore it is required that no reconstructed electromagnetic jet in the Electromagnetic Calorimeter of ATLAS can be matched to an Inner Track as an additional selection requirement. This applies especially for 'probe' tracks stemming from a $t\bar{t}$-event. Here, again, one has to distinguish between inner tracks, which result from the decay of the b-quark or simple QCD-interactions and those, which result from the decay of the W boson. The first case is suppressed by the isolation requirement and can be neglected. The second case can lead to a highly energetic isolated electron, stemming from the decay of the second W boson. These electrons are expected to be vetoed. The Cut-Flow diagram also shows, that each 'probe' muon from background processes can be also associated to Muon Spectrometer track and hence have no negative effect of the efficiency determination.

It is expected that the data sample selected with these selection cuts will lead to an efficiency determination, which is not affected by background processes. This assumption can be tested in the data phase with the methods presented in section 8.2.

The 'tag and probe' method was implemented into the ATHENA software framework to be available for ATLAS collaboration. A short survey can be found in appendix D.2.

8.3.3 Determination of the Muon Spectrometer Reconstruction Efficiency

The reconstruction efficiency of the Muon Spectrometer depends on p_T, η and ϕ of the muons. Hence, one should determine the efficiency appropriately binned in these quantities.

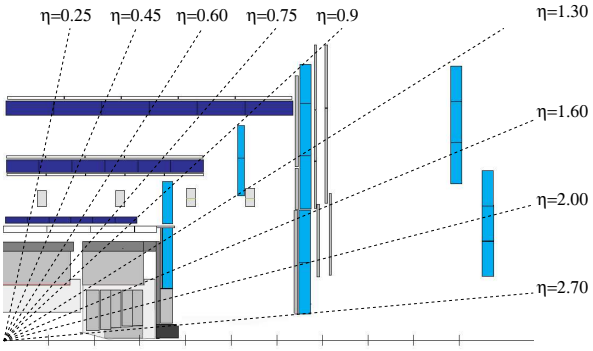

Figure 8.22: Illustration of the choosen η-binning of the Muon Spectrometer

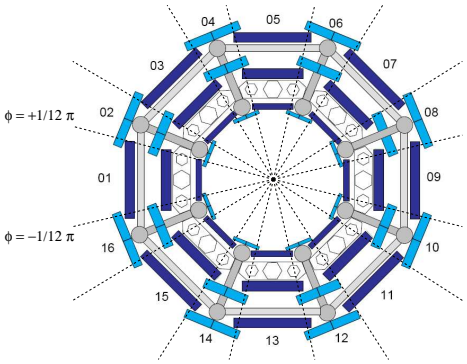

Figure 8.23: Illustration of the chosen ϕ-binning of the Muon Spectrometer

The lowest value of the p_T-binning is given by the selection cuts and set to $20\,GeV$. The highest value is set to $60\,GeV$ and 10 bins are used to ensure high enough statistics within each bin.

The binning in η and ϕ is determined by the Muon Spectrometer geometry. The Muon Spectrometer consists of 16 sectors in the ϕ-plane, small and large MDT-chambers subsequently ordered as illustrated in Figure 8.23. Therefore 16 bins in ϕ-direction are used. The same geometrical argument applies to the η-plane of the detector. Three MDT-chambers which are projective to the interaction point define one tower. 14 Towers can be defined in the η-direction which are the basis for the chosen binning (Figure 8.22). In total 224 sections are defined in the $\eta-, \phi-$plane.

A crucial test of the 'tag and probe' method is the comparison with the efficiencies determined with Monte Carlo Truth information, which is shown in Figure 8.24 for η and in Figure 8.25 for p_T and ϕ. A track matching distance of $d_{\eta,\phi} < 0.07$ was chosen to account for the η and ϕ resolution of the Inner Detector. The efficiencies determined in both ways coincide within their statistical uncertainty for an integrated luminosity of $50 pb^{-1}$. Also the overall Muon Spectrometer efficiency agrees for both measurements. This suggests that possible correlations between 'tag' and 'probe' muons are small and can be neglected for this study.

The statistical error on the reconstruction efficiency ε can be calculated by

$$\Delta\varepsilon = \sqrt{\frac{\varepsilon(1-\varepsilon)}{N}}, \tag{8.10}$$

where N is the number of 'tag' muons. Note that both muons can be chosen as 'tag' muon in most cases of the events, since the Muon Spectrometer is expected to have a reconstruction efficiency of 95% on average. Figure 8.26 and Figure 8.27 show the distribution of the in-situ determined efficiencies and the corresponding statistical uncertainties for all 304 sections. The reconstruction efficiency can be determined to a high statistical precision for relatively low integrated luminosities as illustrated in Figure 8.28 for the overall reconstruction efficiency and in Figure 8.29 for the uncertainty averaged over all 304 sections. It can be seen in Figure 8.28 that an integrated luminosity of less than $1 pb^{-1}$ will lead already to a statistical uncertainty of less than 1%.

Another possible correlation between 'tag' and 'probe' muon could be caused by the trigger. The probability of reconstructing a muon is significantly higher, if it was triggered as shown in Figure 8.30. Hence, it might be suspected that this correlation implies also a correlation in real data, since data events must contain at least one muon which has been triggered. This

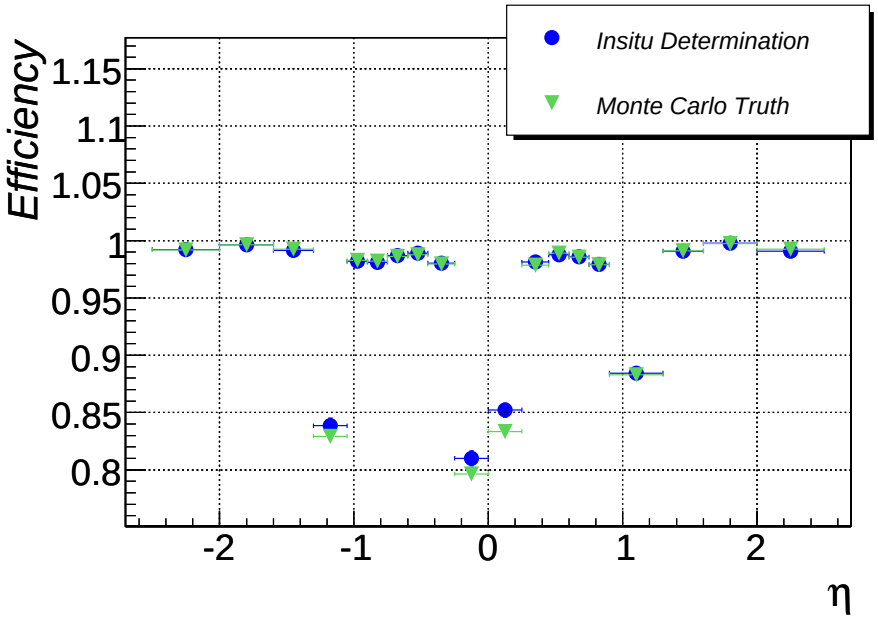

Figure 8.24: Comparison of determined muon reconstruction efficiency of the Muon Spectrometer vs. η by 'tag and probe' method and Monte Carlo Truth information.

is not a problem as long as the trigger requirement must only be applied on the 'tag' muon.

In section 8.3.1 it was already mentioned that the 'tag and probe' approach has problems to detect inefficiencies which have a $\phi \approx \pi$ symmetry. Dividing the data sample in two parts differing in the angle $\Delta\Phi$, could overcome this problem. One part contains reconstructed 'tag' and 'probe' muons with $\Delta\Phi < 2.8\,rad$ the second sample with $\Delta\Phi > 2.8\,rad$. The chosen value of $2.8\,rad$ leads to roughly equally sized samples. Applying the 'tag and probe' method on both sub-samples will lead to different efficiency distributions in case of ϕ-symmetric inefficiencies. No differences are expected for an ideal Muon Spectrometer as it is shown in Figure 8.31. Table 8.7 summarizes statistical and systematic uncertainties of the in-situ determined Muon Spectrometer reconstruction efficiency. The comparison between the Monte Carlo and the in-situ determined efficiency is still consistent with the statistical errors. Keep in mind,

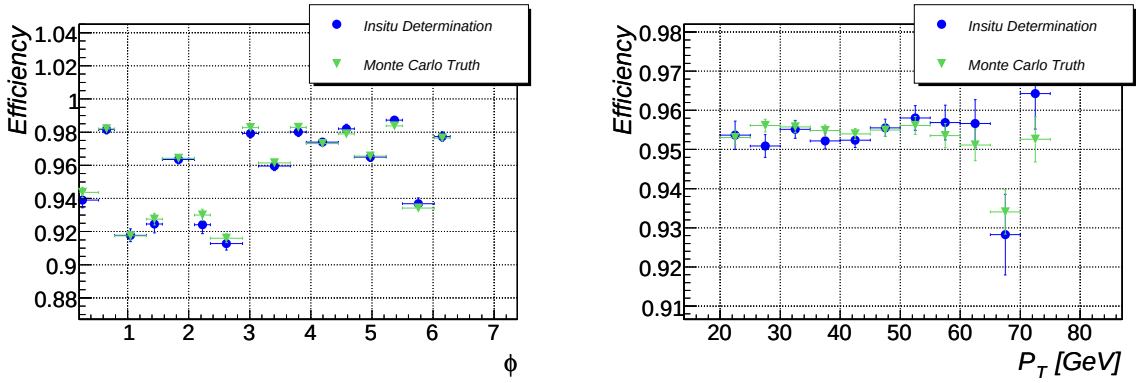

Figure 8.25: Comparison of the muon reconstruction efficiency of the Muon Spectrometer vs. ϕ and p_T determined by the 'tag and probe' method and by the Monte Carlo Truth information.

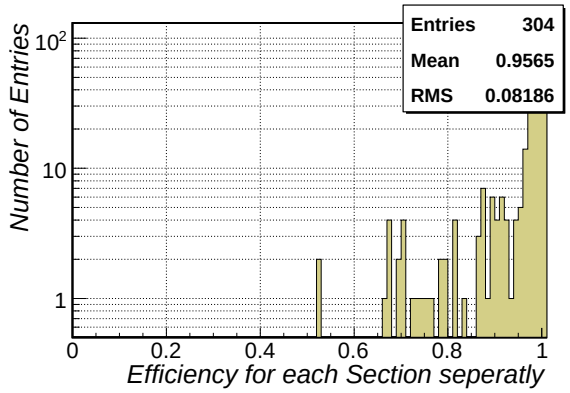

Figure 8.26: Distribution of muon reconstruction efficiency of the 304 Muon Spectrometer sections.

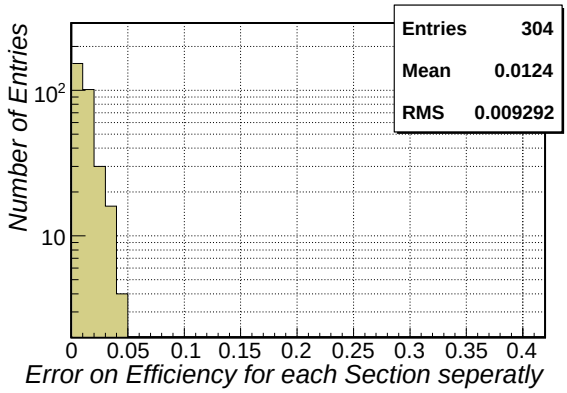

Figure 8.27: Distribution of the statistical error on the muon reconstruction efficiency for 304 sections.

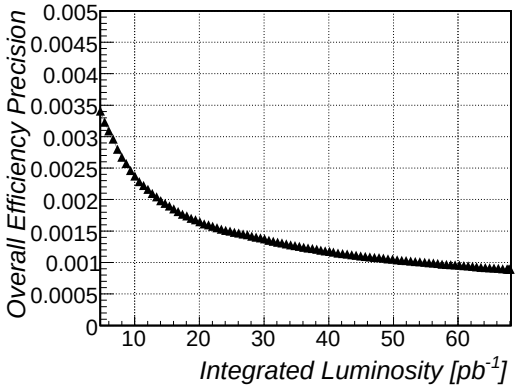

Figure 8.28: Statistical error of the overall Muon Spectrometer reconstruction efficiency vs. integrated luminosity.

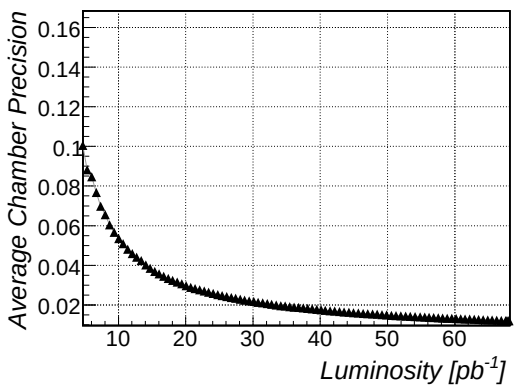

Figure 8.29: Average statistical error of reconstruction efficiency of the 304 sections vs. integrated luminosity.

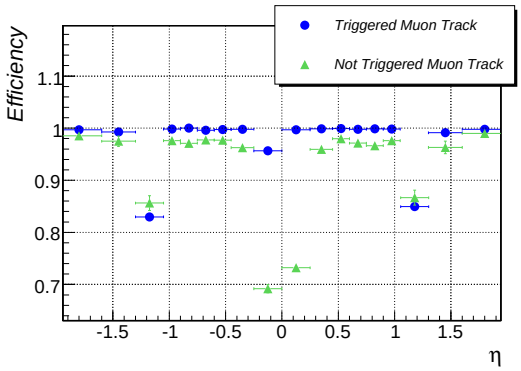

Figure 8.30: Reconstruction efficiency of the Muon Spectrometer for muon tracks which have been triggered and muon tracks which have been not triggered.

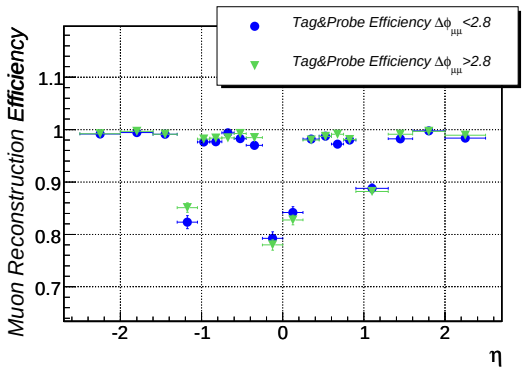

Figure 8.31: Comparision of muon reconstruction efficiencies determined via 'tag and probe' approach for two sets of muons differing by $\Delta\Phi$.

Efficiency	**Statistic Uncertainty**	**Systematic Uncertainties**		
		$\lvert\varepsilon_{true} - \varepsilon_{Insitu}\rvert$	$\lvert\varepsilon_{Insitu,\Delta\phi<2.8} - \varepsilon_{Insitu,\Delta\phi>2.8}\rvert$	
0.9482	0.0008	0.0014	0.0025	
Expected Background Contribution				
$b\bar{b} \to \mu\mu$	$W^{\pm} \to \mu^{\pm}\nu$	$Z/\gamma^* \to \tau\tau$	$t\bar{t} \to W^+bW^-b$	Overall
< 0.002	< 0.0004	0.0	$\approx 0.0002 \pm 0.00004$	< 0.002

Table 8.7: Estimated Uncertainties of in-situ determined Muon Spectrometer reconstruction efficiencies

that also the true efficiency has a statistical uncertainty. The difference in both efficiency distributions for the different $\Delta\Phi$-sample is treated as a further conservative estimation of a possible systematic uncertainty. The background contribution is only estimated by the Monte Carlo prediction and treated as a systematic uncertainty. As discussed in section 8.2 a lower background contribution is expected or can be estimated within data. Overall, we expect to determine the Muon Spectrometer reconstruction efficiency ε_{MS} with $50pb^{-1}$ to a precision of

$$\Delta\varepsilon_{MS} \approx \pm 0.001(stat) \pm 0.003(sys).$$

The Gaussian sum of all three systematic uncertainties, namely $|\varepsilon_{true} - \varepsilon_{Insitu}|$, $|\varepsilon_{Insitu,\Delta\phi<2.8} - \varepsilon_{Insitu,\Delta\phi>2.8}|$ and the background contribution, would be an overestimation of the overall systematic uncertainty, since the first two contributions might be correlated. Hence it was chosen to build the Gaussian sum of the expected background contribution and the larger contribution of $|\varepsilon_{true} - \varepsilon_{Insitu}|$ and $|\varepsilon_{\Delta\phi<2.8} - \varepsilon_{\Delta\phi>2.8}|$. This definition of the systematic uncertainty is used for all quantities which where determined by the 'tag and probe' method.

The given uncertainty estimation assumes that nearly all MDT chambers work and $\varepsilon_{MS} \approx 95\%$. A lower value of ε_{MS} will lead to an increase of the statistical uncertainty via Equation (8.10) and also to a higher systematic uncertainty. For real data a conservative estimation of the systematic uncertainty would be the comparison of the Monte Carlo predicted efficiency and the efficiency determined with data.

8.3.4 Determination of Inner Tracker Reconstruction Efficiencies

The 'tag and probe' method can also be applied to determine the efficiency of the ATLAS Inner Tracker ε_{IT}. Two muon tracks must be reconstructed in the ATLAS Muon Spectrometer, of which at least one must be matched to an inner track. This defines the 'tag' muon. The same cuts are applied as discussed in the previous section. Knowing this efficiency is important for the determination of the combined muon tracking efficiency.

Figure 8.32 shows the comparison to the efficiency determined with Monto Carlo Truth information. We observe a significant difference for large η values. Figure 8.33 implies that a relatively large fake-rate of reconstructed Muon Spectrometer tracks is expected for this region.

A fake muon track as defined in section 5.1 does not necessarily mean that the track is not caused by a real muon, but the true muon does not lie within the defined cone-radius $r_c = 0.07$. Loosening the cone-radius to $r_c = 0.1$ leads to the comparison shown in Figure 8.34. The discrepancy has become much smaller. A further loosened cut on the cone-radius might lead to an over estimation of the real efficiency and hence $r_c = 0.1$ was chosen for the determination of the Inner Detector efficiency.

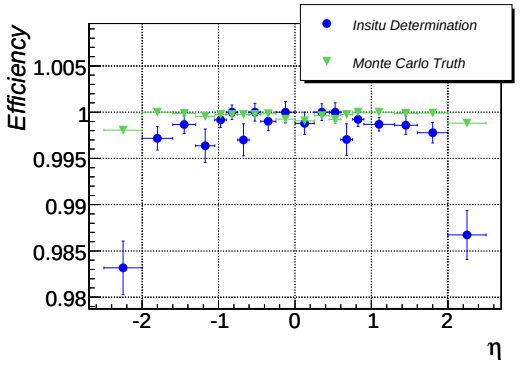

Figure 8.32: Comparison of the track reconstruction efficiency of the inner tracker vs. η determined by the 'tag and probe' method and by the Monte Carlo Truth information

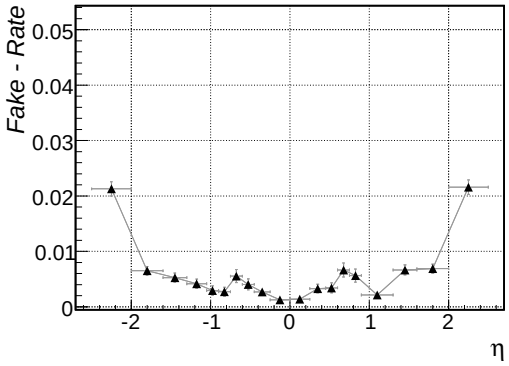

Figure 8.33: Fake-rate of Muon Spectrometer tracks for a reconstructed track to truth track association distance of 0.05

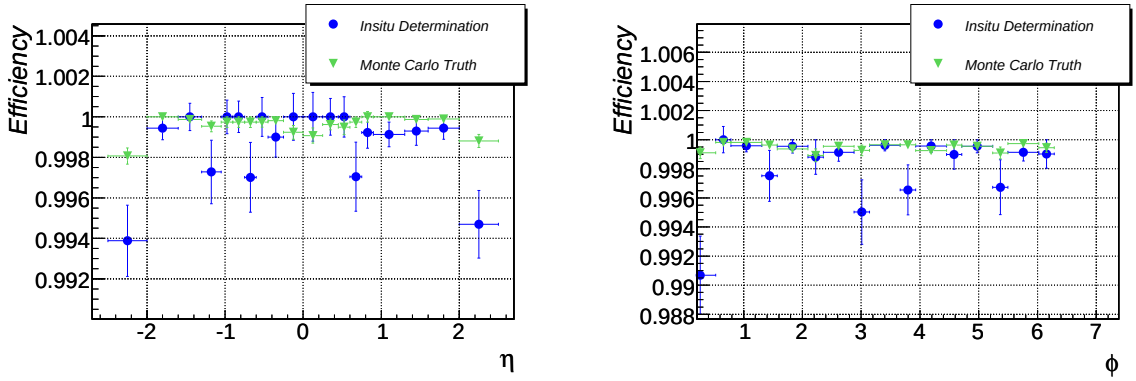

Figure 8.34: Comparison of reconstruction efficiency of the Inner Tracker vs. η and ϕ determined by the 'tag and probe' method and by the Monte Carlo Truth information.

Overall, we expect to determine the Inner Tracker reconstruction efficiency ε_{IT} with $50pb^{-1}$ to a precision of

$$\Delta\varepsilon_{IT} \approx \pm 0.0003(stat) \pm 0.002(sys).$$

Table 8.8 gives a detailed overview of the expected systematic uncertainties of the efficiency determination of the ATLAS Inner Tracker. The systematic uncertainty is significantly larger than the expected statistical contribution, which might be also due to the discussed *fake-rate effect*. The overall background contribution is expected to be much smaller than 0.2%, since in contrast to the Muon Spectrometer efficiency determination we require two reconstructed muon tracks, which is expected to strongly reduce the QCD and $t\bar{t}$ contribution.

8.3.5 Trigger Efficiencies

The efficiency of the LVL1-muon trigger, the LVL2-muon trigger and the *Event-Filter* can be determined in two ways. The first method is to use a data sample which has been triggered by a muon independent trigger e.g. a jet- or an electron-trigger. In this sample it can be counted how often a reconstructed muon has also been triggered at different stages of the trigger menu. The second method is again the 'tag and probe' technique.

Efficiency	**Statistic Uncertainty**	**Systematic Uncertainties**		
		$\lvert\varepsilon_{true} - \varepsilon_{Insitu}\rvert$	$\lvert\varepsilon_{Insitu,\Delta\phi<2.8} - \varepsilon_{Insitu,\Delta\phi>2.8}\rvert$	
0.9983	0.0003	0.0012	0.0020	
Expected Background Contribution				
$b\bar{b} \to \mu\mu$	$W^{\pm} \to \mu^{\pm}\nu$	$Z/\gamma^* \to \tau\tau$	$t\bar{t} \to W^+bW^-b$	Overall
$\ll 0.002$	$\ll 0.0004$	0.0	0.0	$\ll 0.002$

Table 8.8: Estimated Uncertainties of in-situ determined ATLAS Inner Tracker reconstruction efficiencies

This first approach is expected to be very useful for the low p_T-regime of the muon-trigger, since the reconstructed muons are mainly due to QCD-events and it has the additional advantage that it can be used without requiring Z boson events. This has three consequences: First of all, the first method can be used in the very first phase of LHC, secondly it can be also used to determine di-muon trigger efficiency, while the 'tag and probe' method can only be used for studying single (and therefore independent) muon triggers.

The trigger efficiency for the selected muons in this analysis depends on the properties of muon tracks, e.g. p_T or isolation. Hence, the 'tag and probe' approach is used for this study, since it includes by construction all relevant efficiency-correlations due the kinematic and isolation-properties of the muons. The same procedure and cut-selection as described in section 8.1 is used also in this case.

The 'tag and probe' has also the advantage, that the trigger-efficiency of all trigger stages can be determined independently from the muon reconstruction efficiency by using the same approach as described in section 8.3.3. For this study, it is only important to determine the trigger efficiency for muons, which have also been reconstructed, since two reconstructed muons are required in the analysis. It should be noted, that the background contributions can be neglected in this case, since two reconstructed muon tracks are required for the 'tag' and 'probe' muons. If, by chance, a muon track is used, which does not stem from a Z boson, but fulfills all further cut requirements then also this muon can be used to probe the trigger efficiency.

The statistical uncertainty is driven by Equation (8.10). The difference in the predicted trigger efficiency for the two $\Delta\Phi$ sub-samples is treated as further systematic uncertainty.

Figure 8.35 shows the comparison between the efficiencies of both muon LVL1-Trigger and LVL2-Trigger determined by 'tag and probe' and Monte Carlo Truth information[8]. The inefficient regions are due to geometrical properties of the ATLAS detector such as support structures or holes, analogue to the the muon reconstruction efficiency which has been already described in section 5. No significant discrepancy can be observed. Using the 'tag and probe' method also other correlated efficiencies, e.g. the efficiency of reconstructing a muon which has been triggered on or the efficiency of the Level 2 trigger with respect to Level 1 can be determined.

The trigger efficiency has a strong p_T-dependence near its turn-on value, i.e. in this case around $6\,GeV$ or $20\,GeV$. It must be noted that the determination of this behavior might have a relatively large systematic uncertainty, since a lower p_T-cut for the 'probe' muon must be used which will lead to an increase of the QCD-background contribution.

An overview of the statistical and systematic uncertainties of the determination of the trigger efficiencies is shown in Table 8.9. The systematic contributions are within the statistical

[8]The LVL2-Trigger was only correctly implemented in the $|\eta| < 1.0$-region in the available Monte Carlo samples.

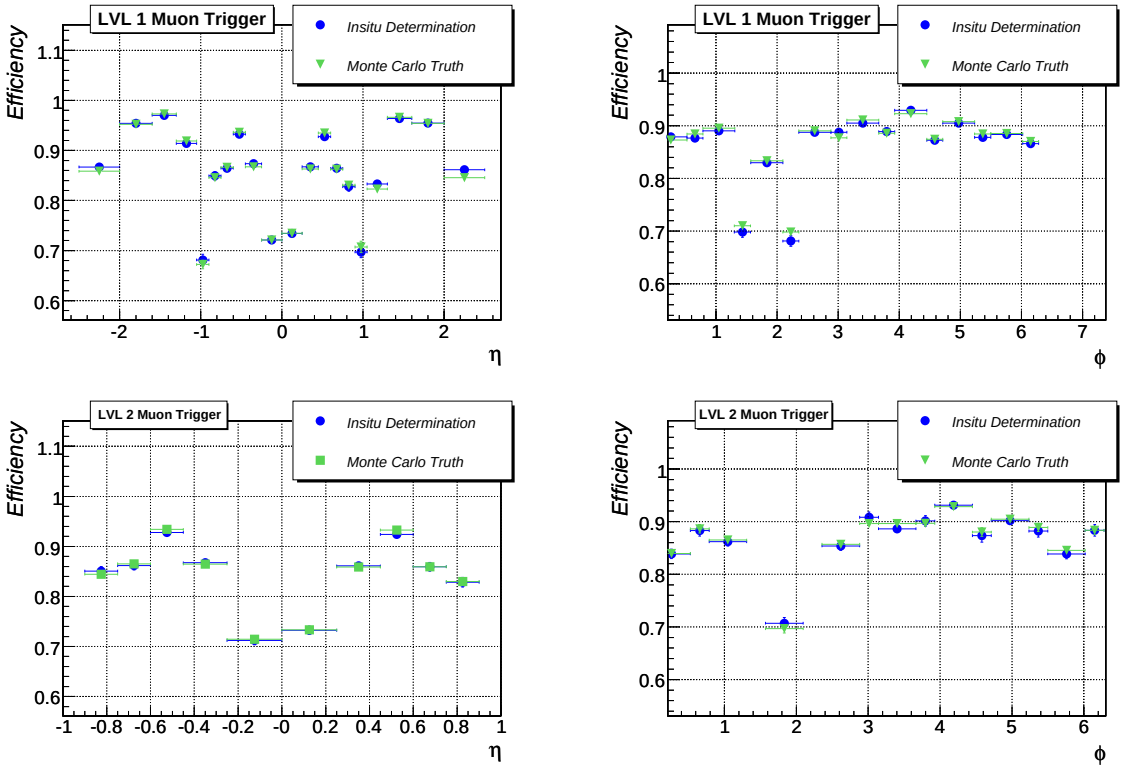

Figure 8.35: Comparison of LVL1 and LVL2 muon trigger efficiencies vs. η and ϕ determined by 'tag and probe' method and Monte Carlo Truth information.

Trigger	Efficiency	Statistical Uncertainty	Systematic Uncertainties	
			$\lvert\varepsilon_{true} - \varepsilon_{Insitu}\rvert$	$\lvert\varepsilon_{\Delta\phi<2.8} - \varepsilon_{\Delta\phi>2.8}\rvert$
Level 1	0.8672	0.0015	0.003	0.003
Level 2	0.8422	0.0017	0.003	0.0025
Event Filter	(0.77)	(0.0023)	(0.003)	(0.0025)

Table 8.9: Estimated Uncertainties of in-situ determined Muon Spectrometer reconstruction efficiencies.

uncertainties [9]. For the study itself, only the precise knowledge of the overall trigger efficiency $\varepsilon_{20\,GeV}$ for $20\,GeV$ muons with respect to the number of produced $Z \rightarrow \mu\mu$ events is relevant, i.e.

$$\varepsilon_{20\,GeV} = \varepsilon^{EventFilter}_{20\,GeV} \cdot \varepsilon^{LVL2}_{20\,GeV} \cdot \varepsilon^{LVL1}_{20\,GeV}$$

Hence it is sufficient to probe if a muon has passed the *EventFilter*, since this already implies that this muon has also passed the LVL1 and LVL2 trigger. In this way also the efficiencies of the previous trigger stages can be determined straight forward, which can be used as cross-checks for the Monte-Carlo prediction of the full ATLAS simulation.

Note that the current available Monte Carlo samples have a known problem for the Level 2 muon trigger information for the end-cap region of the Muon Spectrometer. The stated uncertainties are calculated only with respect to the barrel-region. The *Event Filter* information was not available so far at all. The efficiency distribution of the LVL1 muon trigger for

[9] Note, that also the efficiency determined with Monte Carlo Truth information has a statistical uncertainty comparable to the 'tag and probe' approach

the $\eta-$, $\phi-$plane was chosen and normalized to an overall *Event Filter* efficiency of 0.77[10], which is a conservative estimation. The corresponding systematic uncertainties were taken from the muon LVL2-trigger. With this assumptions, it is expected to determine the *Event Filter* trigger efficiency ε_{EV} with $50pb^{-1}$ to a precision of

$$\Delta\varepsilon_{EV} \approx \pm 0.0023(stat) \pm 0.003(sys).$$

8.3.6 Muon Isolation Efficiency

The isolation properties of muons are directly related to the number of jets in the event. No jets in the event will lead to two tightly isolated muons; many jets in the event will lead to significantly less isolated muons. The isolation property of the 'tag' muon is correlated to the isolation property of the 'probe' muon. Hence, the isolation properties of the two muons are not independent from each other. This would be a crucial requirement of a successful application of the 'tag and probe' method. Ignoring this issue leads to differences in the determined efficiencies as illustrated in Figure 8.36 for the tight isolation requirement.

The last efficiency plot in Figure 8.36 reveals a relative strong dependence of the invariant di-muon mass and the isolation efficiency of muons. This is a further complication since a too tight cut on the invariant di-muon mass will lead to a shift of the measured isolation efficiency. For this reason we choose a larger mass window of $15\,GeV$ around the Z boson mass, to minimize the dependence of the invariant di-muon mass.

The last critical aspect is the fact, that the isolation cut on the 'probe' muon cannot be applied for signal selection, since this property is supposed to be tested. Hence, an increase of the QCD-related background is expected. The requirement of $p_T^{\max} > 30\,GeV$, $p_T^{\min} > 15\,GeV$ and the very tight isolation criteria of the 'tag' muon should account for the omission of the isolation cut on the 'probe' muon track. A higher cut on $p_T^{\min}$ will lead to a further rejection of background events. Yet, this is not applicable, since the signal selection presented in section 8.1 includes a cut on $p_T^{\min} > 15\,GeV$.

As already mentioned, the in-situ determined efficiency vs. η, ϕ and p_T is significantly higher than the Monte Carlo Truth based efficiency (Figure 8.36). This can be explained with the following small exercise. Assume two types of events: the first type of events has no reconstructed jet, the second type has reconstructed jets in the event. It is further assumed that the probability for an event being type 1 or type 2 is 50%. Moreover, the isolation probability for muons in events of type 1 is 80% and 20% for type 2. Hence, the overall isolation probability for a muon is 50%. The application of the 'tag and probe' method requires a 'tag' muon, which is isolated. Assuming 200 events, we expect 80 'tag' muons in events of type 1 and only 20 of 'tag' muons in events of type 2. This implies 64 'probe' muons in events of type 1 and 4 in events of type 2. Overall, this leads to 68 'probe' muons and 100 'tag' muons and leads to an determined efficiency of 68%. Therefore, the difference in in-situ determined isolation efficiency and the true isolation efficiency shown in Figure 8.36 is due to the variation of the isolation efficiency for samples with different numbers of reconstructed jets[11].

The above discussions suggests that the isolation efficiency determined by Monte Carlo Truth and 'tag and probe' method vs. the number reconstructed jets should coincide, which is confirmed by Figure 8.37.

[10] This efficiency was stated in [69]

[11] The isolation efficiency dependence on the Z boson mass can be explained by the fact that the number of high energetic jets is correlated with the opening angle of the two muon tracks and hence also with the Z

Isolation	**Efficiency**	**Statistical Uncertainty**	**Systematic Uncertainties**	
			$\lvert\varepsilon_{true} - \varepsilon_{Insitu}\rvert$	$\lvert\varepsilon_{\Delta\phi<2.8} - \varepsilon_{\Delta\phi>2.8}\rvert$
Loose	0.9915	0.0005	0.0003	0.001
Tight	0.8962	0.0012	0.0013	0.001
Expected Background Contribution				
$b\bar{b} \to \mu\mu$	$W^{\pm} \to \mu^{\pm}\nu$	$Z/\gamma^* \to \tau\tau$	$t\bar{t}$	Overall
< 0.002	$\approx 0.0015 \pm 0.0007$	0.0002 ± 0.0001	0.004 ± 0.001	$\approx 0.008 \pm 0.0025$

Table 8.10: Estimated Uncertainties of in-situ determined isolation efficiencies.

It is expected to determine the isolation efficiencies $\varepsilon_{\mathrm{Iso}}$ with $50pb^{-1}$ to a precision of

$$\Delta\varepsilon_{\mathrm{Iso}}^{Loose} \approx \pm 0.0005(stat) \pm 0.003(sys) \tag{8.11}$$

$$\Delta\varepsilon_{\mathrm{Iso}}^{Tight} \approx \pm 0.0012(stat) \pm 0.003(sys). \tag{8.12}$$

Table 8.10 summarizes the expected uncertainties of the isolation requirements. A significant background contribution from $W \to \mu\nu$ events is expected, since the high $p_T^{\max}$ cut will be passed by the muon resulting from the direct W boson decay. Within the available Monte Carlo statistics no QCD-event passes the selection cuts. Analogous to the previous sections, an estimation of the background contribution $f_{QCD} \approx 0.002 \pm 0.002$ due to QCD processes has been assumed.

boson mass.

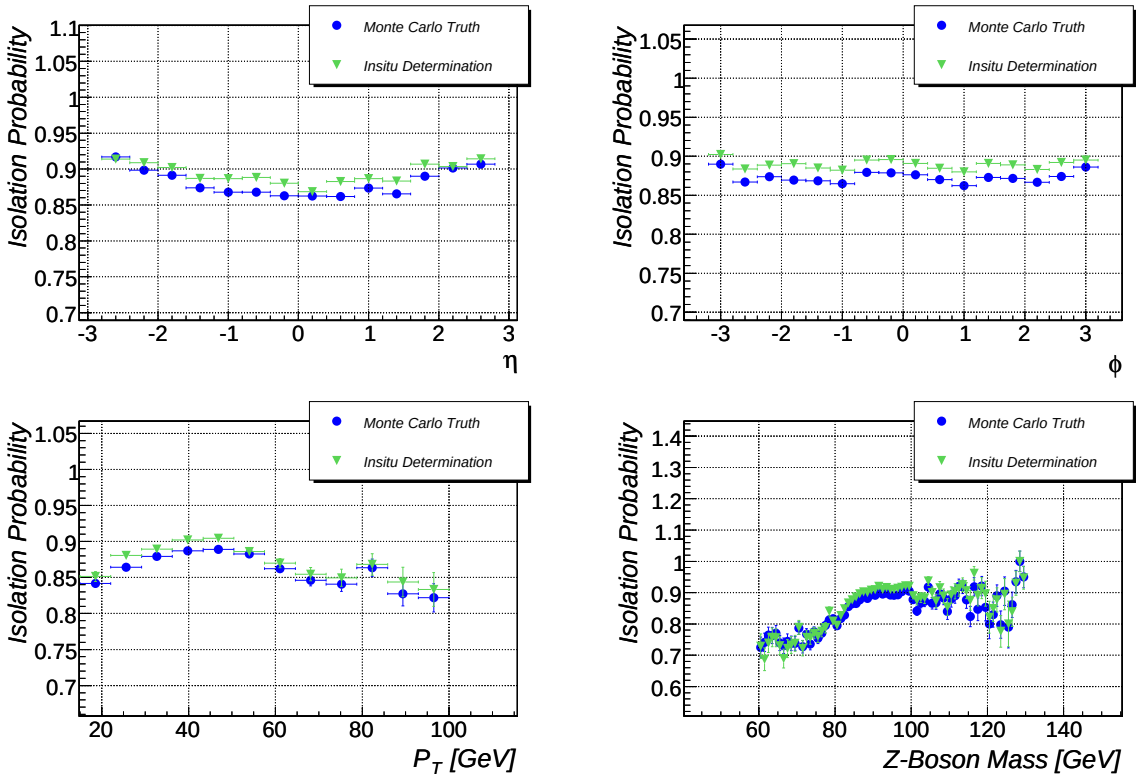

Figure 8.36: Comparisons of the expected probability for a muon resulting from $Z \rightarrow \mu\mu$ to fulfill the tight isolation criteria determined with Monte Carlo Truth information and the 'tag and probe' approach.

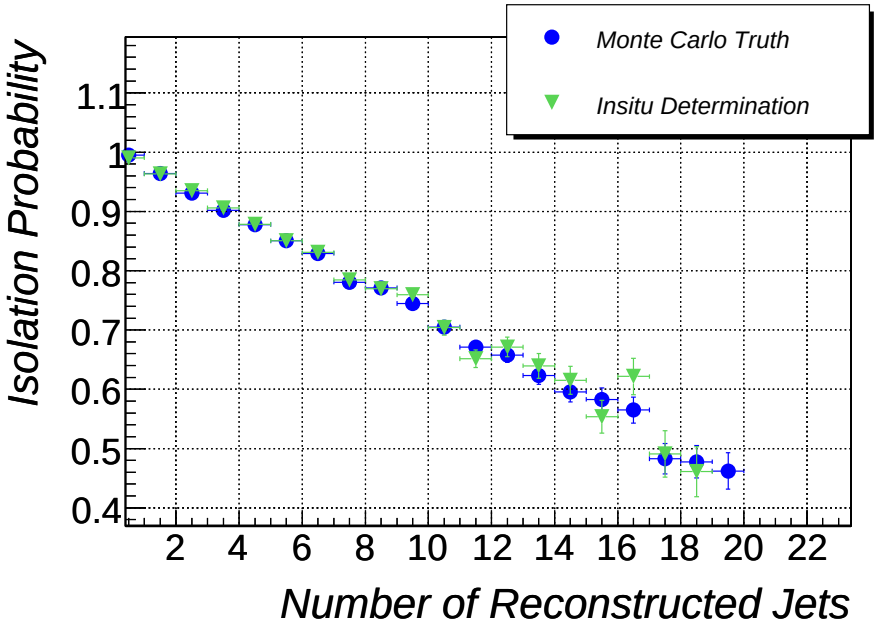

Figure 8.37: Comparisons of the expected probability for a muon resulting from $Z \rightarrow \mu\mu$ to fulfill the tight isolation criteria vs. number of reconstructed jets determined with Monte Carlo Truth information, Monte Carlo truth information with applied kinematics cuts on the muons and the 'tag and probe' approach.

8.4 Determination of the Muon p_T-Resolution

The p_T resolution of combined muon tracking as well as standalone Muon Spectrometer reconstruction depends on an overall momentum scale s and a resolution width σ

$$p_T \rightarrow s \cdot f(p_T, \sigma),$$

where f is a function which smears $1/p_T$ randomly (e.g. by a Gaussian) with a certain width σ. The impact of the p_T-resolution for single muons on the reconstructed Z boson mass is used for the determination of s and σ. Larger values of σ will lead to a broader reconstructed width of the Z boson, while s affects the value of the reconstructed maximum. Note, that this definition of the momentum scale parameter s is independent from the muon's charge and hence is at first order not affected by misalignment effects[12].

The basic idea is to vary the parameters s and σ to reproduce the measured Z boson mass distribution. The reconstructed mass distribution f_Z^{Reco} can be described by the convolution of the Monte Carlo predicted mass distribution f_Z^{MC} with a Gaussian function,

$$f_Z^{Reco}(x_m) = \int A f_Z^{MC}(m_{\mu\mu}) e^{-\frac{(x_m - x_{fit} - m_{\mu\mu})^2}{2\sigma_g^2}} dm_{\mu\mu}, \tag{8.13}$$

where the fitting parameters are A as a global normalization factor, x_{fit} as the mean-value and σ_g as the width of the Gaussian. The function $f_Z^{MC}(m_{\mu\mu})$ gives the probability of having a Z boson with a generated mass $m_{\mu\mu}$, while the final function $f_Z^{Reco}(x_m)$ gives the probability of having a Z boson with a reconstructed mean x_m, assuming that the detector resolution can be described by a Gaussian. The function f_Z^{MC} is defined by the Z boson mass distribution on Monte Carlo generator level[13]. Figure 8.38 shows the function f_Z^{Reco} fitted to the reconstructed di-muon mass distribution for an ideal Muon Spectrometer layout. The relative bad χ^2 of the fit can be explained by the fact, that the simple smearing Gaussian does not reflect all detector effects in detail. First of all, it is not expected, that the p_T-resolution itself is Gaussian but $1/p_T$. Even the $1/p_T$-distribution can only be parameterized to high accuracy by a sum of two Gaussians and a Landau-function. Nevertheless, the simple Gaussian approach gives a stable parameterization of the invariant mass spectrum, which is sufficient for this study.

The p_T-resolution of muons can be modeled in two ways. The first approach is to use a reconstructed track of the full ATLAS Monte Carlo simulation and apply an additional Gaussian smearing function, which might depend on η, ϕ and p_T. This method has the advantage that it includes most of the detector effects which have been modeled within the ATLAS simulation. The second approach does not rely on the ATLAS full detector simulation and has therefore the advantage that it allows easy and fast studies on Monte Carlo generator level. For this study, the first approach was used and is discussed in detail in the following. The Monte Carlo independent approach is presented in Appendix D.3.

It was chosen to determine the muon p_T-resolution for three bins in η-direction as well as three bins in p_T-direction. The binning in η-directions reflects the structure of the Muon Spectrometer and differentiates between barrel ($-1.0 < \eta < 1.0$) and end-cap region. The binning in p_T was chosen in such a way that each bin contains approximately the same number of events, i.e. $15\,GeV - 32\,GeV$, $32\,GeV - 44\,GeV$ and $44\,GeV - 60\,GeV$ as illustrated in Figure 8.39.

[12] A misaligned tower of the Muon Spectrometer will have a different impact on the momentum scale s for positive and negative charged muons

[13] A simple Breit-Wigner function for f_Z^{MC} is not used, since this would not reflect the Z/γ^*-mixing for lower invariant masses.

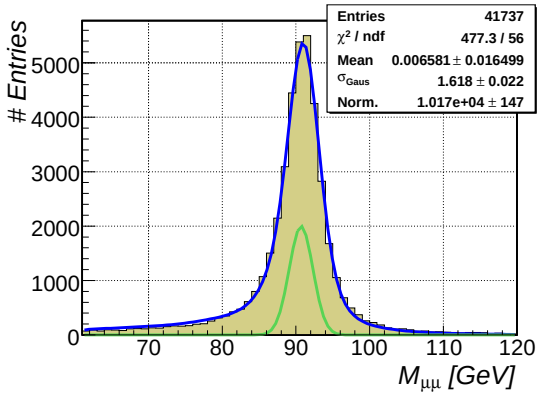

Figure 8.38: Reconstructed invariant mass spectrum for simulated $Z \to \mu\mu$ sample with ideal Muon Spectrometer geometry. The distribution is fitted by f_Z^{Reco}. The convoluted Gaussian of f_Z^{Reco} is shown as green line.

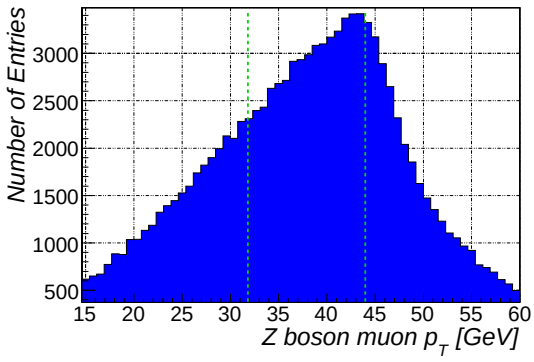

Figure 8.39: Monte Carlo truth p_T distribution of muons originating from a Z boson. The binning for the p_T-resolution determination is indicated.

The reconstructed Z boson events are classified by the η or p_T value of their muons. For example, one histogram contains the reconstructed mass distribution of Z bosons where both muons are reconstructed in one endcap of the Muon Spectrometer, i.e. $\eta > 1.0$. Another histogram contains the reconstructed mass distribution of Z bosons where at least one of the two muons is reconstructed in one endcap of the Muon Spectrometer. In total six histograms are produced in this way for the η-region. The same separation is applied for the binning in p_T, which will also lead to six histograms. The histograms which are based on two muons within the same bin, e.g. the same endcap, have lower statistics by construction, but depend only on p_T-resolution effects for the specified η- or p_T-region. These histograms are called *clean histograms* in the following. The other histograms have significantly higher statistics, but have also contributions from muons which are assigned to another bin and hence mix the p_T-resolution of several η- or p_T-regions.

Some of these histograms are shown in Figure 8.40. Although the χ^2 of the fits is not particularly good, Equation (8.13) can be used to parametrize the expected Z boson mass distribution. The systematic uncertainties due to the chosen parametrization will largely cancel out, since Equation (8.13) will be applied on both, Monte Carlo simulated events and real data. Moreover, Figure 8.40 reveals a clear dependence of the Z boson width becomes obvious. For example, the reconstructed Z boson width of events, where both muons have been reconstructed in the barrel region, i.e. $|\eta| < 1.0$ is $2.36\,GeV$, while the reconstructed width for events, where both muons have been reconstructed in the endcap, is $4.056\,GeV$. This reflects the fact, that the p_T-resolution is better in the barrel than in the endcap region of the Muon Spectrometer.

An exception is the histogram, where the two muons are required to have a p_T larger than $45\,GeV$. In this case, Equation (8.13) does not give an adequate parameterization of the reconstructed distribution. It will be shown, that this has no significant impact on the determination of the p_T-resolution. The algorithm for p_T-determination is structured as follows:

1. Determine the values of m_g and σ_g of Equation 8.13 for all *clean histograms*
2. Vary the momentum scale s_i and the Gaussian smearing width σ_i for each η and p_T-bin i independently until the measured values m_g and σ_g of the *clean histograms* are

reproduced.

3. Set these parameters as start parameters (step $n = 0$) for the following iterative procedure

4. Vary the momentum scale s_i and the Gaussian smearing width σ_i for bin i exclusively to reproduce the measured values m_g and σ_g of the corresponding histograms. Use the values of s_i and σ_i for muon of bin $j \neq i$ of step $n-1$.

5. Repeat step 4 for all bins i

6. Repeat step 4 until convergence

The basic idea of this algorithm is to iteratively adjust the parameters s_i and σ_i for only these muons, which have been reconstructed in bin i, to reproduce the corresponding mass-distribution. In practice this approach converges after a few iterations.

The clean histograms are only used to determine start parameters for s and σ and hence the mentioned problem of fitting the function (8.13) to the *clean histogram* with $p_T > 45\,GeV$ will loose its impact after a few iterations.

Figure 8.41 and 8.42 illustrate the dependence of the measured mean and width[14] of the Z boson mass distribution vs. the momentum scale s and the Gaussian smearing parameter σ. We observe again a linear dependency on the momentum scale s, but a more sophisticated dependency for small σ. This dependency can be parameterized by

$$\sigma_g = \sqrt{\sigma^2 + \sigma_0^2} \tag{8.14}$$

where σ_0 is expected width of the Z boson mass distribution for the case of a perfect Monte Carlo Simulation of ATLAS, which takes all resolution effects correctly into account. For such an extreme case, a relatively large statistical uncertainty is expected, since small variations in σ_g will lead to large uncertainties on σ (Figure 8.42). The parameterization in Equation (8.14) will lead again to a linear dependence for large Gaussian smearing parameters σ, since they will dominate the whole resolution.

Systematic uncertainties arise from several sources. The application of selection cuts might lead to different distributions in Monte Carlo and data even if the p_T-resolution is described correctly in the full ATLAS simulation. This effect was studied, by varying the muon p_T requirements by 10% and the isolation criteria by 20%. This leads to a relative uncertainty on the determined width σ of the p_T- resolution of 0.05. Hence, the systematic uncertainty due to the signal selection is small and will be neglected in this case.

The comparison between the p_T-resolution vs. η determined with this approach and by Monte Carlo Truth is shown in Figure 8.43 for the standalone Muon Spectrometer reconstruction. The difference is treated as systematic uncertainty. The overall p_T-resolution is expected to be determined from $50\,pb^{-1}$ to a *relative* precision of

$$\Delta s \approx \pm 0.001(stat) \pm 0.003(sys)$$

$$\Delta\sigma \approx \pm 0.02(stat) \pm 0.04(sys)$$

[14]Note, that the measured width of the Z boson mass distribution corresponds only to the width of the convoluted Gaussian

It has been assumed that the given systematic uncertainty is the same for each bin and no correlation between the different bins is present.

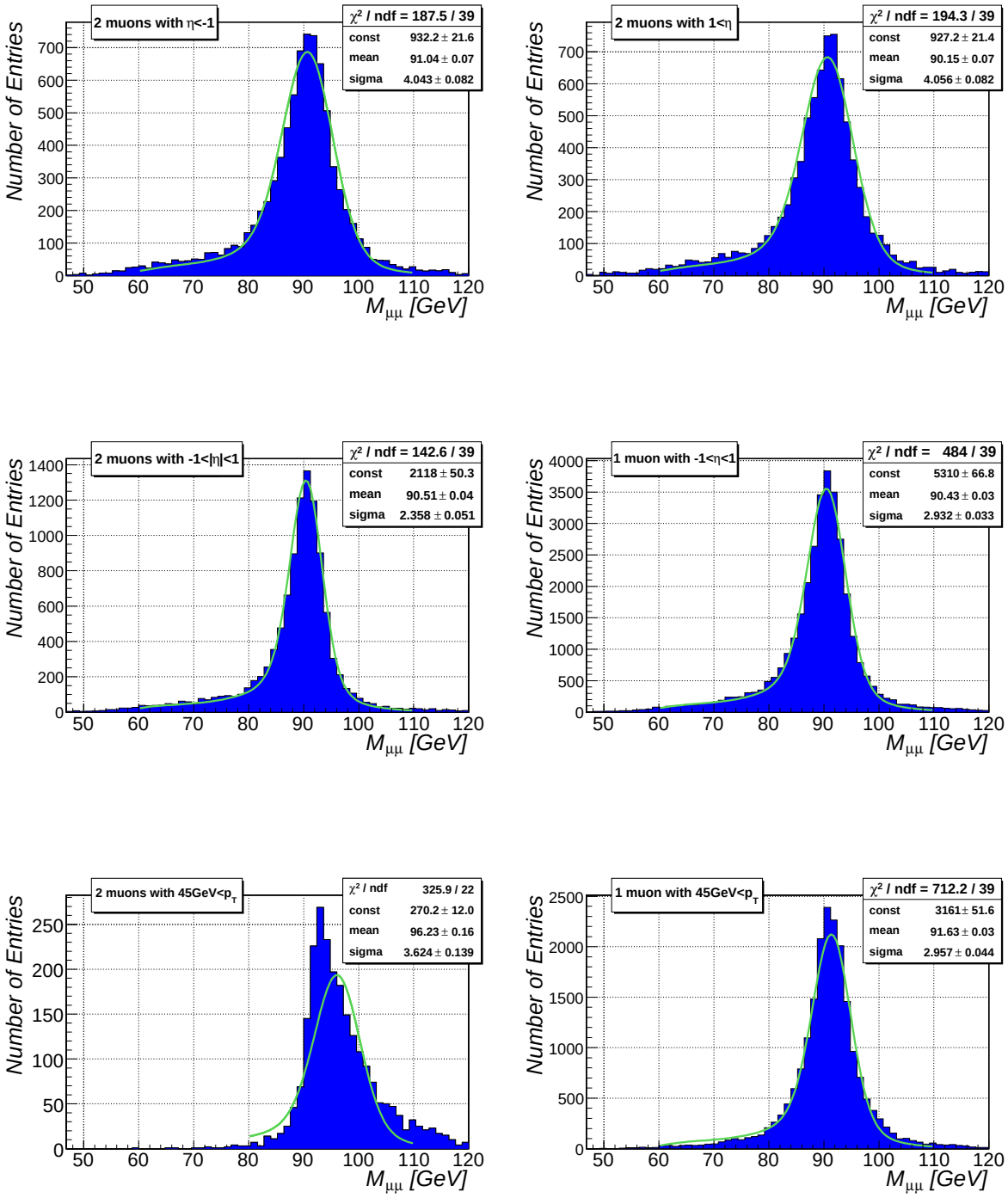

Figure 8.40: Reconstructed invariant mass spectra of two muons resulting from a $Z \to \mu\mu$ decay, for different η and p_T ranges.

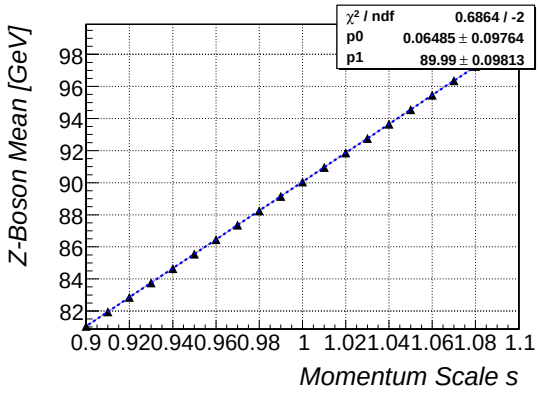

Figure 8.41: Expected mean of Z boson mass distribution vs. the momentum scale s of the smearing function.

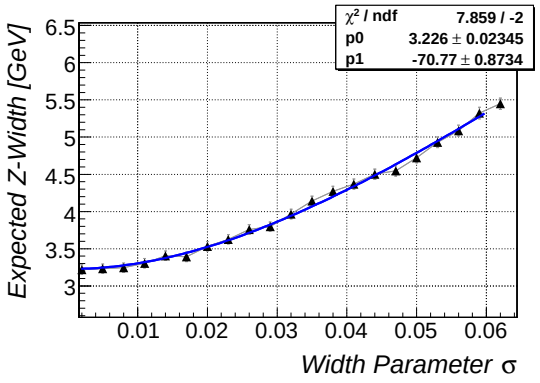

Figure 8.42: Expected width of Z boson mass distribution vs. width σ of gaussian, which is used for an additional smearing of the Monte Carlo p_T resolution.

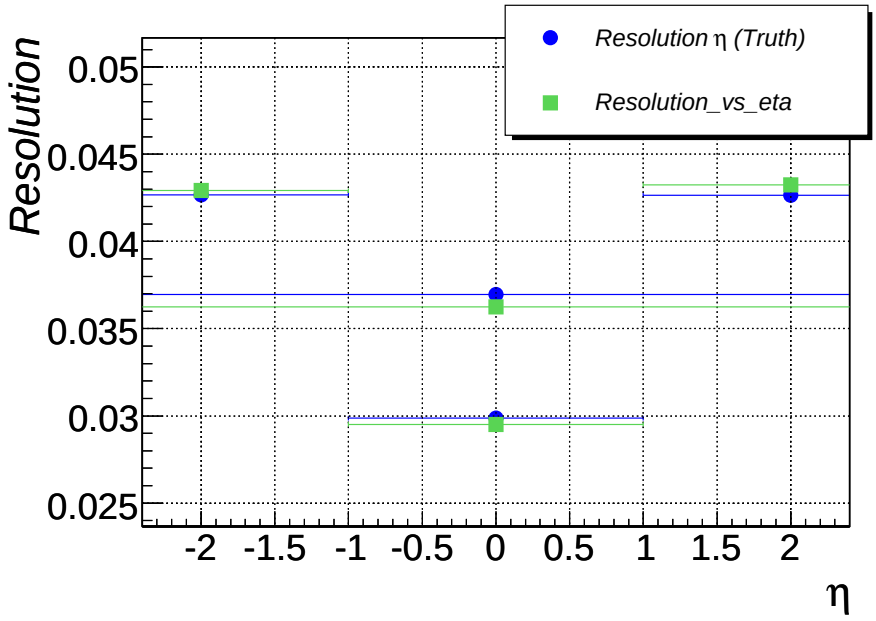

Figure 8.43: Comparison of p_T-resolution determined via Monte-Carlo-Truth and the Monte-Carlo based in-situ approach for combined track reconstruction vs. η.

8.5 Further Studies of Systematic Uncertainties

8.5.1 Impact Parameter

The uncertainty on the expected collision point distribution has an impact on the signal reconstruction efficiency. In current Monte Carlo simulations it is assumed that the collision points are Gaussian distributed, centered at 0 with a width of $50\,mm$. Muon tracks are required to have an absolute η-value below 2.5. Muons which are produced in reality with larger distances in z-direction than in the Monte Carlo simulation, might have an η-value below 2.5 but are not reconstructed. This effect is illustrated in Figure 8.44 and discussed in this section.

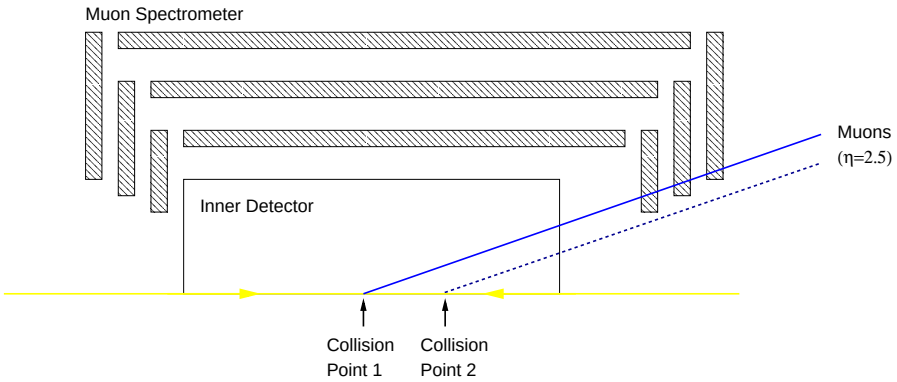

Figure 8.44: Illustration of the impact of the collision point on the signal reconstruction efficiency

To study this effect, the generated collision point in z-direction was modeled with a Gaussian with a width σ_{Z_0} (Figure 8.45). In a second step, it is simulated if the muon could be reconstructed and fulfills the $|\eta < 2.5|$ requirement. The impact of the additional Gaussian smearing width σ_{Z_0} on the reconstruction efficiency is shown in Figure 8.46. An uncorrected net shift of the average collision point by $1\,mm$ in y- and z-direction has also been studied. It turned out for both cases that the relative change of the selection-efficiency is smaller than 0.0005. Hence it seems reasonable to neglect the systematic uncertainty due to these effects, since even a rough description of the collision point distribution, is sufficient for this study.

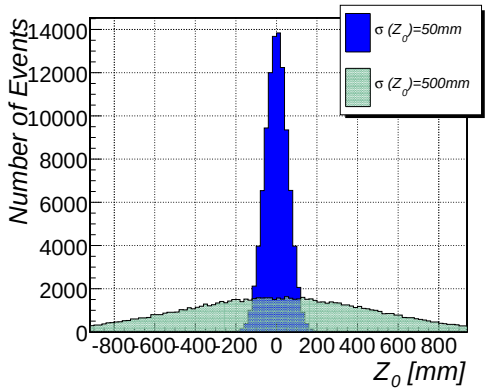

Figure 8.45: Collision point distribution for two values of Z_0.

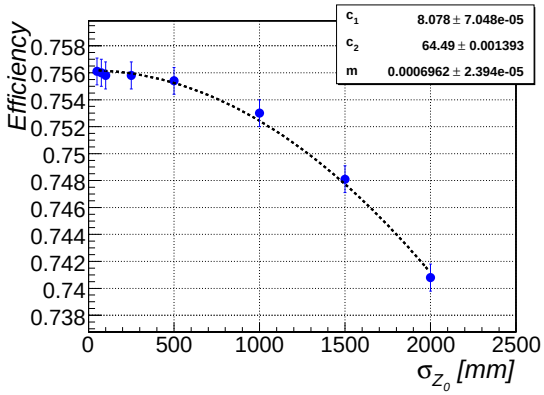

Figure 8.46: Width of collision point distribution Z_0 vs. impact on accpentance

8.5.2 Impacts of Misalignment

Misalignment of the ATLAS Muon Spectrometer is expected to have a significant impact on the p_T-resolution but only a small impact on the reconstruction efficiency [7]. These impacts can be determined with the methods, presented in section 8.3 and 8.4. Impacts of misalignments in the large $|\eta|$-region need special attention, since they may affect the η-determination and hence the acceptance-cut at $|\eta| = 2.5$.

For a first estimation, a single $50\,GeV$ single muon sample has been reconstructed with an ideal and a misaligned Muon Spectrometer layout. The ratio of reconstructed muons with $|\eta| < 2.5$ over the overall number of reconstructed muons has been calculated for both reconstructed samples. The difference of this ratio was found to be 0.0023 ± 0.003, which is compatible with 0.0 within the statistic uncertainty as expected. It should be noted, that deviation of 0.0023 ± 0.003 is due to the limited statistics of the available Monte Carlo sample.

To estimate the effect in more detail, it can be assumed, that the η-measurement is driven by the inner and outer MDT-chamber of the Muon Spectrometer Endcap only and no information of the Inner Detector or a vertex constrained is used. Moreover, it is assumed that all muon tracks can be considered as straight lines in a first approximation. Figure 8.47 illustrates the idea of this simplified η-measurement. A $2\,mm$ shift of the y-position of the outer MDT-chamber with respect to the inner MDT-chamber is a conservative assumption of an uncorrected misalignment [70]. This leads to a measured η-variation of $\Delta\eta \approx 0.0004$ and induces an uncertainty on the number of selected events of $\Delta N_{\eta-mis}/N \approx 1 \times 10^{-5}$. This estimation is conservative, since the assumed $2\,mm$ misaligned chamber position must be applied randomly to all 16 sectors in the ϕ-plane on both sides of the Muon Spectrometer. Hence, in the case of uncorrelated misalignments, these uncertainties are expected to cancel out to a certain extend.

A more serious impact is expected if a correlated shift is introduced, i.e. the Muon Spectrometer is shifted globally in one direction. To estimate this effect, it is assumed, that the η-measurement is driven only by the innermost MDT station by requiring that the muon comes from the interaction point. A shift of $2\,mm$ of the innermost MDT chamber leads to $\Delta\eta \approx 0.002$ and induces an uncertainty on the number of selected events of $\Delta N_{\eta-mis}/N \approx 5 \times 10^{-4}$. Hence, it seems to be justified to neglect a systematic contribution due to this effect.

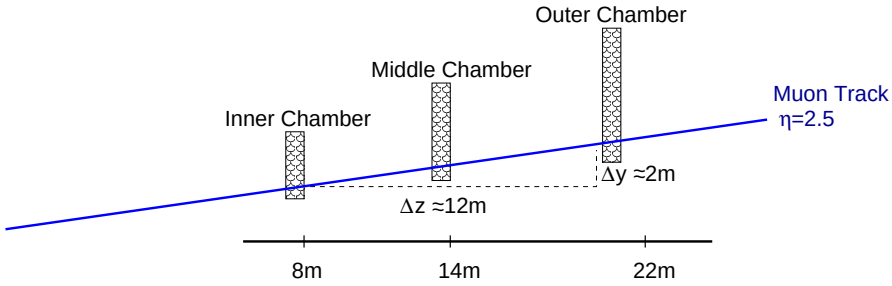

Figure 8.47: Illustration of assumed η-measurement of a muon track in the $|\eta| \approx 2.5$-region.

8.5.3 PDF Contributions

The theoretical uncertainties on the parton distribution functions (PDFs) lead to an impact on the rapidity and kinematic properties of the Z boson, and hence on the acceptance of the

η- and p_T-cuts. These effects have been studied on the PYTHIA generator level.

The CTEQ6.1M description of the PDFs was chosen [24]. The core of the PDF description are the probability density functions for each parton, i.e. one function for the u-quark, one function for d-quark and so on. These functions are determined by experiment and evolved to smaller values of x. Each of PDFs can be varied within the uncertainty of the measurements. It was chosen by the CTEQ collaboration to describe all possible variations of the complete set of functions by 20 orthogonal vectors. The PDF uncertainties are therefore estimated from 40 different PDF sets, each containing the average density functions varied by one error vector in either direction.

To estimate the overall effect on the selection efficiency, $300,000$ $Z \to \mu\mu$ events were generated for each of the 40 different PDF sets. The invserse transverse momentum of all generated muons have been smeared by a Gaussian function to account for the p_T-resolution of the combined tracking of the ATLAS Detector (see Appendix D.3), as well as a cut on the η of the muons has been applied ($|\eta| < 2.5$). In a last step kinematic cuts have been applied on the simulated muons and their invariant di-muon mass.

The detector acceptance α is defined as the fraction of events, which pass the kinematic cuts and the $|\eta| < 2.5$ requirement. The overall acceptances α_i have been calculated for each of the 40 PDF sets, where the index i stands for the PDF set chosen. Also, the acceptance α_s of the average PDF-set has been determined with a higher statistics of two million events in an analogue way.

The quadratic sum of all differences $\alpha_s - \alpha_i$ with the same sign leads to an estimation of the PDF uncertainty impact on the selection efficiency

$$\Delta\varepsilon_{PDF} = ^{+0.012\pm0.003(stat)}_{-0.006\pm0.003(stat)},$$

which is in agreement with [71].

8.6 Expected Precision of the $\sigma(pp \to Z/\gamma^* \to \mu^+\mu^-)$ Measurement

The uncertainty of the cross-section measurement

$$\sigma(pp \to Z/\gamma^* \to \mu^+\mu^-) = \frac{N_0 \cdot (1 - f_{Background})}{\varepsilon_{All} \int Ldt}$$

is determined by the uncertainty of the number of candidate events N_0, the background contribution $f_{Background}$, the overall efficiency ε_{All} and the integrated luminosity.

Detailed studies of luminosity measurements at LHC and ATLAS are under way [72–74] and therefore no error is specified in this thesis, although it might be the dominant contribution for the first phase of LHC. Moreover, the theoretical prediction of $\sigma(pp \to Z/\gamma^* \to \mu^+\mu^-)$ can be used to determine the integrated luminosity and to compare this measurement with other methods of luminosity determination.

8.6.1 Uncertainty of ε_{All}

The overall efficiency ε_{All} includes trigger, reconstruction as well as all cut efficiencies. The uncertainty on the p_T-resolution influences directly the kinematic-cut uncertainties. In the following, two approaches are discussed to estimate the uncertainty of ε_{All}.

Quadratic Summation

Ignoring all correlation between reconstruction efficiencies and kinematic cuts, then the overall efficiency ε_{All} can be calculated by

$$\begin{aligned}\varepsilon_{All} &= \left((\varepsilon_{Trigger})^2 + 2 \cdot \varepsilon_{Trigger} \cdot (1 - \varepsilon_{Trigger})\right) \cdot (\varepsilon_{ID})^2 \cdot (\varepsilon_{MS})^2 \cdot \varepsilon_{kinematics} \cdot \\ &\quad \cdot (\varepsilon_{Loose})^2 \cdot \left((\varepsilon_{Tight})^2 + 2 \cdot \varepsilon_{Tight} \cdot (1 - \varepsilon_{Tight})\right) \end{aligned} \tag{8.15}$$

where $\varepsilon_{Trigger}$ is the trigger efficiency, ε_{ID} is the track reconstruction efficiency of the Inner Detector, ε_{MS} is the reconstruction efficiency of the Muon Spectrometer, $\varepsilon_{kinematics}$ is the efficiency of all kinematic cuts on the muons and their invariant mass, ε_{Loose} is the efficiency for the loose-isolation requirement for a muon and ε_{Tight} is the corresponding probability for the tight-isolation requirement. Some efficiencies are required to be fulfilled for two muons and hence they are included quadratically in Equation (8.15). An example is the reconstruction efficiency of the Muon Spectrometer ε_{MS}, since two reconstructed tracks are required in the analysis. It is sufficient for other efficiencies, e.g. the trigger efficiency, that at least one muon passes the efficiency requirement. Therefore these efficiencies have to be included as $\varepsilon^2 + 2 \cdot \varepsilon \cdot (1 - \varepsilon)$. An exception is $\varepsilon_{kinematics}$ since this efficiency includes already all kinematic cuts on both muons and on the invariant di-muon mass.

The uncertainty of $\varepsilon_{kinematics}$ is directly related to the uncertainty of the muon p_T-resolution. A variation of the width of the p_T-resolution by 4% (see section 8.4) leads to an impact on $\varepsilon_{kinematics}$ which is less than 0.001. Even for an assumed p_T-resolution of 10% and a relative uncertainty of 50% the effect on ε_{All} is expected to be smaller than 0.002. This relatively small impact is expected, since an uncertainty on the momentum resolution leads only to migration effects at the cut boundaries.

In contrast, the uncertainty on the momentum scale is expected to have a larger effect as the cut-range, i.e. an uncertainty of $0.1\,GeV$ in the momentum scale will lead to an uncertainty comparable to the number of events between p_T^{Cut} and $p_T^{Cut} + 0.1\,GeV$. Figure 8.48 shows the in-situ determined momentum scale s_i for an integrated luminosity $50\,pb^{-1}$ for the three chosen p_T-bins i, where s_i is indicated at the average muon p_T in each bin i, e.g. at $25\,GeV$ for the bin from $15\,GeV$ to $32\,GeV$. The basic idea to estimate this effect is to assume a linear dependence of the momentum scale on the p_T of the muons. This linear dependence is estimated by a straight line fit between $s_3 \pm \sigma$ and $s_1 \mp \sigma$ (green markers in Figure 8.48). Since the assumption of a linear dependence is not a priori justified and non-linear effects might be present for lower transverse momenta p_T, a more conservative estimation of $s_3 \pm 2.0\sigma$ and $s_1 \mp 2.0\sigma$ is used to account for these possible non-linear effects (red markers in Figure 8.48). The black lines indicate the final assumed p_T dependence of the uncertainty on the momentum scale. Applying this dependence on the Monte Carlo simulation, it was found that $\Delta\varepsilon_{kinematics} \approx 0.0035$.

The uncertainty of ε_{All} can then be calculated with full error propagation of Equation (8.15), using the uncertainties, which have been discussed in the previous sections and summarized in Table 8.11. This leads to

$$\Delta\varepsilon_{All} \approx 0.002(\text{stat}) \pm 0.007(\text{sys}) \,^{+0.012}_{-0.006}(\text{pdf}) \tag{8.16}$$

For the systematic uncertainty only the larger value of $|\varepsilon_{true} - \varepsilon_{Insitu}|$, and $|\varepsilon_{Insitu,\Delta\phi<2.8} - \varepsilon_{Insitu,\Delta\phi>2.8}|$ has been used for the quadratic summation with the background contribution $\Delta\varepsilon_{kin}$ in order not to overestimate the uncertainty as already discussed in the previous sections. It should be noted that some systematic effects (e.g. the expected background contribution)

will shift the efficiencies determined by the 'tag and probe' approach only in one direction. This shift should be corrected for in the in-situ determined efficiencies. As a conservative estimation, the shift itself is treated as systematic uncertainty.

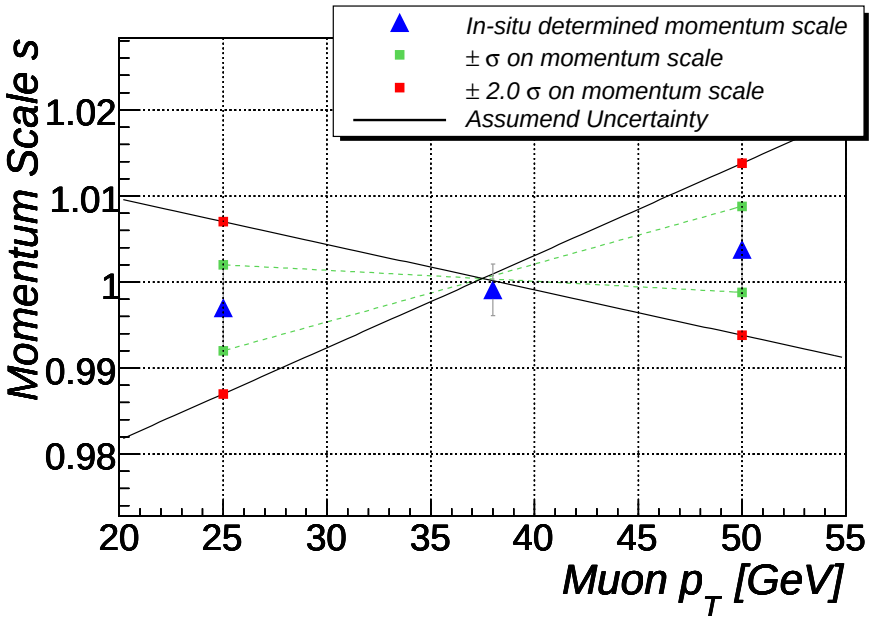

Figure 8.48: In-situ determined momentum scale for an integrated luminosity $50\,pb^{-1}$ for the three chosen p_T-bins. The green lines indicate two conservative functions, which describe the muon p_T dependence on the corresponding momentum scale. The black lines indicate the functions, which were used to estimate the systematic uncertainty which arises from the momentum scale uncertainty.

	Efficiency	**Statistical Uncertainty**	**Systematic Uncertainties**		
			$\lvert\varepsilon_{true} - \varepsilon_{Insitu}\rvert$	$\lvert\varepsilon_{Insitu,\Delta\phi<2.8} - \varepsilon_{Insitu,\Delta\phi>2.8}\rvert$	Background
ε_{MS}	0.9482	0.0008	0.0014	*0.0025*	≈ 0.002
ε_{ID}	0.9983	0.0003	0.0012	*0.002*	≈ 0
ε_{Tight}	0.8962	0.0012	*0.0013*	0.001	≈ 0.0025
ε_{Loose}	0.9915	0.0005	0.0003	*0.001*	≈ 0.0025
$\varepsilon_{Trigger}$	0.7700	0.0023	*0.003*	0.0025	≈ 0
	Efficiency	**Momentum Resolution**	**Momentum Scale**		
ε_{kin}	0.9056	< 0.001	≈ 0.0035		

Table 8.11: Summary of single efficiencies and their expected statistical and systematical uncertainty. ε_{MS} is the reconstruction efficiency of the Muon Spectrometer; ε_{ID} is the track reconstruction efficiency of the Inner Detector; ε_{kin} is the efficiency of all kinematic cuts on the muons and their invariant mass; ε_{Loose} is the efficiency for the loose-isolation requirement for a muon; ε_{Tight} is the efficiency for the tight isolation requirement for a muon; $\varepsilon_{Trigger}$ is the trigger efficiency; only the larger value of $|\varepsilon_{true} - \varepsilon_{Insitu}|$ and $|\varepsilon_{Insitu,\Delta\phi<2.8} - \varepsilon_{Insitu,\Delta\phi>2.8}|$ is taken into account for the overall efficiency uncertainty determination.

Toy Monte Carlo Approach

A more sophisticated approach than the simple quadratic summation is called the Toy Monte Carlo Approach. The trigger- and reconstruction-efficiencies, as well as the isolation efficiencies and the p_T-resolution are determined in dependence of various quantities, like η or p_T,

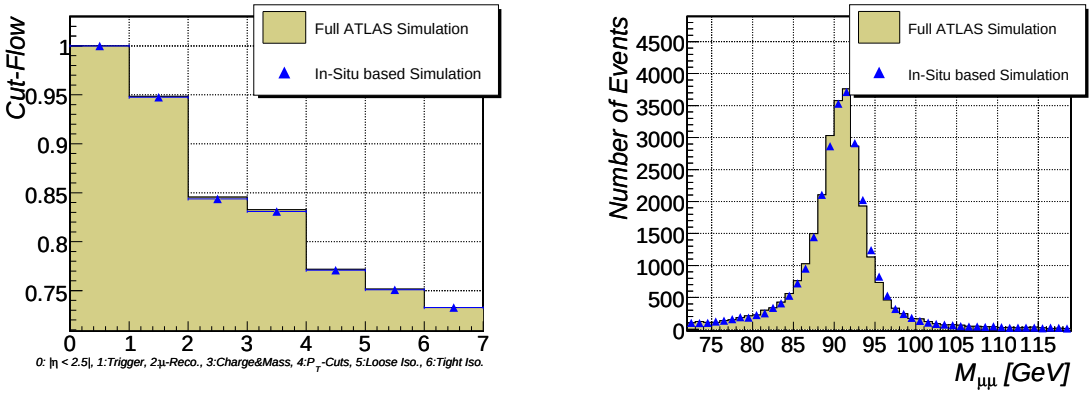

Figure 8.49: Comparison of Cut-Flow and reconstructed di-muon Mass for full ATLAS simulation and insitu-based Toy simulation.

as discussed in section 8.3 and section 8.4. The basic idea of the Toy Monte Carlo approach is to make use of these in-situ determined dependencies to respect all available information and even some possible correlations. The Toy Monte Carlo method is applied on the truth or generator level of a Monte Carlo simulated signal process sample. In this study a sample of 500,000 $Z \to \mu\mu$ events, simulated with PYTHIA was used as a basis.

In a first step, the in-situ determined trigger- and reconstruction-efficiencies are applied on the muons on generator level. In a second step, the determined p_T-resolution, the kinematic cuts and the in-situ determined isolation-efficiency are applied in the correct order on the remaining muons. The cut-flow and the di-muon mass spectra of events from a full Monte Carlo simulation and from the Toy Monte Carlo approach (applied on the truth information of the same sample) were compared in Figure 8.49. The good agreement in both plots is a successful test of this method.

Within the Toy-Monte Carlo approach it is possible to study the overall uncertainty of ε_{All} in an easy way. In a first step, all in-situ determined efficiencies and resolutions are varied with respect to their statistical and/or systematic uncertainties in each bin. The uncertainties are assumed to be Gaussian distributed. This procedure is clarified with the following example. Assume that the determined reconstructed efficiency for one bin in the η-, ϕ-plane is 0.95 ± 0.02. The variation of this efficiency is done by smearing it by a Gaussian function with a width of 0.02. In a second step, these varied efficiencies and resolution are applied within the Toy Monte Carlo simulation on the $500,000$ generated $Z \to \mu\mu$ events. The overall cut-efficiency for this set of varied efficiencies is then given by the ratio of the number of events, which passed the Toy Monte Carlo simulation over $500,000$. This is repeated five hundred times and each value for ε_{All} plotted in a histogram. The large sample size of $500,000$ events ensures a relative small statistical uncertainty for each iteration.

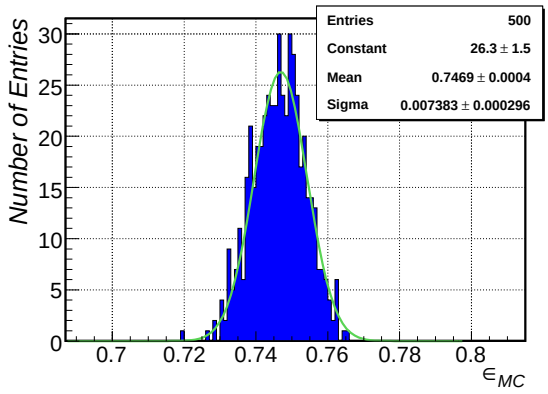

Figure 8.50: Simulated efficiencies for 500 iterations with varied detector efficiencies.

The resulting 500 values of ε_{All} of this procedure are shown in Figure 8.50 for the case, where only the impact of the systematic uncertainties has been studied. The width of a fitted

Gaussian function to the ε_{All}-distribution is defined as the uncertainty of ε_{All}. The advantage of this procedure is that correlations between the reconstruction efficiencies and different cuts are taken approximately into account. Moreover, it can be used for the evaluation of systematic uncertainties of differential cross-section measurements, where these correlations play a larger role.

This second approach is a useful cross-check of the results, based on the quadratic summation. The uncertainty of ε_{All} determined with this method is given by,

$$\Delta\varepsilon_{All} \approx 0.002(\text{stat}) \pm 0.007(\text{sys}), \tag{8.17}$$

where the PDF-uncertainty has been omitted. This agrees nicely to the previous estimated uncertainty given in Equation (8.16).

8.6.2 Further Uncertainties

The uncertainty on N_0 is a simple statistical one. For roughly $30,000$ expected candidate events for an integrated luminosity of $50 pb^{-1}$, the relative uncertainty is

$$\Delta N_0 = \frac{\sqrt{N_0}}{N_0} \approx 0.006. \tag{8.18}$$

The relative uncertainty of $f_{Background}$ was discussed in detail in section 8.2. and is expected to be

$$\Delta f_{Background} \approx 0.003, \tag{8.19}$$

which is treated as systematic effect[15].

8.6.3 Overall Uncertainty

Combining Equations (8.18), (8.19) and (8.16) leads to

$$\frac{\Delta\sigma}{\sigma} \approx 0.006(\text{stat}) \pm 0.008(\text{sys}) \, ^{+0.016}_{-0.008}(\text{pdf}) + \text{Luminosity Uncertainty},$$

where the background uncertainty has been added quadratically to the systematic uncertainty of $\Delta\varepsilon_{All}$. It should be noted that this result only holds, if the ATLAS detector is fully operating. E.g. a reduced number of fully operating muon chambers will lead to a decrease of reconstruction efficiency which has a direct impact on the statistical uncertainty. This leads also to an increase of the systematic uncertainty, since the difference of the in-situ determined efficiencies and the Monte Carlo prediction will be treated as a further systematic uncertainty.

[15] The uncertainty due to higher order corrections was not studied in detail in this analysis. A brief discussion and estimation of this uncertainty can be found in [75].

"Nothing in life is to be feared. It is only to be understood."

Marie Curie[1]

Chapter 9

Measurement of the Transverse Momentum Spectrum of the Z Boson

The number of high energetic muons pairs, resulting from the decay of Z bosons with a large transverse momentum, must be described correctly in Monte Carlo simulations, since it is an important background process for searches for supersymmetric particles or other models beyond the standard model. Moreover, this differential cross section is sensitive to the parton density functions (PDFs) of the proton and various constraints on the PDFs can be specified via a precise measurement.

The goal of the analysis, presented in this chapter, is to determine the achievable precision of the differential cross-section measurement of $\frac{d\sigma(pp\to Z/\gamma^*\to\mu^+\mu^-)}{dp_T^Z}$ with an integrated luminosity of $50\,pb^{-1}$. Moreover, the observation significance of the so-called x-broadening effect with this integrated luminosity is studied.

This study is based on the same fully simulated Monte Carlo samples as the ones used in chapter 8. Also the signal selection and the background estimation has not been changed.

9.1 Measurement of p_T^Z-Spectra

The measurement of a differential cross section is a standard task in high energy physics. The differential cross section $f(x)$ for a variable x is defined by

$$f(x) := \frac{d\sigma}{dx} \tag{9.1}$$

where σ is the overall cross section

[1] One of the few persons who ever received two Nobel Prizes in different categories was Marie Curie, born 1867 in Warsaw. One of her first publications was on the magnetic properties of steal and, as every physics student knows, the so-called Curie-point. In 1898 she announced the discovery of a new element, which she called Polonium. In she same year the also announced together with G. Bemont the discovery of Radium.

$$\sigma_{tot} = \int \frac{d\sigma}{dx} = \int f(x)dx \tag{9.2}$$

Equation (9.2) suggests that it is sufficient to determine the shape of $f(x)$, since the integral over $f(x)$ can be normalized by σ_{tot}.

The measured p_T^Z-distribution with an ideal detector would coincide with the real p_T^Z - distribution. The measured p_T^Z-distribution with a realistic detector will differ significantly from the true distribution due to limited resolution, detector acceptance and various efficiencies. If the Monte Carlo simulation of the detector describes all these effects to high precision, it could be used to conclude from the measured distribution to the true distribution.

Measuring a differential cross section for a variable x makes it is necessary to choose a certain binning in x direction. The maximal number of bins is constrained by the expected statistical uncertainty of each bin, which should not be too large compared to the systematic uncertainty of the bin, and the purity. The purity of a bin i is defined as the fraction of reconstructed events in bin i, which have also been generated in bin i. Hence, an ideal detector would have a purity of one. If the purity of a realistic detector is determined by its detector resolution for the variable x. In this study it was chosen that the minimal purity is defined by $\pm\sigma$ of the detector resolution, i.e. a minimal purity of 0.68 is required. A too low purity does not give additional information about the underlying distribution. Moreover, small purities lead to an increase of systematic uncertainties on the correction of detector effects.

Figure 9.1 shows the purity distribution of the chosen binning for this study. The increasing bin size for larger transverse momenta of the Z boson reflects the fact that the statistical uncertainty increases for larger p_T^Z values.

Bin	**1**	**2**	**3**	**4**	**5**
Range [GeV]	0.0-2.2	2.2-4.4	4.4-6.6	6.6-9.0	9.0-11.3
Bin	**6**	**7**	**8**	**9**	**10**
Range [GeV]	11.3-13.9	13.9-16.9	16.9-20.2	20.2-23.8	23.8-27.7
Bin	**11**	**12**	**13**	**14**	**15**
Range [GeV]	27.7-32.2	32.2-38	38-46	46-56	56-68
Bin	**16**	**17**	**18**	**19**	**20**
Range [GeV]	68-84	84-100	100-120	120-145	145-170

Table 9.1: Chosen bin ranges for the transverse momentum of the Z boson p_T^Z.

The basis of nearly all algorithms to calculate the true distribution from the measured distribution is the so called *migration matrix* M_{ij}. The element M_{ij} of the matrix gives the probability for an event generated in bin j and reconstructed in bin i. Table 9.2 shows the expected *migration matrix* calculated with full Monte Carlo simulation. Note, that the sum of the entries in each column gives one and the overall form of the matrix is close to an identity matrix, which is due to the high purity for large values of p_T^Z. The matrix M_{ij} relates the true distribution t_j with the reconstructed distribution r_i via

$$r_i = M_{ij}t_j \tag{9.3}$$

Assuming a perfect detector simulation leads to a precise knowledge of M_{ij} and the true distribution can be calculated by the inverted matrix M_{ij}^{-1}

$$t_j = M_{ij}^{-1}r_i \tag{9.4}$$

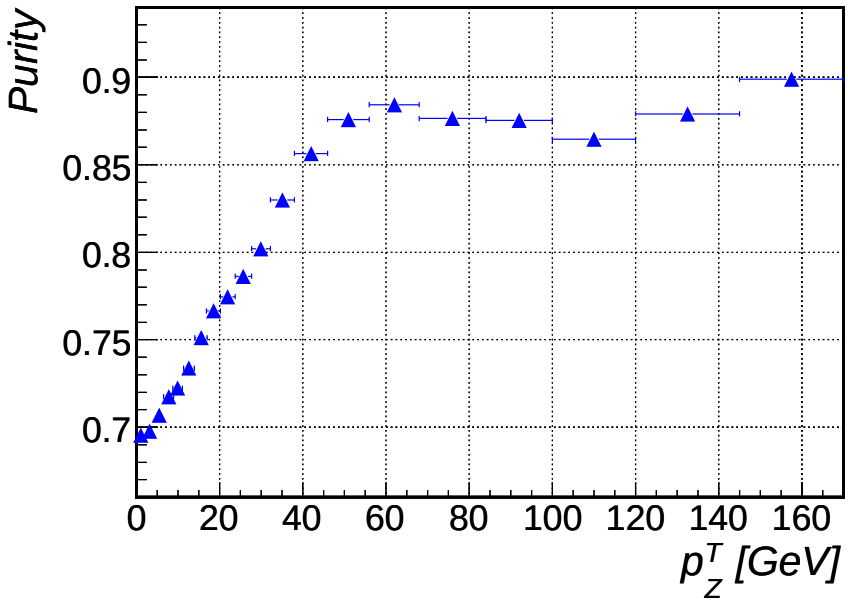

Figure 9.1: Purity of chosen binning

The inversion of the matrix has some problematic issues. First of all, there are numerical problems for a stable inversion of the matrix. Moreover, relatively large uncertainties are expected for bins with limited Monte Carlo statistics, which lead to further uncertainties on the inverted matrix. One approach is the so called *regulated deconvolution*, which basically interpolates the matrix with spline-functions and inverts the interpolated matrix [76].

For this study, another *deconvolution*-technique, called *Bin-by-Bin*-correction, was chosen for simplicity. It turns out in the following that this approach is appropriate for the p_T^Z cross-section measurement. This method approximates only the impact of off-diagonal entries of the migration matrix and corrects each bin separately. The scaling or correction factor ε_i^{CF} for each bin is determined from Monte Carlo simulation

$$\varepsilon_i^{CF} = \frac{\text{Number of generated events in bin } i}{\text{Number of reconstructed events in bin } i}. \tag{9.5}$$

The true number of entries t_i in bin i can then be calculated from the number of measured entries in this bin m_i, via

$$t_i = \varepsilon_i^{CF} m_i \tag{9.6}$$

Migration effects from generated to reconstructed bins are only approximated with this method by construction. Hence, it should not be applied for the deconvolution of matrices which are not similar to the identity matrix i.e. have a small purity.

9.1.1 Correction of Efficiency and Systematic Uncertainties

The application of unfolding methods relies on the precise understanding of the detector and its response functions. The Monte Carlo simulation of the ATLAS Detector gives a good approximation, but it is likely that the simulated resolutions and efficiencies are overestimated during the first phase of LHC. Therefore it is necessary to correct the Monte Carlo simulation

Bins	1	2	3	4	5	6	7	8	9	10	11
1	**70%**	10%	1%								
2	26%	**69%**	12%	1%							
3	3%	19%	**71%**	12%	1%						
4	1%	2%	15%	**72%**	12%	1%					
5			1%	14%	**71%**	14%					
6				1%	14%	**72%**	11%				
7					1%	12%	**75%**	10%			
8						1%	12%	**78%**	11%	1%	
9							1%	11%	**77%**	10%	
10									10%	**79%**	11%
11									1%	10%	**80%**
12											8%

Table 9.2: Migration matrix for the transverse momentum spectrum of the Z boson for first eleven bins. The rows i represent the reconstructed events in bin i, the column j represent the generated events in bin j.

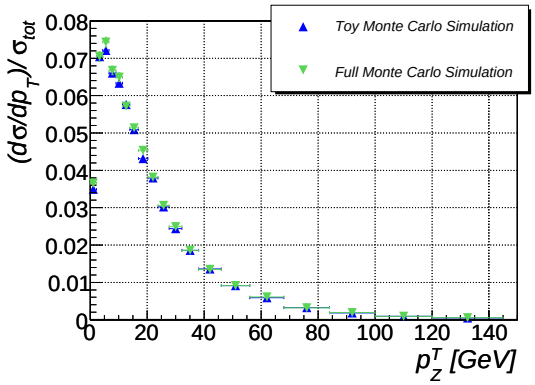

Figure 9.2: Comparison of the p_T^Z distribution of full Monte Carlo simulation and Toy Monte Carlo simulation.

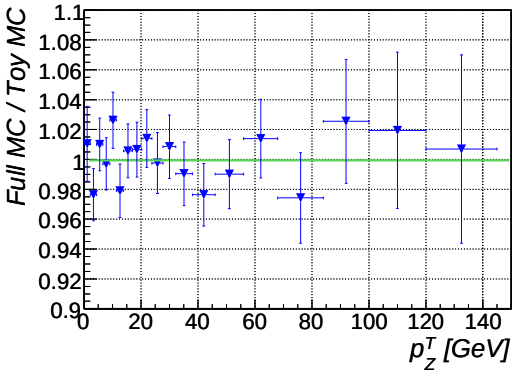

Figure 9.3: Relative comparison of the p_T^Z distribution of full Monte Carlo simulation and Toy Monte Carlo simulation.

by in-situ determined quantities, like reconstruction efficiency, momentum resolution and cut-efficiencies. This has been discussed extensively in chapter 8.

The 'Toy Monte Carlo' approach, which was also introduced in chapter 8, has been chosen to study the overall event reconstruction efficiency for each p_T^Z bin. A full Monte Carlo simulated event sample corresponding to an integrated luminosity of $50pb^{-1}$ was treated as data sample and used for the in-situ determination of all relevant efficiency and resolutions. A $Z \to \mu\mu$ large signal process sample was generated with PYTHIA and the detector response was simulated by the application of the in-situ determined efficiencies and resolutions. The resulting signal sample is therefore referred to as *Toy Monte Carlo* sample in the following.

The comparison of the p_T^Z distribution of the full simulated sample and the *Toy Monte Carlo* sample is shown in Figure 9.2 and Figure 9.3. A good agreement between both distributions can be observed. Figure 9.4 shows the overall efficiency for each bin in the p_T^Z spectrum for the full Monte Carlo simulation of ATLAS and the *Toy Monte Carlo* simulation where both samples are based on the same Monte Carlo Truth information. Both efficiency distributions agree within their statistical uncertainty.

Detector effects or efficiencies which are independent from the p_T of the Z boson have no

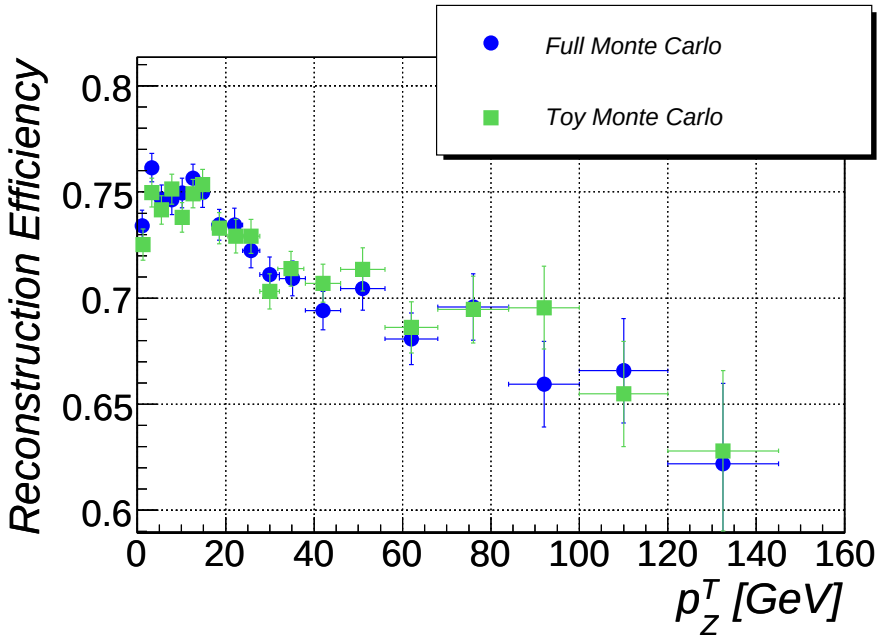

Figure 9.4: Overall efficiency ε_{All} vs. p_T of the Z boson for full Monte Carlo simulation and Toy-Monte Carlo simulation.

impact on the final shape of the p_T-distribution. Therefore only cuts which depend directly or indirectly on p_T^Z have to be treated as a possible source of systematic uncertainties. The impact of various selection cuts on the reconstruction efficiency of each bin is shown in Figure 9.5. The efficiency is normalized to events, where both generated muons fulfill an $\eta < 2.5$ requirement. Applying no isolation and no kinematic cuts on the p_T of the muons, a relatively flat distribution is expected[1]. The application of isolation cuts, but no kinematic cuts, leads to descending efficiencies with higher values of p_T^Z. This can be explained by the fact, that larger transverse momenta of the Z boson are correlated with the number of jets in the event, which itself is correlated with the isolation requirements of the muons. Applying kinematic cuts, but no isolation requirements, leads to a more complicated event shape. The efficiency is rising up to $20\,GeV$ and descending for larger values. This behavior can be explained by the fact, that the transverse momentum and the opening angle of the two resulting muons are strongly correlated with the p_T of both muons. In some cases, the p_T of one muon is shifted to higher values, while the p_T of the other muon is shifted to lower values. In this case, the lower cut on the p_T of the muon is more likely to fail. For other cases, i.e. other directions of boost of the Z boson, this leads to a shift in p_T in the same direction for both muons, which increases the probability that the event passes the p_T cuts on the muons. Figure 9.5 indicates that the main impact on the measured p_T^Z distribution is due to the isolation and the p_T cuts on the muons. Hence, it is expected that the systematic uncertainties arises from an imperfect knowledge of the muon p_T-resolution and of the isolation cut efficiency.

The momentum scale of the muon p_T-resolution is expected to be known with an absolute uncertainty of 0.005 and the width of the p_T-resolution to a relative uncertainty of 0.05 with an integrated luminosity of $50 pb^{-1}$ (See Section 8.4). The systematic uncertainty arising from the limited knowledge of the muon p_T-resolution is illustrated in Figure 9.6 and 9.7. It was determined by comparing the expected number of events for each bin i, once reconstructed with the expected p_T-resolution and once with an increased and decreased resolution by the

[1] Only reconstruction efficiencies have an impact in this setup where no first order p_T^Z dependence is expected.

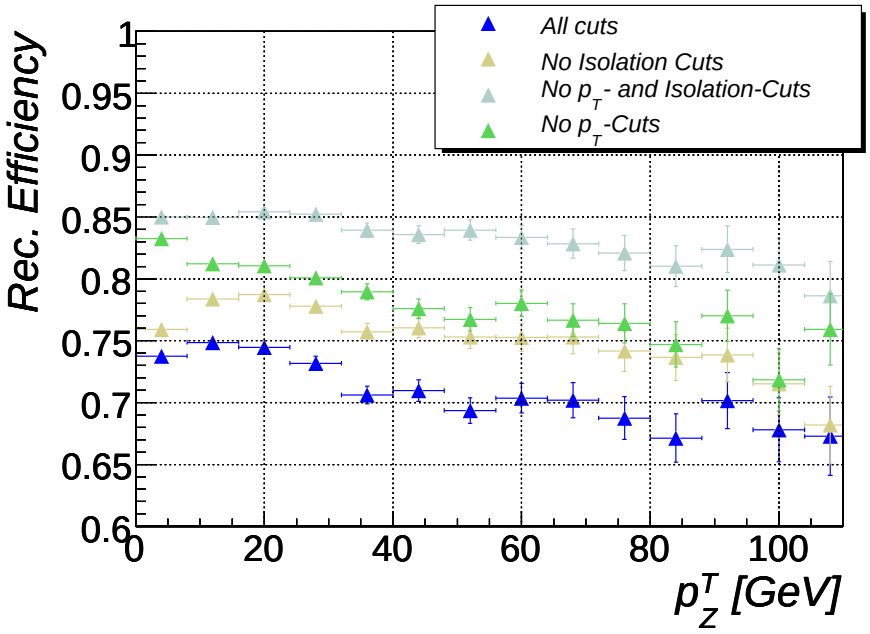

Figure 9.5: Overall efficiency ε_{All} vs. p_T of the Z boson, neglecting p_T- and isolation-cuts.

expected uncertainty. The ratio

$$\Delta = \frac{N_i^{\text{expected}} - N_i^{\text{smeared}}}{N_i^{\text{expected}}},$$

where N_i^{expected} is the number of events, which are reconstructed in bin i assuming the expected p_T-resolution and N_i^{smeared} is the number of events, which are reconstructed in bin i assuming an increased and decreased p_T-resolution by one standard deviation of the error.

The contribution due to the uncertainty of the isolation-cut efficiency is illustrated in Figure 9.8 and assumed to be symmetric. An overall absolute uncertainty of 0.004 for an integrated luminosity of $50 pb^{-1}$ is expected in section 8.3.6.

The overall systematic uncertainty for each bin is assumed to be the quadratic sum of all three single uncertainties. It is illustrated in Figure 9.9. It can be concluded that the overall systematic uncertainty is symmetric to a high extend and in the order of 0.01. Note, that this estimation is valid only for a fully operating ATLAS detector and an integrated luminosity of $50\,pb^{-1}$. Moreover, it is crucial that the combined tracking performance for muons achieves the expected p_T resolution of $2-3\%$ in the corresponding p_T range from $20\,GeV - 70\,GeV$. A poorer resolution will lead to an either larger binning or a lower purity and, therefore, to higher systematic uncertainties.

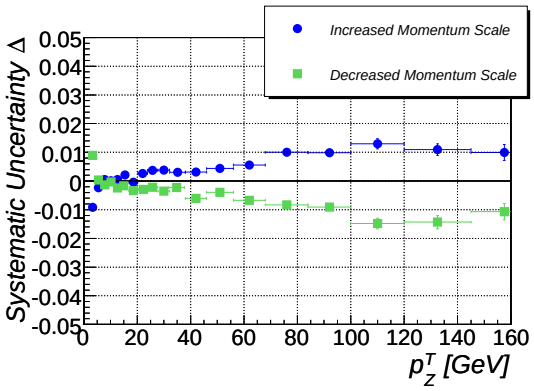

Figure 9.6: Expected uncertainty due to momentum scale uncertainty vs. p_T of the Z boson.

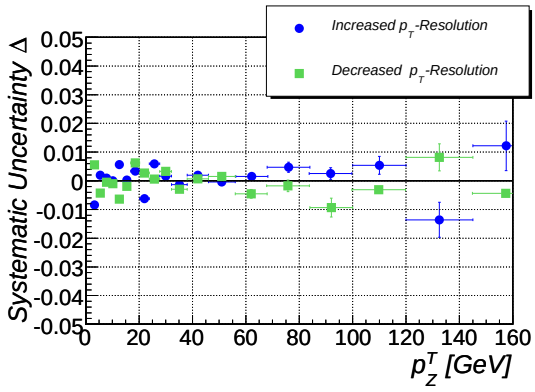

Figure 9.7: Expected uncertainty due to the muon p_T resolution uncertainty vs. p_T of the Z boson.

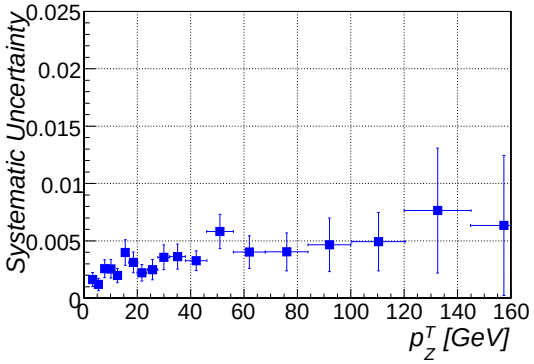

Figure 9.8: Expected uncertainty due to isolation-cut uncertainty vs. p_T of the Z boson.

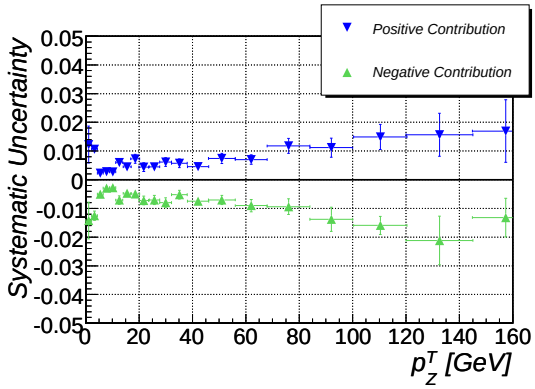

Figure 9.9: Expected overall systematic uncertainty vs. p_T of the Z boson.

9.1.2 Performance of the *Bin-by-Bin* Correction

A first basic test of the *Bin-by-Bin* method is to use fully simulated events as input for data and Monte Carlo reconstruction. The corrected p_T^Z distribution coincides to hundred percent to the Monte Carlo prediction, which is illustrated in Figure 9.10 and Figure 9.11. Figure 9.11 also reveals the consequence if no deconvolution is performed on the measured distribution but only a normalization of the integral to the Monte Carlo truth distribution. Clearly, a correction of the measured spectrum is necessary. It should be noted that the points of the normalized corrected data are strongly correlated, since underlying data is the same for the determination of the correction factors and the simulated data.

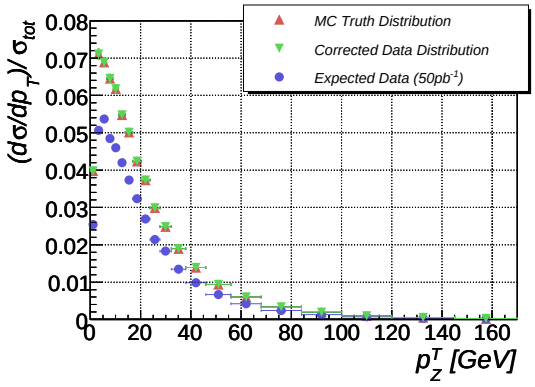

Figure 9.10: p_T^Z-distribution for full Monte Carlo simulation, which is treated as data, the truth Monte Carlo distribution, corresponding to the 'data' and the corrected distribution.

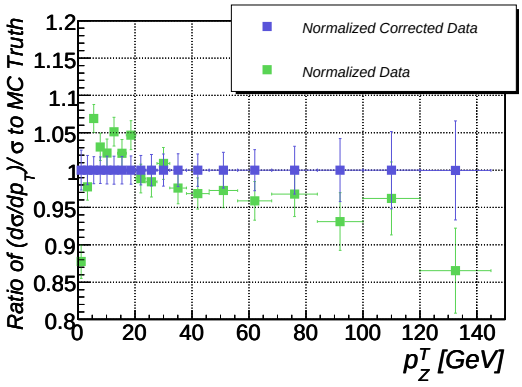

Figure 9.11: Ratio of corrected distribution over truth distribution and reconstructed distribution (normalized to the integral of the truth distribution) over truth distribution.

Figure 9.12 shows the values of ε_i^{CF} based on full Monte Carlo simulation. It can be seen, that the statistical uncertainty is dominating the estimated systematic uncertainty for higher values of p_T^Z. Hence, the scaling factors ε_i^{CF} are determined within the Toy Monte Carlo simulation for the following study due to the limited statistics of full simulated $Z \to \mu\mu$ events. When data is available, fully simulated events should be corrected by in-situ determined quantities, since more sophisticated detector effects, which cannot be detected in data for small integrated luminosities, are considered within the full simulation.

The predicted differential cross section from PYTHIA might differ from the real differential cross section. This difference will have also a direct impact on ε_i^{CF}, since these variables are calculated for the predicted distribution. The measured p_T^Z-distribution will coincide with the simulated distribution, assuming a perfect Monte Carlo simulation, if the real and Monte Carlo predicted cross sections coincide. This fact can be used to tune the predicted cross section. In general, the Monte Carlo prediction is changed until the measured and simulated distributions coincide. An iterative approach was used for this study. In step n $\varepsilon_i^{CF,n}$ is calculated for each bin i from

$$\varepsilon_i^{CF,n} = \frac{N_i^{MCTruth,n}}{N_i^{MCReco,n}}$$

where $N_i^{MCTruth,n}$ is the number of Monte Carlo predicted events in bin i and $N_i^{MCReco,n}$ is the number of reconstructed events within the full Monte Carlo simulation of the ATLAS detector. The corrected measured distribution $N_i^{Reality,n}$ is then given by

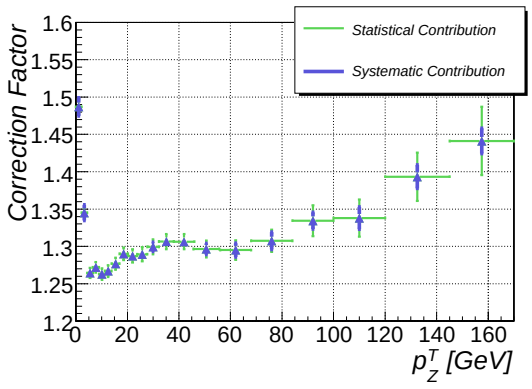

Figure 9.12: Final *correction factors* including systematic uncertainties.

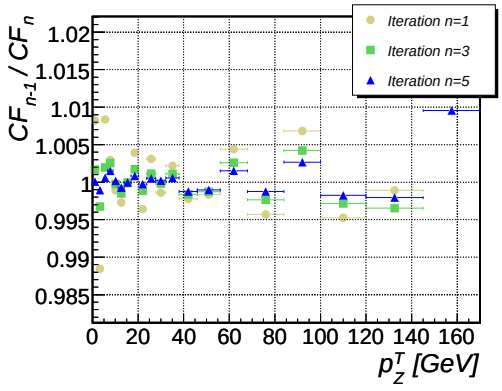

Figure 9.13: Ratio of *correction factors* in step n and step $n-1$ for various iterative steps n.

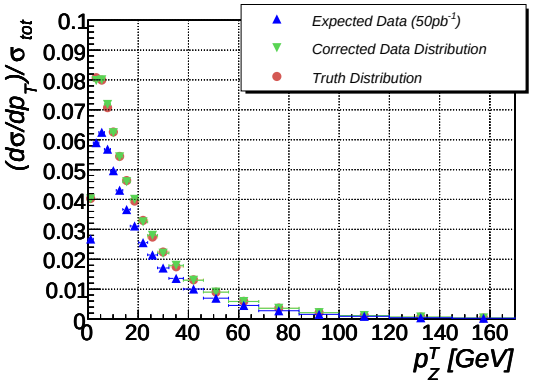

Figure 9.14: p_T^Z-distribution for shifted Monte Carlo simulation, the truth Monte Carlo distribution and the corrected distribution (normalized to the integral of the truth distribution)

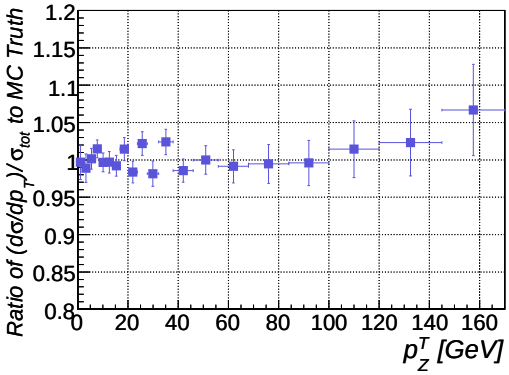

Figure 9.15: Ratio of corrected distribution over truth distribution.

$$N_i^{Reality,n} = \varepsilon_i^{CF,n} \cdot N_i^{Measured}$$

where $N_i^{Measured}$ is the measured number of events in bin i. The variable γ_i^n defined by

$$\gamma_i^n = \frac{N_i^{Reality,n}}{N_i^{MCTruth,n}}$$

will be 1 for each bin i, if the predicted distribution is equal to the distribution in reality. The variables γ_i^n are used to reweight the Monte Carlo truth as well as the corresponding reconstructed p_T^Z for each simulated event. This leads to new values for $N_i^{MCTruth,n+1}$ and $N_i^{MCReco,n+1}$ in step $n+1$. Once this procedure converges, it will lead to the real form of the differential cross section.

As a test of this method, it was chosen to use an additional Monte Carlo sample, where all truth information of the p_T of the decay muons is shifted by 20%. This results in a shifted p_T^Z-distribution, for the Monte Carlo truth and the detector response simulation side. The latter one is used as data sample. The Monte Carlo sample, where no shift was introduced, is

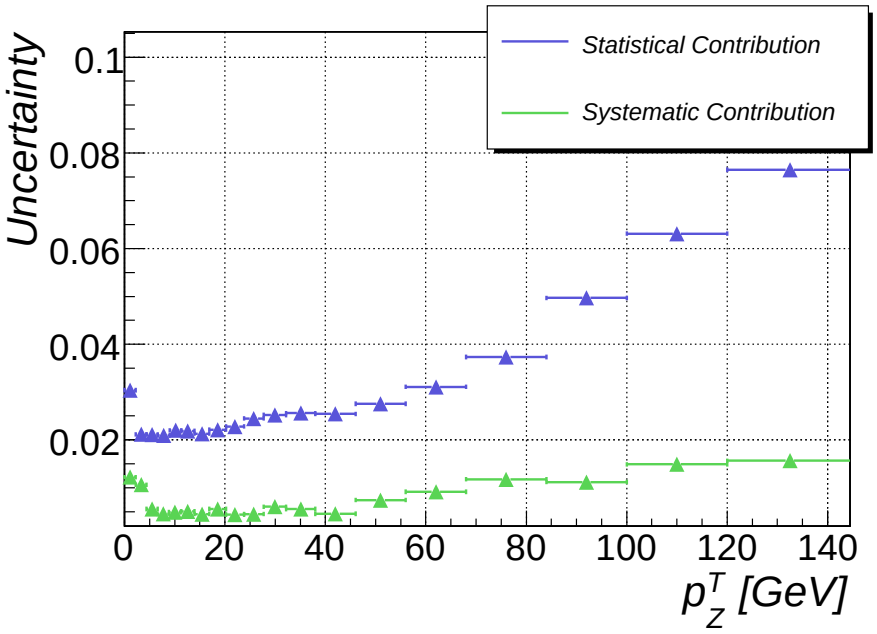

Figure 9.16: Expected systematic and statistical uncertainties for $50 pb^{-1}$.

used as basis for determination of the correction factors $\varepsilon_i^{CF,0}$ in the first iterative step. Figure 9.13 shows the ratio of two succeeding correction factors for several iteration steps. For later iteration steps n, the ratio for all different bins get closer to unity, which is an indication of the convergence of this algorithm.

Figure 9.14 illustrates the resulting distribution after 8 iterations. Figure 9.15 shows the resulting ratios of the corrected and truth distribution, which agree within the statistical uncertainty and no systematic effect can be observed.

9.1.3 Expected Precision

In this section, the final results and the expected precision of the differential cross-section measurement of p_T of the Z boson for an integrated luminosity of $50\,pb^{-1}$ are discussed, having tested the presented methods in the previous sections. Figure 9.16 shows the expected systematic and statistical uncertainty for each bin. It is obvious that the statistical uncertainty is overall dominating and systematic effects can be neglected to a good extend for the assumed integrated luminosity. It is also reasonable to assume, that the statistical uncertainty dominates for far larger integrated luminosities, since also the systematic contribution will get smaller with growing integrated luminosity.

A final test of the method is to treat fully simulated events, corresponding to an expected integrated luminosity of $50\,pb^{-1}$, as data input and the toy simulation, discussed in section 9.1.1, for the determination of the correction factors. The high statistics of $300,000$ events in the toy simulation leads to a negligible statistical uncertainty for the correction factors for each bin. The results are illustrated in Figure 9.17 and 9.18. The Monte Carlo predicted distribution and corrected distribution coincide with their uncertainties. It can be concluded that the differential cross-section measurement can be performed with the methods presented, and that statistical uncertainties will dominate for an integrated luminosity of $50\,pb^{-1}$.

A main systematic contribution to the overall uncertainty in each bin is due to the finite

momentum resolution. In the case of an ideal detector the previous study suggests, that this contribution is under control. In the case of a worse performance of the p_T-reconstruction of muons for real data than it is expected from Monte Carlo simulations, various methods can be applied to improve the p_T-resolution using the fact, that the muons stem from a Z boson. Some of these methods, which can be applied during the first phase of ATLAS are discussed in appendix E.1.

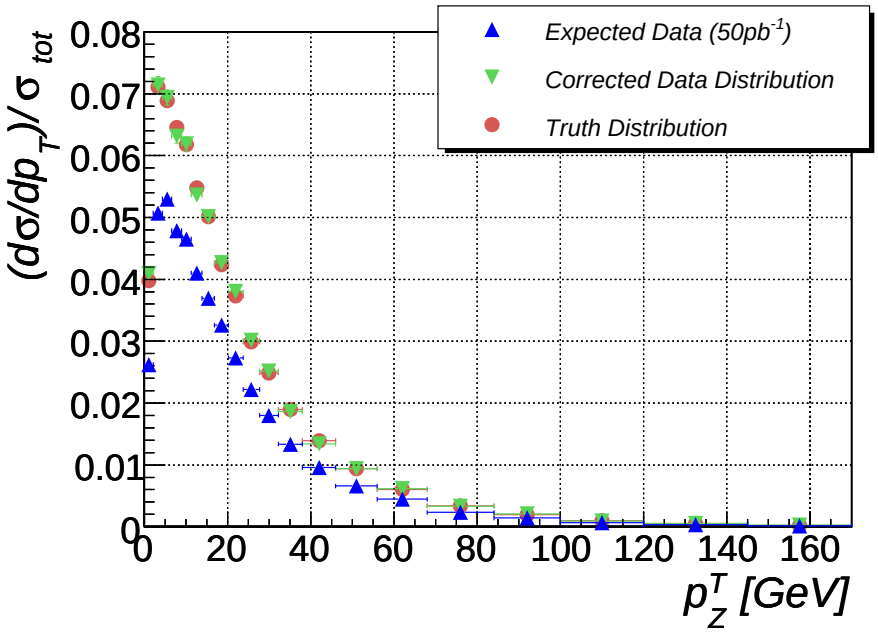

Figure 9.17: p_T^Z-distribution for full Monte Carlo simulation as data, the truth Monte Carlo distribution and the corrected distribution (normalized to the integral of the truth distribution).

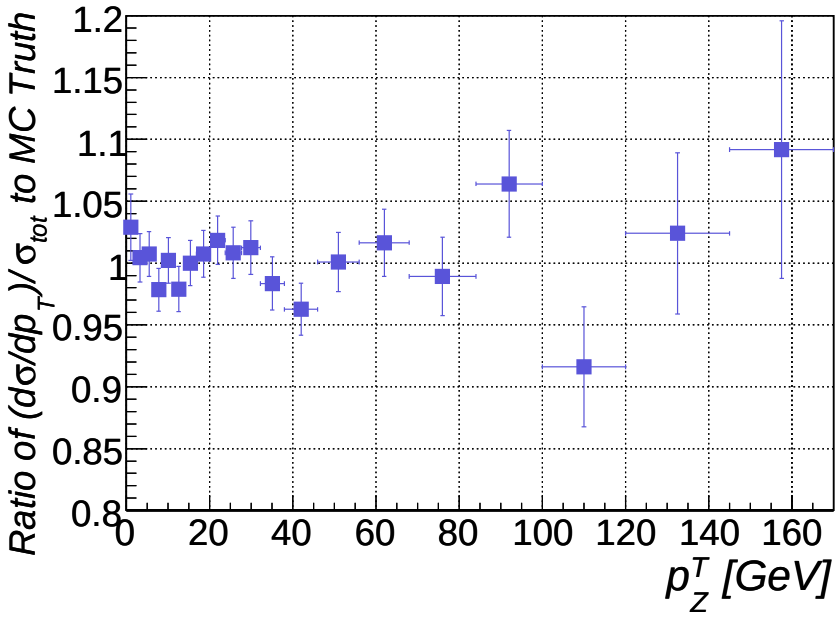

Figure 9.18: Ratio of corrected distribution over truth distribution.

9.2 Observation of the x-Broadening Effect

9.2.1 Theoretical Description of x-Broadening

Measurements at the HERA collider in electron-proton collisions showed a broadening of the transverse momentum distribution of the W and the Z boson [23] in a small x region ($x = 10^{-4} - 10^{-2}$). Current theoretical studies used these results to predict the so-called x-broadening for the production of the W and Z boson in hadron-hadron collision at the Tevatron collider and the LHC [77].

The predictions of these effects are based on the universality of soft and collinear radiative corrections, which dominate the semi-inclusive deep inelastic scattering energy flow data for transverse momenta of the vector boson below $2\,GeV^2$. The basic idea is to modify the phenomenological parameterization for the small cross section for vector bosons with small transverse momenta in order to predict the behavior for the small x-region ($x \lesssim 10^{-2}$). The modified form of the Drell-Yan resumed form factor [77] for $x \lesssim 10^{-2}$ is given by

$$\tilde{W}(b,Q) = \tilde{W}_{BLNY}(b,Q)e^{-\rho(x_A)b^2-\rho(x_B)b^2} \tag{9.7}$$

where $\tilde{W}_{BLNY}(b,Q)$ is the resummed form factor, which has been determined by a global fit to Drell-Yan data [78] and the exponential part parameterizes the x-broadening. The variable Q describes the virtuality of the vector boson and b is the impact parameter.

It is expected that the x-broadening effect for the p_T-distribution of the Z boson can be observed at the Tevatron collider by requiring a cut on the η of the muons, i.e. a cut on the rapidity of the Z boson. This requirement is necessary to probe small x-ranges (Figure 9.19), since the rapidity of a produced Z boson is correlated with the x-values of the two partons. Larger rapidities enhance small values for x. Such a cut is not required at LHC energies due to the seven times higher collision energies. Figure 9.20 illustrates the differential cross section of the transverse momentum of the Z boson for the case of no x-broadening and the theoretically predicted x-broadening effect. In the following it has been studied if this effect can be observed within first data, e.g. an integrated luminosity of $50\,pb^{-1}$.

[2]Detailed reference can be found in [77].

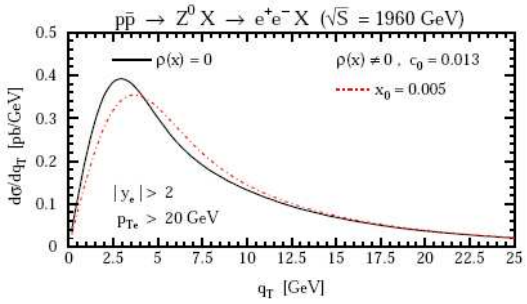

Figure 9.19: Theoretically expected shift of the p_T-spectrum of the Z boson at Tevatron, requiring $\eta > 2$ for both muons (Taken from [77]).

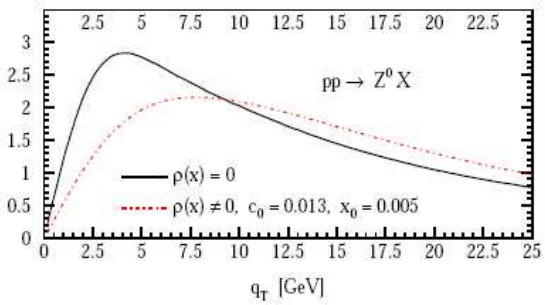

Figure 9.20: Theoretically expected shift of the p_T-spectrum of the Z boson at LHC (Taken from [77]).

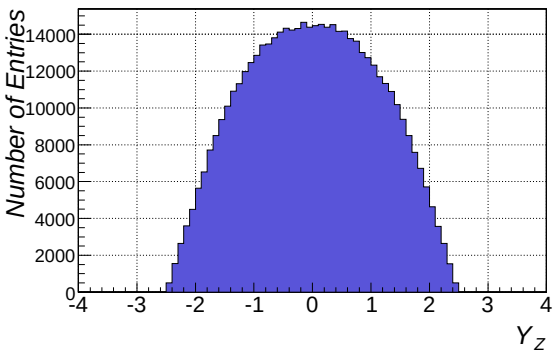

Figure 9.21: Expected rapidity distribution of the Z boson requiring $|\eta| < 2.5$ for both muons.

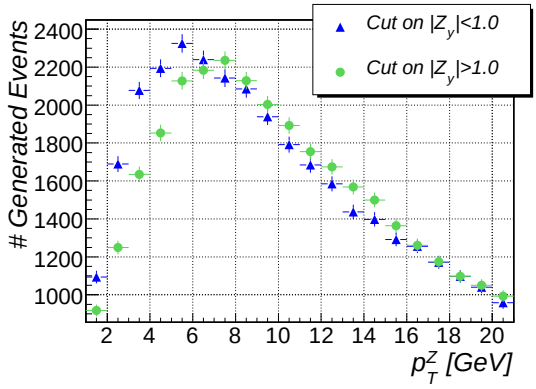

Figure 9.22: Comparison of the generated Z boson p_T distributions for $y_Z < 1.0$ and $y_Z > 1.0$ including the x-broadening effect.

9.2.2 Proposed Method

One possible way to discover a possible x-broadening effect is to compare the corrected data-distribution to the theoretical prediction of two models, one with x-broadening and one without x-broadening. The disadvantage of this approach is, that the coincidence of two distributions might not be caused by a physical effect but by not understood systematic effects. Therefore we suggest to make use of the Z rapidity y_Z dependence on the x-broadening effect and compare two distributions based on data samples with different Z rapidities y_Z. The expected Z rapidity of reconstructed events is shown in Figure 9.21, requiring two reconstructed muons with $\eta < 2.5$. Two roughly equally sized samples will be defined by requiring $|y_Z| < 1.0$ for the first and $|y_Z| > 1.0$ for the second sub-sample. All systematic effects which do not depend on y_Z have the same effect on both sub-sample, so a larger x-broadening effect is expected for the second sub-sample, as mentioned in section 9.2.1. Figure 9.22 shows the theoretical prediction of both sub-samples using the ResBos Monte Carlo generator [32,33]. It should be noted that the spectrum corresponding the sub sample defined by $|y_Z| > 1.0$ is broadened and has a shifted maximum, which will be labeled as $p_{T,\max}^Z$ in the following.

The suggested approach allows a direct comparison of data-based samples and does not rely on a specific theoretical model. The x-broadening effect is disfavored, if the corrected distributions of both sub-samples agree within their uncertainties. A significant difference in the expected direction, i.e. a shift of $p_{T,\max}^Z$ to higher values, might be a first indication of the effect.

Defining more sub-samples by different cuts on y_Z allows a more detailed study of expected correlations between y_Z, x and $p_{T,\max}^Z$, respectively. Obviously the number of sub-samples is limited by the statistics of data. The basic idea is to determine $p_{T,\max}^Z$ for the different samples and prove the systematic increase for sub-samples containing Z boson with larger rapidities. The determination of $p_{T,\max}^Z$ is achieved by fitting a phenomenological parameterization $f_{\text{Z-max}}$ to the p_T^Z-distribution. The function $f_{\text{Z-max}}$ was chosen the be

$$f_{\text{Z-max}} = A_1 \cdot \frac{1}{1 + \beta \cdot e^{-\sigma_1 \cdot (x - x_m)}} \cdot e^{-\sigma_2 x} \tag{9.8}$$

as a Fermi-function multiplied with a exponential decay, with five fit-parameters A_1, σ_1, x_m, σ_2 and β. Figure 9.23 illustrates the fit of $f_{\text{Z-max}}$ to the theoretical predicted p_T^Z-distribution of the ResBos Monte Carlo generator in the case of no x-broadening effect. It can be seen, that

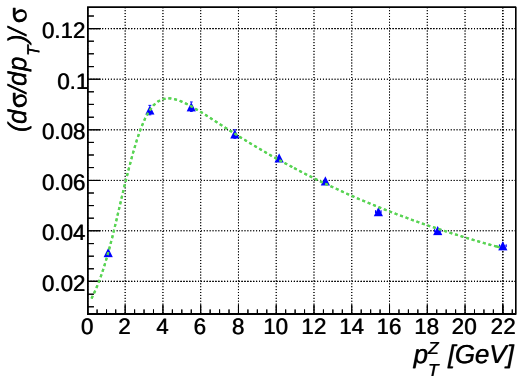

Figure 9.23: Illustration of the fit of $f_{\text{Z-max}}$ to the theoretical predicted p_T^Z-distribution of the ResBos Monte Carlo generator in the case of no x-broadening effect.

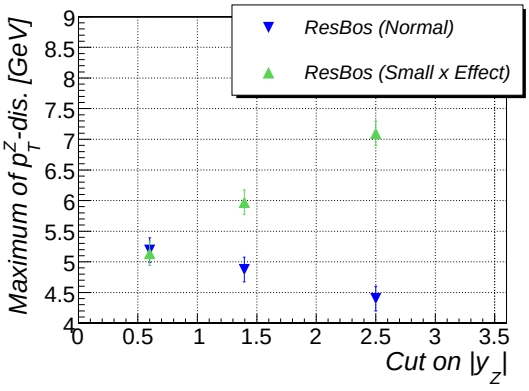

Figure 9.24: Comparison of $p_{T,\text{max}}^Z$ for different cut-regions on $|y_Z|$ for the theoretical prediction by ResBos with and without the x-broadening effect corresponding to $\int \mathscr{L} = 50\,pb^{-1}$.

the function describes the predicted distribution very well for transverse momenta between $0\,GeV$ and $20\,GeV$. The maximum of $f_{\text{Z-max}}$ can then be determined straight forward and can be understood as the $p_{T,\text{max}}^Z$. In the following it was chosen to define three sub-samples by $|y_Z| < 0.6$, $0.6 < |y_Z| < 1.4$ and $1.4 < |y_Z|$ which contain also roughly the same number of Z boson events.

A more powerful evidence of the effect is the expected dependence of $p_{T,\text{max}}^Z$ on the $|y_Z|$-cut, which is shown in Figure 9.24 for two different theoretical models with and without the x-broadening effect. Two things should be noted: First of all, there is good agreement between the two models for small Z boson rapidities, since in this case, the x-broadening effect is expected to be very small. Secondly, a significant difference can be seen for the other two cut-regions. Hence, the measurement of $p_{T,\text{max}}^Z$ could reveal the x-broadening effect in more detail.

9.2.3 Observation Significance

Since the ResBos Monte Carlo Generator is not yet implemented in the Athena software framework, it was decided to simulate the detector response within the *Toy Monte Carlo* approach. It is obvious that the iterative *Bin-by-Bin*-approach must be applied to data, since the naive theoretical prediction of the Monte-Carlo samples might differ from reality in case of the x-broadening effect. The bin-by-bin correction factors have been determined also within the *Toy Monte Carlo* simulation, but are based on a simple Pythia generator sample. Figure 9.27 and Figure 9.28 show the comparison of the predicted p_T^Z-distribution and the bin-by-bin corrected simulated data distribution for the two cases, i.e. $|y_Z| < 1.0$ and $|y_Z| > 1.0$, respectively. The uncertainties shown include the predicted systematic and statistical uncertainties for an integrated luminosity of $50\,pb^{-1}$. The corrected data distribution and the theoretical prediction agree for both cases.

Figure 9.25 shows the comparison of the corrected data distributions for the two cases. The expected difference is observable. To quantify the difference a Kolmogorov test, which probes the probability that two distributions coincide within their given uncertainties, has been applied. The resulting probability is $3.0 \cdot 10^{-9}$. This disagreement of these two distributions would be a strong hint to the observation of the x-broadening effect, but might be also caused by other uncertainties of the PDFs. A more powerful indication of the effect is the expected

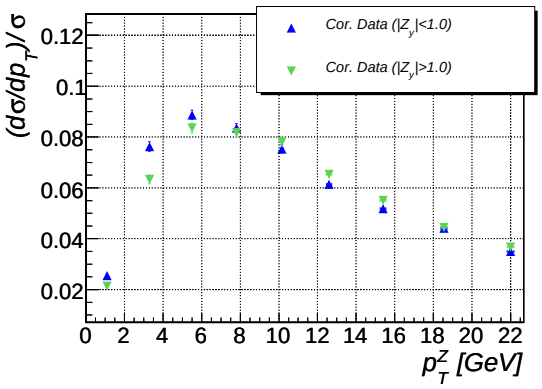

Figure 9.25: Comparison of the simulated and corrected p_T^Z data distributions for two data sets with $|y_Z| < 1.0$ and $|y_Z| > 1.0$, respectively.

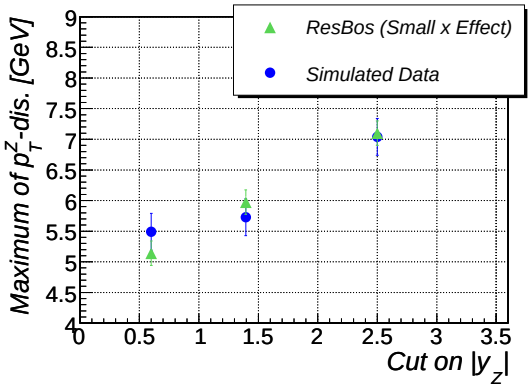

Figure 9.26: Comparison of $p_{T,\max}^Z$ for different cut-regions on $|y_Z|$ for the theoretical prediction by ResBos with x-broadening effect and simulated data.

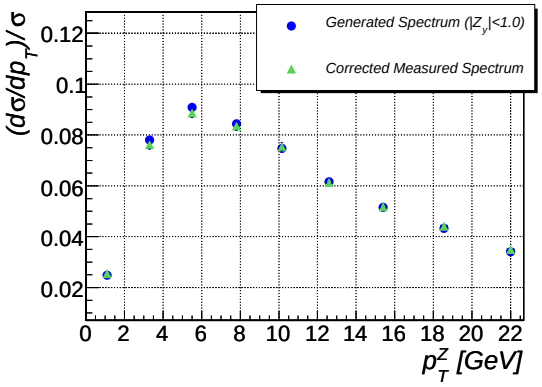

Figure 9.27: Comparison of the simulated and corrected p_T^Z data distribution and the theoretical prediction for events with $|y_Z| < 1.0$.

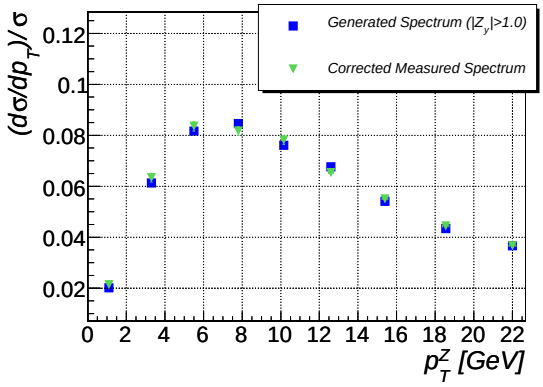

Figure 9.28: Comparison of the simulated and corrected p_T^Z data distribution and the theoretical prediction for events with $|y_Z| > 1.0$.

dependence of $p_{T,\max}^Z$ on the $|y_Z|$-cut, which is shown in Figure 9.26 for the theoretical model and the simulated data, where both includes the x-broadening effect. A good agreement within the given uncertainties can be observed. Hence, it is likely that the x-broadening effect, if existing, can be observed by the ATLAS experiment with rather early data.

A higher granularity for the $|y_Z|$-cut bins can be chosen for higher integrated luminosities. This allows an even more detailed study of the dependence of the p_T^Z-distribution on the rapidity y_Z, which could constrain various parameters of Equation (9.7).

"Nobody cares about your method. People remember only your last number."

S.C.C. Ting[1]

Chapter 10

Conclusion and Outlook

The measurement of the cross-section σ for the process $pp \to Z/\gamma^* \to \mu^+\mu^-$ will be amongst the earliest conducted with the ATLAS detector.

For this measurement it is crucial to understand the response of the ATLAS detector, especially the Muon Spectrometer, which is responsible for the identification and the precise measurement of highly energetic muons. The simulation of MDT chambers, which are responsible for the precise muon tracking, has been validated by measurements using cosmic muons at the Cosmic Ray Measurement Facility in Garching, Germany.

One of the largest impact on the Muon Spectrometer performance during the start-up phase of ATLAS, are possible misalignments, i.e. misplacements of detector elements. The impact of a misaligned Muon Spectrometer layout, which is assumed to model real misplacements at the beginning of the experiment, on the reconstruction efficiency was found to be small ($< 0.5\%$), while a strong degradation of the p_T-resolution could be observed.

During the data taking period, it will be essential to determine the Muon Spectrometer performance using recorded data in order not to rely on Monte Carlo predictions. Several methods have been developed and discussed in the context of the total cross-section measurement of $pp \to Z/\gamma^* \to \mu^+\mu^-$.

A measurement strategy of the cross section σ for the process $pp \to Z/\gamma^* \to \mu^+\mu^-$ at the ATLAS experiment during its startup phase has been presented. This strategy is tuned for an integrated luminosity of $50\,pb^{-1}$ but can easily be adjusted for later periods of the experiment. A precision of

$$\frac{\Delta\sigma}{\sigma} \approx 0.006(\text{stat}) \pm 0.008(\text{sys})\, ^{+0.016}_{-0.008}(\text{pdf}) + \text{Luminosity Uncertainty}$$

is expected, assuming a fully operational ATLAS detector, not including uncertainties of the luminosity measurements. The given systematic uncertainties arise from imperfect knowledge

1 Samuel Chao Chung Ting was born in Michigan, USA, in 1936 but grew up in China. During his career, he work at CERN and at DESY and became professor at MIT in 1969. He received the Nobel Prize together with Burton Richter in 1976 for the discovery of the J/Ψ-particle.

of the detector and of possible background contributions. It was a major goal of the presented approach to minimize the dependence on Monte Carlo simulations. Hence, several methods for the determination of the detector response based on recorded data have been studied. Detector efficiencies, like the muon reconstruction efficiency, are suggested to be determined with the so-called 'tag and probe' technique. The reconstructed Z boson mass distribution is suggested to determine the transverse momentum resolution of the ATLAS detector and its subsystems. Moreover, various methods for the estimation of background processes are introduced and discussed. Special attention was given to the systematic uncertainties of these methods.

The differential cross-section measurement $\frac{d\sigma}{dp_T^Z}$ of the transverse momentum of the Z boson has also been discussed in this thesis. The presented approach focused also on the first data taking period and is expected to be at least valid to an integrated luminosity of $50\,pb^{-1}$. The statistical uncertainty is expected to dominate when measuring the differential cross section during this first data taking period. Systematic contributions are expected to become dominant for far larger integrated luminosities ($\approx 200 pb^{-1}$). The predicted high p_T resolution of the ATLAS Inner Detector and the Muon Spectrometer allows the observation of the so-called x-broadening effect even with the first recorded data.

ATLAS will measure the first proton-proton collision with a center of mass energy of $14\,TeV$ in 2008. The proposed methods largely avoid Monte Carlo predictions and are developed to be based on measured data only. Hence, they can be used for the early measurement of Z boson production cross section in a new energy domain. The observation of the x-broadening effect is only a starting point of the potential of the ATLAS detector and it is hoped that striking discoveries will follow in the succeeding years.

"Nothing is impossible for the man who doesn't have to do the work."

Weiler's law

Appendix A

Muon Software Validation

The validation of the Muon Spectrometer software (i.e. the geometrical description, the digitization and the reconstruction algorithms) is not only crucial for the presented physics analysis, but also for the whole ATLAS muon working group as a performance measure for new developments in the underlying software. Hence a significant part of this thesis was to develop an automatic validation software package, which is briefly introduced in section A.2.

Section A.1 is dedicated to the detection and removal of clashes in the geometry description of the ATLAS Muon Spectrometer, which was the basis for the implementation of a realistic Muon Spectrometer layout, i.e. a layout where the different components can be shifted and rotated by small amounts.

A.1 Detection of Geometry Clashes

The Muon Spectrometer Detector Description system has undergone specific visual debugging during in 2005, addressed to the detection of geometrical conflicts among the volumes. The detection of the overlaps is complicated by the complexity of the geometry of the Muon Spectrometer. However their removal has been especially crucial to allow, where possible, tolerance between components in view of the chamber misalignment inclusion. Chamber conflicts can cause unpredictable behavior by the simulation, from job crashes to subtle changes to particle multiplicity and physics effects.

The volume clashes can be classified into three different types (see Figure A.1):

- **Overshootings**: when a given volume (A in Figure A.1) sticks outside its mother volume
- **Overlappings**: when two daughter volumes overlap (A and B, or C and D)
- **Solids**: when a solid volume has one or more null dimension(s)

Geant4 has a dedicated tool, the `recursive_test`, which recursively loops over the full volume tree detecting the overlaps, and dumps a list of the conflicts and their positions in different systems of reference. The *Geant4* visualization tools then help to check the clashes, once it is clear where and between which volumes they occur.

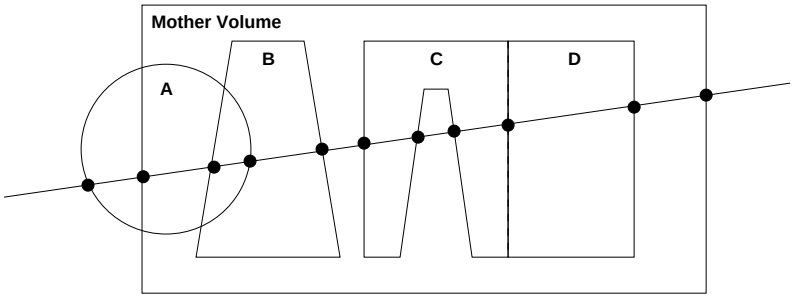

Figure A.1: Representation of the three different types of clashes between volumes. Overlapping errors: between A and the mother volume. Overshooting errors: between the two daughter volumes A and B, or C and D. Solid errors are not represented here, they correspond to the situation when one or more dimension(s) defining the solid volumes happen to be null.

ATHENA release	*11.0.4*	*12.0.3*
Overlappings	266673	1358
Overshootings	5763	1772

Table A.1: Amount of clashes at the time of the first check on the geometry (first column) and after the massive clash cleaning (second column).

By intensively applying this procedure, a sensible reduction of the clashes has been gained. Table A.1 shows the amount of volume conflicts at the time of the first check (MUONGEOMODEL-00-02-47, ATHENA release 11.0.4) and the current status at the current time (MUONGEOMODEL-00-02-69, ATHENA release 12.0.3).

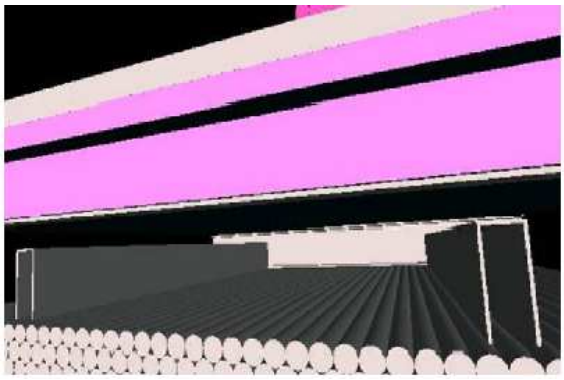

Figure A.2: For all the BMF chambers, clash of the longbeam volumes of the chamber spacer with the chamber multilayers.

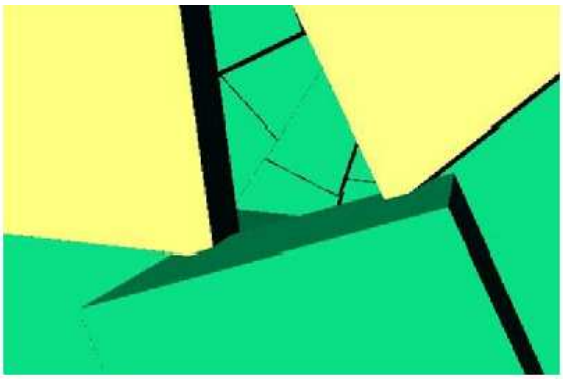

Figure A.3: Overlappings of the EIS1 chamber with CSL1 chamber. This was due to the fact that CSL stations had no *coffin shape* at this stage of implementation.

In the following, some of the solved overlaps are shown. A detailed documentation of the clash removal can be found under [79]. The few surviving clashes, listed for database `R_Light` in Table A.2, are strictly related to *GeoModel* functionality. They, anyway, have been proven not to spoil the robustness of the simulation.

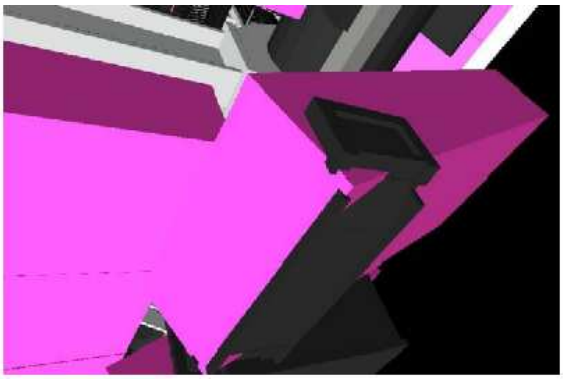

Figure A.4: BOF and StdFeetGirder clash.

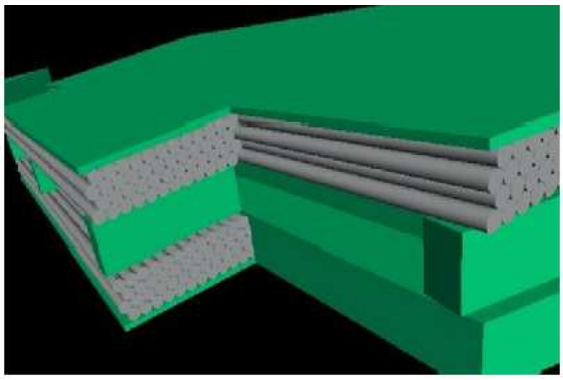

Figure A.5: Overlapping of the EIL8 and the EIL9 stations. This clash has been solved by modifying the database in order to create some clearance between the chambers.

Overlappings	BMS, BOF and BOG chamber overlapping with the Feet and the Barrel Toroids CSL1 and EIS1 station overlapping Feet and BT overlapping BMF and E* chambers overlapping with the Spacer and MultiLayer components
Overshootings	components of the BOG, CSL, CSS and of all the endcap chambers extending outside the mother volume

Table A.2: List of the remaining clashes in MuonGeoModel-00-02-69 and following, after the massive debugging. They cannot be trivially solved, since they depend on *GeoModel* functionality. The star (*) denotes any type of endcap chambers.

A.2 The MuonValidation Package

The aim of the `MuonValidation` package is threefold:

- to ensure the compatibility and reproducibility of data samples produced at different sites (site validation)
- to monitor the changes and the improvements of the ATLAS detector geometry and simulation by means of a detailed check on an event by event basis, for each step in the muon software chain;
- to check the physics content of the generated samples (physics validation), the top priority for the ATLAS Computing system commissioning phase.

The structure of the `MuonValidation` applications, which is part of the ATLAS offline software, is shown in Figure A.6.

The quality of the simulation and digitization procedures can be monitored by histogramming various characteristic and properties of the hit and digits objects. Two validation algorithms have been created to produce an Athena-Aware Ntuple (AANtuple) [80] running on the simulation or digitization output files. The `MuonHitTest` and `MuonDigitTest` algorithms,

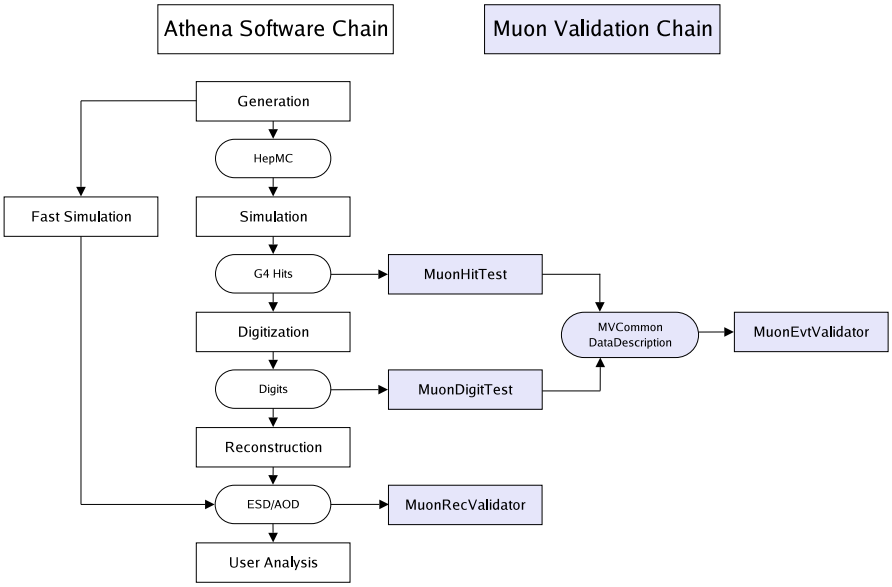

Figure A.6: Schematic representation of the MuonValidationChain.

have been designed to perform checks and validation of the muon hit objects and and muon digit objects, for each muon technology.

The `MuonEvtValidator` algorithm has been designed as an interface to easily compare the outcome information of `MuonHitTest` and `MuonDigitTest`. The main advantage of this interface structure is its flexibility, being independent from the original format of the input information. This allows not only the validation of simulation and digitization, but also the validation of different ATHENA releases or/and Muon Spectrometer geometries and, in future, the validation of cosmic data or real physics data. The `MuonEvtValidator` algorithms compares the contents of two input files, using relevant variables:

- the total number of hits/digits per station; this allows an identification of inefficiencies when assuming the same number of events in each input collection.
- the average number of hits/digits per station and per event; this allows a detection of these inefficiencies but is independent from the number of events in each input collection.

The validation variables are calculated at station level. The main part of the whole package is therefore the `MVCommonStationData` class which represents the parameters unique to a station (e.g. η, ϕ, `StationNameID` identifier), together with its hits and digits information on an event by event basis.

The underlying ATHENA algorithm of the `MuonEvtValidator` package is the `MVCombined` class. In a first step, the input information of the packages `MuonHitTest` and `MuonDigitTest` are read and distributed in the corresponding `MVCommonStationData` objects. In a second step all validation plots are created by various loops over the station identifiers using the `MVCommonStationData` methods to retrieve the necessary validation information. The validation plots are created via the `MSRootInterface` class which provides different tools for the creation of formatted ROOT graphs and histograms inside the ATHENA software framework.

The overall structure of this algorithm allows also an easy way to compare distributions of hits or digits for different versions, since the internal representations of hits and digits

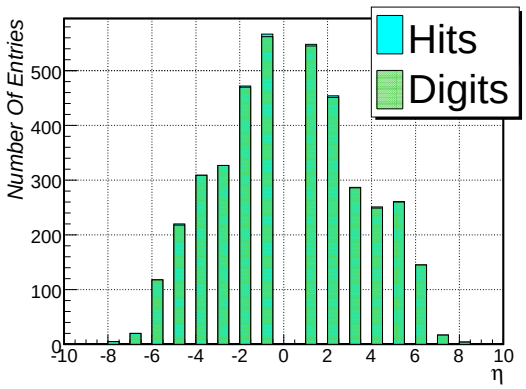

Figure A.7: Comparison of the overall number of MDT *hits* and *digits* versus η identifier.

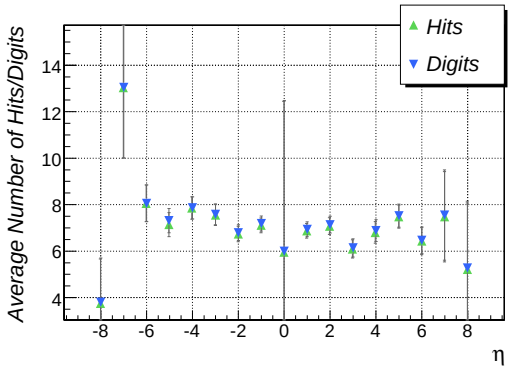

Figure A.8: Comparison of the average number of MDT *hits* and *digits* per event versus η identifier.

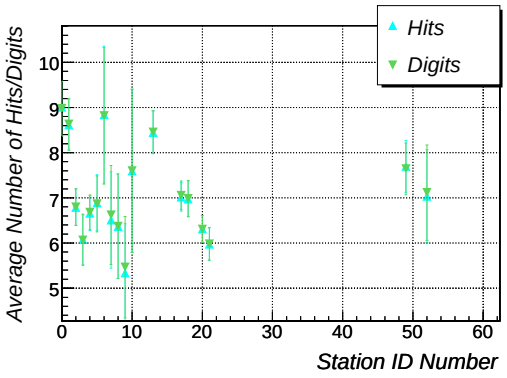

Figure A.9: Comparison of the overall number of MDT *hits* and *digits* for 1K events versus station name identifier.

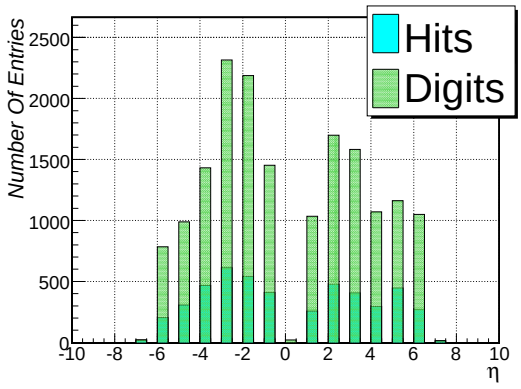

Figure A.10: Comparison of the overall number of RPC *hits* and *digits* per event versus station name identifier.

are identical. Therefore it makes no difference for the package if one input file contains hit information while the other input file contains digit information, or if both input files contain the same sort of data.

Based on the same procedure, the `MuonRecValidator` algorithm validates reconstructed `AOD` files [81]. It generates plots of the main performance variables, as functions of η, ϕ and p_T. Its design allows comparison between different reconstruction algorithms, as well as between Muon Spectrometer geometries of ATHENA releases.

The `MuonRecValidator` package uses the features of the Run Time Tester (RTT) framework [82] to monitor the basic functionality of the package and the most meaningful comparisons. The RTT allows one to define a series of tests to be performed automatically at each nightly build of the ATLAS offline software. This series of tests is standardized and rapidly applicable on every new release. It is a powerful automatic tool to identify and detect bugs and problems.

A.2.1 Simulation and Digitization Validation Results

Some control plots for the simulation and the digitization using a single muon sample[1] are shown in Figures from A.11 to A.14. These plots can be generated by running the

[1]Single muons with $p_T = 50$ GeV/c, ATHENA-Release 12.0.3, ATLAS-DC3-01 Detector Description.

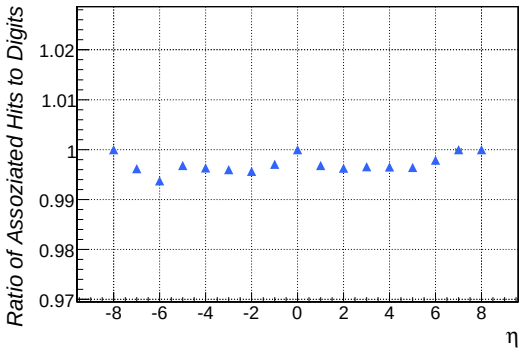

Figure A.11: Association probability of MDT *digits* to *hits* for 1K events versus η identifier.

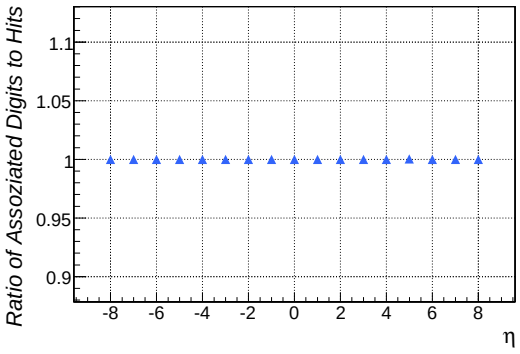

Figure A.12: Association probability of MDT *hits* to *digits* for 1K events versus η identifier.

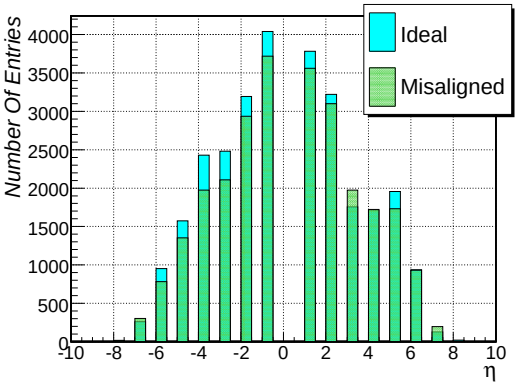

Figure A.13: Comparison of the overall number of MDT *digits* for two different geometries versus η identifier.

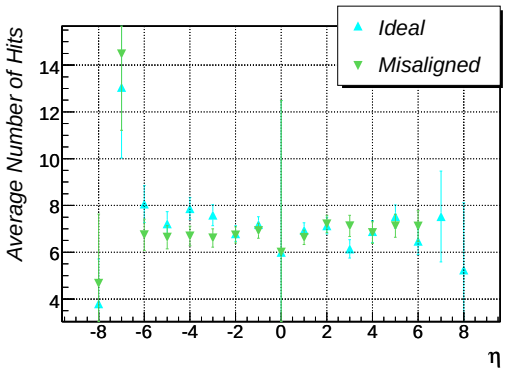

Figure A.14: Comparison of the average number of MDT *digits* for two different geometries per event versus η identifier.

`MuonEvtValidator` package inside the ATHENA software framework[2].

In these Figures, which refer to ATHENA version `12.0.3`, no significant differences in term of the overall number and the average number of hits and digits can be seen for the MDT chambers. Good agreement is expected since the algorithm prevents double-counting of hits in one tube per event.

More hits than digits are expected for MDT chambers, since muons interact with the gas inside one MDT tube several times when passing through. Only one hit per tube and event is thus accepted for the validation step at the MDT level and secondary hits are neglected. These quantities are calculated for each station separately as well as for all stations with the same η, ϕ and `StationNameId`. The latter choice is done since the number of stations is too large to be compared one by one effectively. Not only the hits/digits multiplicity comparison might be used as a validation quantity. The absolute value of the average number of digits per event for a given station type is also of interest: e.g. BOS stations consist of two multilayers with three tubes each. We expect roughly six digits per muon passing through one BOS station, which is perfectly consistent with the average value shown in Figure A.9 (The station name identifier for BOS stations is 5).

The validation procedure of RPC, TGC and CSC chambers is more complicated, since their structure implies that one hit in a simulation step can lead to several digits. This explains the large excess of digits shown in Figure A.10. A more detailed validation of these chambers

[2]https://twiki.cern.ch/twiki/bin/view/Atlas/AtlasComputing?topic=MuonRecValidator

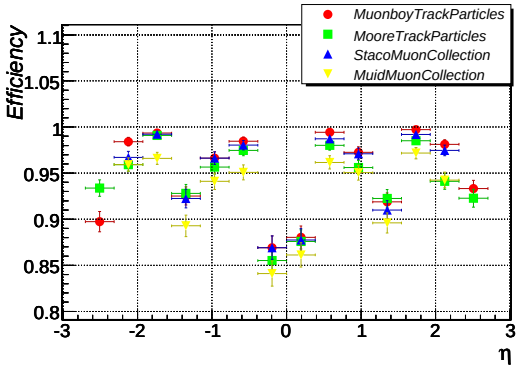

Figure A.15: Efficiency of different reconstruction algorithms for 50 GeV simulated muons vs η.

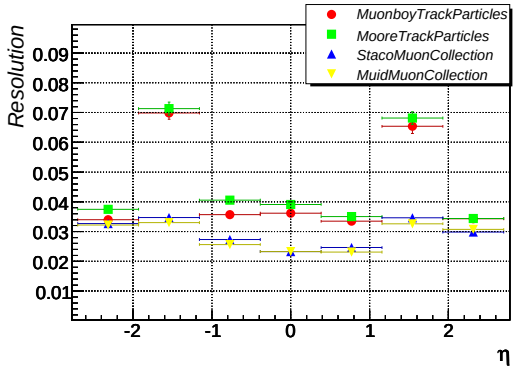

Figure A.16: p_T Resolution of different reconstruction algorithms for 50 GeV simulated muons vs η.

can be achieved by comparing the results of different ATHENA software releases.

With the variables defined so far, only inefficiencies on the station but not on lower levels, e.g. on the tube level for MDT stations, can be detected. The package `MuonEvtValidator` provides also important validation plots at lower levels, which is described in the following by the example of MDT chambers. If no inefficiencies at the MDT tube level are assumed, it is expected that each digit has a parent hit at simulation level. The inverse association is not that trivial since some hits might not be digitized for different reasons. Figures A.11 and A.12 show the association-probability for the above sample.

It can clearly be seen here that the association probability for digits to hits is 100% as expected. The inverse association probability is less than 100%, which is a hint that not all hits gets digitized. This explains the small excess of hits seen in Figure A.9.

The `MuonEvtValidator` package provides not only a comparison functionality of the simulated and digitized data, but also the validation of the hit or digit information throughout different ATHENA releases and Muon Spectrometer geometries. In Figures A.13 and A.14 the comparison of the digit information for two different Muon Spectrometer geometries is shown. Both input data are based on the same generator file, but simulated and digitized with different Muon Spectrometer geometries. The first geometry layout (labeled as *Ideal*) describes the ideal positioning of the chambers, while the second layout describes a misaligned Muon Spectrometer (labeled as *Misaligned*). The positions of the all chambers are shifted randomly on average by 1 mm in each direction and are tilted by 1 mrad for each angle in the second case.

We see a larger amount of *digits* in the *ideal* than in the *misaligned* layout, which might be due to overlapping of chambers in the latter case. No significant difference can be seen for RPC, CSC and TGC stations.

A.2.2 Validation of Muon Reconstruction

As already mentioned, the performance evaluation of the Muon Spectrometers is mainly based on terms of *efficiency*, *fake-rate* and *resolution*, which have been defined in section 5.

Figures A.15 and A.16 show a excerpt of the control plots generated by the `MuonRecValidator` package. The bin size of these variables can be specified via a *jobOptions file*. Different muon reconstruction algorithms for the same simulated events are compared for a 50 *GeV* single muon sample. The combined reconstruction algorithms have a lower efficiency than

the standalone Muon Spectrometer based algorithms but also a lower fake rate, as naively expected. Further control plots, like χ^2-distributions or impact parameter resolutions are also automatically produced within the `MuonRecValidator` package.

The p_T resolution is significantly worse for standalone reconstruction algorithms between $1 < |\eta| < 2$ which corresponds to the overlap of barrel and endcap region of the Muon Spectrometer.

The `MuonRecValidator` package allows also to compare the performance variables for two different input files, e.g. reconstructed with different ATHENA software releases.

"Experience is that marvelous thing that enables you to recognise a mistake when you make it again."

F.P.Jones

Appendix B

Study of the Sagitta Resolution of MDT-Chambers with Cosmic Muons

B.1 Sagitta study for the Cosmic Ray Measurement Facility

B.1.1 Definitions and Algorithms

An incident cosmic muon passes six multilayers - two multilayers per chamber - on its way through the measurement facility, which was already introduced in chapter 6. This corresponds in the ideal case to 18 measured drift circles. The aim is to fit a parabola tangential to these 18 drift circles which could be done by the χ^2-method. The χ^2-algorithm finds parameters for a given function that minimizes the distances of the function to the drift circles. In this case the parameters a,b and c of a parabola $f(x) = ax^2 + bx + c$ have to be found.

Since there is no magnetic field and the measured cosmic muons have high momentum ($\geq 600\,MeV$), small sagittae in comparison with the arc length are expected. In this limit the circle can be well approximated by a parabola. In order to achieve an optimal approximation by a parabola, a transformation of the global coordinate system into a new coordinate system, whose x-axis is defined to be parallel to the slope of the incoming muon as shown in Figure B.1, is performed. This ensures that the vertex of the parabola is placed in the center of the measured muon track section. The slope of the incident muon is determined by a simple straight line fit to the measured drift circles.

Figure B.2 shows schematically a parabola which has been fitted to the measured drift circles. The intersections of the parabola and the center planes of the reference chambers at $z_1 = 570\,mm$ and $z_2 = -570\,mm$ define an arc segment which is the basis for the definition of the sagitta.

The ambiguities of fitting a function to the drift circles lead to local minima, since the χ^2 of the fitted function gets minimal on both sides for each drift circle. Clearly only one side corresponds to the real muon track. One possible solution to that problem is to ignore the

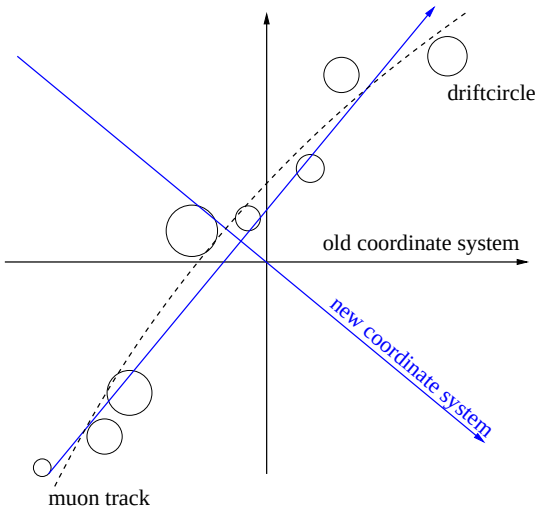

Figure B.1: Approximation of a track with a parabola

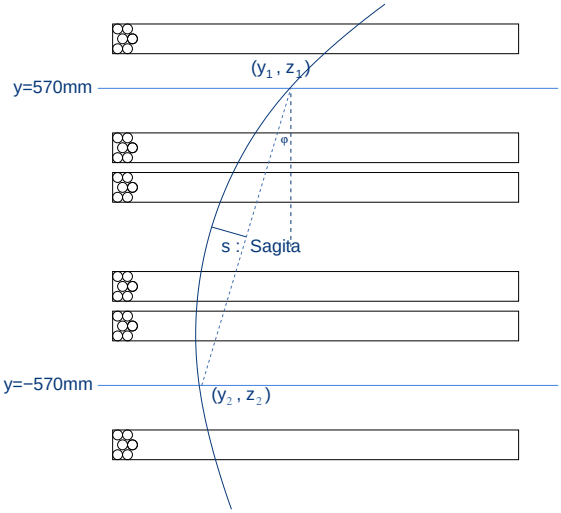

Figure B.2: Definition of Sagitta at the cosmic ray measurement facility

drift-radius-information in a first step and fit the parabola only to the centers of the drift-circles. The aim of this procedure is to find suitable starting parameters of the fitting function that should lie on the correct side of the drift-circles. These parameters are used as starting-values for a second fit which makes use of the drift-radius information. A Monte-Carlo study of this method shows that the chance of finding only a local minimum could be reduced from 2.8% to 1.1%.

In the following the overall procedure from data to the measured sagitta is summarized:

1. Apply pattern recognition to identify the drift circles which correspond to an incident muon and generate a group of drift circles.
2. Fit a straight line to the centers of the drift circles in order to measure the slope of the incident muon. Rotate the coordinates of the drift circles so that their x-axis is parallel to the measured slope.
3. Fit a parabola to the centers of the drift circles.
4. Delete the drift circles out of the group which have a minimal distance of more than 18 mm from the fitted parabola. These drift circles were wrongly identified by the pattern recognition.
5. Optimize the parabola fit of step 3 by using the drift radius information to reduce the problem of finding only a local minimum solution
6. Calculate the relative residuum R_σ of each drift circle

$$R_\sigma = \frac{r_{dc} - r_p}{\sigma}$$

   where r_{dc} is the radius of the drift circle, r_p is the minimal distance of the drift circle to the fitted parabola and σ is the error on the measured drift circle.
7. Delete the drift circle with the largest R_σ from the group and repeat step 3.
8. Calculate the corresponding sagitta, if there are at least 16 drift circles left in the group

Step 7 is optional since no significant change in the measured sagitta resolution was observed. This step was introduced to minimize δ-electron effects. It was also tested to neglect hits which were close to the wire, since the measured drift radius has a large error, but also here no significant change on the sagitta distribution could be observed. It turned out that some tubes have significantly more hits with $R_\sigma > 10$ than all others. This is a hint to a systematic error e.g. due to noise and therefore signals from these tubes were neglected during this study.

B.1.2 Geant4 Simulation of the Cosmic Ray Measurement Facility

The simulation of the cosmic ray measurement facility (CMF-Simulation) is based on Geant4 and was fully implemented within the ATHENA framework. One should note that an implementation of the GeoModel description [56] of the measurement facility and the digitization part of simulation was developed, which is independent of the meanwhile existing implementation in the official ATLAS muon software release. The ATHENA package *Cosmic Generator* was used to generate cosmic muons with the correct energy and momentum spectrum.

Furthermore, all aspects of the simulation were validated to be properly implemented: It was reviewed that the simulation uses the correct rt-relation and single tube resolution and also takes into account the flight time of the muons and the signal propagation along the wire. In addition, further details such as wire-sagging were implemented.

B.1.3 Theoretical Expected Resolutions

Theoretical Estimation of Sagitta Resolution at the Cosmic Ray Measurement Facility

The expected sagitta resolution of the CMF δs_{CMF} is determined by the single tube resolution and multiple scattering effects. The overall resolution is therefore given by

$$\delta s_{CMF} = \sqrt{\delta s^2_{Drifttube} + \delta s^2_{MultipleScattering}} \tag{B.1}$$

The magnitude of $s_{Drifttube}$ can be estimated with the *Glückstern* formula [83]. A parabola

$$y = \frac{1}{2}ax^2 + bx + c \tag{B.2}$$

can be fitted to N equidistant measurement points x_i, where uncorrelated errors ε on each single measurement are assumed. The errors on the parameters a, b and c are then given by

$$< a^2 >= \frac{\varepsilon^2}{L^4} A_N \tag{B.3}$$

$$< ba >= -\frac{1}{2}\frac{\varepsilon^2}{L^3} A_N \tag{B.4}$$

$$< b^2 >= \frac{\varepsilon^2}{L^2} B_N \tag{B.5}$$

where L is the projected trajectory length $L(x_0 = 0, x_n = 1)$. For $N > 10$ the parameters A_N und B_N were found to be:

$$A_N = \frac{720}{N+5} \tag{B.6}$$

$$B_N = \frac{192}{N+4} \tag{B.7}$$

This procedure can be applied to the CMF. The six multilayers are equidistant to a good approximation and the single tube resolution is about $100\,\mu m$ (averaged over all radii) which results in a estimated multilayer resolution of $100\,\mu m/\sqrt{3} \approx 60\,\mu m$. The projected muon trajectory has an estimated length of $L = 1080\,mm$ for vertical incident muons since small sagittae are expected. Equations (B.3) and (B.6) lead then to the estimated error on the opening parameter α of the parabola

$$< \alpha^2 >= 1.7 \times 10^{-7} \frac{1}{m^2} \rightarrow \alpha = 4.1 \times 10^{-4} \frac{1}{m} \tag{B.8}$$

which corresponds to a sagitta resolution of

$$\Delta s = 120 \mu m. \tag{B.9}$$

This value is only due to the single tube resolution. It is expected that the overall sagitta resolution of the Cosmic Ray Measurement Facility (CMF) is dominated by multiple scattering effects since the muons are low energetic and traverse a relative large amount of aluminum. Each drift tube has a wall thickness of $0.4\,mm$.

To estimate the contribution of $\delta s_{MultipleScattering}$, the following formula was used for calculating the multiple scattering angle

$$\theta_0 = \frac{13.6MeV}{p\beta c} z_c \sqrt{\frac{s}{X_L}} [1 + 0.038 \ln\left(\frac{s}{X_L}\right)] \tag{B.10}$$

where p is the momentum of the scattered particle, βc its velocity, z_c its charge and s the thickness of the transversed material. The parameter X_L is the radiation length of the scattering medium. This formula is based on the assumption that the muons are only scattered once inside the CMF. The middle part of the CMF is therefore approximated by an aluminum block with an effective thickness of one MDT-chamber which leads to the situation described in Fig.B.3. For this case the parameters $X_L = 0.089m$, $s = 0.4\,mm \times 24$ and $p \approx 4GeV$ were chosen which leads to a scattering angle of $\theta_0 = 1.03 \times 10^{-3}$. The overall estimated resolution is

$$\Delta s = 0.565 \frac{\theta_0}{2} \approx 290 \mu m. \tag{B.11}$$

The overall sagitta resolution of the CMF can be calculated with Equation (B.1) and has a numerical value of $310\mu m$. This estimation is based on several approximations and should be considered with care. Nevertheless it can be concluded that the overall sagitta resolution is clearly dominated by the multiple scattering contribution.

Theoretical Estimation of Sagitta Resolution of a Single MDT chamber

In this section the sagitta resolution of a single MDT chamber is estimated, ignoring the information of the other two chambers. We expect an average angle variation of $\theta_0 \approx 5.4 \times 10^{-4}$ of an incident muon in the upper multilayer due to multiple scattering effects. A single

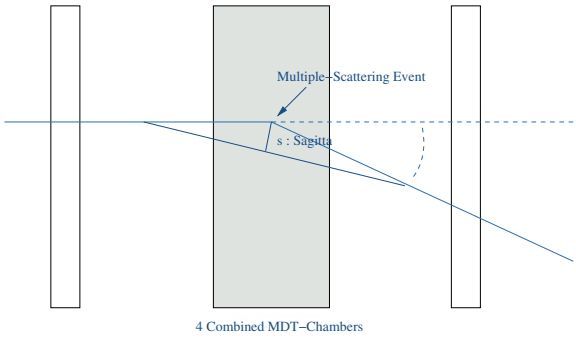

Figure B.3: Approximation of the CMF for the estimation of multiple scattering effect

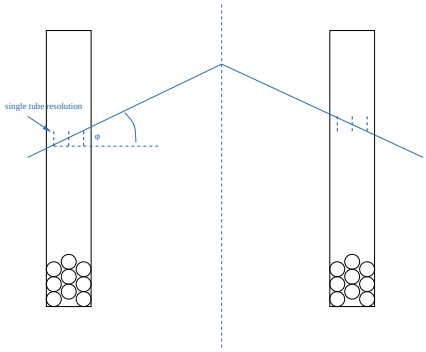

Figure B.4: Approximation of the sagitta calculation with a single MDT chamber

tube resolution of $40\mu m$ would be needed to measure this effect, which is better than the actual resolution. Therefore the sagitta measurement within a single MDT chamber is not sensitive to multiple scattering effects.

To estimate the sagitta resolution in this case, one has to study the parabolas which can be fitted within the errors of the six measurement points. A parabola can be described by two straight lines in a first approximation as sketched in Figure B.4.

This leads to an estimated sagitta resolution of

$$\Delta s = \frac{200\,mm \times \sigma_e}{90\,mm} \tag{B.12}$$

where σ_e is the single tube resolution, $90\,mm$ the thickness of one multilayer and $200\,mm$ the distance to the middle of the MDT chamber. A single tube resolution of $100\mu m$ leads to an expected sagitta resolution of $200\mu m$ which agrees well with the measured value.

B.1.4 Results and Comparison between Real and Simulated Data

Sagitta study with three chambers

The distribution in Figure B.5 shows the measured sagitta for about 100,000 events that have been recorded at the cosmic ray measurement facility. The simulated sagitta distribution for about 30,000 events can be seen in Figure B.6.

Two effects influence the sagitta resolution, as already mentioned in section 1: Multiple scattering, which is energy dependent and the single tube resolution which is energy independent. Figure B.7 shows the energy dependence of the reconstructed sagitta for simulated events, where the energy is known from the Monte Carlo truth.

As expected, Figure B.7 exhibits a strong energy dependence. Figure B.8 and Figure B.9 confirm that this observation is not due to the lower statistics at higher energies. There is a wide sagitta distribution for low muon energies since multiple scattering effects are dominating in this regime. It is useful to study the different energy regions separately in order to analyze the overall distribution (summed over all energies), which is the only accessible quantity at the cosmic ray measurement facility since no magnetic field is applied. A gaussian function can be used to describe the sagitta distribution of the simulation in each energy range separately as shown in Figure B.8 for the energy region $2.0\,GeV$ to $2.2\,GeV$ and in Figure B.9 for the energy region $5.0\,GeV$ to $6.0\,GeV$. In Figure B.10 the width of the fitted Gauss functions

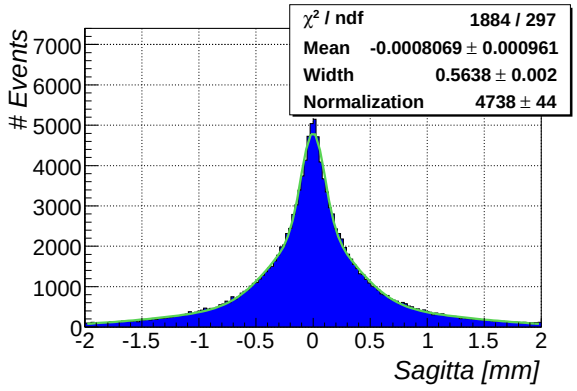

Figure B.5: Measured sagitta distribution for 100,000 events. The blue curved corresponds to Equation (B.16)

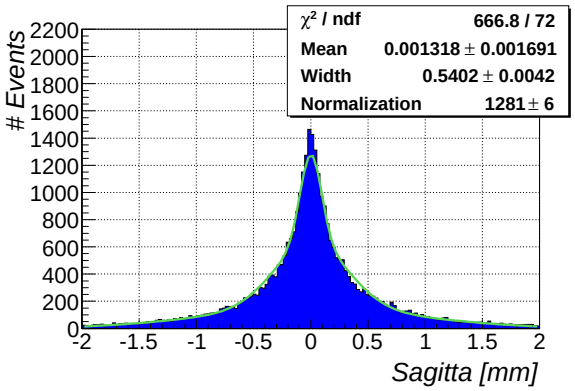

Figure B.6: Simulated sagitta distribution of the cosmic ray measurement facility

vs. the muon energies is shown. The single tube resolution begins to dominate the sagitta resolution at a muon energy of about $10\,GeV$, where the error from multiple scattering falls below $\sim 60\mu m$.

In order to describe the overall sagitta distribution an Ansatz was tried, based on a sum of three gaussian functions (Function B.13) to account for the wide range of muon energies. Each of the three gaussian should therefore describe one energy region while the sum of the three gaussians describes the overall sagitta distribution.

$$y(x, x_m, A_1, A_2, A_3, \sigma_1, \sigma_2, \sigma_3) = \frac{A_1}{\sqrt{2\pi}\sigma_1} e^{-\frac{(x-x_m)^2}{\sigma_1^2}} + \frac{A_2}{\sqrt{2\pi}\sigma_2} e^{-\frac{(x-x_m)^2}{\sigma_2^2}} + \frac{A_3}{\sqrt{2\pi}\sigma_3} e^{-\frac{(x-x_m)^2}{\sigma_3^2}} \tag{B.13}$$

In a first step function B.13 was fitted to the measured sagitta distribution of chamber BOS-4C-16. It is seen in Figure B.11 that the choice of three Gaussian is sufficient to describe the measured sagitta distribution. The resulting values of the fitting parameters are shown in Table 1. This function has seven free parameters, and therefore it is difficult to directly compare the real and simulated sagitta distribution. Hence it is desirable to have a fitting function depending only on one width and one normalization parameter which describes the overall sagitta distribution. We assume that the ratios

$$a_1 = \frac{A_1}{A_2} = 0.4, \quad a_3 = \frac{A_3}{A_2} = 0.9, \quad s_1 = \frac{\sigma_1}{\sigma_2} = 0.28, \quad s_3 = \frac{\sigma_3}{\sigma_2} = 2.84 \tag{B.14}$$

are constant for all studied sagitta distributions. The definition of

$$\sigma = n_\sigma \sigma_2, \;\; A = A_2 \tag{B.15}$$

leads to a fitting function depending only on a single width parameter σ and a single normalisation parameter A. The parameter n_σ is arbitrary and can be choosen in such a way that an interval $[x_m \pm \sigma]$ contains 68% of all events. This definition allows a direct comparison between real and simulated data. The fitting function for the measured and simulated data is hence given by

$$y(x, x_m, A, \sigma) = \frac{1.57A}{\sqrt{2\pi}\sigma} e^{-\frac{(x-x_m)^2}{0.065\sigma^2}} + \frac{1.14A}{\sqrt{2\pi}\sigma} e^{-\frac{(x-x_m)^2}{0.77\sigma^2}} + \frac{0.35A}{\sqrt{2\pi}\sigma} e^{-\frac{(x-x_m)^2}{6.51\sigma^2}} \tag{B.16}$$

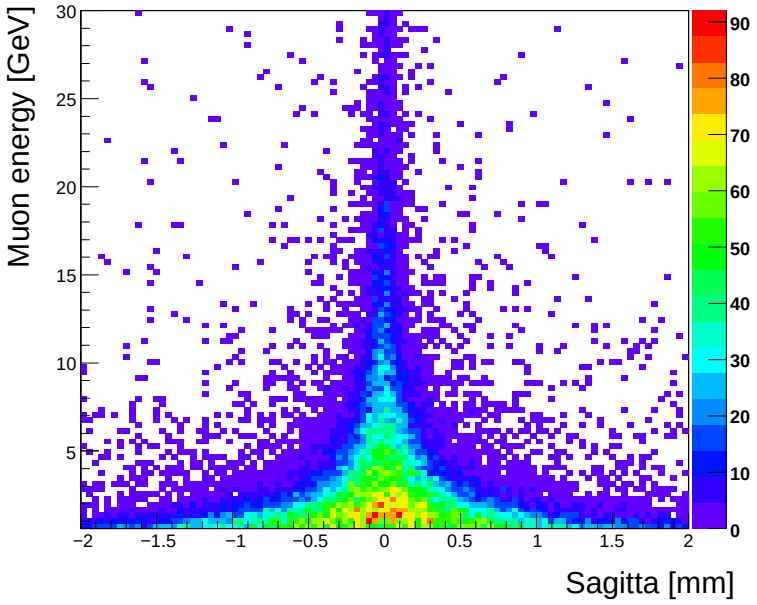

Figure B.7: Simulation of the sagitta vs. corresponding muon energy. The color scale indicates the number of events in a given bin.

where x_m is the mean value, A the normalization and, σ the width of the distribution. These three parameters are fit parameters of the overall distribution. The parameter n_σ was set to 0.88. With these choises, the interval $[x_m \pm \sigma]$ contains 68% and the interval $[x_m \pm 2\sigma]$ 91% of all events.

The function of Equation (B.16) is drawn as blue line in Figure B.5 and Figure B.6. The width σ of the distribution was found to be $\sigma = 0.569\,mm$ on this grounds. The width σ_{data} describing the real data agrees within 5% to the width σ_{sim} for the simulated data, i.e.

$$\frac{\sigma_{data} - \sigma_{sim}}{\sigma_{data}} \approx 5\% \tag{B.17}$$

This result seems to confirm that the Geant4 simulation of multiple scattering, the material

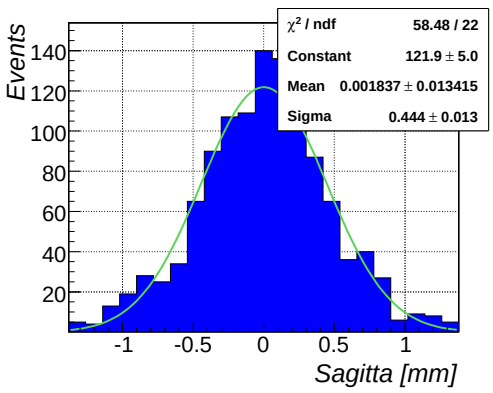

Figure B.8: Description of the simulated sagitta distribution with a Gaussian function between muon energies of 2.0 GeV to 2.2 GeV

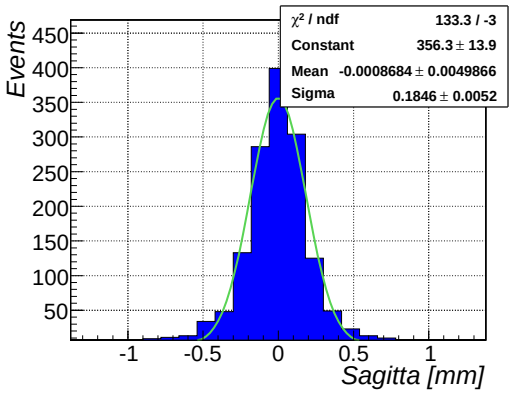

Figure B.9: Description of the simulated sagitta distribution with a Gaussian function between muon energies of 5.0 GeV to 6.0 GeV

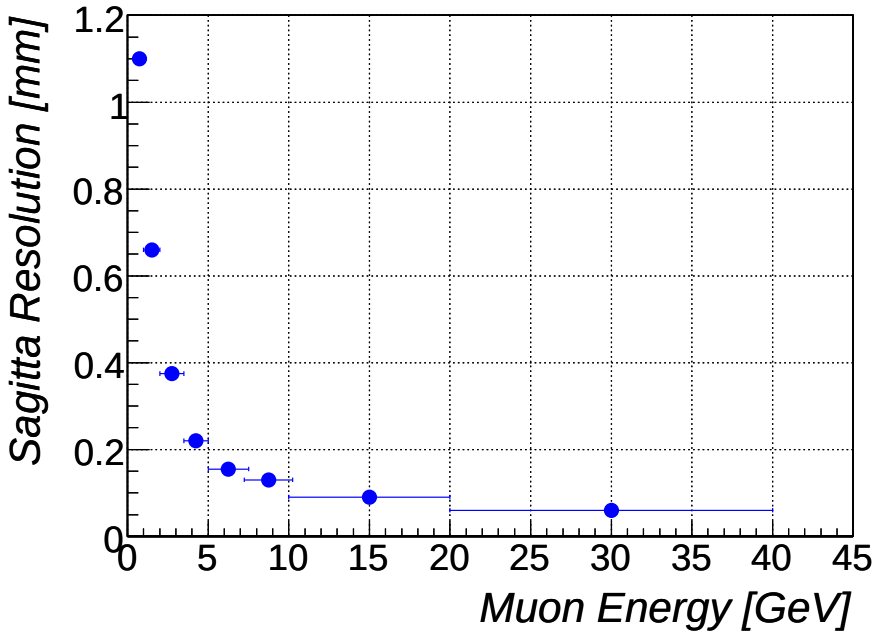

Figure B.10: Reconstructed sagitta resolution of the CMF simulation in dependence of muon energy.

x_m	σ_1	σ_2	σ_3	A_1	A_2	A_3
0.0008	0.14*mm*	0.50*mm*	1.42*mm*	3563	8899	7877

Table B.1: Fitted parameters of function B.13 to the measured sagitta resolution of chamber BOS-4C-16

description and the energy spectrum of cosmic muons are implemented with reasonable accuracy in the CMF-simulation. In fact, the energy spetrum is quite soft, which leads to a high sensitivity to the simulation of multiple scattering and to material description [1].

Sagitta Studies with a Single MDT-chamber

As discussed in the previous subsection the sagitta resolution of the whole measurement facility is dominated by multiple scattering effects and not by the single tube resolution. A single MDT chamber, however, provides a good opportunity to study effects of the single tube resolution, because there is comparatively much less scattering material between the first and the last measured point. (Figure B.12). Furthermore, the sagitta resolution of a single MDT chamber could be an important tool for alignment and B-field studies.

The same procedure as in the previous section is used: In a first step, the simulated sagitta distribution is studied in order to find a suitable function which describes the measured overall sagitta distribution. Gaussian functions were fitted to the simulated sagitta distributions for several energy regions. The energy dependence is much smaller compared to the study of the whole measurement facility as shown in Figure B.13. It can be concluded that multiple scattering effects are not dominating for the sagitta measurement within a single MDT-chamber above 1 GeV.

The sagitta distributions of the real and simulated measurements can be discussed as shown in Figure B.14 and Figure B.15, respectively. Because of the small energy dependence it is

[1] Also other functions (single gaussian function, Breit-Wigner function) where used to describe the overall sagitta distribution in real data and simulation which led to no significant improvement

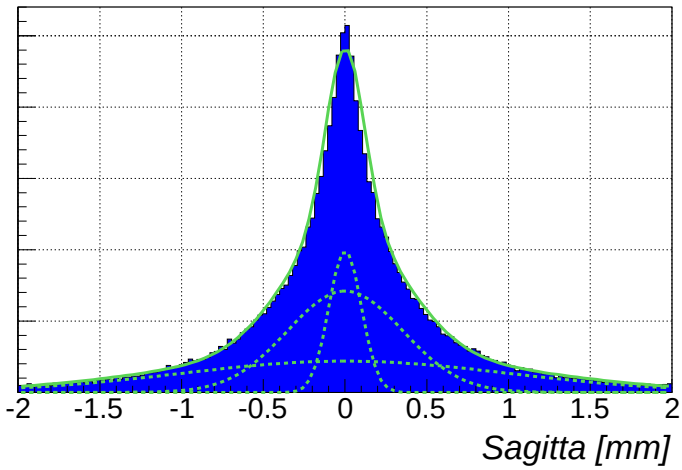

Figure B.11: Fitting the overall sagitta distribution with the sum of three Gaussians from Equation (B.16).

sufficient in this case to use a single Gaussian function with constant background to describe the overall sagitta distribution. The sagitta resolution of a single MDT-chamber was found to be $\sigma = 0.237\,mm$. As shown in Figure B.15 and Figure B.14 the width parameters of the fitting Gaussian function match within the statistical errors, which is a convincing indication that the single tube resolution and other effects like the rt-relation, the flight time of the muons, the signal propagation along the wire or wire-sagging on this level of simulation are well understood.

B.1.5 Alignment

In general the nominal position of the test chamber in the measurement facility differs from its real position. This leads to systematic errors during reconstruction since wrong wire positions and therefore wrong centers of the drift circles are assumed. The mean value of the sagitta distribution in z- and y-direction is in principle sensitive to displacements of the test chamber. A displacement in y-direction will affect the mean value of the sagitta distribution strongly since most of the incident muons are nearly perpendicular to the y-axis. A displacement in the z-direction becomes only detectable with muons that have a large angle of incidence.

The test chamber has been displaced independently in z- and y-direction within the simulation, in order to get a quantitative relation between the displacement in both directions and the mean value of the sagitta distribution. Subsequently the simulated data have been analyzed and the mean value of the sagitta distribution was calculated. The results are shown in Figure B.16 for the displacement in y-direction and in Figure B.17 for the displacement in z-direction.

The relation for both directions can be described by a linear function between the mean value and the displacement which is valid at least for small displacements. The linear functions are given by

$$x_{m,y} = (0.393 \pm 0.001) y_{dis} + (0.005 \pm 0.0019)\,[\text{mm}] \tag{B.18}$$

$$x_{m,z} = (-0.184 \pm 0.001) z_{dis} + (0.004 \pm 0.0024)\,[\text{mm}] \tag{B.19}$$

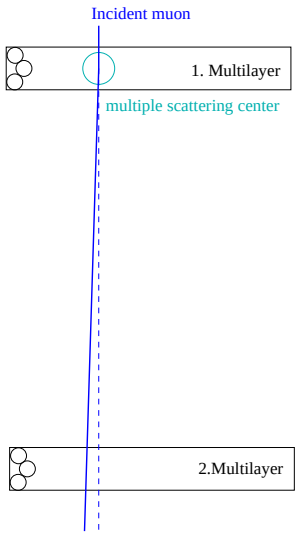

Figure B.12: Illustration of multiple scattering in a single MDT chamber

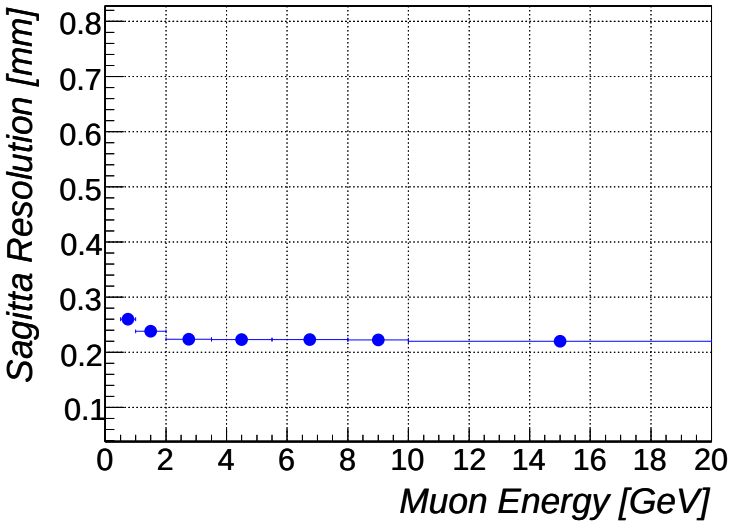

Figure B.13: CMF-simulation: Sagitta resolution of one MDT-chamber vs. muon energy

where y_{dis} is the displacement of the chamber in y-direction and z_{dis} the displacement of the chamber in z-direction. Naively, it might be expected that the displacement of the chamber translates fully into a shift of the mean value of the sagitta distribution by the same amount. However, the defining distance for the definition of sagitta starts and ends in the center of the upper and lower reference chamber as illustrated in Figure B.2 and therefore the misaligned chamber is part of the overall fitting procedure. Furthermore, the definition of sagitta in this study is more complex because there are not only 3 measurement points for the definition of sagitta but on average 18. This explains the deviation of the slope in Equation (B.18) from 1.

A full and powerful set of alignment algorithms was developed for the cosmic ray measurement facility and have been applied before reconstructing the muon tracks [62]. The precision of these alignment algorithms could be tested with Equation (B.18) and B.19, since a misaligned test-chamber results in a displacement of the mean of the sagitta distribution. The constant offset terms of $4\,\mu m$ resp. $5\,\mu m$ in both equations can be neglected for displacements above $O(20\,\mu m)$ in y-direction and above $O(50\,\mu m)$ in z-direction.

The mean of the fitting function B.16 of the sagitta-distribution for the chamber BOS-4C-16 was found to be $-0.81\,\mu m \pm 0.9\,\mu m$ (Figure B.5). Using this value the maximum displacement in both directions can be calculated by Equation (B.18) and Equation (B.19), respectively.

$$-0.00081 = (0.393 \pm 0.001) y_{dis} + 0.005 \;\rightarrow\; y_{dis} \approx -0.01\,[\text{mm}]$$

$$-0.00081 = (-0.184 \pm 0.001) z_{dis} + 0.004 \;\rightarrow\; z_{dis} \approx 0.03\,[\text{mm}]$$

This leads to the conclusion that the alignment algorithms work within a precision of $O(10\,\mu m)$ in y- and $O(30\,\mu m)$ in z-direction. This is a conservative estimation, since these values are dominated by the constant offset terms in Equation (B.18) and (B.19) which are expected to be zero for larger statistics. The width of the sagitta distribution is not significantly altered by a small displacement of the chamber.

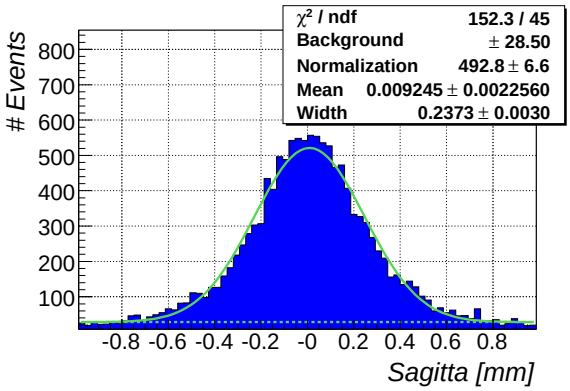

Figure B.14: Measured sagitta distribution of one MDT-chamber. The dotted lines describe the constant background and the pure gaussian part. The full line corresponds to the sum of the two dotted lines.

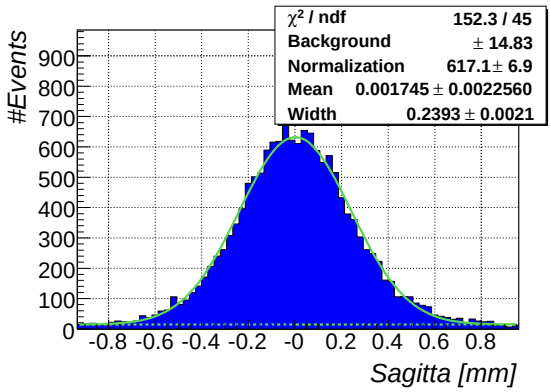

Figure B.15: Simulated sagitta distribution of one MDT-chamber. The dotted lines describe the constant background and the pure gaussian part. The full line corresponds to the sum of the two dotted lines.

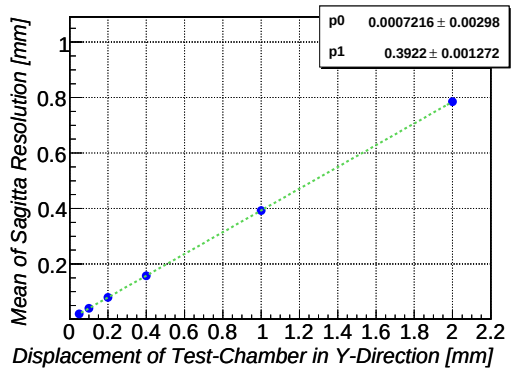

Figure B.16: Displacement of the test-chamber in *y*-direction vs. mean value of sagitta distribution

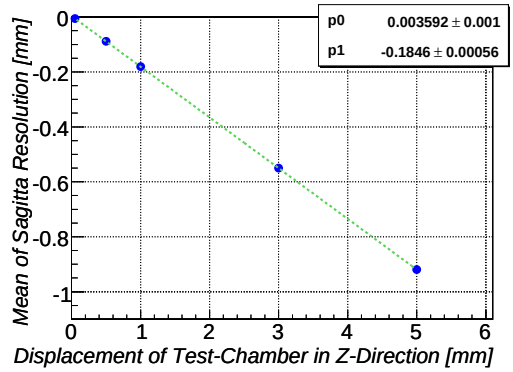

Figure B.17: Displacement of the test-chamber in z-direction vs. mean value of sagitta distribution

B.2 H8 Testbeam and Further ATLAS Studies

B.2.1 Setup of the Simulation

The CMF-Simulation describes well the response of MDT chambers to cosmic muons, as shown in the previous section. It is a useful exercise to use the simulation validated by the cosmic ray measurement facility and extend it for the testbeam setup at H8. In order to create a H8-like simulation three similar MDT-chambers were placed at distances corresponding to the ones at H8 [2].As already in the ATLAS-like simulation, blocks with the dimensions of the RPCs which consists out of the respective materials were introduced in the simulation. The incident muons are assumed to come from a point-like source with a small opening angle. The muons were generated with energies between 30 GeV and 300 GeV as in the H8-testbeam.

Figure B.18 shows the measured and simulated sagitta resolutions in the Geant4 simulation. The sagitta distributions within a small energy region can be described with a standard Gaussian function (Figure B.19). The measured sagitta resolutions for different energies in

[2]The distances between the centers of the chambers are 2199 mm and 2514 mm and correspond to the center of the chambers

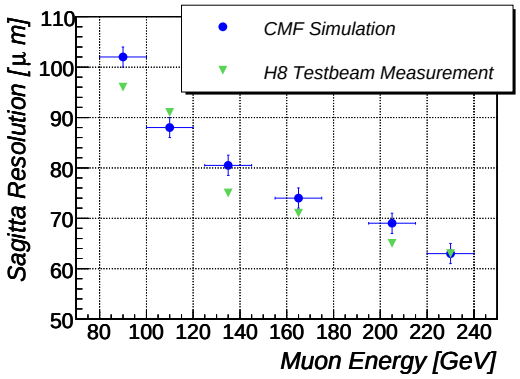

Figure B.18: Simulated sagitta resolution (circle) and measured sagitta resolution (triangle) in the H8 setup as a function of the muon energy [4]

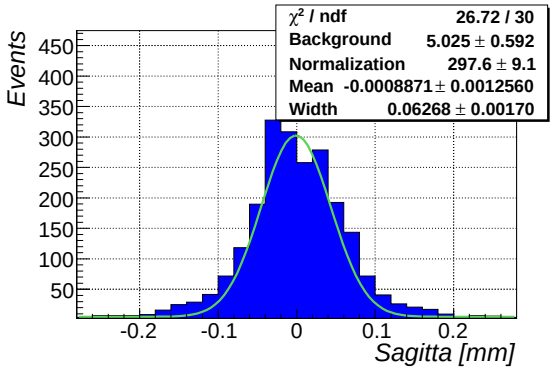

Figure B.19: Sagitta resolution of the simulated H8 setup for muons with an energy between 220 *GeV* and 240 *GeV*.

the H8-testbeam are also shown in Figure B.18 [84]. The comparison of the results shows that the simulated sagitta resolution is slightly worse than the measurements of the H8-testbeam. Keeping in mind the rough approach of this simulation it is nevertheless a quite good agreement.

B.2.2 Alignment at the ATLAS Muon Spectrometer

Effects of misalignment on sagitta can also be studied using the CMF-Simulation, which was modified corresponding to the ATLAS geometry, which was introduced in chapter 6. Within this setup a direct proportionality between a misalignment of the middle chamber in y-direction and the mean value is expected. The results of this study are shown in Figure B.20 and the dependence can be described by the phenomenological function

$$x_{m,y} = 1.128\, y_{dis} - 0.002\,[\text{mm}] \tag{B.20}$$

which agrees with the expectation of a proportionality factor close to unity for the MDT geometry in the ATLAS detector. Hence, a strong effect is seen on the mean of the sagitta distribution.

B.2.3 Effects of Wire-Displacement

Another important aspect is the precision of the wire positions. The effect on the sagitta resolution has been studied both for a single MDT-chamber and for the ATLAS-geometry. In order to study the effect of the precision of wire position on the sagitta resolution each wire-position was shifted by δy in y-direction and δz in z-direction in the simulation. The displacement parameters δy and δz were set randomly to values between $[-d, d]$, simulating the deviations between the nominal and the true wire positions. 10.000 events were generated and reconstructed for several value of d.

The dependence of the sagitta resolution on the maximal displacement d is shown in Figure B.21 for the modified CMF-Simulation, where muons with an energy of 1 TeV have been used to study the effect.

As expected, the sagitta resolution is dominated by the single tube resolution for small displacements of the nominal wire position. For values of d around 0.06 mm the wire dis-

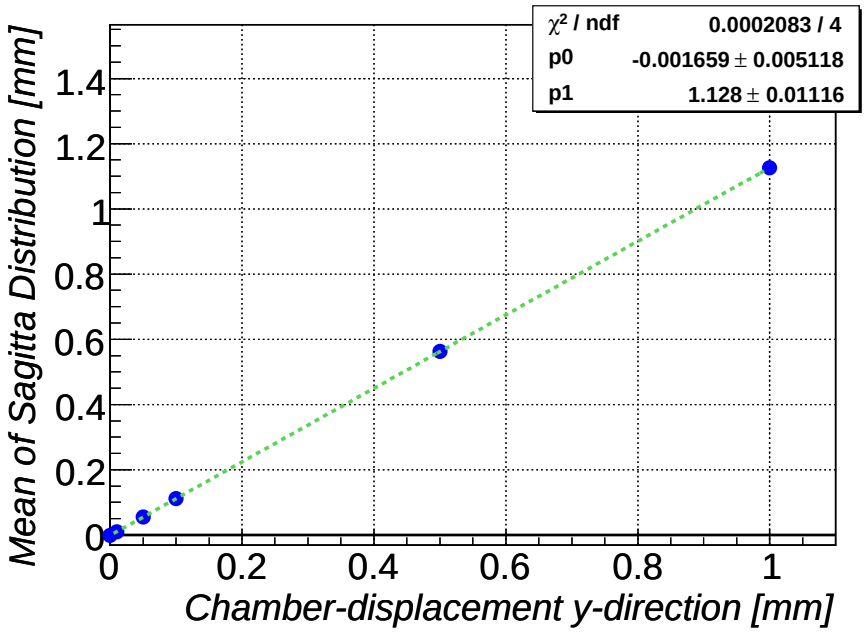

Figure B.20: Impact of the displacement of the middle MDT-chamber on the mean value of the sagitta distribution.

placements start to dominate the sagitta resolution, for larger values of d the dependence becomes linear. This behaviour can be phenomenologically described by

$$\sigma_{sagitta} = \sqrt{a^2 + b^2 d^2} + c\,[\mathrm{mm}]\,. \tag{B.21}$$

The single tube resolution is described by $a + c$, while b is the proportional factor of the linear dependence. This functions is fitted to measured data. In case of the ATLAS-setup the fitted values are

$$a_{ATLAS} = 0.02\,\mathrm{mm}\,, b_{ATLAS} = 0.25\,\mathrm{mm}\,, c_{ATLAS} = 0.043\,\mathrm{mm} \tag{B.22}$$

and for a single MDT-chamber

$$a_{MDT} = 0.13\,\mathrm{mm}\,, b_{MDT} = 1.01\,\mathrm{mm}\,, c_{MDT} = 0.12\,\mathrm{mm} \tag{B.23}$$

B.2.4 Effects of the Single Tube Resolution

Last but not least the effect of the single tube resolution on the sagitta resolution was studied. Figure B.22 shows the sagitta resolution for the modified CMF-Simulation in dependence of the single tube resolution. Muons with energies between $0.95 - 1.0\,\mathrm{TeV}$ have been used to study this dependence in the adapted CMF-Simulation to avoid large multiple scattering effects. The simulated data in Figure B.22 can be fitted by the linear function

$$\sigma_{sagitta}\,[\mathrm{mm}] = 0.5\sigma_{st}\,[\mathrm{mm}] + 0.02\,[\mathrm{mm}]\,. \tag{B.24}$$

where σ_{st} describes the single tube resolution.

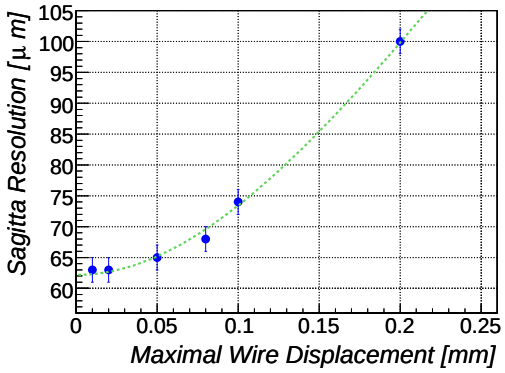

Figure B.21: Sagitta resolution of the simulated ATLAS setup in dependence of the maximal displacement of the wire positions

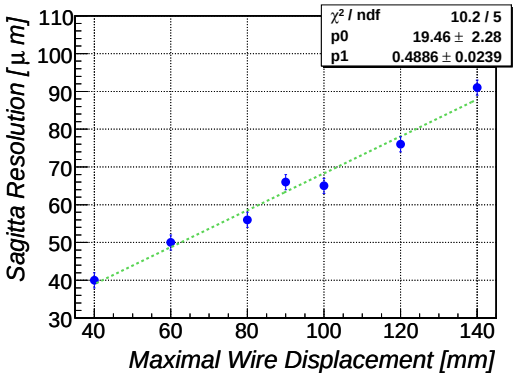

Figure B.22: Sagitta resolution of the simulated ATLAS setup in dependence of the single tube resolution

B.3 Summary

The cosmic ray measurement facility offers an excellent opportunity to compare real data of ATLAS-components with a Geant4 simulation. The sagitta resolution predicted by a Geant4 simulation of the entire measurement facility agrees with the real data to within 5%. This measurement, which uses a setup of three MDT-chambers, is dominated by multiple scattering effects. In contrast, the sagitta measurement based on a single MDT chamber is dominated by single tube resolution. We find good agreement between the simulated sagitta resolution of a single MDT-chamber (BOS-Type) and the real data within the statistical uncertainties. Hence the two main input parameters on the sagitta resolution (single tube resolution and multiple scattering) could be verified to be simulated correctly.

Several aspects of the sagitta resolution were studied with this validated simulation of the MDT-chamber: The alignment algorithms for the MDT chambers in the cosmic ray measurement facility could be confirmed with a precision of $4\mu m$ in y-direction and $8\mu m$ in z-direction.

Furthermore, this simulation was extrapolated both to the setup of the MDT chambers for the H8 testbeam measurements and to the final MDT setup in ATLAS. We found good agreement between the adapted simulation on the one hand and the sagitta resolution measured in H8 and the momentum resolution as presented in the ATLAS TDR, respectively. Finally, the impact of single wire displacements and the single tube resolution on the sagitta resolution in the ATLAS setup was studied.

"This is known as Cardan's Solution, though it was originally given by Tartaglia. He unwisely told Cardan, who promptly published it as his own."

The Math Forum Project

Appendix C

Impact of Misalignment Effects on the Muon Spectrometer Performance

This chapter is published in [2,7] and is structured as follows: Section C.1 is dedicated to the implementation, validation and impacts of random misalignments on single muons. In section C.2 the validation of the so-called *Egg-Shape-Layout* is presented. The chapter closes with a short overview of possible alignment strategies and presents an alignment-method based on the decay of Z bosons into muons in section C.3.

The study is mainly based on a single *10,000* muon sample, with a transverse momentum of $50\,GeV$, simulated and reconstructed within ATHENA release 12.0.6 for section C.1 and release 10.0.4 for C.2. The transverse momentum of $50\,GeV$ was chosen, because the Muon Spectrometer is expected to have its best performance in this energy-regime. Moreover, standard physics processes like the decay of the W or Z boson, which play an important role already in the first phase of LHC, have also final state muons in this energy-regime.

C.1 Random Misalignment

C.1.1 Implementation

In order to describe the misplacements and rotations in a common way for all chambers, a new coordinate system is defined for each MDT-chamber separately, which is illustrated in Figure C.1. The s-axis is defined as the tube direction, the z-axis is in the plane defined by one multilayer and perpendicular to the s-axis. The t-axis is defined to be perpendicular to the other two axis. The corresponding rotations are also illustrated in Figure C.1. The rotation around the s-axis is defined by the angle γ and is applied on one end of the MDT-chamber. The corresponding rotations around the z-axis and t-axis are defined by the angles β and α, respectively.

The principle of this method is to have different descriptions of the Muon Spectrometer ge-

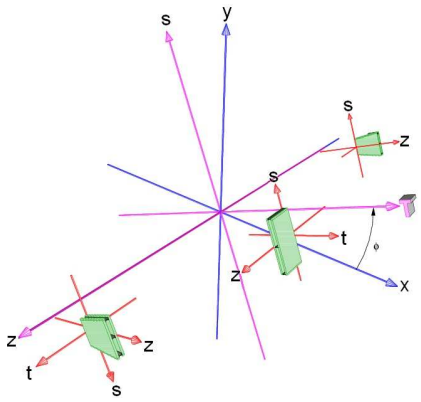

Figure C.1: Illustration of Misalgined Chambers.

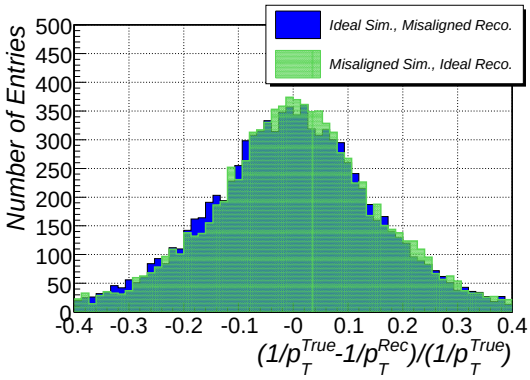

Figure C.2: Comparison of two p_T-resolution distributions for a $50\,GeV$ single muon sample, simulated with nominal layout and reconstructed with misaligned layout and via versa.

ometry at the simulation and reconstruction levels. Hereafter the simulation description will be called *simulation layout* and the reconstruction description will be called *reconstruction layout*. In order to study these differences in principle one has to use a misaligned Muon Spectrometer layout during the simulation step and an ideal or a misaligned Muon Spectrometer layout during reconstruction.

The Geant4 simulation and the corresponding digitization of events requires an intensive computational calculation, while the reconstruction of such an event from the simulated digitized data is orders of magnitude faster. In order to be able to test the effects of several different misaligned Muon Spectrometer layouts it is very helpful to test the equivalence of the misalignment impacts on the Muon Spectrometer performance for the following two cases:

- Case 1: using a misaligned *simulation layout*[1] and an ideal *reconstruction layout* .
- Case 2: using an ideal *simulation layout* and a misaligned *reconstruction layout*.

Figure C.2 shows the overall comparison of the p_T-resolution distribution for a $50\,GeV$ single muon sample for both cases. Figure C.3 and C.4 show the corresponding p_T-resolution and reconstruction efficiency comparison versus η, for both cases, respectively. No significant differences can be observed for the reconstruction efficiency, but a slightly better p_T-resolution for case 1 (Figure C.3). The same η-dependence of the resolution can be observed for both cases. The relative difference of the p_T-resolution is in the order of 2.5%, which must be treated as systematic uncertainty if one draws conclusions from case 1 to case 2 or the other way round. Several effects can cause this relatively small difference. One possibility is the difference in the magnetic field, which is assumed during the simulation and the reconstruction, since the muons interact with the gas in the tubes at different positions for both layouts. Hence a different effect on positive and negative muons is expected.

Moreover a small difference between case 1 and 2 in the momentum scale can be observed, which is 0.006 ± 0.002. This is explained in detail in the following.

First of all it must be noted, that case 1 and 2 are not equivalent on an event by event basis, i.e. comparing the reconstruction of muons for both cases, where the muons are based on the same truth information (η, ϕ and p_T), will reveal differences in the reconstructed muon track

[1]The definition of a misaligned Muon Spectrometer layout is given in chapter 7

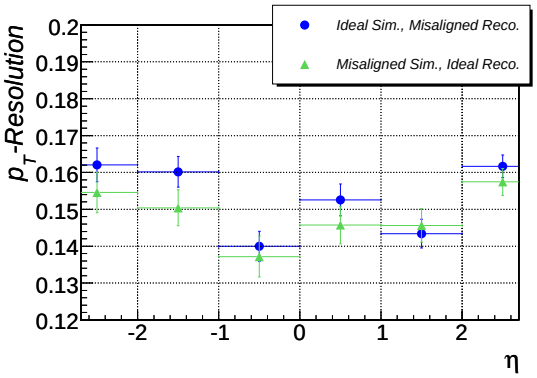

Figure C.3: Comparison of two p_T-resolution distributions for a $50\,GeV$ single muon sample, simulated with nominal layout and reconstructed with misaligned layout and via versa vs. η.

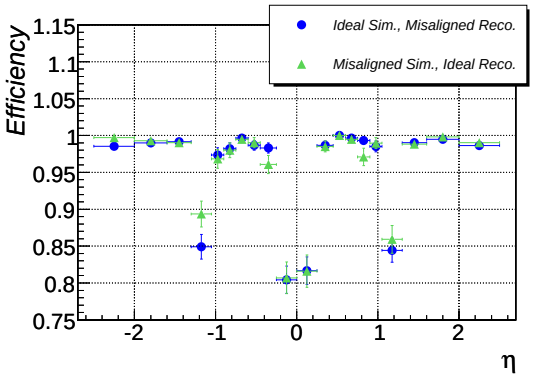

Figure C.4: Comparison of reconstruction efficiency for a $50\,GeV$ single muon sample, simulated with nominal layout and reconstructed with misaligned layout and via versa.

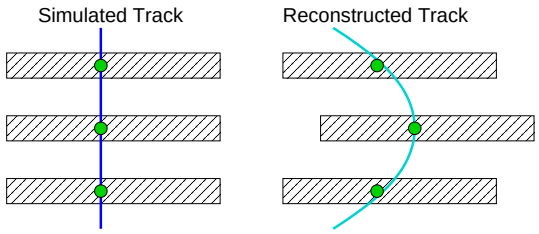

Figure C.5: Illustration of the impact on reconstructed tracks using an ideal *simulation layout* and a misaligned *reconstruction layout*.

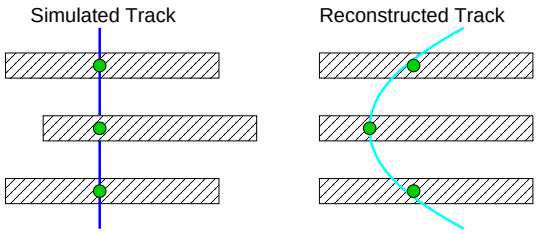

Figure C.6: Illustration of the impact on reconstructed tracks using a misaligned *simulation layout* and an ideal *reconstruction layout*.

for each event. This can be easily understood, since shifts of a misaligned layout will lead to opposite effects if they are used during simulation or during reconstruction. This effect is illustrated in Figure C.5 and Figure C.6.

This effect can be studied, by comparing positive and negative muons separately. The effect on the reconstructed momentum scale versus η is shown separately for positive and negative muons in Figure C.7.

Note, that each eta bin averages over 16 chambers in ϕ-direction and over two or more sectors in the η-direction, hence a net-shift is expected. A net-shift Δs on the sagitta s leads to a shift of the reconstructed transverse momenta:

$$p_T^{\mu_+} \sim \frac{1}{s + \Delta s}, \qquad p_T^{\mu_-} \sim \frac{1}{s - \Delta s}.$$

Thus as observed, momentum scale in a given η-bin and a given muon charge is not expected to be null.

In addition it is expected that the net-shift in case 1 and 2 differs only by the sign. Thus as observed, one expects that the momentum scale shift for a given muon charge will differ only by the sign of the charge.

Finally, since it is expected that for a given reconstruction case, the momentum scale shift will reverse with the muon charge sign, it is expected that the momentum scale shifts will be

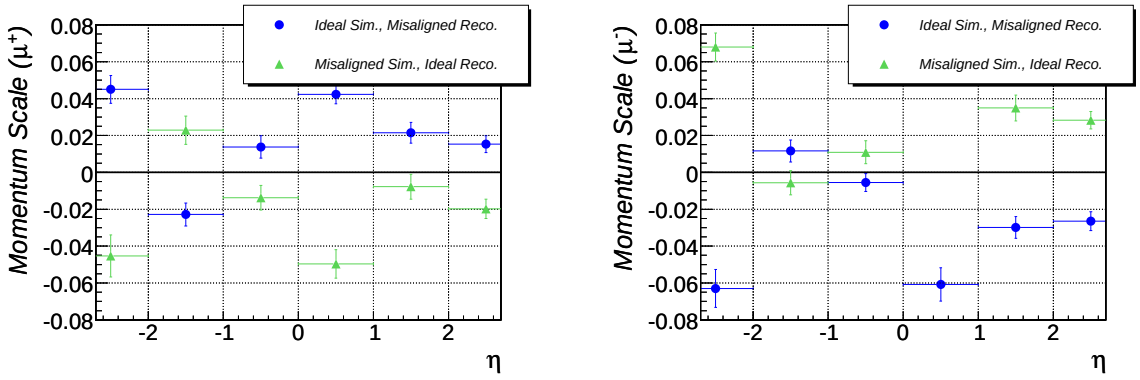

Figure C.7: Comparison of the momentum scale for 50 *GeV* muons simulated with ideal layout and reconstructed with misaligned layout and vice versa: For positive charged muons (a), for negative charged muons (b).

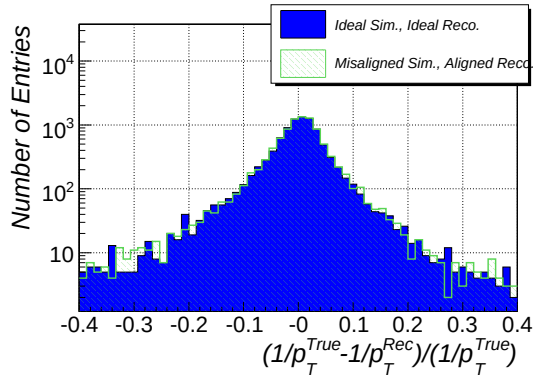

Figure C.8: Comparison of p_T-resolution distribution for an aligned nominal Muon Spectrometer layout and an aligned distorted Muon Spectrometer layout.

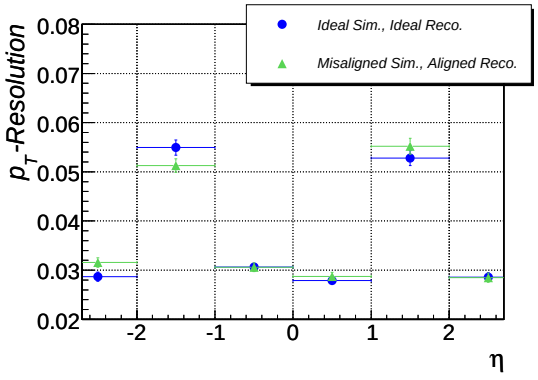

Figure C.9: Comparison of p_T-resolution distribution for an aligned nominal Muon Spectrometer layout and an aligned distorted Muon Spectrometer layout, versus η.

opposite for positive and negative muons. As seen by comparing the two plots of Figure C.7, this is true up to statistical fluctuations.

The other aspect is to study the equivalence of using the ideal Muon Spectrometer layout during the simulation and the reconstruction step, and an misaligned Muon Spectrometer layout during simulation and the corrected, i.e. perfectly aligned, layout during reconstruction. The latter case is nothing more than using the same misaligned layout for reconstruction that is used for simulation. An equivalence is a strong hint that the alignment of the ATLAS Muon Spectrometer leads to the expected design performance. The position of each MDT-chamber in space is not too relevant as long the position is known to a high accuracy. Figure C.8 illustrates the comparison of the overall p_T-resolution and Figure C.9 the p_T-resolution vs. η for both cases. Both results coincide within their statistical uncertainty.

The comparison of the muon reconstruction efficiency vs. the η of the muons is shown in Figure C.10. Also here, no statistically significant difference can be observed. Note, that some features of a non ideal layout induce degradation of Muon Spectrometer performance, even if the geometry is perfectly known. For example, this is the case of the non parallelism of tube station to station. If for instance the outer and inner tubes are parallel and if the

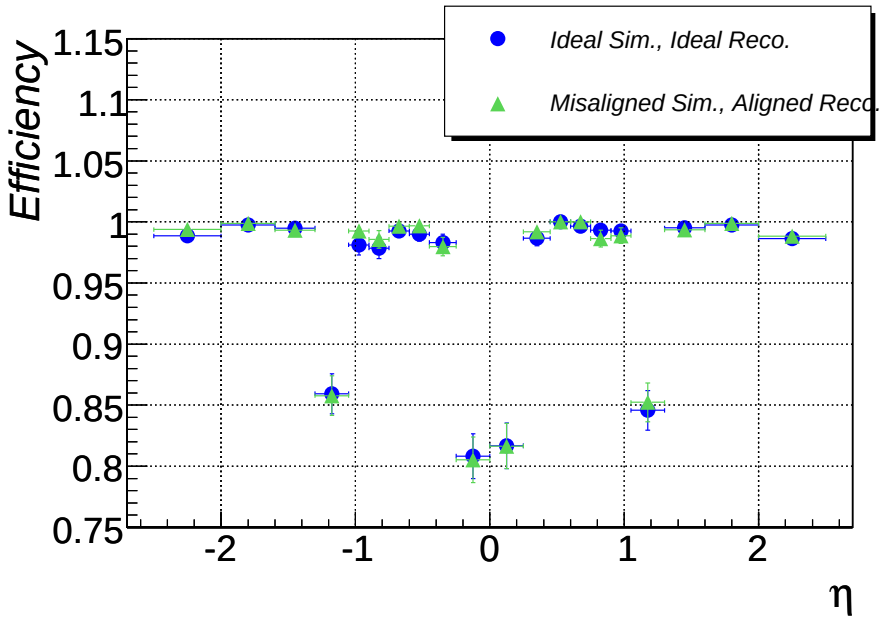

Figure C.10: Comparison of reconstruction efficiency for an aligned nominal Muon Spectrometer layout and an aligned distorted Muon Spectrometer layout vs. η, respectively.

middle tubes are not parallel with respect to the other two layers, then the precision on the 2nd coordinate will enter in the precision of the position measured in the bending plane, ideally given by the middle tubes precision only. Even if the non parallelism is perfectly known this cannot be recovered. The available statistics were too small to observe these small effects.

C.1.2 Shifts in Special Directions

So far only misalignment parameters have been studied, which affect all translations and rotations (see chapter 7). In this section the effect of translations and rotations of MDT-chambers is studied independently. Figure C.11 shows the p_T-resolution versus η for misaligned layouts which are based on misalignment parameters $\sigma_m^{s,t,z} = 1$. It is expected that the effect of misalignment along the z-axis has a dominant effect, since this translation directly affects the sagitta measurement. The misalignment along the s-axis should have no effect on the p_T-measurement, since it corresponds to a translation along the drift-tubes. Also the misalignment along the t-axis of each chamber is expected to have only a very limited contribution to the p_T-resolution since this translation is parallel to the muon trajectory. All these expectations are fulfilled as can be seen in Figure C.11.

The impact of $\sigma_m^{Rot} = 1$, where only random rotations are applied, on the p_T-resolution are shown in Figure C.12. Note that a significantly larger effect due to rotations compared to translations on the p_T-resolution can be observed. This can be explained by the definition of the misalignment parameter and the application of rotations. The rotation of one MDT-chamber with a length of $6\,m$ by $1\,mrad$ leads to a difference in the position of $6\,mm$ for the tubes at both ends. This-relative shift of $6\,mm$ is dominant compared to a translation of $1\,mm$, both induced by a misalignment parameter $\sigma_m^{All} = 1$.

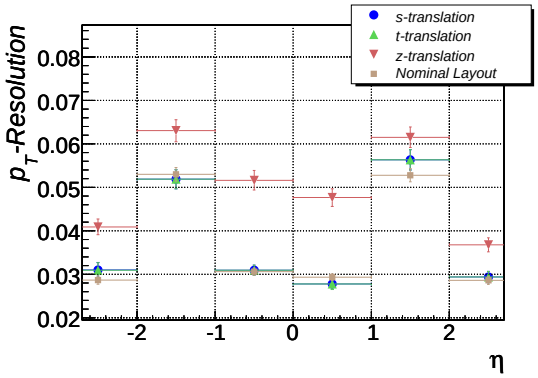

Figure C.11: p_T-resolution distribution for the independently translations.

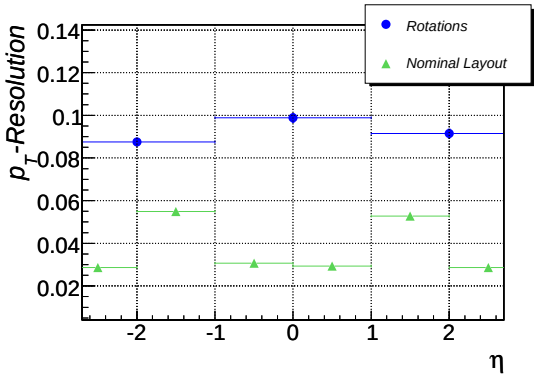

Figure C.12: p_T-resolution distribution for the independently rotations.

C.2 Egg-shape Layout Validation

Deformations of the ATLAS detector during the life-time of the experiment are expected due to the enormous weight of roughly 7.000 tons. To account for these deformations and to have a perfect circular symmetry after the first years of operation, it was decided to built the ATLAS Muon Spectrometer not with a perfect circular symmetry, but with a small egg-shape deviation, as schematically illustrated in Figure C.13. This layout was implemented in the geometry description of the ATLAS Muon Spectrometer. The chambers in sector 5 are systematically shifted by $7\,mm$ in y-direction, the chambers in sector 1 and 9 are shifted by $3.5mm$ in x- and y-direction in the global coordinate system. The MDT-chambers in sector 13 as well as the endcap-region of the spectrometer are not affected by the chosen layout. All other chambers were rotated and shifted to be tangential to the assumed egg-shape of the layout. Hence, the egg-shape layout introduced a ϕ-asymmetry in the Muon Spectrometer geometry[2].

It was chosen to use the egg-shape layout during the reconstruction step, while the simulation was based on the ideal symmetric Muon Spectrometer layout. No effects on the width of the p_T-resolution, as well as on the reconstruction efficiency could be observed, within the available Monte Carlo statistics. This is expected since the relevant displacements of the chambers are along axes which have only a weak effect on a possible shift of the sagitta, which was shown in section C.1.2. Nevertheless, a detailed study of the egg-shape layout offered the possibility to validate the standalone reconstruction algorithms based on minor changes in the geometry description.

As already mentioned, the impact of the egg-shape layout on the muon p_T-resolution is very small and the p_T-resolution of an ideally aligned Muon Spectrometer is already dominating and therefore covering the expected effects. Hence it was chosen to compare muon tracks reconstructed with an ideal spectrometer layout and the egg-shape layout on an event by event basis, i.e. the reconstructed track within one layout was directly compared to the reconstructed track of the same simulated muon within another layout.

The difference of the reconstructed transverse momenta for both layouts should show a ϕ-dependence in the barrel region. No difference is expected for sector 13, and a relative small impact for sector 1, 5 and 9. Figure C.14 confirms this expectation.

[2]Note, that the assumed shift of $7\,mm$ in the simulated layout is overestimated. The actual shift in the Muon Spectrometer is only $4\,mm$ in reality

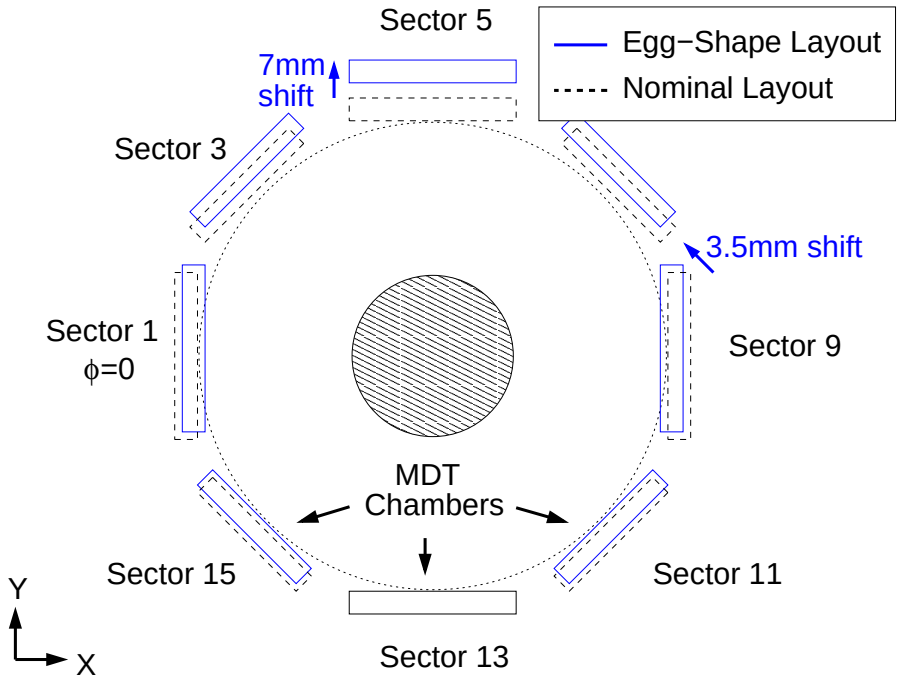

Figure C.13: Schematic illustration of the *Egg-Shape* layout.

The longitudinal impact parameter z_0 describes the distance of closest approach of a reconstructed track, to the interaction point, which is defined in the ATLAS coordinate system at (0,0,0). Note, that a muon track, which has been reconstructed standalone in the Muon Spectrometer, must be extrapolated to the beam line. The longitudinal impact parameter z_0 is also effected by the egg-shape layout. This can be most easily understood, considering a MDT-chamber in sector 5 next to the endcap. The corresponding η-value of this chamber is 1, which corresponds to an angle of 45°. Assuming that muon tracks are straight lines, which is justified for 50 GeV muons, a shift in y-direction for the chambers leads to an equivalent shift in z-direction for tracks at beam level, which has been illustrated in Figure C.15. No effect is expected for chambers at 0°. The average difference of the reconstructed impact parameters z_0 for both layouts versus η of the muons, is shown in Figure C.17 and Figure C.18 for sector 1 and sector 5 respectively. As expected, a linear dependence starting from $7mm$ in case of sector 1 and from $3.5mm$ in case of sector 5 to $-7mm$ and $-3.5mm$ is observed.

Introducing the quantity L_0, which is defined by

$$L_0 = d\phi \cdot d + dR_0 \tag{C.1}$$

allows a further validation, which is based on the ϕ measurement of the ATLAS Muon Spectrometer. The quantity $d\phi$ is the difference of the measured ϕ-value comparing the reconstruction of a muon track for both layouts, dR_0 is the difference of the reconstructed transverse impact parameters d_0[3]. The distance d from the beam pipe to the outer chamber is approximately $9800\,mm$. It is assumed that the ϕ-measurement is driven by the outer MDT- and RPC-chambers in the barrel region. The quantity L_0 can be interpreted most easily for sector 1 and 9, where it reflects the chamber shift in y-direction. The interpretation for sectors 3 and 7 is illustrated in Figure C.16, where it corresponds to the overall displacement

[3]The impact parameter d_0 is defined by $\sqrt{x_0^2 + y_0^2}$ and hence is the minimal distance of the track to the line $x = y = 0$

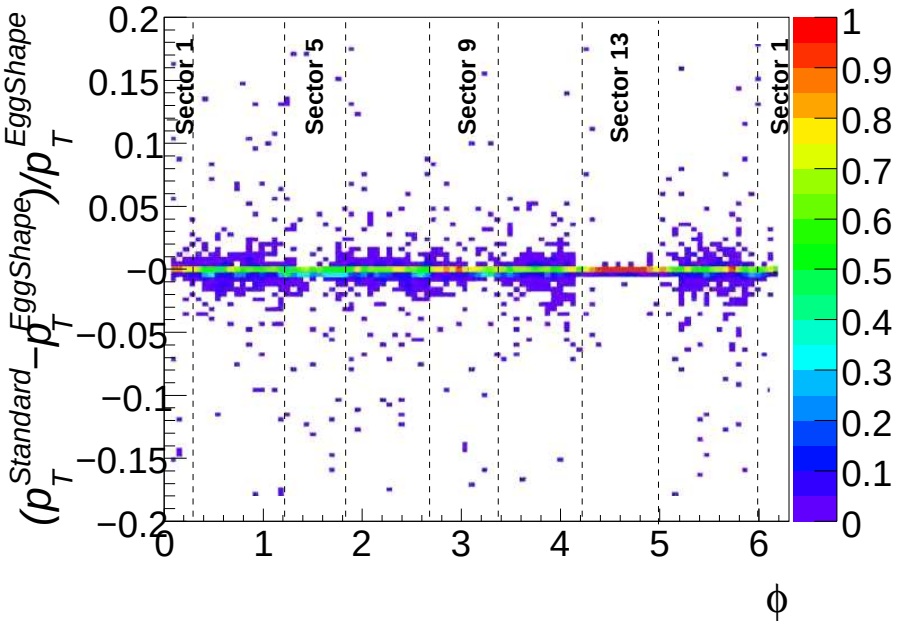

Figure C.14: Difference of reconstructed p_T's with nominal layout and reconstructed p_T's with *Egg-Shape* layout vs. ϕ.

of the chambers along the s-axis, defined in Figure C.1.

The measured average values for $d\phi$, dR_0, the resulting measured L_0 as well as the values, which are expected by geometrical considerations (Figure C.16), for four sectors are shown in Table C.2. The measured and expected values of L_0 coincide within their statistical uncertainty. The presented validation tests can be considered as a first hint, that the standalone reconstruction algorithms interpret even very sophisticated layouts like the Egg-Shape layout correctly.

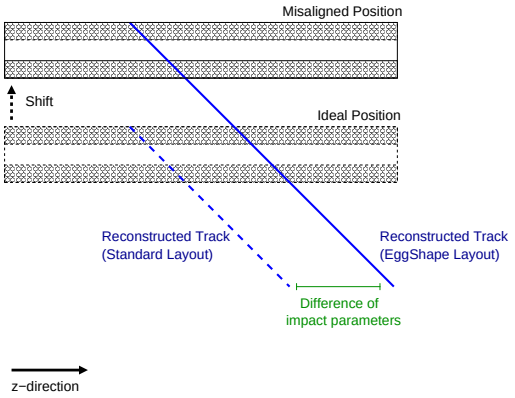

Figure C.15: Schematic illustration of the *Egg-shape* effect on the longitudinal impact parameter z_0.

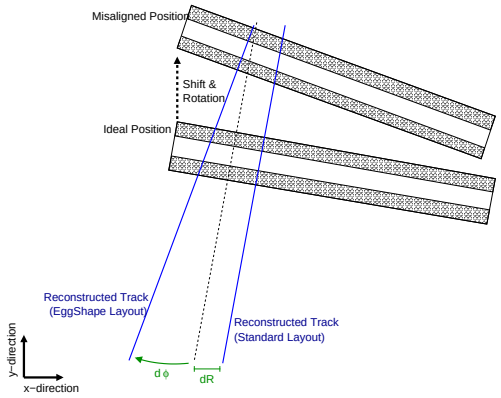

Figure C.16: Schematic illustration of the *Egg-shape* effect on the transverse impact parameter d_0.

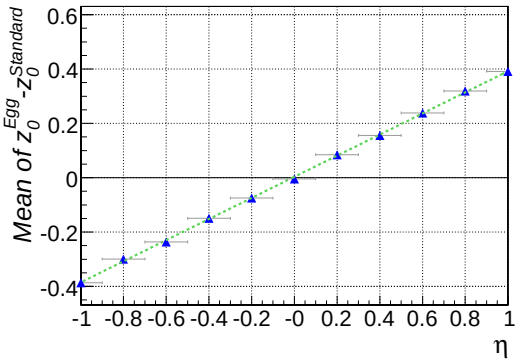

Figure C.17: Difference of reconstructed impact parameter z_0 with nominal layout and with *Egg-Shape* layout vs. η for Sector 1.

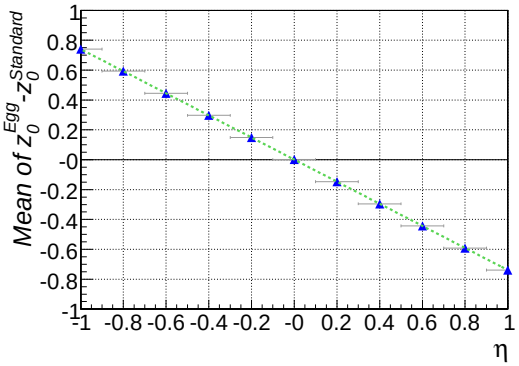

Figure C.18: Difference of reconstructed impact parameter z_0 with nominal layout and with *Egg-Shape* layout vs. η for Sector 5.

Sector	$d\phi$	dR_0 [mm]	**Measured L_0 [mm]**	**Expected L_0[mm]**
1	$(-2.7 \pm 0.3) \cdot 10^{-4}$	-1.1 ± 0.1	-3.65 ± 0.3	-3.5
3	$(-3.0 \pm 0.3) \cdot 10^{-4}$	-1.5 ± 0.2	-4.44 ± 0.4	-4.9
7	$(+2.8 \pm 0.3) \cdot 10^{-4}$	1.7 ± 0.2	$+4.44 \pm 0.4$	+4.9
9	$(+2.5 \pm 0.3) \cdot 10^{-4}$	1.4 ± 0.1	$+3.85 \pm 0.3$	+3.5

Table C.1: Comparison of measured and expected values of L_0 for different sectors.

C.3 Alignment and Determination of Sagitta-Shifts with the Process $Z \rightarrow \mu\mu$

As it was discussed in section C.1, the alignment of the Muon Spectrometer is a very important issue to ensure the expected performance. The general alignment-method of the Muon Spectrometer is the optical alignment system, which is expected to reach a relative precision of the chambers within one tower up to $30\,\mu m$ and an absolute precision in space of $300\,\mu m$ for large MDT-chambers [49]. The precision for small MDT-chamber is less precise and therefore it is foreseen to use a track-based alignment between large and small chambers [85].

Further methods for the alignment have been proposed to allow independent cross-checks of the optical alignment method. One approach, studied in detail in [86], makes use of the measured deflection angle in the inner and outer stations to extrapolate the relative positions of the MDT-chambers. A relative alignment can be also achieved by measuring the p_T in each MDT-chamber separately, which was first proposed in section B.1.4, and used and studied also in [86].

The extrapolation of tracks, which have been reconstructed only in the ATLAS Inner Tracker, could lead to an absolute alignment of the Muon Spectrometer. In a first step, the extrapolated inner track should be compared to a corresponding measured segment in an inner MDT-station. This comparison will lead to alignment information of the MDT-chamber. Having aligned all inner MDT-stations, the extrapolation can be extended to the middle stations and in a final step to the outer stations. This procedure has the advantage, that it allows an alignment relative to the ATLAS Inner Tracker. The serious disadvantages are obvious. First of all, the method relies on a perfect aligned Inner Tracker, secondly the material description between the Inner Tracker and the Muon Spectrometer must be very precise in order to account correctly for multiple scattering and energy loss fluctuations mainly in the

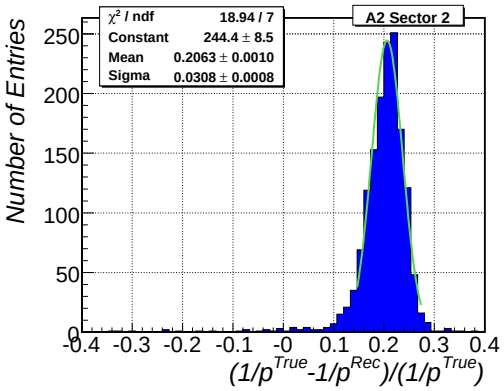

Figure C.19: Momentum resolution for a single misaligned MDT-tower (Endcap A-2, ϕ-sector 1) for 50 GeV positive charger muons.

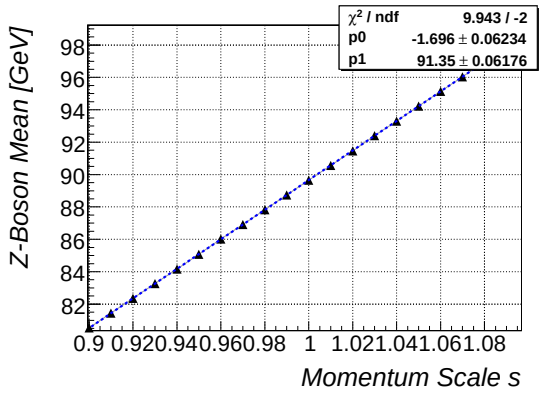

Figure C.20: Expected mean of Z boson mass distribution vs. the momentum scale s.

calorimeter.

The method presented here, is based on the decay of Z bosons into two muons. The goal is to determine the net-shift in the sagitta for each tower, i.e. always three MDT-stations, but not to determine the exact positions of the MDT-chambers in space. First of all, it has to be tested if the assumption of an overall shift in sagitta is justified. Figure C.19 shows the p_T-resolution of positive muons for the three MDT-chambers in *endcap A-2*[4] and ϕ-sector 1, where the positions of the chambers were misaligned based on $\sigma_m^{All} = 1$. The width of the p_T-resolution has slightly broadened, but even more important, a significant shift of the mean can be observed. Negative charged muons are expected to have a shift in the opposite direction by the same amount. This is a first hint, that the p_T-resolution for each tower can be modeled in a first approximation by a shifted ideal p_T-resolution distribution. The broadening of the overall p_T-resolution can be therefore interpreted as the sum of several shifted ideal p_T-resolution distributions. Note, that the net-sagitta Δs of each tower is directly associated to the shift of the p_T-resolution, via

$$p_T \sim \frac{1}{\frac{1}{p_T} + \Delta s} \approx p_T(1 + p_T \Delta s) \tag{C.2}$$

The basic idea of the method is to make use of the correlation between the measured mean of the Z boson resonance and the momentum scale of the muons. An independent momentum scale $s_i^{\pm}$, which can be introduced for each tower i, changes the measured transverse momentum $p_{T,i}$ of each muon track, via

$$p_{T,i}^{scaled} = p_{T,i}(1 + s_i^{\pm}) \tag{C.3}$$

and increases or decreases the measured momentum. The value of $s_i^{\pm}$ might be chosen so that

$$s_i^{\pm} = c_\mu s_i \tag{C.4}$$

where c_μ is the charge of the muon, i.e. the shift on the momentum scale is symmetric for both cases. This is correct to first order approximation, but the momentum scales must be determined independently for positive and negative charged muons in second order . The

[4]This corresponds to an η-region of $0.2 < \eta < 0.45$

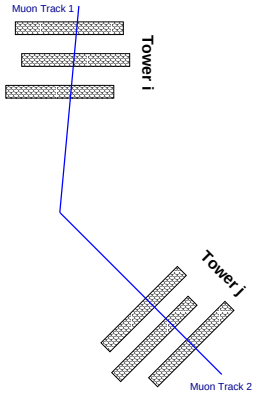

Figure C.21: Illustration of two misaligned towers and two muon track resoluting from a Z boson decay.

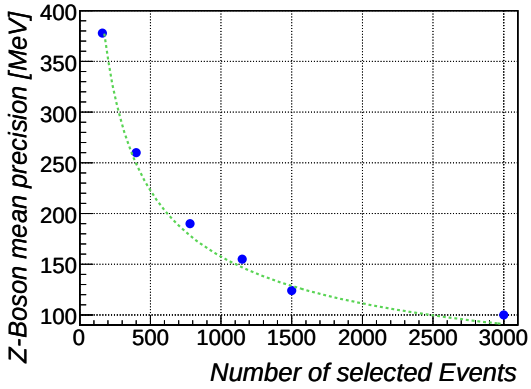

Figure C.22: Precision of the measured mean of the Z boson resonance vs. number of selected events.

shift on the momentum scale leads to a linear dependence with the measured mean of the Z boson resonance (See Figure C.20). The momentum scale changes the reconstructed Z bosons mass from two muons, which have been reconstructed in tower i and j as follows

$$M_{Z,ij}^{scale} = \sqrt{2.p_{T,1}^{scaled} p_{T,2}^{scaled}.(\cosh(\Delta\eta) - \cos(\Delta\Phi))} = M_{Z,ij}\sqrt{(1+s_i^{\pm})(1+s_j^{\pm})} \tag{C.5}$$

where $M_{Z,ij}$ refers to the unscaled Z boson mass. This can be further approximated by

$$M_{Z,ij}^{scale} \approx M_{Z,ij}\left(1 + \frac{s_i^{\pm} + s_j^{\pm}}{2}\right) \tag{C.6}$$

The momentum scales values of s_i and s_j can be determined by minimizing the negative likelihood function

$$-\ln L = \sum_{k=1}^{N} -\ln P\left(M_{Z,k} \cdot (1 + \frac{s_i^{\pm} + s_j^{\pm}}{2})\right) \tag{C.7}$$

where the function P gives the probability[5] for a certain Z boson mass peak, N is the number of total events and i and j indicate the corresponding towers used in event k. The maximization can be performed with a standard minimization program like *Minuit*. With this method, the momentum scales s_i are determined for each tower in such a way, that the measured Z boson mass is reproduced by the Monte Carlo simulation, which scales the simulated transverse momenta with the corresponding scaling factors.

In a final step, one has to relate Equation C.2 with Equation C.3. The impact of different values for Δs on the reconstructed muon momenta is studied within a Monte Carlo simulation. The value of Δs which reproduces the measured scaling factors s_i^+ and s_i^- is considered to be the net sagitta-shift of the chosen tower.

The statistical limitation of this method can be estimated by the precision of which the mean of the reconstructed Z boson mass distribution can be determined for each tower. Figure C.22 illustrates the precision of measured mean value of the Z boson resonance distribution in dependence of the number of selected events. To reach a precision for the net sagitta value Δs of $100\mu m$, in the order of 400 muons with the same charge per tower, resulting from a Z

[5]The probability function is given by the Monte Carlo predicted Z boson mass distribution.

boson decay, have to be selected and analyzed[6]. This corresponds to an integrated luminosity of roughly $100\,pb^{-1}$, assuming a signal cross-section of $1495\,pb$, to achieve a relative alignment of the ATLAS Muon Spectrometer. Therefore the method will not be applicable for the first days of the ATLAS experiment, but might be used during the high luminosity phase for a daily cross-check.

It should be noted, that these are only the expected statistical limitations. Systematic uncertainties arise from the final state radiation of muons, energy loss in the calorimeter and imperfect magnetic field calculations and have not been considered in this discussion.

[6] As a rule of thumb, a $50\,GeV$-track corresponds to a sagitta of $1cm$

"The trouble with doing something right the first time is that nobody appreciates how difficult it was."

Appendix D

Further Details to the Total Cross-Section Measurement

D.1 Alternative Method for Efficiency Determination

Another possibility to determine the reconstruction efficiency within data is to dispense the isolation cuts and apply only the two given cuts on p_T and a relative close mass window around $91\,GeV$. This leads to a dominant background contribution to the 'tag' and 'probe' muon sample in the lower $M_{\mu\mu}$-mass region as shown in Figure D.1. The background contribution can be estimated by applying an exponential function to the mass region between $45\,GeV$ and $60\,GeV$ and extrapolating this function into the Z boson mass peak as also shown in Figure D.1. The number of Z boson events in the 'tag' and 'probe' muon sample N_{TP} can be estimated by subtracting the function. The same approach is used to determine the number of Z boson events N_{MS} which have two reconstructed tracks in the Muon Spectrometer (Figure D.2). The efficiency of the Muon Spectrometer can then be calculated with N_{TP} and N_{MS} by

$$\varepsilon_{MS} \approx \frac{2 \cdot N_{MS}}{N_{TP} + N_{MS}} \tag{D.1}$$

The advantage of this method is that one has not to rely on a clean muon sample but in contrast make use of the dominant background contribution. The functional fit for the background contribution does not always converge and has a relatively large systematic uncertainty. The systematic uncertainty of N_{TP} is in the order of 3%, the systematic uncertainty of N_{MS} even in the order of 6%. The systematic uncertainty has been estimated by the variation on the fitting ranges between $45\,GeV$ and $60\,GeV$. Moreover this method can only be applied for relatively high statistics in order to allow a stable fitting. Assuming only the given systematic uncertainties, the reconstruction efficiency ε_{MS} is expected to have a systematic uncertainty in the order of 7%, which is worse than the results presented in section 8.3.

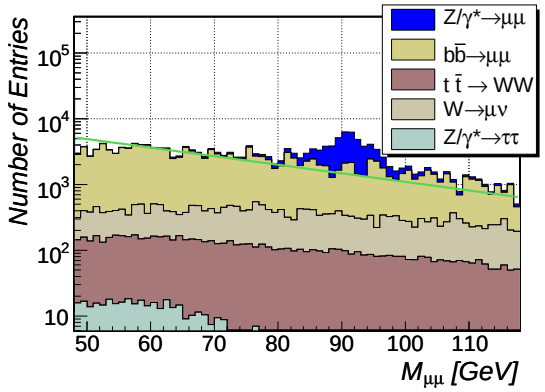

Figure D.1: Expected invariant Masses $M_{\mu\mu}$ resulting from two inner tracks where at least one of the muons must be matched to a Muon Spectrometer tracks

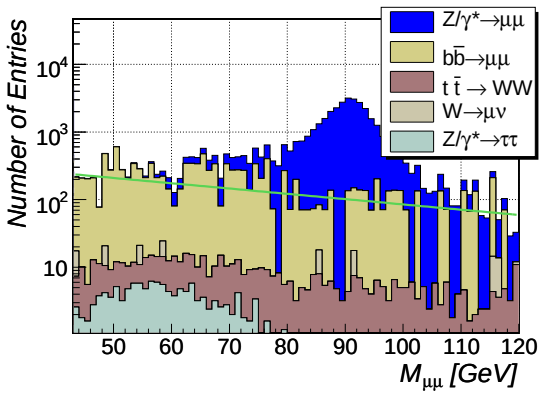

Figure D.2: Expected invariant Masses $M_{\mu\mu}$ resulting from two inner tracks where both can be be matched to Muon Spectrometer tracks

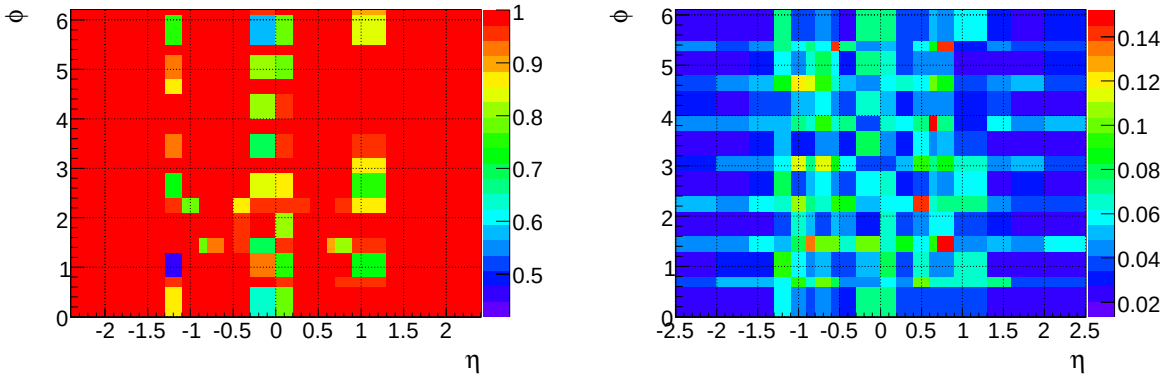

Figure D.3: Insitu-determined information of the Muon Spectrometer reconstruction efficiency which is provided for the ATLAS collaboration

D.2 ATHENA Algorithm for the In-Situ Determination of Efficiencies

The in-situ determination of the reconstruction efficiency is not only important for this study, but for all which depend on the Muon Spectrometer reconstruction of muon tracks. Therefore this algorithm was integrated in the ATHENA software framework. A detailed description can be found under *https://twiki.cern.ch/twiki/bin/view/Atlas/MuonRecValidator*. The package provides an in-situ efficiency determination in the $\eta-, \phi-$ plane and the corresponding uncertainties. An example of the output histograms of this ATHENA algorithm is shown in Figure D.3. The algorithm is fully flexible and can be adjusted to the users needs. Binning, cut selection and reconstruction algorithm can be specified for each data sample.

The given algorithm can also be used for the determination of muon trigger efficiencies at Level 1, Level 2 and *EventFilter*. Some example efficiency plots for the 6 GeV muon trigger for Level 1 and Level 2 can be seen in Figure D.4 and Figure D.5

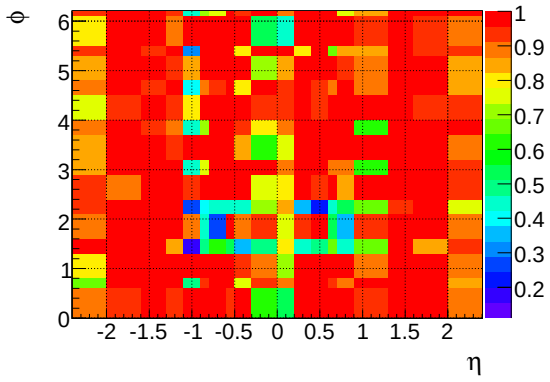

Figure D.4: Efficiency of LV1 Trigger vs. η and ϕ

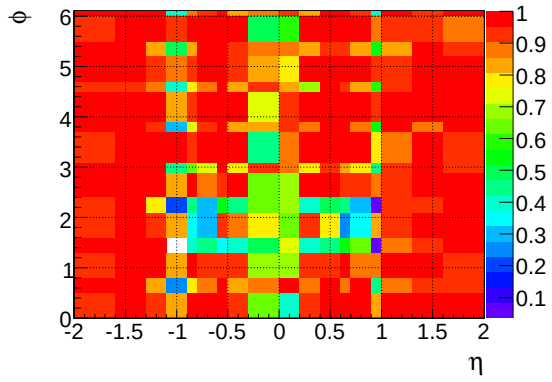

Figure D.5: Efficiency of LV2 Trigger with respect to initial data vs. η and ϕ

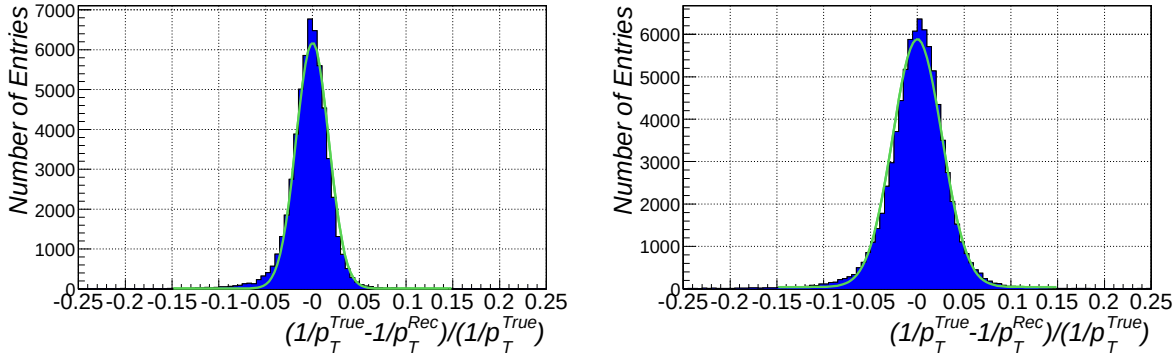

Figure D.6: p_T resolution of combined track reconstruction algorithm for a $Z \rightarrow \mu\mu$ sample for the barrel-region (left) and the endcap-region (right). Both distributions are fitted by a single Gaussian plus a constant background

D.3 Determination of p_T-Resolution without Explicit Monte Carlo Simulation Predictions

This approach for the p_T-resolution determination does not assume a Monte Carlo prediction of the p_T-resolution, but it is assumed that the resolution can be described in general by a Gaussian form for $1/p_T$ plus a small constant background to account for false reconstructed tracks. Figure D.6 shows the muon p_T-resolution predicted by full Monte-Carlo for combined tracking, fitted by a Gaussian with constant background. It can be concluded, that the Gaussian approximation is only applicable as a first order approximation, since it describes only the central part of the distribution but not the tail-region.

Figure D.7 and Figure D.8 illustrate the dependence of the measured mean and width of the Z boson mass distribution vs. the momentum scale s and the Gaussian smearing parameter σ. We observe a linear dependence for both variables. The statistical uncertainty on s and σ is therefore directly proportional to the measured mean and width of the Z boson mass distribution.

A systematic effect of this method arises mainly from the tail-fraction in Figure D.6, i.e. those muons which are not described correctly by assuming a Gaussian p_T-resolution. The impact of this systematic effect was studied by comparing the predicted resolution of a simple

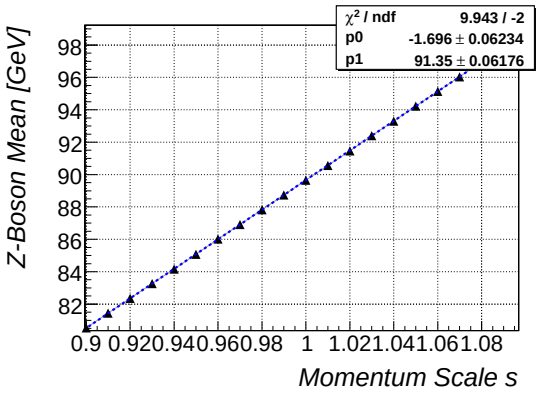

Figure D.7: Expected mean of Z boson mass distribution vs. the momentum scale s of the smearing function

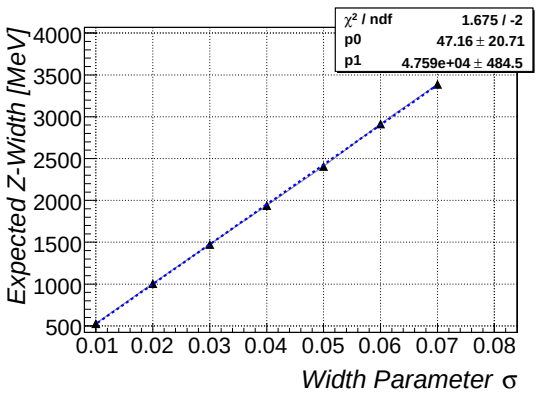

Figure D.8: Expected width of Z boson mass distribution vs. width σ of the smearing function f_s, which is used for the simulation of the p_T resolution.

Gaussian to the resolution predicted by a Gaussian plus constant background. A relative difference of 0.3 between the two determined resolutions is observed which is treated as systematic uncertainty of this approach. Finally, Figure D.9 shows the comparison of the in-situ determined resolution to Monte Carlo Truth prediction.

The overall p_T-resolution can be determined with this method and a luminosity of $50pb^{-1}$ to an expected relative precision of

$$\Delta s \approx 0.001(stat) + 0.002(sys) \qquad \Delta\sigma \approx 0.02(stat) + 0.3(sys)$$

where the systematic uncertainty is assumed to be a Gaussian sum of the difference between Monte Carlo truth and in-situ determined resolution, uncertainty due to the tail-fraction and due to the selection cuts. It is also assumed, that this systematic uncertainty is the same for each bin and not correlated. These results suggests, that even the rough Gaussian approximation of the p_T-resolution delivers reasonable results both for the momentum scale and the p_T-resolution itself. Hence, this approach might be used in the first phase of the ATLAS experiment, when one does not want to rely on a full Monte Carlo simulation of the experiment.

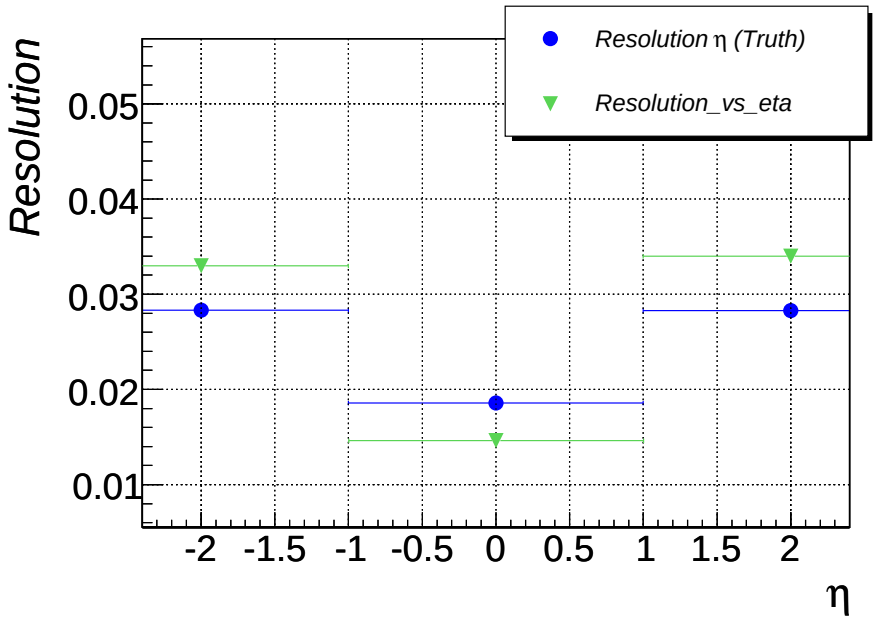

Figure D.9: Comparison of p_T-resolution determined via Monte-Carlo-Truth and the in-situ approach for combined track reconstruction vs. η

"If you don't have data, use color."

Appendix E

Further Details to the Differential Cross-Section Measurement

E.1 Improvement of the Muon p_T-Resolution for $Z \to \mu\mu$ Events

The transverse momentum of the Z boson is calculated from the measured transverse momenta of the decay muons,

$$p_T^Z = \sqrt{(\vec{p}_{T,1} + \vec{p}_{T,2})^2} \tag{E.1}$$

The muons decay mainly back to back in the ϕ-plane of the detector if the Z boson has a small transverse momentum. Therefore the value of p_T^Z is the difference between the two relatively large muon transverse momenta. This explains the relative poor p_T^Z-resolution for small p_T^Z as illustrated in Figure E.1. Larger transverse momenta of the Z boson lead to a smaller $\Delta\phi$ opening-angle and therefore to a better relative resolution.

An improvement of the muon p_T-resolution would also lead to an improved p_T^Z-resolution. This would allow a finer binning, especially in the lower p_T^Z-regions, where the statistical uncertainty is not dominating. Moreover, systematic uncertainties due to the purity of bins could be decreased in this way. In the following, three possible approaches are discussed to improve the p_T-resolution both for Muon Spectrometer standalone and combined muon track reconstruction. The basic idea of all presented methods is to use the precise knowledge of the Z boson mass as an additional constraint for the measured transverse momentum of the muons resulting from a Z boson decay.

E.1.1 Z Boson Mass Constraint and Kinematic Fit

The mass of the Z boson can be calculated with the four momenta of both decay muons by

$$M_Z^2 = \left[\begin{pmatrix} E_1 \\ \vec{p}_1 \end{pmatrix} + \begin{pmatrix} E_2 \\ \vec{p}_2 \end{pmatrix} \right]^2 \approx 2p_1 p_2 (1 - \cos\alpha)$$

where the mass of the muons is neglected and α is the opening angle between both muons. This equation can be rewritten to

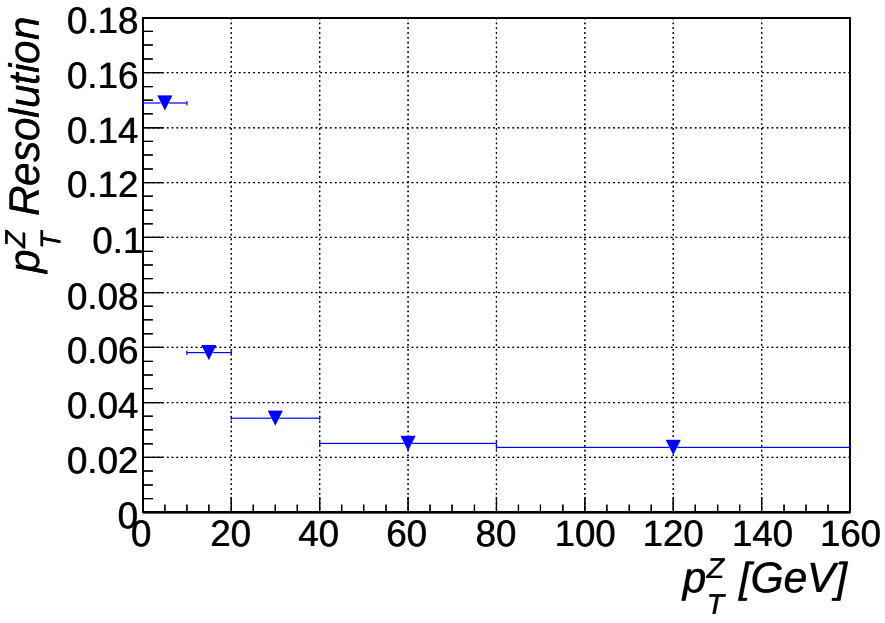

Figure E.1: p_T^Z-Resolution of combined muon reconstruction vs. p_T^Z

$$M_Z^2 = 2 \cdot p_{T,1} p_{T,2} \cdot (\cosh(\Delta\eta) - \cos(\Delta\Phi)) \tag{E.2}$$

using the pseudo-rapidity definition $\eta = -\ln(\tan(\frac{\theta}{2}))$. It is assumed that the difference $\Delta p_T := |p_T^{Rec} - p_T^{Truth}|$ of the reconstructed transverse momentum of the muon p_T^{Rec} to its true value p_T^{Truth} is proportional to the square of the muon's transverse momentum,

$$\Delta p_T \sim p_T^2.$$

With this assumption, the reconstructed value of p_T^{Rec} can be corrected via

$$p_T^{Rec} \rightarrow p_T^{Rec}.(1 + \varepsilon p_T^{Rec}) \tag{E.3}$$

Since the mass of the Z boson is known to very high precision, it can be used to determine the value for ε independently for both muons by the Z mass constraint by

$$\left(p_{T,1}^{Rec} + \varepsilon_1 \cdot \left(p_{T,1}^{Rec}\right)^2\right)\left(p_{T,2}^{Rec} + \varepsilon_2 \cdot \left(p_{T,2}^{Rec}\right)^2\right) = \frac{M_Z^2}{2 \cdot (\cosh(\Delta\eta) - \cos(\Delta\phi))} \tag{E.4}$$

where ε_1 is the correction for the first muon and ε_2 for the second muon. Equation E.4 has two unknown variables and hence one more assumption is needed to find a unique solution. It was chosen to assume for this study, that the correction factors for both muons are equal $\varepsilon_1 = \varepsilon_2 = \varepsilon$, which leads to the following solution for ε

$$\varepsilon_{a,b} = -\frac{1}{2}.\left(\left(\frac{1}{p_{T,1}} + \frac{1}{p_{T,2}}\right) \pm \frac{1}{(p_{T,1} \cdot p_{T,2})}\sqrt{((p_{T,1} - p_{T,2})^2 + \frac{2 \cdot M_Z^2}{(\cosh(\Delta\eta) - \cos(\Delta\phi))}}\right) \tag{E.5}$$

The correct solution can be identified by the requirement, that the correct transversal momentum must be positive.

Two approximations are made in this method. First of all, it is assumed that the Z boson mass is $\sim 91.2\,GeV$ and has no width. Secondly, it is assumed, that both muons are measured equally bad.

A similar approach is called *kinematic fit*, which also uses the Z boson mass constraint but modifies the measured transverse momentum of the muons with the following constraint. The difference of the measured p_T and the corrected p_T of each muon should be minimal, in order to result on the Z boson mass. In order to fulfil this constraints, the χ^2-function

$$\chi^2(p^C_{T,1}) = \left(\frac{\frac{1}{p^M_{T,1}} - \frac{1}{p^C_{T,1}}}{\Delta\frac{1}{p^M_{T,1}}} \right)^2 + \left(\frac{\frac{1}{p^M_{T,2}} - \frac{1}{p^C_{T,2}}}{\Delta\frac{1}{p^M_{T,2}}} \right)^2 \tag{E.6}$$

must be minimized, where $p^M_{T,i}$ is the measured and $p^C_{T,i}$ the corrected transverse momentum of muon i. The uncertainty of $\Delta\frac{1}{p^M_{T,1}}$ is determined by the muon track fit algorithm. The corrected transverse momentum of the second muon is calculated via the Z boson mass constraint

$$p^2_T = \frac{M^2_Z}{2 \cdot p^1_T \cdot (\cosh(\Delta\eta) - \cos(\Delta\phi))}$$

The value of $p^{1,C}_T$ which minimizes Equation E.6 is determined with the *Minuit-Fit* algorithm.

Applying these two methods on muon tracks reconstructed with a Muon Spectrometer standalone and a combined reconstruction leads to the overall p_T-resolution distributions, shown in Figure E.2, E.3, E.4 and E.5, respectively.

For both methods a shift in the momentum scale by 0.005 and broadening of the p_T-resolution can be observed, which worsens the expected muon reconstruction performance.

So far, only the overall effect of the various correction methods on the muon p_T-resolution has been studied. It is reasonable to assume that the p_T-resolution of muons can be improved for some special configurations like high p_T muons or for special η-regions in the detector.

Figure E.6 shows the comparison of the p_T-resolution of the standalone muon reconstruction for the different methods versus η, where no significant η-dependence can be observed. For all η values a degradation of the resolution is seen for both methods to roughly equal extend. It is likely that the reason for the degradation lies in the assumption on the fixed mass constrainted of $91.2\,GeV$. Figure E.7 shows also the p_T-resolution of muons versus η but this time the correct truth di-muon mass information from Monte Carlo generator level was used for the mass constraint. An overall improvement of the resolution is the consequence.

One might naively expect that large differences of the reconstructed di-muon mass to the Z Boson mass, i.e. $|M^{Rec}_{\mu\mu} - 91.2\,GeV|$, enhance an improvement of the p_T resolution. Large differences $|M^{Rec}_{\mu\mu} - 91.2\,GeV|$ indicate that the p_T measurement of the muons must have a relatively large error, since the reconstructed width of the Z Boson is significantly larger than the truth width. Hence, the mass constraint should lead to an improvement of the p_T resolution.

For small differences $|M^{Rec}_{\mu\mu} - 91.2\,GeV| < 2\,GeV$, no significant improvement can be observed, which is shown in Figure E.8 and Figure E.9. The p_T resolution for the usual standalone muon reconstruction and the mass constrained reconstruction for larger differences $10\,GeV < |M^{Rec}_{\mu\mu} - 91.2\,GeV| < 12\,GeV$ is shown in Figure E.10 and Figure E.11, respectively. Also in this case, no improvement can be seen. In contrary, the p_T resolution degrades. This is explained in the following.

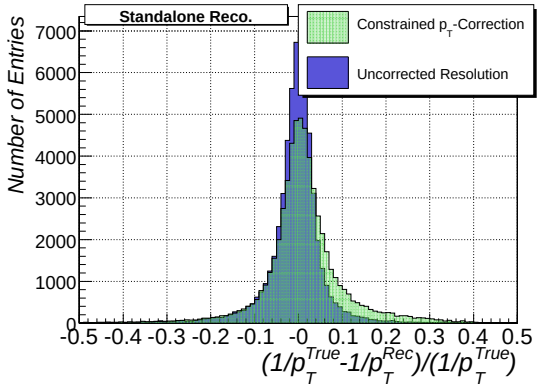

Figure E.2: Comparison of the uncorrected standalone p_T-resolution and the corrected p_T-resolution with the Z mass constraint for Muon Spectrometer standalone reconstruction.

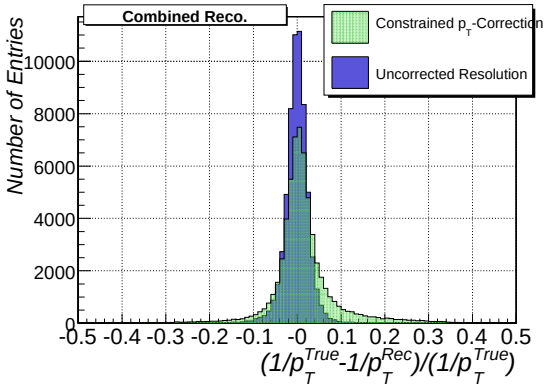

Figure E.3: Comparison of the uncorrected combined p_T-resolution and the corrected p_T-resolution with the Z mass constraint for combined muon reconstruction.

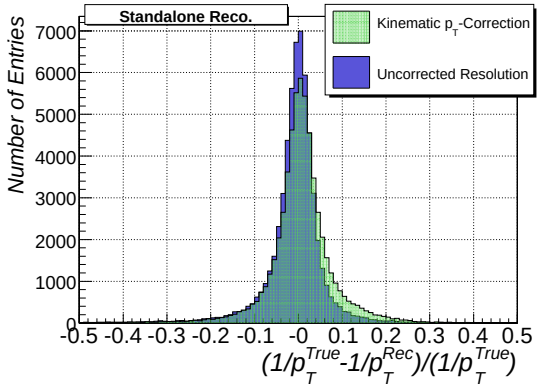

Figure E.4: Comparison of the uncorrected standalone p_T-resolution and the corrected p_T-resolution with the kinematic fit.

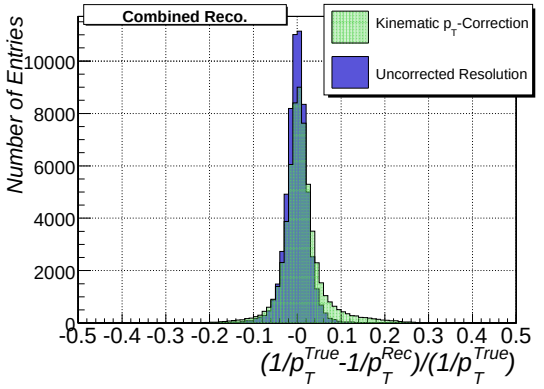

Figure E.5: Comparison of the uncorrected combined p_T-resolution and the corrected p_T-resolution with the kinematic fit.

The probability that a lower reconstructed di-muon mass also originates from a lower truth di-muon mass rises with higher differences to $91.2\,GeV$. Hence, this wrong assumption leads to a wrong correction factor for both muons. This argument is supported by the green shaded distribution in Figure E.10, which is for the events with $|M_{\mu\mu}^{Truth} - 91.2\,GeV| < 8\ GeV$. These events have a large difference of the reconstructed to the truth di-muon mass and hence we expect a broader distribution. The peak, which is still visible, reflects the fact that only one muon might have been measured wrongly.

For these events one might argue that the mass constraint results in some improvement when comparing to Figure E.11. However, the non overlapping blue part represents events where the large difference of $M_{\mu\mu}^{Rec}$ to $91.2\,GeV$ is due to a already large difference of $M_{\mu\mu}^{Truth}$ to $91.2\,GeV$. Clearly, this causes a large degradation of the resolution.

There is also a second effect which could cause the degradation of the p_T resolution when applying the mass-constraint correction. One assumption of the mass-constraint p_T-correction is that $\varepsilon_1 = \varepsilon_2 = \varepsilon$. To test this assumption, two new variables are introduced:

$$\sigma_{max}^{\mu} = max(\sigma_1^{\mu}, \sigma_2^{\mu}), \qquad \sigma_{min}^{\mu} = min(\sigma_1^{\mu}, \sigma_2^{\mu})$$

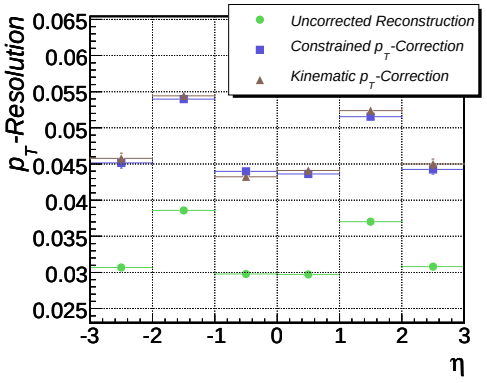

Figure E.6: Comparison of the uncorrected p_T-resolution and the corrected p_T-resolution for standalone reconstruction vs. η of the muons.

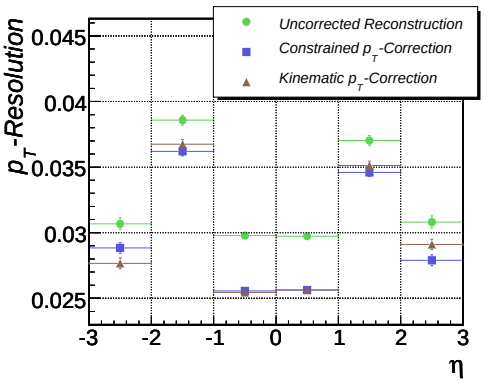

Figure E.7: Comparison of the uncorrected p_T-resolution and the corrected p_T-resolution for standalone reconstruction vs. η of the muons when the truth di-muon mass was used for the correction.

with

$$\sigma_i = \left|\frac{p_{T,i}^{True}}{p_{T,i}^{Rec}} - 1.0\right|$$

where $p_{T,1}^{True}$ is the true momentum and $p_{T,1}^{Rec}$ is the reconstructed momentum of muon 1, i.e. σ_i represents the momentum resolution of the i-th muon. Plotting the average value of σ_{max}^{μ} and σ_{min}^{μ} versus $|M_{\mu\mu}^{Rec} - 91.2\,GeV|$ reveals that σ_{min}^{μ} is constant at the expected resolution of the Muon Spectrometer to a good extend for all differences, while the average value of σ_{max}^{μ} is significant larger (Figure E.13). Clearly, the assumption $\varepsilon_1 \approx \varepsilon_2 \approx \varepsilon$ does not hold. Moreover, a strong dependence of σ_{max}^{μ} to the mass difference can be observed in the edge region of the Z Boson resonance. This dependence indicates that in the regime of $4\,GeV < |M_{\mu\mu}^{Rec} - 91.2\,GeV| < 10\,GeV$ events with one mis-reconstructed muon (and $M_{\mu\mu}^{true} \approx 91.2\,GeV$) still dominates while events with a large $|M_{\mu\mu}^{True} - 91.2\,GeV|$ difference get more important for $10\,GeV < |M_{\mu\mu}^{Rec} - 91.2\,GeV|$.

Figure E.12 shows the p_T resolution for muons with an invariant di-muon mass of $10\,GeV < |M_{\mu\mu}^{Rec} - 91.2\,GeV| < 12\,GeV$ using the Monte Carlo truth di-muon mass for the mass constrained correction. The two extrema which were present in Figure E.11 vanish and a improvement of the overall p_T resolution can be observed. Hence the effect of wrongly assuming the $91.2\,GeV$ seems to be dominant, since the $\varepsilon_1 = \varepsilon_2 = \varepsilon$ does not hold also in this case. This also explains that the kinematic fit gives comparable results to the mass-constraint fit in Figure E.6 and Figure E.7, since only the Z boson mass assumption was made but not $\varepsilon_1 = \varepsilon_2 = \varepsilon$.

It should be noted, that these results apply only for a calibrated and aligned Muon Spectrometer. Possible misalignment effects lead to a significant degradation of the expected muon momentum resolution and the discussed methods might lead to a significant improvement. To verify this, these methods have also been tested on a simulated Z boson sample which is based on a misaligned geometry of the ATLAS Muon Spectrometer (See section 7). An overall improvement of the p_T-resolution of 20% has been observed. This indicates that the presented algorithms might become relevant in the first phase ATLAS when alignment and calibration issues are not fully understood.

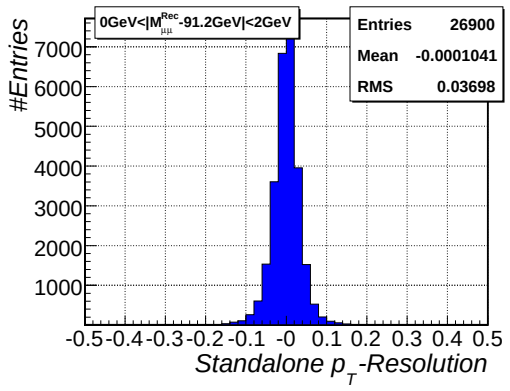

Figure E.8: p_T-resolution for standalone reconstruction for the muons with an invariant mass $0\,GeV < |M^{Rec}_{\mu\mu} - 91.2\,GeV| < 2\,GeV$.

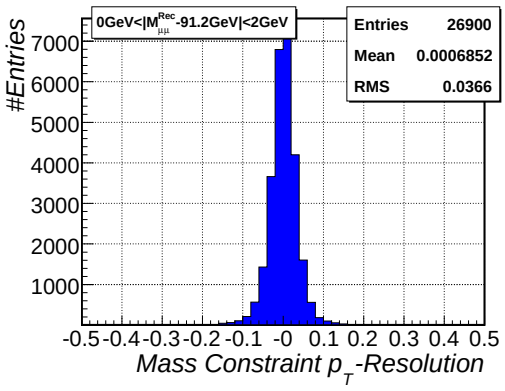

Figure E.9: Corrected p_T-resolution for standalone reconstruction for the muons with an invariant mass $0\,GeV < |M^{Rec}_{\mu\mu} - 91.2\,GeV| < 2\,GeV$.

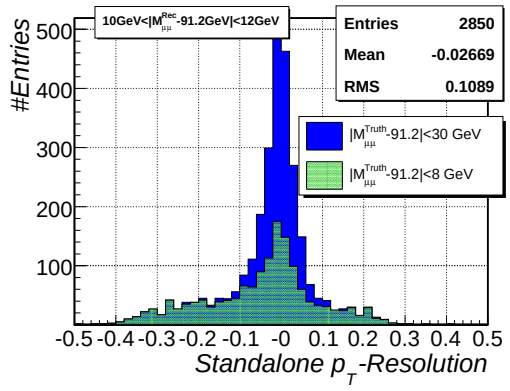

Figure E.10: p_T-resolution for standalone reconstruction for the muons with an invariant mass $10\,GeV < |M^{Rec}_{\mu\mu} - 91.2\,GeV| < 12\,GeV$. The distribution for the events with $|M^{Truth}_{\mu\mu} - 91.2\,GeV| < 8\,GeV$ is indicated as green shaded area.

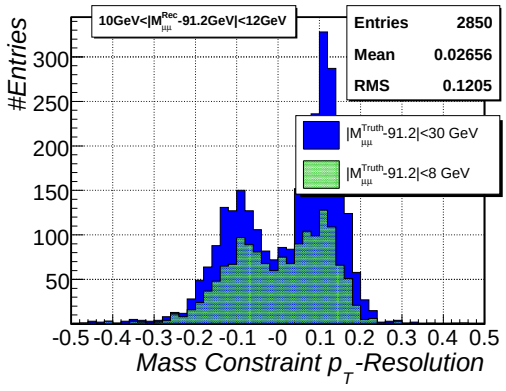

Figure E.11: Corrected p_T-resolution for standalone reconstruction for the muons with an invariant mass $10\,GeV < |M^{Rec}_{\mu\mu} - 91.2\,GeV| < 12\,GeV$. The distribution for the events with $|M^{Truth}_{\mu\mu} - 91.2\,GeV| < 8\,GeV$ is indicated as green shaded area.

E.1.2 Improved Kinematic Fit

One possibility to improve the kinematic fit, is to make use of the measured missing transverse energy $\vec{\not{E}}_T$, which is correlated to the transverse momentum of the hadronic recoil. The sum of $\vec{\not{E}}_T$ and the muon based reconstructed transverse momentum of the Z boson should be zero. This information could be used as an additional constraint in Equation E.6. This approach was not chosen for this study, since the missing transverse energy is a rather complex quantity and might not be understood in full detail for the first phase of LHC.

As already seen in section E.1.1, it is advantageous to make use of the truth di-muon mass and not use a fixed mass constrained of $91.2\,GeV$, which is not correct in general. To overcome this problem an new method is proposed which accounts for the width of the Z boson mass distribution, by defining the following χ^2-function

$$\chi^2(p^C_{T,1}, p^C_{T,2}) = \left(\frac{\frac{1}{p^{Rec}_{T,1}} - \frac{1}{p^C_{T,1}}}{\Delta\frac{1}{p^{Rec}_{T,1}}} \right)^2 + \left(\frac{\frac{1}{p^{Rec}_{T,2}} - \frac{1}{p^C_{T,2}}}{\Delta\frac{1}{p^{Rec}_{T,2}}} \right)^2 - \log(p(M_{\mu\mu}(p^2_{T,1}, p^2_{T,2}))). \tag{E.7}$$

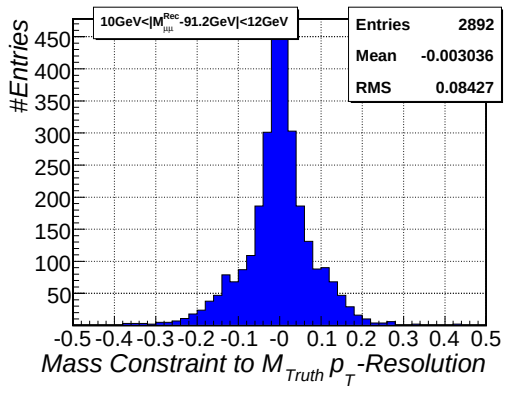

Figure E.12: Corrected p_T-resolution for standalone reconstruction for the muons with an invariant mass $10\,GeV < |M^{Rec}_{\mu\mu} - 91.2\,GeV| < 12\,GeV$ when using the truth di-muon mass for the correction.

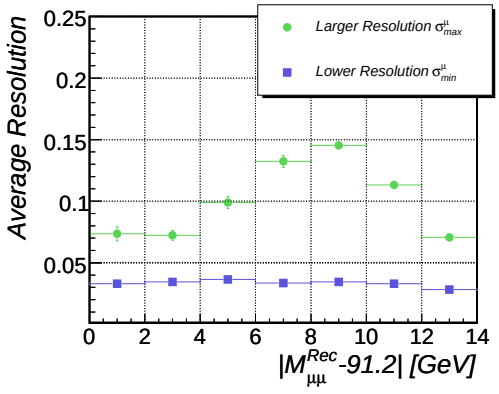

Figure E.13: The average value of σ^{μ}_{max} and σ^{μ}_{min} versus the difference $|M^{Rec}_{\mu\mu} - 91.2\,GeV|$. A strong depedence of σ^{μ}_{max} in the edge-region of the Z boson resonance can be seen.

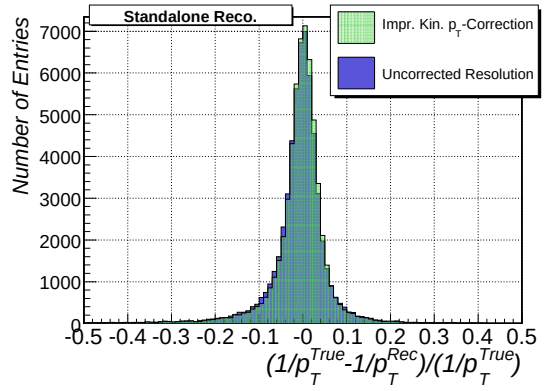

Figure E.14: Comparison of the uncorrected standalone p_T-resolution and the corrected p_T-resolution with the improved kinematic fit.

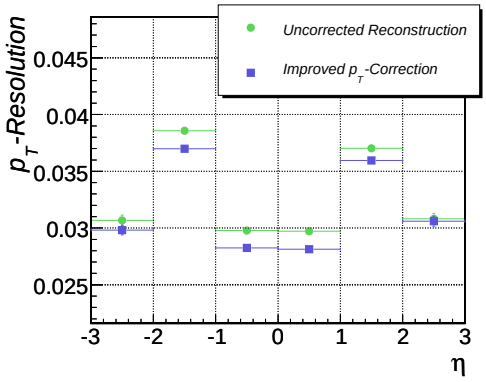

Figure E.15: Comparison of the uncorrected p_T-resolution and the corrected p_T-resolution for standalone reconstruction vs. η of the muons.

The function p is the probability for a di-muon mass $M_{\mu\mu}$, predicted by PYTHIA. This term introduces a dependence of the fit on reconstructed di-muon mass. The p_T of the muons are not forced anymore to give the Z boson mass of $91.2\,GeV$, but can vary according the expected Z boson mass distribution. The values for $p^C_{T,1}$ and $p^C_{T,2}$ which minimize Equation E.7 are again calculated with a *Minuit-Fit* algorithm. The results for the *improved kinematic fit* is shown in Figure E.14 for standalone reconstruction. We observe no significant change in the momentum scale and an improvement in the width of the p_T-resolution.

The overall improvement of the p_T resolution versus η can be also seen in Figure E.15 for the stand alone muon reconstruction. The improvement of the combined reconstruction p_T resolution is negligible, assuming a fully operating and perfectly calibrated ATLAS detector. Nevertheless, the presented *improved kinematic fit* has the best performance of all studied methods and might be applicable in the first phase of the ATLAS experiment, when alignment and calibration tasks are still in progress.

Bibliography

[1] M. Schott. Measurement of $pp \to z \to \mu\mu$ cross section at the ATLAS experiment with first data. *Acta Physica Polonica B*, 38:483–488, 2007.

[2] M. Schott, N. Benekos, L. Chevalier, and J.-F. Laporte. Impacts of misalignment in the ATLAS Muon Spectrometer on the measured z boson resonance. *Nucl. Instrum. Meth.*, 572:16–17, 2007.

[3] N. C. Benekos, S. Baranov, A. Barashkou, L. Chevalier amd J. F. Laporte, J. F., D. Pomarede, S. Goldfarb, T. Moore, D. Rebuzzi, M. Schott, S. Spagnolo, and I. Trigger. Muon detector description as built and its simulation for the ATLAS experiment. *Nucl. Instrum. Meth.*, 572:14–15, 2007.

[4] M. Schott. Cross section measurement. *ATLAS Communication*, ATL-COM-PHYS-2007-032, 2008.

[5] M. Schott. Differential cross section measurement. *ATLAS Communication*, ATL-COM-PHYS-2007-033, 2008.

[6] M. Schott, G. Duckeck, and M. Obermaier. Study of the sagitta resolution of mdt-chambers. *ATLAS Public Note*, ATL-MUON-PUB-2006-010, 2006.

[7] M. Schott, N. Benekos, J.-F. Laporte, and L. Chevalier. Impacts of misalignments of the muon spectrometer performance. *ATLAS Communication*, ATL-COM-MUON-2007-007, 2008.

[8] N.C. Benekos, G. Dedes, D. Rebuzzi, and M. Schott. ATLAS Muon Spectrometer simulation and its validation algorithms. *ATLAS Communication*, ATL-COM-MUON-2007-003, 2007.

[9] P. A. M. Dirac. A theory of electrons and protons. *Proc. Roy. Soc. Lond.*, A126:360, 1930.

[10] M. E. Peskin and D. V. Schroeder. An introduction to quantum field theory. Reading, USA: Addison-Wesley (1995) 842 p.

[11] F. Halzen and A. D. Martin. Quarks and Leptons: An introductory course in modern particle physics. New York, Usa: Wiley (1984) 396p.

[12] J. Goldstone, , A. Salam, and S. Weinberg. Broken symmetries. *Phys. Rev.*, 127:965–970, 1962.

[13] W. M. Yao et al. Review of particle physics. *J. Phys.*, G33:1–1232, 2006.

[14] Peter W. Higgs. Broken symmetries, massless particles and gauge fields. *Phys. Lett.*, 12:132–133, 1964.

[15] T. W. B. Kibble. Symmetry breaking in non-abelian gauge theories. *Phys. Rev.*, 155:1554–1561, 1967.

[16] R. P. Feynman. Mathematical formulation of the quantum theory of electromagnetic interaction. *Phys. Rev.*, 80:440–457, 1950.

[17] G. Altarelli and G. Parisi. Asymptotic freedom in parton language. *Nucl. Phys.*, B126:298, 1977.

[18] G. 't Hooft and M. J. G. Veltman. Regularization and renormalization of gauge fields. *Nucl. Phys.*, B44:189–213, 1972.

[19] G. Abbiendi et al. Tests of the standard model and constraints on new physics from measurements of fermion pair production at 183-gev at LEP. *Eur. Phys. J.*, C6:1–18, 1999.

[20] P. Ramond. Supersymmetry in physics: An algebraic overview. *Physica*, 15D:25, 1985.

[21] W. Buchmuller, R. Ruckl, and D. Wyler. Leptoquarks in lepton quark collisions. *Phys. Lett.*, B191:442–448, 1987.

[22] S. Hossenfelder. The minimal length and large extra dimensions. *Mod. Phys. Lett.*, A19:2727–2744, 2004.

[23] P. Nadolsky, D. R. Stump, and C. P. Yuan. Semi-inclusive hadron production at hera: The effect of QCD gluon resummation. *Phys. Rev.*, D61:014003, 2000.

[24] J. Botts et al. Cteq parton distributions and flavor dependence of sea quarks. *Phys. Lett.*, B304:159–166, 1993.

[25] G. Altarelli, G. Parisi, and R. Petronzio. Transverse momentum in drell-yan processes. *Phys. Lett.*, B76:351, 1978.

[26] Y. Nambu. Qcd and the string model. *Phys. Lett.*, B80:372, 1979.

[27] M. Wagner. *The pseudoparticle approach in SU(2) Yang-Mills theory.* PhD thesis, Friedrich-Alexander-Universität, Erlangen, Germany, 2006.

[28] T. D. Gottschalk. An improved description of hadronization in the qcd cluster model for e+ e- annihilation. *Nucl. Phys.*, B239:349, 1984.

[29] T. Sjostrand, S. Mrenna, and P. Skands. Pythia 6.4 physics and manual. *JHEP*, 05:026, 2006.

[30] G. Marchesini et al. Herwig: A monte carlo event generator for simulating hadron emission reactions with interfering gluons. version 5.1 - april 1991. *Comput. Phys. Commun.*, 67:465–508, 1992.

[31] S. Frixione and B. R. Webber. The mc@nlo event generator. 2002.

[32] G. A. Ladinsky and C. P. Yuan. The nonperturbative regime in qcd resummation for gauge boson production at hadron colliders. *Phys. Rev.*, D50:4239, 1994.

[33] F. Landry, R. Brock, P. M. Nadolsky, and C. P. Yuan. Tevatron run-1 z boson data and collins-soper-sterman resummation formalism. *Phys. Rev.*, D67:073016, 2003.

[34] F. Landry, R. Brock, G. Ladinsky, and C. P. Yuan. New fits for the non-perturbative parameters in the css resummation formalism. *Phys. Rev.*, D63:013004, 2001.

[35] Precision electroweak measurements on the z resonance. *Phys. Rept.*, 427:257, 2006.

[36] R. K. Ellis, W. J. Stirling, and B. R. B. R. Webber. QCD and collider physics. *Camb. Monogr. Part. Phys. Nucl. Phys. Cosmol.*, 8:1–435, 1996.

[37] S. Myers. The LEP collider, from design to approval and commissioning. Presented at CERN Accelerator School: The LEP Collider from Design to Approval and Commissioning, Geneva, Switzerland, Nov 26, 1990, CAS: CERN accelerator school, 6th John Adams Memorial lecture.

[38] M. Ahlers, A. Ringwald, and H. Tu. Cosmic rays at ultra high energies (neutrinos!). *Astropart. Phys.*, 24:438–450, 2006.

[39] O. Bruning (Ed.) et al. Lhc design report. vol. i: The lhc main ring. CERN-2004-003-V-1.

[40] ATLAS Collaboration. ATLAS: Detector and physics performance technical design report. volume 1. CERN-LHCC-99-14.

[41] ATLAS Collaboration. ATLAS magnet system: Technical design report. CERN-LHCC-97-18.

[42] ATLAS Collaboration. ATLAS inner detector: Technical design report. vol. 1. CERN-LHCC-97-16.

[43] ATLAS Collaboration. ATLAS detector and physics performance. technical design report. vol. 2. CERN-LHCC-99-15.

[44] A. J. Barr et al. Beamtests of prototype ATLAS SCT modules at CERN H8 in 2000. Prepared for 7th Workshop on Electronics for LHC Experiments, Stockholm, Sweden, 10-14 Sep 2001.

[45] K. Kleinknecht. Detektoren fuer teilchenstrahlung. Germany: Teubner (2005) 245p.

[46] A. Airapetian et al. ATLAS calorimeter performance. CERN-LHCC-96-40.

[47] C. Clement, March 2000. CALOR2000 Conference, Annecy, France.

[48] ATLAS Collaboration. ATLAS Tile Calorimeter. Technical Design Report. CERN/LHCC 96-42.

[49] ATLAS Collaboration. ATLAS muon spectrometer: Technical design report. CERN-LHCC-97-22.

[50] ATLAS Collaboration. ATLAS high-level trigger, data acquisition and controls: Technical design report. CERN-LHCC-2003-022.

[51] I. Aitchison. Supersymmetry and the mssm: An elementary introduction. 2005.

[52] G. Brooijmans. Top quark mass measurements at the tevatron. 2000.

[53] G. D'Agostini and G. Degrassi. Constraining the higgs boson mass through the combination of direct search and precision measurement results. 2000.

[54] G. Duckeck (ed.) et al. ATLAS computing: Technical design report. CERN-LHCC-2005-022.

[55] S. Agostinelli et al. Geant4: A simulation toolkit. *Nucl. Instrum. Meth.*, A506:250–303, 2003.

[56] J. Boudreau and V. Tsulaia. The GeoModel toolkit for the ATLAS detector. Proceedings of the CHEP04 Conference, Interlaken, Switzerland, 2004.

[57] I. Bird (ed.) et al. Lhc computing grid. technical design report. CERN-LHCC-2005-024.

[58] M. Virchaux et al. Muonbox: a full 3d tracking programme for muon reconstruction in the ATLAS spectrometer. *ATLAS Note*, ATL-MUON-97-198, 1997.

[59] Combined muon track reconstruction with STACO. http://atlas-samusog.web.cern.ch/atlas-samusog/muonboy/DocPublishedTexts/phytdr.staco.pdf, 2007.

[60] J.F. Laporte et al. Impact of the initial layout on the ATLAS Muon Spectrometer performance. *ATLAS Communication*, ATL-COM-MUON-2005-007, 2005.

[61] O. Biebel et al. A cosmic ray measurement facility for ATLAS muon chambers. *ATLAS Note*, ATL-MUON-2004-004, 2003.

[62] M. Obermaier. *Integration of calibration and alignment procedures for the reconstruction of muons in the ATLAS detector*. PhD thesis, Ludwig-Maximilians-Universität, Munich, Germany, 2005.

[63] L. Chevalier and A. Bruni. Measured and simulated B-field contributions, April 2007. ATLAS Magnetic Field Workshop.

[64] D. Rebuzzi. Reconstruction studies with ATLAS-CSC-01-XX-00 databases, January 2007. ATLAS Higgs Working Group meeting.

[65] F. Rauscher. *Untersuchung des Verhaltens von Driftrohren bei starker γ Bestrahlung sowie Vermessung von Driftrohrkammern mit Hilfe von Myonen der kosmischen Höhenstrahlung*. PhD thesis, Ludwig-Maximilians-Universität, Munich, Germany, 2005.

[66] G. Reiter. Studien zur myonisolation, May 2007. LMU Group Meeting, LS Schaile.

[67] M. Boonekamp et. al. Cosmic Ray, Beam-Halo and Beam-Gas Rate Studies for ATLAS Commissioning. *ATLAS Note*, ATL-GEN-2004-001, 2004.

[68] P. Petroff. W and z boson production in $p\bar{p}$ collisions from run ii of the tevatron collider. 2005.

[69] M. Bellomo. *ATLAS muon trigger performance and luminosity measurements of W boson*. PhD thesis, UniversitÃ degli Studi di Pavia, Pavia, Italy, 2006.

[70] L. Kashif. Effects of chamber misalignment, March 2007. Combined Muon Reco and Common Tracking Working Group Meeting.

[71] S. Frixione and M. L. Mangano. How accurately can we measure the W cross section? *JHEP*, 05:056, 2004.

[72] M. Boonekamp. Luminosity measurement in ATLAS. Prepared for 12th International Workshop on Deep Inelastic Scattering (DIS 2004), Strbske Pleso, Slovakia, 14-18 Apr 2004.

[73] M. Rijssenbeek. Luminosity measurement at the lhc. Prepared for 14th Topical Conference on Hadron Collider Physics (HCP 2002), Karlsruhe, Germany, 29 Sep - 4 Oct 2002.

[74] Bryan Lawrence Caron. Luminosity measurement at the large hadron collider. UMI-NR-13944.

[75] CMS Collaboration. Cms physics tdr: Volume ii (ptdr2), physics performance. *Nucl. Part. Phys.*, 34:995–1579, 2006.

[76] B. Leonhardt. *Das Transversalimpulsspektrum des Z-Bosons in $p\bar{p}$ Kollisionen am Tevatron.* PhD thesis, Ludwig-Maximilians-Universität, Munich, Germany, 2004.

[77] S. Berge, P. Nadolsky, F. Olness, and C. P. Yuan. Transverse momentum resummation at small x for the Tevatron and LHC. *Phys. Rev.*, D72:033015, 2005.

[78] S. Berge, P. Nadolsky, F. Olness, and C. P. Yuan. Tevatron Run-1 Z boson data and Collins-Soper-Sterman resummation formalism. *Phys. Rev.*, D67:073016, 2003.

[79] ATLAS Wiki page for the muon geometry in data challenge 3. https://twiki.cern.ch/twiki/bin/view/Atlas/MuonGeometryDC3, 2007.

[80] D. Rousseau. Informpation about the Athena-Aware NTuple. https://twiki.cern.ch/twiki/bin/view/Atlas/AthenaAwareNTuple, 2007.

[81] K.A. Assamagan et al. Final Report of the ATLAS AOD/ESD Definition Task Force. *ATLAS Internal note*, ATLAS-SOFT-2004-006, 2004.

[82] RunTimeTest Web Page. http://www.hep.ucl.ac.uk/atlas/AtlasTesting/RTTUserGuide/RTTUserGuide.html, 2007.

[83] R. L. Gluckstern. Uncertainties in track momentum and direction, due to multiple scattering and measurement errors. *Nucl. Instrum. Meth.*, 24:381–389, 1963.

[84] E. Ezion and S. Rosati. System test of the ATLAS muon spectrometer in the H8 beam at the Cern SPS, 2004. Presentation given at the IEEE Nuclear Science Symposium, Rome, Italy.

[85] S. Kotov. Alignment of muon chambers with tracks, 2006. Presentation given at the ATLAS-D workshop Heidelberg.

[86] J. Schmaler. *Track-based Alignment of the ATLAS Muon Spectrometer.* PhD thesis, Max Planck Institut für Physik, Munich, Germany, 2007.

Acknowledgments

Above all, I thank my beloved wife Kathrin for enduring my travels to Munich and Geneva over last two and a half years with her never ending patience and understanding. I want to thank her for her support, for her love, for giving me encouragement and for tolerating my moods even in difficult times.

It is also a great pleasure to thank my thesis advisor Prof. Dorothee Schaile, not only for helping me to focus on the important questions - even when I got lost again - in the details of my analysis, but especially for trusting me in the first place by giving me, coming from nuclear theoretical physics, this opportunity to do a PhD in high energy experimental physics.

I have very much enjoyed the intensive work with Günter Duckeck. It is due to his patience, experience and prospective that I found a quick way into experimental physics. I also greatly benefited from working together with Raimund Ströhmer, who has a really unbelievable feeling for correlations. Results which in the first place seemed strange to me turned out - after a short discussion - to be expected and not strange at all. My lack of theoretical understanding of physics was always cured by long discussions with Prof. Otmar Biebel and I am very thankful to him for answering all my questions.

I wouldn't have been able to finish this thesis in time without meeting Nectarios Benekos during my stay at CERN. He introduced me to the ATLAS collaboration, became a friend and influenced my stay in Geneva in the best possible way. I also want to thank the only two persons, who I think capable of thinking in four dimensions: Laurent and Jean-Francois, who helped me greatly in some tricky parts of this thesis. I appreciated the numerous discussions with my former CERN office partner David Primor in the restaurant, which always helped me to relax after a long night full of work. This late-night work was eased by the company of my MPI-colleagues Jörg Dubbert and Georgios Dedes. I also tremendously enjoyed the relaxing coffee meetings all over Europe with Selma Uhlig and Arne Weber, the most clever PhD students in theoretical physics I know. The standard-model convenors, Maarten Boonekamp and Tom LeCompte, as well as Lucia Di Ciaccio and their support and input for my thesis must not be forgotten. I am also grateful to have Oliver Kortner as a partner editor for our CSC-note especially due to his outstanding organizing talent.

The members of the Munich group, Johannes Elmsheuser, Frank Fiedler, Julien de Graat, Petra Haefner, Ralf Hertenberger, John Kennedy, Christian Kummer, Martin Lamprecht, Doris Merkl, Thomas Nunnemann, Matthias Obermaier, Felix Rauscher, Gaby Reiter, Benjamin Ruckert, Cedric Serfon and Britta Tiller, managed to create a most stimulating environment for a graduate student, which was one of the main reasons to spend so many hours on the train to Munich. In particular I want to mention Raphael Mameghani, Alexander Grohsjean, Thomas Müller, Gernot Krobath, Philippe Calfayan and especially Marion Lambacher who have became far more than colleagues over the past years.

The financial support of my PhD scholarship of the *Studienstiftung der deutschen Wirtschaft* allowed me the greatest possible freedom during my graduate years. I am even more grateful for the company of the other scholarship holders from Bavaria. In this context I would like to mention Sabine Döschl especially who has become a friend during this time.

With the end of my graduate time, a new chapter in my life begins and I think it is worth looking back and thanking those, who helped me to get this far. I am thankful to my former physics teacher at school Mr. Miericke who taught me not only basic physics, but also inspired me with his enthusiasm for CERN. During my studies, Prof. Rudolf Maier from Jülich and Prof. Frieder Lenz from Erlangen allowed me a first glance at the beauty of physics, an inspiration which has never left me. It is due to my tutor Dr. Jan Pawlowski and my diploma thesis advisor Prof. Manfred Dillig that physics is not only fascinating but

also fun and my passion. Also my former short-term boss, Dr. Peter Molar from Siemens Managements Consulting, must be mentioned here who gave me the decisive piece of advice: “Go to CERN to get your PhD and you will learn everything you need in life.” - I have the feeling he was right.

Words are not enough to express my gratitude to my parents, Renate and Helmut, and also my siblings, Christian and Mareike. They helped me in every possible way during the last years. Also the support of my wifes family, Heidi, Jürgen, Markus and Florian will never be forgotten. Finally, I don’t want to forget those persons in my life, who have accompanied me for several years in every possible situation and have kept me sane: My oldest friends Tom and Verena; my Cambridge friends Yin, the best medical scientist I know, Robert, my personal advocate and Naweed, our near future European parliamentarian; not to forget my old friend Alexander who taught me a healthy degree of self-esteem and Meike, my train travel-mate for over two years now. Last but not least, I want to thank my closest friend and best man Marc.

Curriculum Vitae

Matthias Schott

Birthday:	23.Feb.1979
Birthplace:	Nuremberg/Germany
Family status:	married / no children

Academic Carrer

Sept. 2004 -
Doctorate Studies in Physics

Ludwig-Maximilian-University, Munich/Germany and CERN, Geneva/ Switzerland Topic of PhD-thesis:

- Study of the Vector-Boson Production at the ATLAS Experiment at LHC (Experimental Physics)

Oct. 1999 - May 2004
Physics diploma
(Grade: 1,0)

Friedrich-Alexander-University, Erlangen/Germany
Topic of Diploma thesis

- Barionic systems on the lightcone (Theoretical Physics)

May 2000 - Sept. 2003
Bachelor of Science (Mathematics)

Friedrich-Alexander-University, Erlangen/Germany
Topic of Bachelor thesis

- Development of a neural network model based on the sea snail Aplysia (Computer Science)

Sept. 2001 - June 2002
Natural Science Part II

University of Cambridge, Cambridge/United Kingdom

June 1998
Abitur

Hardenberg-Gymnasium Fuerth, Bavaria/Germany
Equivalent to A-levels in GB. Followed by Civil Service at the Malteser-Hilfsdienst, Nuremberg/Germany (1998-1999)

Teaching

May 2005 -
CERN-Guide

Official guide for CERN-visitors for all experiments. Since March 2007 also CERN-lecturer.

May 2005 - July 2005
Tutor

Ludwig-Maximilian-University, Munich/Germany
Experimental Physics II

Nov. 2003 - July 2004
Tutor

Friedrich-Alexander-Universität, Erlangen/Germany

- Introduction to Theoretical Physics
- Theoretical Physics I: Mechanics

Summer Schools

August 2006 Summer-School	CERN-Fermilab Hadron Collider Physics Summer School Fermilab, USA
September 2004 Summer-School	Saalburg Summer-school, Seifhennersdorf/Germany Designed for PhD-students in theoretical physics
July/August 2002 Summer-School	DESY, Hamburg/Germany Summer-student with Dr. Ringwald and the topic: • Cross-section of Instanton-processes in the MSSM-model
August 1999 Summer-School	Research Centre Jülich, Jülich/Germany Summer-student with Prof. Meier and the topic: • Determination of the emmitance of a proton beam

Professional Experience

April-June 2004 Temporary Consultant	Siemens Management Consulting (SMC), Munich/Germany SMC is an internal Top-Management Consulting for the Siemens AG.
2001-2002 Freelancer	medien—design, Nuremberg/Germany medien—design is a medium-sized enterprise which offers customer orientated IT-solutions.
April 2000 Intern	Center for Research in Computer Graphics (CRCG) with Dr. Coleman, Providence/USA CRCG is a profit orientated research lab for Computer Graphics.

Awards and Scholarships

Jan. 2005 - Scholarship	Stiftung der dt. Wirtschaft (Foundation of the German Economy) PhD-scholarship
Sept. - Dec. 2004 Scholarship	Post Graduate Program *New Frontiers in High Energy Physics* of the DFG (German Research Association) PhD-scholarship
2002-2004 Scholarship	Stiftung der dt. Wirtschaft (Foundation of the German Economy) Undergraduate Scholarship
March - May 1999 Jugend-forscht	State and National Competition for young researchers Development of a biometric identification system via face and voice recognition • 1. place in the state competition. • 5. place in the national competition.